Structure and Dynamics of Magnetorheological Fluids Confined in Microfluidic Devices

by

Ramin Haghgooie

B.S.E. Chemical Engineering, University of Michigan (2001),
M.Eng. Chemical Engineering Practice, Massachusetts Institute of Technology (2003).

Submitted to the Department of Chemical Engineering
in partial fulfillment of the requirements for the degree of

Doctor of Philosophy in Chemical Engineering

at the

MASSACHUSETTS INSTITUTE OF TECHNOLOGY
[September 2006]
August 2006

Author_____
Department of Chemical Engineering
August 9, 2006

Certified by_____
Patrick S. Doyle
Doherty Associate Professor of Chemical Engineering
Thesis Supervisor

Accepted by_____
William M. Deen
Chairman, Department Committee on Graduate Students

Structure and Dynamics of Magnetorheological Fluids Confined in Microfluidic Devices

by
Ramin Haghgooie

Submitted to the Department of Chemical Engineering
on August 9, 2006, in partial fulfillment of the
requirements for the degree of
Doctor of Philosophy in Chemical Engineering

Abstract

Microfluidic devices and magnetorheological (MR) fluids have been two areas of intense research for several years. Traditionally, these two fields have remained separated from one another by scale. MR fluids are best known for their use in large-scale applications such as seismic dampers for the foundations of buildings. Recently however, there has been strong interest in utilizing the micro-structure formed by self-assembled MR fluids as structural components in microfluidic devices.

MR fluids are composed of micron-sized paramagnetic colloids suspended in a non-magnetic carrier fluid. When an external magnetic field is applied to the MR fluid it induces dipole moments in the paramagnetic colloids causing them to interact and self-assemble into solid-like structures. In the past few years, self-assembled MR fluids have found use as structural components in a variety of micro-scale applications since their use provides an attractive alternative to traditional lithography as a means to create micro-scale structures. The advantages of using MR fluids include the ability to easily and inexpensively create sub-micron structures as well as the ability to create "dynamic structures" that can be controlled with an external magnetic field. In order for self-assembled MR fluids to be useful as structural components in microfluidic devices, we must understand the mechanisms and parameters governing their self-assembly under the confinement induced by the microfluidic channels.

In this thesis we present a series of studies merging the areas of microfluidics and MR fluids. The systems we studied are technologically relevant as well as ideal for understanding the fundamental processes at work in the self-assembly of MR fluids under confinement. Using the Brownian dynamics simulation technique as well as experimental studies with microfluidic channels, we have illuminated many of the governing physical mechanisms involved in the self-assembly of MR fluids confined in microfluidic channels. In particular, we determined that the channel dimensions play a crucial role in dictating both the final structure as well as the dynamics of the MR fluid structures in these systems. We performed a systematic study of the structure and dynamics of MR fluids confined in two-dimensional (2D) channels with an external magnetic field directed normal to the channel in order to produce a state-diagram for the system as a function of the channel width and the magnetic field strength (the two controlling thermodynamic parameters). We further investigated the effects of the channel height and characterized the behavior of the system in the transition from quasi-2D to 3D microchannels. The behavior of the MR fluid structures in this transition region was found to depend heavily upon the volume fraction of the MR fluid and the

height of the microchannel. We fully characterized the pore-size between clusters for dilute MR fluids self-assembled in quasi-2D microchannels, as it is an important parameter for microfluidic DNA mapping devices. Both the 2D and quasi-2D model systems provided valuable insight into the important mechanisms governing confined self-assembly.

The impact of this work will be two-fold. Our study of the model systems of 2D channels and the transition from quasi-2D to 3D have made an important contribution to the literature on the physics of condensed matter systems. In particular, 2D colloidal systems are of great interest as models for self-assembly and phase transitions. Our work has illustrated how the presence of confining boundaries affects the behavior of 2D colloidal systems. Furthermore, the study of the quasi-2D system has shown how the interaction energy between MR fluid clusters dictates the structure that forms in this geometry. In addition to the fundamental scientific questions we have addressed, our work will also have a broad impact on the design of microfluidic devices utilizing self-assembled MR fluids. We have illustrated this design process with two examples but the possibilities for merging microfluidic device technology with MR fluids will provide many more applications in the years to come.

Thesis Supervisor: Patrick S. Doyle
Title: Doherty Associate Professor of Chemical Engineering

Acknowledgments

As is the case with most accomplishments in life, this work could not have been done without the support of many caring people. I would first like to thank my advisor Pat Doyle for everything he has done for me over the past five years. I could not have asked for a better guide as I made my way through the ups and downs of PhD research. Pat has served not only as a research advisor but also as a motivator and a career advisor. He has helped me countless times with any number of problems ranging from difficulties with my research to career choices and assistance. I have been truly lucky to be a member of the Doyle group at MIT and I know it will continue to benefit me in the years to come.

Professors Gareth McKinley and Alan Hatton have also been an extremely helpful addition to my thesis committee. They have been most helpful with offering advice on my research and in helping with my career planning. In addition, I'd like to thank the other faculty and staff in the Chemical Engineering Department at MIT that have helped me along the way.

I would also like to thank all of the members of the Doyle group for their friendship and academic support. In particular, I owe a large debt of gratitude to Patrick Underhill and Thierry Savin who entered MIT at the same time as I did. Patrick has been an invaluable resource and sounding board over the years as I have encountered obstacles in my research. Thierry contributed greatly to the analysis of my experiments especially in the use of IDL for multiple particle tracking. They have both been true friends and I have enjoyed sharing my life with them for the past five years. In addition to Patrick and Thierry, I would like to thank Greg Randall, Dhananjay Dendukuri, and

Dan Pregibon for their help with getting my experiments to work. They are all talented experimental researchers and have offered me many useful tips on performing microfluidic experiments. Chen Li also deserves my gratitude for her tireless work as an undergraduate researcher to help me gather experimental data.

In addition to the academic support offered by the group members mentioned above, I would like to thank all past and present members of the Doyle group for their friendship and moral support. I will always remember our trips to get coffee in the morning (especially with Ju Min Kim), our gossip sessions in the office (my source shall remain anonymous ... Double D), and all of the interesting office games that we have played over the years with Greg, Patrick, Dan, and Dhananjay. I have also made a host of other friends while at MIT who have helped me academically but mostly morally by engaging in many fun activities outside of the office. I would especially like to thank (in alphabetical order) Adi Augustine, Chad Augustine, Brad Cicciarelli, Wanda Lau, Anna Pisania, Daryl Powers, Mike Rappel, Keith Tyo, and Patrick Underhill for their great friendship.

I would finally like to thank my family for their tremendous support, which remains ongoing after 27 years! Special thanks to my mom and dad, Marcella and Mohammad Haghgooie, for their unconditional love and support during all of the phases of my life. My sister Anna Haghgooie has always been supportive and has kept me in touch with the reality that exists outside the walls of MIT for which I am ever thankful. I'd like to thank my nana, Mary O'Brien, who lives in the Boston area and has provided me with a sanctuary where I can escape from the rigors of MIT and enjoy great conversations and chicken salad. Additionally, my uncle, Paul O'Brien, has helped me fix my car at least five times over the past five years and has always been willing to help me with any problem I might have. I would like to thank my parents in law, Michael and Sia Pisania for their support and for warmly welcoming me into their family. My brother in law Nikolas Pisanias deserves my thanks for all of his help in learning about Greek culture which brings me to my final thank you. Last but not least, I would like to express my deepest gratitude to my wife, Anna Pisania, who I met at the new student orientation here at MIT. Without her, I would not have been able to maintain my sanity through this process. She has been nothing but wonderful and supportive since the day I met her and I am truly thankful to have her in my life. I look forward to many happy years together after we leave MIT. *Ευχαριστώ πολύ αγάπη μου.*

Funding for this research was provided by the MIT Institute for Soldier Nanotechnologies and NSF Grant No. CTS-0304128

Table of Contents

List of Figures

CHAPTER 1

Introduction

The work in this thesis represents the intersection of two vibrant areas of research, field-responsive fluids and microfluidic devices. Individually, these areas have been the subject of intense research for many years [1, 2] and only recently have they been merged into a new field where the structures formed by field-responsive fluids have been used as structural components in microfluidic devices [3, 4].

1.1 Magnetorheological Fluids

A magnetorheological fluid, or MR fluid, is a field-responsive fluid that changes it's properties under the application of an external magnetic field. MR fluids are composed of micron-sized super-paramagnetic colloidal particles suspended in a non-magnetic carrier fluid (Figure 1.1a). Paramagnetic materials have no net dipole moment in the absence of magnetic fields but acquire a dipole moment when subjected to an external magnetic field. Super-paramagnetic colloids are paramagnetic colloids capable of forming large-scale clusters that overcome the thermal forces trying to break them apart. Therefore, when an external magnetic field is applied to the MR fluid, the colloids acquire dipole moments aligned with the external field causing them to interact and form large-scale clusters spanning the size of the entire sample (Figure 1.1b). The formation of these large-scale clusters causes a change in the rheological properties of the MR fluid, increasing its apparent viscosity. When the external field is removed, the paramagnetic colloids lose their

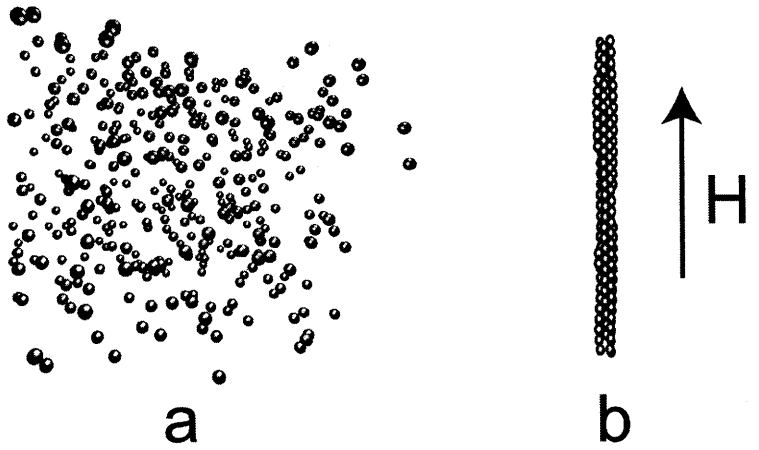

Fig. 1.1: *(a) Schematic of a suspension of MR colloids with no external magnetic field applied. (b) Cluster of MR colloids formed under the application of a uniform external magnetic field.*

magnetization and the MR fluid returns to the simple colloidal suspension state with no more magnetic interactions between the colloids. MR fluids are distinct from a similar class of magnetic fluids known as ferrofluids in the following ways. Ferrofluids are composed of nanometer-sized ferromagnetic colloidal particles suspended in a non-magnetic carrier fluid. Ferromagnetic materials have a permanent dipole moment even in the absence of external magnetic fields unlike paramagnetic materials which only have induced dipoles as mentioned previously. The dipole moments in ferrofluid colloids are much smaller than in MR colloids and therefore the large aggregates found in MR fluids under the application of a magnetic field do not occur in ferrofluids. Subsequently the change in rheological properties is much smaller for ferrofluids than in MR fluids. Ferrofluids do, however, exhibit some very interesting pattern formation and free surface properties under the application of a magnetic field and have therefore been studied extensively [5]. Additionally, in many cases, the theories used to model the behavior and structure of ferrofluids due to external magnetic fields, can also be applied to MR fluids.

The MR effect was first discovered in 1948 by Jacob Rabinow who immediately recognized the implications of such field-responsive fluids for use in electro-mechanical devices [1]. Concurrently however, Willis Winslow published the first detailed report in 1949 on the analogous electrorheological (ER) phenomenon [6]. Winslow studied suspensions of silica gel particles suspended in low viscosity oils and he reported the following features of ER fluids. When an external electric field is applied to the suspension, the colloids cluster into long fibrous structures aligned with the field and spanning the distance between the electrodes. When the external field is removed, the clusters dissolve and the system returns to the colloidal suspension state. While the external field is applied, the ER fluid behaves as a solid at very low shear stresses and the force required to shear the ER fluid increases proportionally to the square of the magnitude of the external field. Finally, the ER effect increases with the volume fraction of colloids in the suspension and as the dielectric constant of the colloids is increased.

The properties of ER fluids observed by Winslow are generally identical to the properties of MR fluids. As a class of field-responsive fluids however, MR fluids have proven advantageous over ER fluids. ER fluids are limited by dielectric breakdown and therefore can not be used under the application of large magnitude external fields. MR fluids on the other hand can be placed in large magnitude magnetic fields and are only limited by the saturation magnetization of the paramagnetic material. This feature means that the yield strengths of MR fluids can be 10-100 times larger than for ER fluids. Additionally, ER fluids tend to be caustic and therefore not particularly suited for long-life commercial applications. For these reasons, a number of current commercial applications utilize MR fluids such as seat suspension systems for cars, tunable resistance aerobic equipment, and seismic dampers for damping the effects of an earthquake on the foundations of buildings.

1.1.1 Interactions Between MR Colloids

MR colloids are typically composed of a non-magnetic structure or scaffolding in which ferromagnetic material is embedded in the form of ~10 nm particles containing a permanent dipole moment. The ferromagnetic particles are generally uniformly distributed throughout the volume of the colloid and are randomly oriented due to thermal energy. When a magnetic field is applied to an MR colloid the ferromagnetic particles within that colloid align with the field either by physically rotating in the direction of the field or by rotating the direction of the permanent dipole in each particle. This alignment of the ferromagnetic particles causes the MR colloid to become magnetized. When the external field is removed the magnetization of the MR colloid disappears by the same mechanisms, either physical rotation of the ferromagnetic particles or Nèel relaxation [7] of the dipole moment (both mechanisms are due to the thermal energy in the system). The magnetization (in SI units) of a single MR colloid is closely represented by an adaptation of Langevin's classical theory for the magnetization of a gas of paramagnetic molecules [5] and is given by

$$\frac{M}{\phi_{\mathrm{f}} M_{\mathrm{f}}} = \coth \alpha - \frac{1}{\alpha} \tag{1.1}$$

where M is the magnetization of the MR colloid, ϕ_{f} is the volume fraction of ferromagnetic material in the MR colloid, and M_{f} is the saturation magnetization of the ferromagnetic material. The parameter α is given by

$$\alpha = \frac{\pi}{6} \frac{\mu_0 M_{\mathrm{f}} H_0 d_{\mathrm{f}}^3}{k_{\mathrm{B}} T} \tag{1.2}$$

where μ_0 is the magnetic permeability of free space, H_0 is the magnetic field acting on the MR colloid, and d_{f} is the diameter of a ferromagnetic particle. The Langevin theory assumes negligible interaction between the ferromagnetic particles embedded in the MR colloid which is true for small ϕ_{f} and H_0. Equations 1.1 and 1.2 indicate that the magnetization of an MR colloid increases linearly from zero for small applied fields before saturating at large magnitude external fields. The magnetic susceptibility (χ) of an MR colloid is therefore constant for low magnetic field strengths. A small α expansion of Equation 1.1 combined with Equation 1.2 yields

$$\chi = \frac{M}{H_0} = \frac{\pi \phi_{\mathrm{f}} \mu_0 M_{\mathrm{f}}^2 d_{\mathrm{f}}^3}{18 k_{\mathrm{B}} T} \tag{1.3}$$

The magnetic field due to a uniformly magnetized sphere (or MR colloid) is identical to that of

a pure dipole, outside the sphere, with the dipole moment given by

$$\mathbf{m} = \frac{\pi}{6} d^3 \mathbf{M} \tag{1.4}$$

where d is the diameter of the colloid. Therefore, the energy of interaction between two MR colloids can be written as the energy of interaction between two point dipoles

$$U_{ij} = \frac{\mu_0}{4\pi} \frac{\mathbf{m}_i \cdot \mathbf{m}_j - 3\left(\hat{\mathbf{r}}_{ij} \cdot \mathbf{m}_i\right)\left(\hat{\mathbf{r}}_{ij} \cdot \mathbf{m}_j\right)}{r_{ij}^3} \tag{1.5}$$

where $\mathbf{r}_{ij}$ is the vector connecting the centers of colloids i and j and $\hat{\mathbf{r}}_{ij}$ is the unit vector in the $\mathbf{r}_{ij}$ direction. The magnitudes of each dipole moment (m_i and m_j) are found by combining Equations 1.3 and 1.4 yielding

$$m_i = \frac{\pi}{6} d_i^3 \chi H_{0,i} \tag{1.6}$$

and the direction of m_i is identical to the direction of $H_{0,i}$ (the magnetic field acting on colloid i).

A common assumption made in the modelling of MR fluids is that all of the MR colloids have identical dipole moments which are only a function of the external magnetic field. The magnetic field acting on colloid i is given by

$$\mathbf{H}_{0,i} = \mathbf{H}_{\text{ext}} + \sum_{j \neq i}^{N} \mathbf{H}_j\left(\mathbf{r}_i\right) \tag{1.7}$$

where $\mathbf{H}_{\text{ext}}$ is the externally applied magnetic field, $\mathbf{H}_j\left(\mathbf{r}_i\right)$ is the magnetic field due to colloid j acting at the center of colloid i ($\mathbf{r}_i$), and N is the number of colloids in the system. When the magnitude of the external field is large and the distances between MR colloids is large then the approximation is made that $\mathbf{H}_{0,i} \simeq \mathbf{H}_{\text{ext}}$. As a result of this approximation, Equation 1.5 reduces to

$$U_{ij}\left(r_{ij}, \theta_{ij}\right) = \frac{m^2 \mu_0}{4\pi} \frac{1 - 3\cos^2 \theta_{ij}}{r_{ij}^3} \tag{1.8}$$

where θ_{ij} is the angle made by the vector connecting the centers of colloids i and j ($\mathbf{r}_{ij}$) and the external field vector ($\mathbf{H}_{\text{ext}}$) (Figure 1.2). Equation 1.8 is the usual description of the energy of interaction between two identical MR colloids in a uniform external magnetic field [8]. If we were to consider the effect of the magnetic fields due to the other colloids in the system (Equation 1.7) then we would have to solve, self-consistently, for the field effects of each colloid in the system on each other colloid in the system. Fortunately, the approximation $\mathbf{H}_{0,i} \simeq \mathbf{H}_{\text{ext}}$ works well for modelling the self-assembly of MR fluids.

Structure formation in MR fluids occurs when the attractive energy between MR colloids is able to overcome the thermal energy causing them to undergo Brownian motion. The parameter λ is the ratio of the maximum magnetic attraction energy to the thermal energy defined as

$$\lambda \equiv \frac{-U\left(d, 0\right)}{k_{\text{B}} T} = \frac{\pi \mu_0 d^3 \chi^2 H_{\text{ext}}^2}{72 k_{\text{B}} T}. \tag{1.9}$$

When $\lambda \gg 1$ the magnetic attractions between MR colloids are strong enough to form structures composed of clusters of MR colloids aligned in the direction of the field. The types of structures that

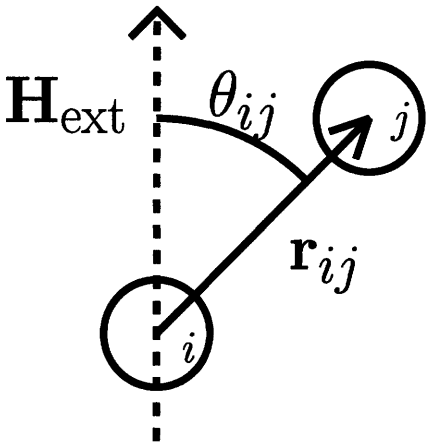

Fig. 1.2: *Schematic of the coordinate system defined to determine the interaction between two MR colloids in a uniform external field* $\mathbf{H}_{ext}$.

form for $\lambda \gg 1$ depend upon the volume fraction of the MR fluid (ϕ) and the confining geometry if any [9, 10, 11]. Combining Equations 1.8 and 1.9 yields the final form of the interaction energy between two identical MR colloids in a uniform external magnetic field, given as

$$U_{ij}\left(r_{ij}, \theta_{ij}\right) = \frac{1}{2}\lambda d^3 k_{\mathrm{B}} T \frac{1 - 3\cos^2\theta_{ij}}{r_{ij}^3} \tag{1.10}$$

1.2 Microfluidics

We are interested in understanding the factors affecting self-assembly of MR fluids in microfluidic geometries. Generally, "microfluidic geometries" implies that at least one of the three dimensions of the fluidic channel has a size of order 1μm to 100μm. The colloids in an MR fluid have a size of $\sim 1\mu$m and therefore the confinement in a microfluidic device can range from a single colloid diameter to 100's of colloid diameters.

Microfluidic devices have been of general interest for a number of years [2] but recently there has been an explosion in research related to microfluidics [12]. Much of the research has focused upon creating a "lab-on-chip" technology whereby procedures which are normally performed on the lab scale can be miniaturized and performed on the micron (or chip) scale. The idea of a lab-on-chip has several advantages over the more macro scale processes. Smaller quantities of reagents are needed for microfluidic devices, a very important consideration when the reagents are expensive or dangerous. Additionally, experiments performed at the micro scale are more easily reproduced because of the laminar nature of the fluid flow in such small scale devices. Microfluidic devices have also been used to perform tasks that are simply impossible on the macro scale such as the continuous synthesis of anisotropic colloidal particles [13]

1.2.1 Soft Lithography

To fabricate the microfluidic devices used in this research, we used the technique of soft lithography. Soft lithography is a lithographic process where at least one of the elements (mask, stamp, or mold) used to fabricate a microdevice are made of an elastomer [14]. This technique has proven advantageous over traditional photolithographic techniques in that it allows for a wide variety of materials and surface chemistries as well as making three dimensional structures. Additionally, soft lithography is much less expensive than photolithography and the materials used are easy to handle experimentally (i.e. they do not require a clean room). Our material of choice for fabricating microfluidic devices using soft lithography is poly(dimethylsiloxane) (PDMS). PDMS is an elastomer which can be molded on a master template with features as small as several nanometers. The specific protocol used to create the PDMS microchannels contains three parts; master template fabrication with photolithography, master template preparation for molding, and PDMS molding.

Master Template Fabrication

Using AutoCAD software, two-dimensional channels are drawn in white on a black background within a circle of diameter 3.5 inches. The channels are drawn with the dimensions of the final microfluidic channels to be fabricated. For instance, in order to fabricate a 50μm channel, a 50μm wide white line is drawn in the AutoCAD file. The image from the AutoCAD file is then printed on a high-resolution transparency to be used as a mask to filter UV light in the photolithography process.

Silicon wafers with a 4 inch diameter are typically used as supports for the creation of a master template used in this soft lithography procedure. A layer of photoresist is deposited on the surface of the wafer using a spin-coating technique. The class of photoresist used in our photolithography process is called SU-8 (MicroChem). The thickness of the photoresist layer can be controlled by altering both the type of photoresist used and the rotational speed of the spin-coater. Generally, different types of SU-8 are capable of spin-coating layers ranging in thickness from $\sim$ 2 to 100s of microns. Once the wafer is coated with the desired thickness of photoresist, it is exposed to 365nm light through the transparency mask with the channels drawn in it. SU-8 photoresist is a negative resist meaning that it undergoes a photo-initiated crosslinking when it is exposed to light at this wavelength. Therefore, wherever the mask does not have black ink (the places where white lines were drawn in the AutoCAD file) the light will pass through the mask and crosslink the photoresist. After the crosslinking, the wafer is washed with a solvent in order to remove the un-crosslinked photoresist. Once the solvent has acted, the wafer is further washed with isopropyl alcohol and de-ionized water to remove any traces of the solvent and un-crosslinked photoresist. At the conclusion of this procedure, the silicon wafer contains projections (or features) of photoresist in the locations dictated by the geometry of the transparency mask.

Master Template Preparation

Once the master template has been created using the photolithography procedure, its surface must be treated in order to allow for easy removal of the PDMS during the molding step. Therefore, the wafer is placed in a vacuum chamber inside a fume hood along with an open glass vial containing $\sim$ 0.5mL of a silanizing agent ($Si - Cl_3\,(CH_2)_2 - (CF_2)_5 - CF_3$, United Chemical Technologies, T2492-KG, Bristol, PA). The silanizing agent is very toxic and must only be handled with glass

instruments. The air is evacuated from the vacuum chamber and the wafer is left inside the chamber for at least 4 hours. The silanizing agent undergoes a physical deposition process whereby it evaporates from the vial and is re-deposited on all of the surfaces in the vacuum chamber including the surface of the silicon wafer. After the wafer is coated, the vacuum is removed and the wafer is placed in a clean petri dish. Any remaining liquid silanizing agent in the vial is allowed to evaporate inside the fume hood.

PDMS Molding

After treating the master template wafer with the silanizing agent it can be molded with the PDMS elastomer. The molding procedure can be repeated an indefinite number of times. This feature of the soft lithography process is the major advantage over other techniques. The PDMS silicone elastomer is mixed with a curing agent in a mass ratio of 10:1 until the two parts are thoroughly mixed. The PDMS mixture is then degassed in a vacuum chamber at 15inHg to remove all of the air bubbles that were entrained during the mixing process. Once the PDMS mixture is degassed, it is poured over the silicon master template inside the petri dish. The whole system is then cured overnight inside a vacuum oven at 65°C and 15inHg. After curing, the PDMS film is peeled off of the master template and placed in another clean petri dish with the "channel face" down. The photoresist features on the surface of the master have been transferred to the PDMS as depressions which, when placed face down upon glass, plastic, or another sheet of PDMS become microfluidic channels with a height equal to the photoresist thickness and a width as defined in the AutoCAD file.

1.3 MR Fluids in Microfluidics

There have been a number of studies on confined systems of MR fluids in recent years ranging from determination of fundamental properties of the self-assembly to applications utilizing the self-assembled structures. A particularly common microfluidic geometry is the thin-slit where the width of the channel is much larger than the height. Self-assembly of MR fluids in the thin slit geometry with a uniform magnetic field directed normal to the thin-slit, has been well studied and the types of structures that form in this geometry have been generally characterized [10, 15, 11]. At low volume fractions, the MR fluid self-assembles into uniformly spaced columns that span the height of the slit [10]. At higher volume fractions, in thin slits, more complex structures can be formed that are highly dependent upon the thickness of the slit [11]. Using more complex magnetic fields, such as a rotating field, periodic planar structures have been observed in the plane of the rotating field between parallel walls [15]. As mentioned previously, there are several recent applications where the structures formed by MR fluids are used in microfluidic geometries. Generally, these applications fall into two categories; 1) applications utilizing the dynamic nature of the structures formed and 2) applications utilizing the properties of static MR fluid structures.

Among the applications in the first category are devices that use MR fluid structures as valves, pumps, and mixers in microfluidic channels [16, 17, 18]. These applications utilize an external magnetic field which changes in time in order to move the MR fluid structures within the channel. Another class of microfluidic devices contained in the first category are devices which utilize fluid flow to move the MR fluid structures throughout the channels [19, 20]. This has proven to be a convenient way to move and control functionalized MR colloids used in cell or protein capture [21].

The static structures formed by MR fluids have been used as a sieving matrix for the separation of DNA by electrophoresis in microfluidic devices [3, 4]. These devices use low volume fraction MR fluids in thin-slit microfluidic channels with a uniform external magnetic field directed perpendicular to the thin slit. Again, the structures that self-assemble under these conditions resemble columns spanning the height of the channel and separated by a characteristic distance or pore size. As a sample of DNA is driven through the channel using electrophoresis it passes through the region of columnar obstacles and collides with the columns therefore delaying its passage [22]. These size dependant events result in a separation of the sample where the smaller pieces of DNA traverse the obstacle region faster than the larger pieces. This separation technique is less expensive, faster, and has equivalent resolution to traditional gel-electrophoresis devices.

All of the microfluidic devices mentioned in this section share the common feature of MR fluids self-assembling in microfluidic geometries. The self-assembled structures may or may not be exposed to a secondary force such as flow or electric fields. There is a definite need for the ability to understand the physical processes governing this self-assembly and subsequent exposure to external forces in microfluidic geometries. The aim of this thesis is to address this need by studying the self-assembly of MR fluids in extremely confining geometries.

1.4 Objectives

The objectives of the work presented in this thesis are as follows. The first objective is to develop a Brownian dynamics (BD) code capable of simulating the self-assembly of MR colloids in complex microfluidic geometries. The description of the BD code developed in this work is given in Chapter 2. Using the tools of BD simulations and microfluidic experiments the second objective is undertaken which is to study two model systems where MR fluids self-assemble under tight confinement. The model systems are presented in Chapters 3 and 4. The final objective is to study self-assembled MR fluids under the application of a secondary force. In Chapters 5 and 6 we present two studies of MR fluid structures experiencing pressure driven flow in a microfluidic channel. We summarize the work in this thesis and present a global outlook in Chapter 7.

CHAPTER 2

Brownian Dynamics

Although it had been observed very soon after the invention of the microscope, the name "Brownian motion" is attributed to the British botanist Robert Brown for his work in 1827-1828 where he reported on the irregular and unpredictable motion of pollen particles in water even in the absence of external forces [23]. This general phenomenon applies to any particle, or colloid, with a size $\sim$ 10nm to $\sim 10\mu$m suspended in a surrounding fluid consisting of much smaller particles. Due to the high frequency of collisions between the Brownian colloid and the surrounding fluid particles, the Brownian colloid moves with a random, un-correlated motion. The Brownian dynamics (BD) simulation technique is a mesoscopic technique which accurately models the Brownian motion of colloids by introducing a stochastic term representing the random fluctuations in position due to momentum transfer from the collision of solvent molecules with the Brownian colloid [24]. Unlike the similar simulation technique known as molecular dynamics (MD), the BD algorithm does not attempt to model every interaction between solvent molecules and Brownian colloids but rather "lumps" the contributions due to solvent-colloid collisions into one stochastic term.

2.1 Stochastic Differential Equation

The equation of motion of a Brownian colloid is approximated by the stochastic differential equation [24]

$$\mathrm{d}\mathbf{r}_i(t) \simeq \frac{1}{\zeta}\mathbf{F}_{\mathrm{D},i}(t)\,\mathrm{d}t + \frac{1}{\zeta}\mathbf{F}_{\mathrm{B},i}(t)\,\mathrm{d}t, \tag{2.1}$$

where the inertia of the colloids is neglected. The term $\mathbf{F}_{\mathrm{D},i}$ represents all of the deterministic forces acting upon colloid i and ζ is the drag coefficient on a single colloid. The term $\mathbf{F}_{\mathrm{B},i}$ represents the stochastic process which is used to model the Brownian force acting on the colloid due to collisions with the solvent molecules. Physically, the Brownian force term replicates the diffusive behavior of the colloid. In the work presented in this thesis, we assume that the colloids in an MR fluid diffuse as if they are in a very dilute solution. In other words, we neglect the hydrodynamic interactions (HI) between colloids which has several consequences for the modelling of MR fluids. Neglecting HI greatly reduces the computation time necessary to simulate MR fluids making the simulation of large ($> 10,000$ colloid) systems possible. Although the rheological properties of MR fluids are not captured when HI are neglected, the structural properties and many of the dynamic time scales involved in structure formation are captured. Furthermore, tight confinement, such as in microfluidic channels, screens the HI between colloids greatly reducing its influence on the dynamics of the system.

When HI are neglected and ζ is constant, the Brownian force term in Equation 2.1 can be written as [24]

$$\mathbf{F}_{\mathrm{B},i}(t) = \sqrt{2\zeta k_{\mathrm{B}}T}\frac{\mathrm{d}\mathbf{W}_i(t)}{\mathrm{d}t}. \tag{2.2}$$

The parameter $\mathbf{W}_i$ is a Wiener process with

$$\begin{aligned}\left\langle \frac{\mathrm{d}\mathbf{W}_i(t)}{\mathrm{d}t} \right\rangle &= 0 \\ \left\langle \frac{\mathrm{d}\mathbf{W}_i(t)}{\mathrm{d}t}\frac{\mathrm{d}\mathbf{W}_j(t')}{\mathrm{d}t'} \right\rangle &= \delta_{ij}\delta(t-t')\,\boldsymbol{\delta}\end{aligned} \tag{2.3}$$

where δ_{ij} is the Kronecker delta, δ is the Dirac delta function, and $\boldsymbol{\delta}$ is the identity tensor. Equations 2.2 and 2.3 imply that the diffusion of the colloids due to Brownian forces is isotropic in space and independent in the three cartesian directions.

The deterministic forces in Equation 2.1 ($\mathbf{F}_{\mathrm{D},i}$) are due to the magnetic interactions between the colloids and bulk hydrodynamic flow (if any). All of the work presented in this thesis contains deterministic forces due to magnetic interactions which we will describe here. In Chapters 5 and 6 we will introduce the deterministic forces due to hydrodynamic flow. The energy of interaction between two identical MR colloids in a uniform external magnetic field is given by Equation 1.10. Therefore the deterministic force acting on colloid i due to it's magnetic interactions with the other colloids in the system is given by

$$\mathbf{F}_{\mathrm{D},i}^{\mathrm{mag}}(t) \equiv \sum_{i\neq j}^{N} -\boldsymbol{\nabla} U_{ij}\left(r_{ij}(t), \theta_{ij}(t)\right) \tag{2.4}$$

where N is the number of colloids in the system. The gradient of the energy between colloid i and j is written as

$$-\boldsymbol{\nabla} U_{ij}(r_{ij}, \theta_{ij}) = -\frac{3}{2}\frac{\lambda k_{\mathrm{B}}T d^3}{r_{ij}^5}\mathbf{r}_{ij}\left[5\left(\frac{\mathbf{r}_{ij}\cdot\mathbf{e}_{\mathbf{z}}}{r_{ij}}\right)^2 - 1\right] + \frac{3\lambda k_{\mathrm{B}}T d^3}{r_{ij}^5}\left(\mathbf{r}_{ij}\cdot\mathbf{e}_{\mathbf{z}}\right)\mathbf{e}_{\mathbf{z}} \tag{2.5}$$

where $\mathbf{e}_{\mathbf{z}}$ is the unit vector in the z-direction. In Equation 2.5 the uniform external magnetic field

is directed in the z-direction.

Combining Equations 2.1 to 2.5 results in the full equation of motion for colloid i due to Brownian motion and magnetic interactions with the other colloids in the system. It is useful to non-dimensionalize the equation of motion in order to obtain general results applicable to any system with the same dimensionless parameters. Therefore, we use the characteristic length scale d and the characteristic time scale $\left(d^2\zeta\right) / \left(k_{\mathrm{B}}T\right)$ (the time for an MR colloid to freely diffuse a distance of one diameter) to non-dimensionalize our equation of motion. Equation 2.1 in dimensionless form is written as

$$\mathrm{d}\widetilde{\mathbf{r}}_i\left(\widetilde{t}\right) \simeq \widetilde{\mathbf{F}}_{\mathrm{D},i}\left(\widetilde{t}\right)\mathrm{d}\widetilde{t} + \widetilde{\mathbf{F}}_{\mathrm{B},i}\left(\widetilde{t}\right)\mathrm{d}\widetilde{t}, \tag{2.6}$$

where $\mathrm{d}\widetilde{\mathbf{r}}_i = \mathrm{d}\mathbf{r}_i/d$ and $\mathrm{d}\widetilde{t} = \mathrm{d}t\left(k_{\mathrm{B}}T\right) / \left(d^2\zeta\right)$. The dimensionless Brownian force $\left(\widetilde{\mathbf{F}}_{\mathrm{B},i}\right)$ is given by

$$\widetilde{\mathbf{F}}_{\mathrm{B},i}\left(\widetilde{t}\right) = \sqrt{2}\frac{\mathrm{d}\widetilde{\mathbf{W}}_i}{\mathrm{d}\widetilde{t}} \tag{2.7}$$

where the dimensionless Wiener process has the properties

$$\begin{aligned} \left\langle \frac{\mathrm{d}\widetilde{\mathbf{W}}_i\left(\widetilde{t}\right)}{\mathrm{d}\widetilde{t}} \right\rangle &= 0 \\ \left\langle \frac{\mathrm{d}\widetilde{\mathbf{W}}_i\left(\widetilde{t}\right)}{\mathrm{d}\widetilde{t}} \frac{\mathrm{d}\widetilde{\mathbf{W}}_j\left(\widetilde{t}'\right)}{\mathrm{d}\widetilde{t}'} \right\rangle &= \delta_{ij}\delta\left(\widetilde{t} - \widetilde{t}'\right)\boldsymbol{\delta}. \end{aligned} \tag{2.8}$$

The dimensionless magnetic force $\left(\widetilde{\mathbf{F}}_{\mathrm{D},i}^{\mathrm{mag}}\right)$ is given by

$$\widetilde{\mathbf{F}}_{\mathrm{D},i}^{\mathrm{mag}}\left(\widetilde{t}\right) = \sum_{j\neq i}^{N} -\frac{3}{2}\lambda\frac{\widetilde{\mathbf{r}}_{ij}}{\widetilde{r}_{ij}^5}\left[5\left(\frac{\widetilde{\mathbf{r}}_{ij}\cdot\mathbf{e}_{\mathbf{z}}}{\widetilde{r}_{ij}}\right)^2 - 1\right] + \frac{3\lambda}{\widetilde{r}_{ij}^5}\left(\widetilde{\mathbf{r}}_{ij}\cdot\mathbf{e}_{\mathbf{z}}\right)\mathbf{e}_{\mathbf{z}} \tag{2.9}$$

where the separation $\widetilde{\mathbf{r}}_{ij}$ is taken at time $\widetilde{t}$. Taken together, Equations 2.6 to 2.9 give the stochastic differential equation describing the motion of colloid i.

2.2 Algorithm

The simplest way to integrate the equation of motion given by Equations 2.6 to 2.9 is to use an explicit Euler integration scheme [24]. In other words Equation 2.6 is written in discrete form as

$$\widetilde{\mathbf{r}}_i\left(\widetilde{t} + \Delta\widetilde{t}\right) \simeq \widetilde{\mathbf{r}}_i\left(\widetilde{t}\right) + \widetilde{\mathbf{F}}_{\mathrm{D},i}\left(\widetilde{t}\right)\Delta\widetilde{t} + \widetilde{\mathbf{F}}_{\mathrm{B},i}\left(\widetilde{t}\right)\Delta\widetilde{t}, \tag{2.10}$$

where $\Delta\widetilde{t}$ is the dimensionless time step used to integrate the equation of motion forward in time. The discrete integration has a consequence for the form of the Brownian force given by Equations 2.7

and 2.8. Namely, the discrete dimensionless Wiener process has the following properties

$$\begin{aligned} \left\langle \frac{\mathrm{d}\widetilde{\mathbf{W}}_i\left(\widetilde{t}\right)}{\mathrm{d}\widetilde{t}} \right\rangle &= 0 \\ \left\langle \frac{\mathrm{d}\widetilde{\mathbf{W}}_i\left(\widetilde{t}\right)}{\mathrm{d}\widetilde{t}} \frac{\mathrm{d}\widetilde{\mathbf{W}}_j\left(\widetilde{t'}\right)}{\mathrm{d}\widetilde{t'}} \right\rangle &= \frac{\delta_{ij}\delta_{\widetilde{t}\widetilde{t'}}\boldsymbol{\delta}}{\Delta\widetilde{t}}. \end{aligned} \tag{2.11}$$

We model the Wiener process defined by Equation 2.11 using a uniform random number distribution between -0.5 and 0.5. The Central Limit Theorem states that any independent random "hopping" process in which the mean displacement and mean-square displacement are finite will result in a Gaussian probability distribution for the position of the hopping entity in the long time limit. Freely diffusing colloids have a Gaussian probability distribution, thus we can use the uniform distribution as stated and after many time-steps, we will reproduce the diffusive behavior of the colloids. We used a random number generator developed by H. C. Öttinger [24] (RANULS) which generates random floating point numbers between 0 and 1. The random numbers are shifted by -0.5 in order to generate a set of random numbers between -0.5 and 0.5 ($\mathbb{R}$), a distribution with $\langle \mathbb{R} \rangle = 0$ and $\langle \mathbb{R}\mathbb{R} \rangle = 1/12$. The Brownian force in our simulations is thus modeled as

$$\widetilde{\mathbf{F}}_{\mathrm{B},i}\left(\widetilde{t}\right) = \sqrt{\frac{24}{\widetilde{\Delta t}}}\mathbb{R} \tag{2.12}$$

Therefore, with Equations 2.9, 2.10, and 2.12 we have fully specified the discrete stochastic equation describing the motion and interactions of Brownian MR colloids under the application of a uniform external magnetic field.

If we were to calculate the magnetic interactions between the MR colloids in the system using the sum over all particles as shown in Equation 2.4 then the computation time for this problem would scale $\sim N^2$. This is inefficient as the interactions between two MR colloids separated by a large distance are not nearly as important (or strong) as the interactions between two colloids in close proximity. Therefore, we implemented a cutoff distance for the magnetic interactions between colloids along with a linked-list binning algorithm [25] where the bin sizes were slightly larger than the cutoff value. The cutoff value depends upon the specific system being studied and only interactions between colloids separated by a distance less than the cutoff are considered. The binning algorithm reduces the computation time so that it scales $< N^2$.

2.2.1 Excluded Volume

There is another property of the magnetic interactions between MR colloids which deserves consideration. To this point we have not included the fact that the colloids in our system have a finite size. The form of the magnetic force that we have used (Equation 2.9) is the force between two identical point dipoles and there is no mechanism in the equations to keep the distance r_{ij} from equalling zero. When $r_{ij} = 0$ the magnetic force becomes infinite which is obviously un-physical. Therefore, we must enforce the "excluded volume" or finite size of the MR colloids in our model.

Generally, MR colloids are stabilized in solution in some manner which will not allow them to aggregate due to Van der Waals forces when there is no external magnetic field present [5]. The form of stabilization can range from steric stabilization (e.g. polymer brushes on the surface of the

colloids) to screened electrostatic stabilization (e.g. negatively charged molecules grafted on the surface of the colloids) [26]. In both of these cases the interactions are very short ranged ($\lesssim 0.1d$) but can be very strongly repulsive when the colloids are close enough together. The combination of these two properties means that the equations describing the energy of interaction due to excluded volume can be very stiff and therefore require an extremely small time-step in the explicit Euler integration scheme mentioned previously.

An alternative method for modelling the excluded volume interactions between MR colloids is to implement a hard-sphere constraint. The advantage of this approach is that the excluded volume interactions are taken into account without having to integrate a stiff repulsive potential between colloids. Several algorithms have been developed in the literature for implementing hard-sphere constraints into BD codes [27, 28, 29]. We will briefly introduce two hard-sphere algorithms and discuss their relative advantages and disadvantages as applied to the problem of MR fluid self-assembly in confined geometries.

Displacement Algorithm. The first hard-sphere algorithm we will introduce was developed by Heyes and Melrose in 1993 [27]. At the end of a time-step in the BD algorithm, colloids can be overlapped due to their magnetic interactions or Brownian motion. Therefore, after the time-step, hard-sphere excluded volume interactions are treated by displacing overlapped colloids along the line connecting their centers until they are just contacting each other. This procedure is performed in a pairwise fashion and is iterated until all overlaps are removed. The BD algorithm then proceeds to the next time step. In this manner, un-physical moves that may have occurred during the course of a time-step are projected out. This method has been used to successfully reproduce physical properties of real systems containing hard-sphere colloids [27, 30]. The advantage of this algorithm is that it is computationally simple and therefore does not require large amounts of memory or computation time. The disadvantage of this algorithm is that all overlaps are corrected by placing the colloids at contact meaning that there is a singular large probability that two colloids will be contacting one another. This singular error propagates to any system property that is calculated as a function of the density correlation function at contact. However, the singularity is integrable and therefore, coarsening the density correlation function in space reduces the magnitude of the error. Additionally, reducing the time-step in the simulations reduces the error due to the singularity in this algorithm as it is inversely proportional to the square root of the time-step.

In order to quantify the errors due to the Displacement Algorithm, we used a simple test problem of a Brownian colloid diffusing in a 1D hard-wall well as illustrated in Fig. 2.1a. We used our BD algorithm without magnetic forces to simulate the motion of the colloid for several thousand dimensionless times until the probability density function (PDF) for the location of the bead reached a steady state as shown in Fig. 2.1b. The large magnitude peaks in the measured PDF at the two hard walls are due to the singularity in this algorithm.

We model the PDF for this simple case as

$$P(x) = C + E\delta(x - \mathbb{L}) + E\delta(x + \mathbb{L}) \tag{2.13}$$

where $\mathbb{L}$ is the location of the hard wall as shown in Fig. 2.2a and x is the position of the colloid. The PDF in Equation 2.13 is normalized meaning that $C = (1/2 - E)/\mathbb{L}$. We define the probability

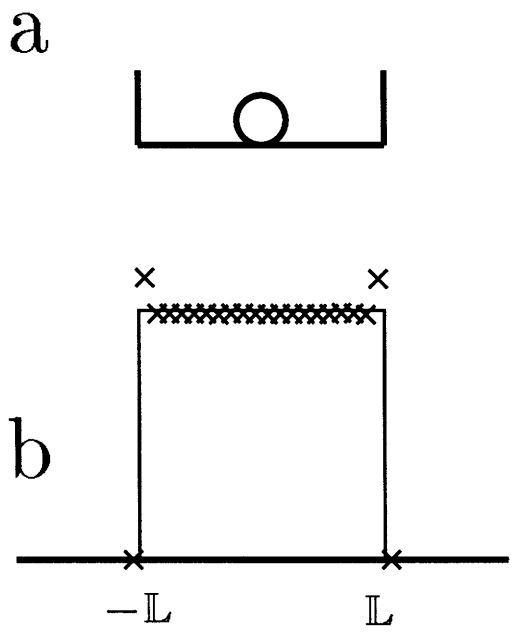

Fig. 2.1: *(a) Schematic of the 1D test problem for the Displacement Algorithm. The diffusion of a Brownian colloid was simulated in a 1D well with hard walls. (b) The long-time steady-state probability density function for the location of the colloid inside the 1D well. The solid line is the analytical solution and the* $\times$ *symbols show the steady-state density profile measured from the BD simulations with a dimensionless time-step of* 10^{-4}*. Note the large peaks in the measured density profile at the two hard walls.*

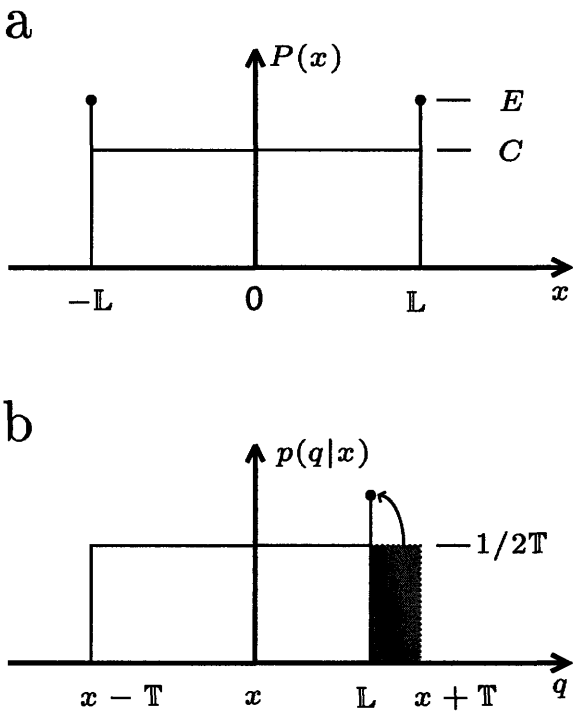

Fig. 2.2: *(a) The probability density function given by Equation 2.13 for the position of a Brownian colloid diffusing in a 1D well with hard walls at* $-\mathbb{L}$ *and* $\mathbb{L}$. *(b) The probability of a Brownian colloid diffusing to a position* q *near a hard wall located at* $\mathbb{L}$.

of moving to a position q during a time-step as

$$p(q|x) = \begin{cases} \frac{1}{2\mathbb{T}} + \frac{\mathbb{T}-x-\mathbb{L}}{2\mathbb{T}}\delta(q+\mathbb{L}) & \text{for } -\mathbb{L} \leq x \leq \mathbb{T}-\mathbb{L} \\ \frac{1}{2\mathbb{T}}\left[H(q-x-\mathbb{T})-1\right]\left[H(x-\mathbb{T}-q)-1\right] & \text{for } \mathbb{T}-\mathbb{L} < x < \mathbb{L}-\mathbb{T} \\ \frac{1}{2\mathbb{T}} + \frac{x+\mathbb{T}-\mathbb{L}}{2\mathbb{T}}\delta(q-\mathbb{L}) & \text{for } \mathbb{L}-\mathbb{T} \leq x \leq \mathbb{L} \end{cases} \tag{2.14}$$

where $\mathbb{T}$ is the half-width of the uniform random number distribution in our algorithm ($\mathbb{T} = \sqrt{6\Delta\tilde{t}}$) and H is the Heaviside function. The Dirac delta comes from the part of the uniform random number distribution which lies outside the well as shown in Fig. 2.2b.

At steady state, the probability of a colloid being located at a position q after one time-step is given by

$$P(q) = \int_{-\mathbb{L}}^{\mathbb{L}} P(x)p(q|x)\mathrm{d}x. \tag{2.15}$$

Integrating Equation 2.15 we obtain

$$P(q) = \begin{cases} \frac{C}{2} + \frac{E}{2\mathbb{T}} + \frac{E}{2}\delta(q+\mathbb{L}) + \frac{C\mathbb{T}}{4}\delta(q+\mathbb{L}) + \frac{C(\mathbb{L}+q)}{2\mathbb{T}} & \text{for } -\mathbb{L} \leq q \leq 2\mathbb{T} - \mathbb{L} \\ C & \text{for } 2\mathbb{T} - \mathbb{L} < q < \mathbb{L} - 2\mathbb{T} \\ \frac{C}{2} + \frac{E}{2\mathbb{T}} + \frac{E}{2}\delta(q-\mathbb{L}) + \frac{C\mathbb{T}}{4}\delta(q-\mathbb{L}) + \frac{C(\mathbb{L}-q)}{2\mathbb{T}} & \text{for } \mathbb{L} - 2\mathbb{T} \leq q \leq \mathbb{L} \end{cases} \tag{2.16}$$

The error E occurs at the walls of the well and we are interested in estimating E so we match the probability from the two PDFs given by Equations 2.13 and 2.16 at the wall by integrating over a width ε away from the wall

$$\int_{\mathbb{L}-\varepsilon}^{\mathbb{L}} P(x)\mathrm{d}x = \int_{\mathbb{L}-\varepsilon}^{\mathbb{L}} P(q)\mathrm{d}q \tag{2.17}$$

to arrive at the following equality

$$\frac{C\varepsilon}{2} + \frac{E\varepsilon}{2\mathbb{T}} + \frac{E}{2} + \frac{C\mathbb{T}}{4} - \frac{C\varepsilon^2}{4\mathbb{T}} = C\varepsilon + E. \tag{2.18}$$

Letting ε go to zero, we are left with the following expression for the error

$$E = \frac{C\mathbb{T}}{2}. \tag{2.19}$$

When measuring a density profile in a BD simulation, the coordinates of the colloid are binned into discrete positions separated by a dimensionless distance (or bin-size) $\Delta\widetilde{\epsilon}$. The peak E next to the hard-wall is therefore lumped into a bin of width $\Delta\widetilde{\epsilon}$ causing the total probability in the bin next to the wall to be $C\Delta\widetilde{\epsilon} + E$. The analytical solution has a total probability of $C\Delta\widetilde{\epsilon}$ in the bin next to the wall so the relative error in the probability due to the displacement algorithm is finally given as

$$\text{Rel. Err.} = \frac{E}{C\Delta\widetilde{\epsilon}} = \frac{\mathbb{T}}{2\Delta\widetilde{\epsilon}} = \frac{\sqrt{6\Delta\widetilde{t}}}{2\Delta\widetilde{\epsilon}} \tag{2.20}$$

This analysis predicts that the error due to the Displacement Algorithm is proportional to the square root of the time-step in the simulation. Furthermore, it predicts that the error will be inversely proportional to the bin-size during the discrete calculation of the PDF in the 1D well. These two scalings are confirmed in Fig. 2.3 where we show results from the simple BD simulations plotted as open circles and the prediction given by Equation 2.20 as a solid line. The exact prediction in Equation 2.20 is slightly higher than the errors measured in the simple test simulations because the two PDFs given by Equations 2.13 and 2.16 are not exactly identical meaning that our above analysis is not quite self-consistent. However, it does correctly predict the sources of error at the walls and how that error scales with the time-step and the bin-size. Knowing the source and the magnitude of the error due to the Displacement Algorithm allows us to choose our time-step and bin-size in order to minimize its contribution to the total error in our BD simulations.

Elastic Collision Algorithm. The hard-sphere algorithm developed by Strating in 1999 [28] treats overlaps between hard-spheres as perfectly elastic collisions. At the end of a time-step in the BD algorithm, if two colloids are overlapped, their initial positions along with the length of the time-step are used to calculate the "time" and position where they first collided assuming that they travelled with a constant velocity during the course of the time-step. Their trajectories for

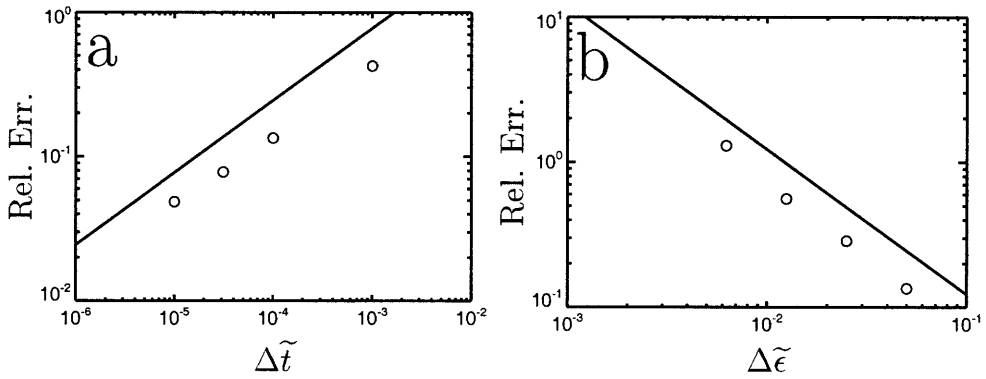

Fig. 2.3: *(a) Relative error in the density distribution for the 1D well as a function of time-step. The bin-size in this case was taken as* $\Delta\widetilde{\epsilon} = 0.05$. *The solid line is the prediction given by Equation 2.20 and the open circles are results from BD simulations. (b) Relative error in the density distribution for the 1D well as a function of bin-size. The time-step in this case was taken as* $\Delta\widetilde{t} = 10^{-4}$. *The solid line is the prediction given by Equation 2.20 and the open circles are results from BD simulations.*

the rest of the time-step are then calculated from the collision time and position assuming that they underwent a perfectly elastic collision. This is repeated for all overlaps that occurred during the course of a time-step. This algorithm has the advantage of removing the singularity that occurs in the Displacement Algorithm. However, there are many disadvantages of this algorithm, the first of which is that it does not represent the true physics of diffusion. During the course of a time-step a Brownian colloid diffuses in many directions rather than with a single velocity as assumed in the Elastic Collision Algorithm. From a computational standpoint, this algorithm requires longer computation times due to the need to calculate the collision times for all overlapped colloids. Additionally, all of the collision times must be calculated first and then the collisions are handled in the order in which they occur.

There are even more complex algorithms that have been developed to accurately model the interaction between a hard sphere and a hard-wall such as the algorithm developed by Peters and Barenbrug [31] but these algorithms are generally not adaptable to the case of hard sphere interactions except in special cases [29]. We have used the Displacement Algorithm developed by Heyes and Melrose in our BD simulations of MR fluid self-assembly because it is not computationally intensive and the errors are controllable as long as one keeps their source in mind. Additionally, this algorithm is very easy to generalize for the case of hard-walls; another important consideration in our BD simulations.

2.2.2 Hard Walls

The boundary conditions of the simulation box in our BD code can either be periodic or hard-walls. Each of the three cartesian directions are independent of one another meaning that we can model self-assembly in free solution, thin-slits, rectangular channels, or rectangular boxes by having

periodic boundaries in three, two, one, or zero of the cartesian directions respectively. In the case of hard-walls, the Displacement Algorithm is easily implemented for any geometry that appears smooth over the length scale of the colloids d.

Flat Walls

In the case of flat hard-walls, the algorithm is straight forward. At the end of a time step, any colloids that are overlapped with the walls of the simulation box are displaced normal to the wall until they are just contacting the wall. For instance, if a colloid is overlapped with a hard-wall in the x-y plane (located at $\widetilde{z} = 0$) then it is displaced until it is just contacting the wall meaning it's dimensionless z coordinate is simply set equal to 0.5 (or one colloid radius).

Other Hard Walls

If the hard-walls being implemented in the BD algorithm are not flat but rather have some functional form which appears smooth over the length scale of the colloids (such as a sinusoidal function) then the Displacement Algorithm can also be used with success. If the hard-wall in the x direction is described by the equation

$$\widetilde{x}_{\mathrm{HW}} = f\left(\widetilde{y}\right) \tag{2.21}$$

then at the end of a time-step, if a colloid is overlapped with the hard-wall (has crossed the line defined by Equation 2.21) then it must be displaced until it is just contacting the wall. If the overlapped colloid has coordinates $(\widetilde{x}_0, \widetilde{y}_0, \widetilde{z}_0)$ in the x, y, and z directions respectively then it must be repositioned to the coordinates $(\widetilde{x}_1, \widetilde{y}_1, \widetilde{z}_1)$ where

$$\begin{aligned} \widetilde{x}_1 &= \widetilde{x}_{\mathrm{HW}} \pm \frac{0.5}{\sqrt{1 + \left(\mathrm{d}\widetilde{x}_{\mathrm{HW}}/\mathrm{d}\widetilde{y}\right)^2}} \\ \widetilde{y}_1 &= \widetilde{y}_0 \pm \frac{0.5\left(\mathrm{d}\widetilde{x}_{\mathrm{HW}}/\mathrm{d}\widetilde{y}\right)}{\sqrt{1 + \left(\mathrm{d}\widetilde{x}_{\mathrm{HW}}/\mathrm{d}\widetilde{y}\right)^2}} \\ \widetilde{z}_1 &= \widetilde{z}_0. \end{aligned} \tag{2.22}$$

Thus, with the Displacement Algorithm, non-flat hard-walls can be easily included in the BD algorithm.

This method can also be used to model walls with sharp corners, such as stepped (or terraced) walls. If the corners are concave (i.e. the colloid is "enclosed" by the corner region) then the Displacement Algorithm works exactly except for the singularity at the walls. If the corners are convex (i.e. the colloid is "outside" the corner region) then there are errors near the corner due to the Displacement Algorithm which again scale with the square root of the time-step.

2.3 Summary

The BD code that was developed for this thesis is quite versatile in that it allows for the simulation of the self-assembly of MR fluids under a variety of geometric constraints and external forces. The algorithm outlined in this chapter is a basic BD algorithm with the added functionality of a "potential-less" hard-sphere excluded volume constraint between the colloids. This hard-sphere

constraint has additionally been applied to the case of hard-walls. Since the equation of motion is de-coupled in the three cartesian directions in this algorithm, we can simply "turn off" any of the three cartesian dimensions in our BD code in order to simulate simpler systems. This is relevant for the work presented in Chapter 3

CHAPTER 3

Two Dimensional Systems

The self-assembled structure of MR fluids in thin-slit microfluidic channels has been used as a sieving matrix for the size-dependent separation of DNA by electrophoresis [3, 4]. When viewed from the top of the channel (in the field direction), the structure of the MR fluid appears to be a two-dimensional (2D) field of columns of MR colloids. Therefore, it is prudent to begin any study of MR fluid self-assembly in these microfluidic channels by investigating the self-assembly in 2D first. The 2D model fails to capture the effects of chain coalescence that occur in a truly 3D system [32], but it serves as a starting point for understanding the inter-column structure in the channel system. The characteristic length scales in microfluidic devices are becoming smaller every day and a 2D self-assembled system of MR colloids is rapidly becoming an important subject of study. In this chapter we will investigate the self-assembly of MR fluids in 2D microfluidic channels. The results presented in this chapter have been published in the following references [33, 34, 35].

3.1 Background

Self-assembly of field-responsive colloids in 2D has been widely studied because it is a model system with very interesting physics. The most studied aspect of these systems is the nature of the solid-liquid phase transition. In the unbounded (infinite plane) 2D system, it has been theorized that the nature of the solid-liquid phase transition is second order with an intermediate stable hexatic phase [36, 37, 38]. There is compelling experimental evidence supporting the existence of a hexatic phase in the case of purely repulsive dipoles [39, 40, 41]. While many simulation studies have been performed upon a variety of 2D colloidal systems, the nature of the phase transition has not yet been conclusively determined in simulations [42, 43, 44, 45, 46, 47].

In addition to the nature of the phase transition, many researchers have been interested in the properties of 2D colloids confined laterally. Much of this research has focused on circular confinements [48, 49, 50, 51, 52, 53]. This confinement imposes a circular shell-like structure upon the crystal and leads to very unique properties of the phase transition. Nonhomogeneous melting has been observed in these systems where the melting begins at the boundary between the shell-like structure and the more hexagonal structure in the center of the circular confinement [51, 52]. Additionally, re-entrant freezing was observed in small clusters of colloids confined in 2D circles due to radial fluctuations of the colloids in the crystal [48, 49, 50]. As the interaction strength between the colloids was decreased the clusters transitioned from solid-like to liquid-like. However, as the interaction strength was further decreased, increased radial fluctuations of the colloids caused the rings in the shell-like structure to become locked in register with one another and produced re-entrant freezing behavior. This type of re-entrant phase behavior was also observed in systems of 2D colloids confined in periodic 1D light fields [54, 55, 56].

Another very important form of constraint for 2D colloidal systems is channel-like confinement. This type of system has the obvious application towards studying microfluidic geometries. Additionally, channel-like confinement breaks the radial symmetry that exists in circular confinements leading to different structures and dynamics. A few experimental studies have been done on colloidal-like systems confined in quasi-2D channels [57, 58, 59]. Teng *et al.* [57] observed anisotropic diffusion, enhanced in the direction parallel to the confining walls when studying a dusty plasma system confined in a quasi-2D channel. The dusty plasma system was not a truly 2D system in that the "colloids" were actually short chains of colloids aligned in the direction normal to the plane of observation. These chains interact differently than repulsive dipoles causing significant differences between the behavior of dusty plasma system and the one studied here. The other studies were performed on spherical block copolymers confined in a 2D channel [58, 59]. The authors observed that the orientational order of the colloidal crystal decayed in the regions farther from the wall. The width of the channel in this study was three orders of magnitude larger than the block copolymers so the effects of tight confinement were not probed. Recently, simulations and theory have been performed on a system of colloids in narrow 2D channels interacting with a Yukawa potential [60]. The channel walls in these studies consisted of a parabolic confining potential. The authors observed re-entrant behavior as a function of the density of colloids in the channels and they characterized the structural and melting transitions that occur in this system.

In addition to the general nature of the effects of confinement on 2D colloidal systems, the nature of the boundaries can drastically affect the structure of self-assembled colloidal systems either by providing a template for extreme ordering or by disrupting the natural structure of the system [61, 62, 63, 64]. For instance, the structure of clusters of colloids confined in 2D circles

has been characterized as having an outer region of ring-like structure and an inner region of hexagonal structure, independent of the nature of the circular confining potential [51, 52, 53]. This illustrates a case where the boundary imposes an unusual local structure while the center of the cluster relaxes back to the unconfined structure. In colloidal systems boundaries can appear in different forms, as an impurity or as a confinement. Self-assembly in the presence of boundaries is of great, and growing, importance in a variety of applications ranging from photonic band-gaps and semiconductors [65, 66] to medical devices [67, 68, 3]. Much research has been done to characterize the effects of boundaries upon the self-assembly of colloidal systems as they are both important industrially and from a fundamental scientific standpoint. Much effort has also gone into exerting control over the self-assembly of colloidal systems using boundaries and confinement [69, 70, 71]. In particular, two-dimensional (2D) colloidal systems are ideal for studying the specifics of self-assembly near boundaries because of their reduced geometry and their accessible length and time scales.

3.2 Simulations of 2D MR colloids

The system studied consisted of MR colloids confined to a 2D plane with a uniform external magnetic field directed normal (z-direction) to the confining plane. We have modeled the MR colloids as hard spheres with repulsive point dipoles at their centers. This approach has been used widely in the literature [72, 73, 33] and has been shown to be a good approximation for the magnetic behavior of MR colloids [74]. The large separation distances between the colloids in this system ensure that the dominant magnetic field is the external field and the effect of mutual induction between colloids is negligible. In this system, the colloids interact with a purely repulsive dipolar potential and therefore the equation for the magnetic force between colloids (Equation 2.9) reduces to

$$\widetilde{\mathbf{F}}_{\mathrm{D},i}^{\mathrm{mag}}\left(\widetilde{t}\right) = \sum_{j\neq i}^{N} \frac{3}{2}\lambda \frac{(\widetilde{\mathbf{x}}_{ij} + \widetilde{\mathbf{y}}_{ij})}{\widetilde{r}_{ij}^{5}} \tag{3.1}$$

since the distance $\widetilde{\mathbf{z}}_{ij}$ is identically zero. The interactions between the colloids are purely repulsive in this system and therefore, the important length scale is no longer the colloid diameter. The important length scale becomes the spacing between the colloids R where $R = a\sin 60$ and a is the lattice spacing in a perfectly hexagonal 2D colloidal crystal. The lattice spacing is a purely geometric property and is a function of the number density in the system (n) such that $a = (n\sqrt{3}/2)^{-1/2}$. The number density is defined as the number of colloids in the system divided by the total area available to the centers of the colloids. Therefore, the length scale in terms of the number density in the system is written as

$$R = \left(\frac{2}{\sqrt{3}}n\right)^{-1/2}. \tag{3.2}$$

The change in length scale also brings about a change in the energy scale in the system. The appropriate energy scale for the 2D system is defined as

$$\Gamma = \frac{1}{2}\lambda\left(\frac{d}{R}\right)^{3} \tag{3.3}$$

Defining the energy scale as in Equation 3.3 results in the interesting observation that all 2D dipolar systems at the same Γ behave identically, as long as R is the only relevant length scale in the system (i.e., $d \ll R$) [73] as is the case for all of the results reported here.

3.2.1 Simulation Details

Brownian dynamics simulations were used to study this system with the dimensionless equation of motion derived in Chapter 2 (Equation 2.10). Since the important length scale in this system is R and not d the time scale given in Chapter 2 must be altered in the 2D system. Therefore, the time scale in the 2D system is given as $\left(\zeta R^2\right) / \left(k_{\mathrm{B}} T\right)$, the time necessary for a colloid to freely diffuse a unit distance R. Additionally, due to the large magnitude of the repulsive interactions compared to the thermal motion in our 2D systems (at the field strengths we simulated) we never observed overlaps between colloids, only overlaps between the colloids and the walls.

Simulations of the unbounded system were performed with 14,784 colloids where we imposed periodic boundary conditions in the x- and y-directions and the magnetic field was aligned in the z-direction. Simulations of the channel systems were done with 960 - 3,840 colloids where we imposed periodic boundary conditions in the y-direction and hard walls in the x-direction. The number of colloids in each simulation was chosen in order to ensure that the properties of the system did not depend upon the system size. A time step of $\Delta\widetilde{t} = 7.5 \times 10^{-5}$ was used and a cutoff for the dipole-dipole interaction of $6.5R$ was implemented. All of the simulations were determined to be converged in system size, time step, and cutoff for the dipole-dipole interaction.

The number density in the simulations reported here was held constant at $n = 0.0462$ such that $d \ll R$. For the channel systems, the width of the channel was taken to be the width accessible to the centers of the colloids. This definition implies that the width of the channel used for calculating the number density is in fact the true width of the channel minus d. Defining the channel width in this way ensures that we remove any system dependence on the colloid diameter d. In the unbounded systems the area is simply the true area since we have periodic boundary conditions in all directions.

3.2.2 Unbounded 2D System

The simulations of the unbounded systems were equilibrated from a perfect hexagonal lattice. The total defect concentration was tracked as a function of time and the system was determined to be at equilibrium when the defect concentration (C_{def}) remained unchanged over a dimensionless time of 373. A defect is defined as a colloid with more or less than six nearest neighbors. Statistics were taken after the system was determined to be equilibrated. Examples of the equilibration curves are shown in Figure 3.1a. In the liquid phase, near the transition field strength, the equilibration was slower than for systems farther away from the phase boundary. This is shown in Figure 3.1a where the equilibration of the unbounded system at a dimensionless field strength of 12.41 is much faster than at a dimensionless field strength of 14.89. Fluctuations in the defect concentration also increase near the phase boundary which is consistent with the recent work of Reichhardt and Reichhardt [75].

The state of the unbounded system was determined by calculating the bond-order correlation function in time ($g_6(\widetilde{\tau})$) [76]. The correlation function is given by the equation

$$g_6(\widetilde{\tau}) = \langle \Psi_6^*(0) \Psi_6(\widetilde{\tau}) \rangle, \tag{3.4}$$

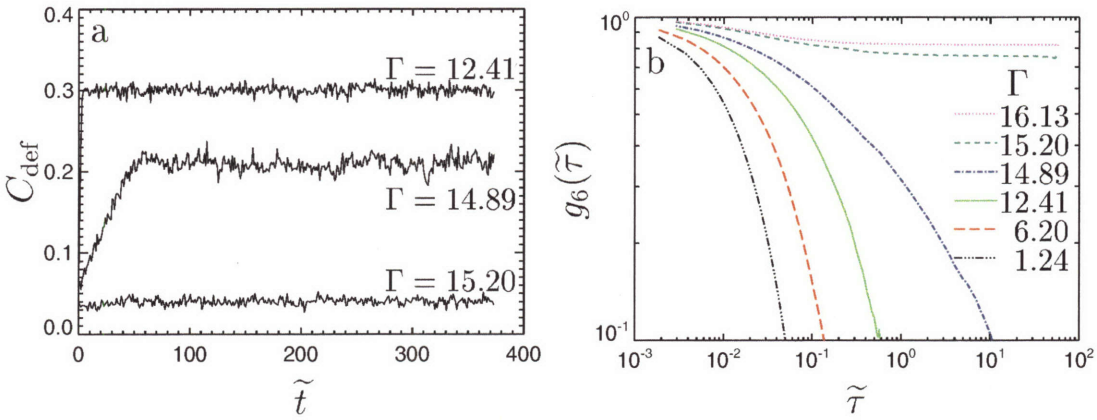

Fig. 3.1: *(a) Defect concentration as a function of time during the equilibration of the unbounded system at three dimensionless field strengths. (b) The bond-order correlation function for unbounded 2D systems at several dimensionless field strengths. Above a dimensionless field strength of* 15.20 *the system behaves as a solid crystal and below a dimensionless field strength of* 14.89 *the system behaves as a liquid.*

where $\widetilde{\tau}$ is the dimensionless lag time and Ψ_6 is the local bond order parameter

$$\Psi_6 = \frac{1}{m}\sum_{k=1}^{m} e^{i6\theta_k}. \tag{3.5}$$

In Equation 3.5 m is the number of nearest neighbors for a given colloid and θ_k is the angle between the vector connecting the colloid and its kth nearest neighbor and an arbitrary reference axis. The nearest neighbors are determined by performing a Delaunay triangulation. Theory predicts that the behavior of $g_6(\widetilde{\tau})$ in time can be used to determine the phase of the unbounded system [76]. In the solid phase, $g_6(\widetilde{\tau})$ remains constant for all lag times while in the liquid phase $g_6(\widetilde{\tau})$ decays exponentially to zero as a function of lag time. In the hexatic phase, $g_6(\widetilde{\tau})$ decays algebraically to zero as a function of lag time. The bond-order correlation function is plotted in Figure 3.1b for a variety of dimensionless field strengths. We were able to equilibrate the liquid phase up to a dimensionless field strength of 14.89 and the solid phase down to a dimensionless field strength of 15.2. Between these two field strengths we were not able to converge our unbounded system due to the diverging correlation lengths and times near the phase transition [77] and therefore we are not able to comment upon the existence of a hexatic phase in this system. However, our results clearly indicate that the solid-liquid phase transition occurs between a dimensionless field strength of 14.89 and 15.2. This range is in good agreement with the simulation results of Löwen [78] for the same type of system. However, Löwen used an empirical criterion to determine the transition point and the system size was much smaller ($N = 961$) than the current study. Experimental studies have shown the existence of a hexatic phase between a dimensionless field strength of 12.14 and 13.93 with a liquid phase below 12.14 and a solid phase above 13.93 [41], a slightly lower range than our

simulation results. However, our determination of the phase boundary region in the unbounded system serves as a base case for our simulation study which we will perturb by introducing parallel walls into our 2D system.

3.2.3 Infinite Field Structures in 2D Channels

The 2D channel system underwent simulated annealing from an equilibrated liquid state to a very high field strength ($\Gamma = 50$). As mentioned above, the 2D dipole system is found to be in the solid phase at this field strength. The annealing process was performed at varying rates and with sequential heating and cooling to ensure an equilibrium structure at $\Gamma = 50$. The system was then quenched by setting the stochastic term in Equation 2.10 to zero. This turns off the Brownian motion effectively causing Γ to go to infinity. The quenching was done from a variety of different starting configurations within the equilibrated crystal and the final internal energy of all the quenched systems for a given dimensionless channel width did not vary by more than 1%.

The quenched crystal was observed to align with one of its lattice-vectors along the length of the channel, parallel to the confining walls as seen in the top of Figure 3.2b. From this observation we note that there should be certain channel widths, magic numbers, that are fully commensurate with the natural spacing of an unbounded crystal aligned in the direction parallel to the walls. We will show, however, that these magic numbers are not simply integer multiples of R, as implied by the alignment of the crystal, but are affected by a number of the properties of the 2D crystal in channels.

A characteristic of the infinite field structures in channels is the dimensionless wall-spacing $\widetilde{a}_w$ which is defined as the distance between adjacent colloids along the walls. In Figure 3.2a the dimensionless wall-spacing is seen to follow exactly the 1D lattice spacing for channel widths less than ~ 2. The 1D lattice spacing (dashed line in Figure 3.2a) is the calculated wall-spacing for a constant n channel system in which the colloids are aligned in two rows, one at each wall. In the large channel limit the wall-spacing approaches a constant showing the behavior of a semi-infinite system. The value that is approached ($\sim 0.83a$) is actually less than the spacing of the 2D unbounded crystal meaning that the line-density of the lattice-line on the wall is larger than that of a lattice-line in the unbounded 2D crystal. The line-density is defined as the number of colloids per unit length along a lattice-line and is a constant equal to a^{-1} along the lattice-lines of an unbounded 2D lattice. The increased line-density along the wall is explained by noting that the walls remove some of the energetic penalty associated with a higher line-density. In the unbounded 2D crystal, increasing the line-density of a row in the crystal results in a higher interaction energy between the colloids in that row (ie. the spacing between colloids in the row is reduced) and a higher interaction energy between that row and adjacent rows. In the channel system, the row of colloids at the wall has only one neighboring row, not two, so the energetic penalty for increasing the line-density along the wall is lower than for the unbounded 2D crystal. The consequences of the higher density of colloids along the wall will be discussed further in Section 3.2.4.

In Figure 3.2a there is a non-monotonic decrease in the wall-spacing characterized by a series of decaying oscillations as the channel width is increased. The largest oscillation occurs near a channel width of 2. For very narrow channels, the colloids are aligned in two parallel rows but as the channel width is increased, it becomes energetically favorable for colloids to be in the center of the channel so they leave the walls, thus increasing the wall-spacing. As the channel width is further increased and the center of the channel is filled in with colloids, it becomes less energetically

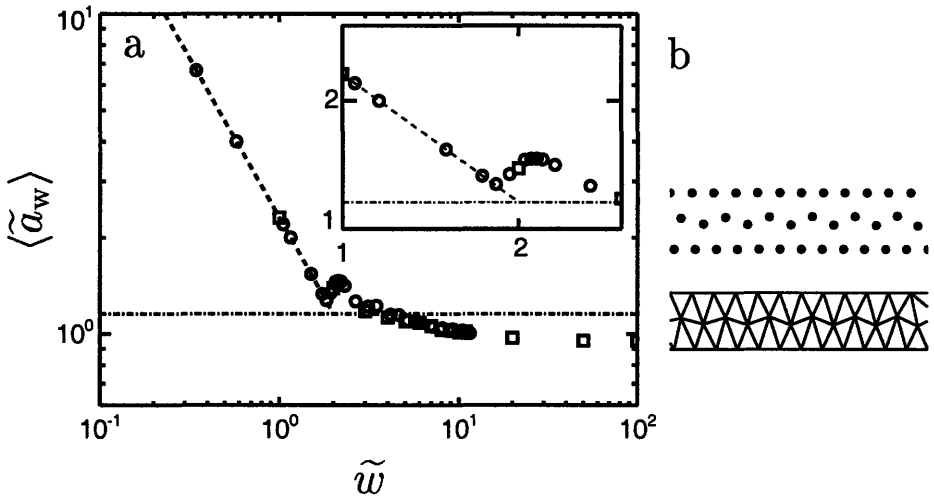

Fig. 3.2: *(a) The average dimensionless wall-spacing for different dimensionless channel widths; square symbols correspond to integer channel widths and circle symbols correspond to non-integer channel widths. The dash-dot line corresponds to the dimensionless 2D unbounded lattice spacing and the dashed line corresponds to the dimensionless 1D lattice spacing. The oscillations in wall-spacing as a function of channel width are continuous (inset). (b) The crystal aligns with the channel walls (top) and remains hexagonal in the Delaunay triangulation (bottom) for a dimensionless channel width of* 3.

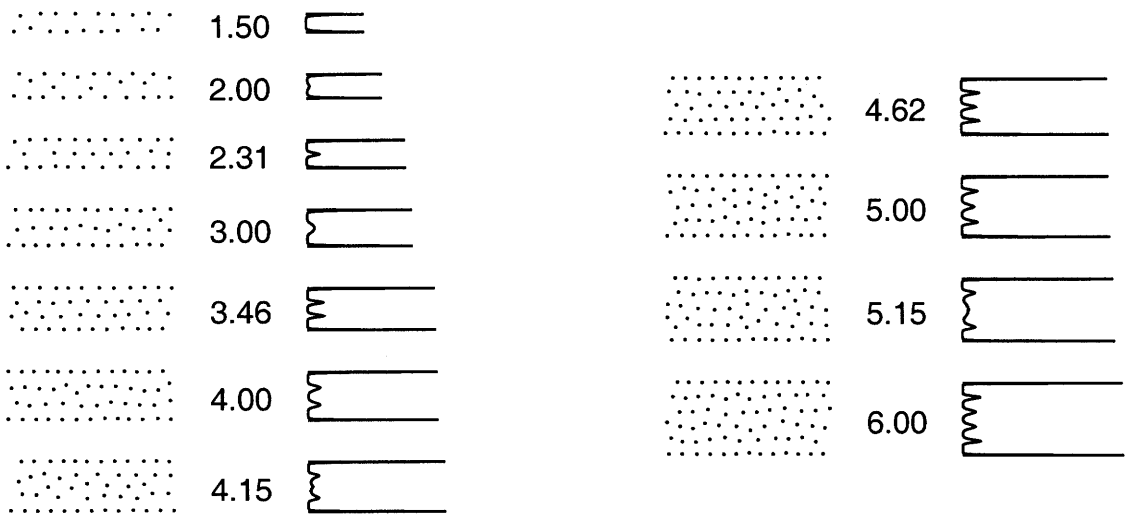

Fig. 3.3: *Configuration snapshots and equilibrium density profiles for selected dimensionless channel widths at a dimensionless field strength of* $\Gamma = 16.13$.

favorable for the colloids to be in the center of the channel and again the wall-spacing decreases following approximately the 1D scaling. This process continues as the channel width is increased but the walls become farther removed from the center of the channel and therefore are less affected by the changes occurring there. Thus, the oscillations in the wall-spacing decay after a channel width of ~ 5 where there is a buffer of at least one lattice-line between the wall and the center of the channel. These oscillations are continuous as shown by the inset in Figure 3.2a indicating that the addition of a new row in the center of the channel is a continuous process as the channel width is increased. The presence of these oscillations indicates that the channel width plays an important role in the types of structures that form in the 2D channel system. The oscillations in the wall-spacing occur with a period $\sim R$ but the maxima and minima do not occur at integer multiples of R indicating that the magic numbers are not simply integer multiples of R.

3.2.4 Finite Field Structures in 2D Channels

In order to study the properties of the crystal at finite field strengths, where thermal fluctuations are important, the 2D channel system was annealed to $\Gamma = 16.13$. One measure that has been widely used to characterize the structure of a system confined between parallel planes is the equilibrium density profile of that system normal to the confining planes [79]. Figure 3.3 shows equilibrium density profiles transverse to the walls for a selection of channel widths at $\Gamma = 16.13$. A characteristic feature of the density profiles is that they show a well defined layered structure parallel to the walls similar to the aforementioned dusty plasma study [57]. This layered structure is evident even for dimensionless channel widths of 100 implying that the system is in a solid state with rows that are parallel to the walls of the channel for all channel widths.

The sharpness of the peaks in the center of the channel varies non-monotonically as the channel width is increased. The broadening and sharpening of the peaks always occurs near the center of

the channel indicating that the layering near the walls is weakly affected by the increase in channel width but the structure in the center of the channel undergoes large changes. The change in the structural properties in the center of the channel will prove important in characterizing the 2D dipole system in channels.

The most unique feature of the density profiles is the large peak in the profile occurring at each wall which was not observed in the dusty plasma study [57]. This peak is the result of the convolution of two collaborating effects. The increase in channel width causes an increase in the line-density of the colloids along the wall as seen in Figure 3.2a. Additionally, the long ranged nature of the dipole-dipole interaction results in a net increase in the localization of the colloids at the walls as the channel width is increased.

Transverse mobility at walls

The most direct measure of the transverse mobility of the colloids localized at the wall is their mean squared displacement (MSD) in the direction normal to the wall $\langle \Delta\widetilde{x}^2(\widetilde{\tau})\rangle$ where $\widetilde{\tau}$ is the dimensionless lag time. The wall-colloids are defined as colloids located within a distance $R/2$ from the wall. The MSD of the wall-colloids was observed to approach a plateau at long lag times (Figure 3.4 inset) implying that the colloids are localized at the wall for significant lengths of time. Eventually, the wall-colloids will migrate away from the wall but this was only rarely observed over the timescale of observation in Figure 3.4. Additionally, this escape became increasingly unlikely as the channel width was increased. It was observed that the plateau value of the MSD decreases as the channel width is increased (Figure 3.4) implying that the wall-colloids become more localized. This increased localization is a direct result of the long ranged nature of the dipole interactions, combined with the presence of a hard wall, and contributes to the large peaks at the walls in the density profiles. In the limit of large channels, the MSD approaches a constant with a correction of order $\widetilde{w}^{-1}$. This form for the MSD is expected when the potential near the walls is approximated by the sum of a near and a far contribution

$$\frac{U'(\widetilde{x},\widetilde{w})}{k_{\mathrm{B}}T} = \widetilde{U'}_{\mathrm{near}}(\widetilde{x},\widetilde{w}) + \widetilde{U'}_{\mathrm{far}}(\widetilde{x},\widetilde{w}). \tag{3.6}$$

The two parts of the potential are defined as

$$\widetilde{U'}_{\mathrm{near}}(\widetilde{x},\widetilde{w}) = \Gamma R\rho_{\mathrm{L}} \int_{-\infty}^{\infty} \frac{\mathrm{d}\widetilde{y}}{((\widetilde{c}-\widetilde{x})^2+\widetilde{y}^2)^{3/2}} \tag{3.7}$$

$$\widetilde{U'}_{\mathrm{far}}(\widetilde{x},\widetilde{w}) = \Gamma R^2 n \int_{2\widetilde{c}}^{\widetilde{w}} \int_{-\infty}^{\infty} \frac{\mathrm{d}\widetilde{y}\,\mathrm{d}X}{((X-\widetilde{x})^2+\widetilde{y}^2)^{3/2}}, \tag{3.8}$$

where $\widetilde{c}$ is the x-position of the first row away from the wall (the arbitrary cutoff between the near and far parts of the potential) and ρ_{L} is the line-density of the row. This definition of the potentials approximates the rows neighboring the walls as a continuum. This approximation introduces some error into the quantitative prediction for the MSD but does not affect the qualitative nature of the

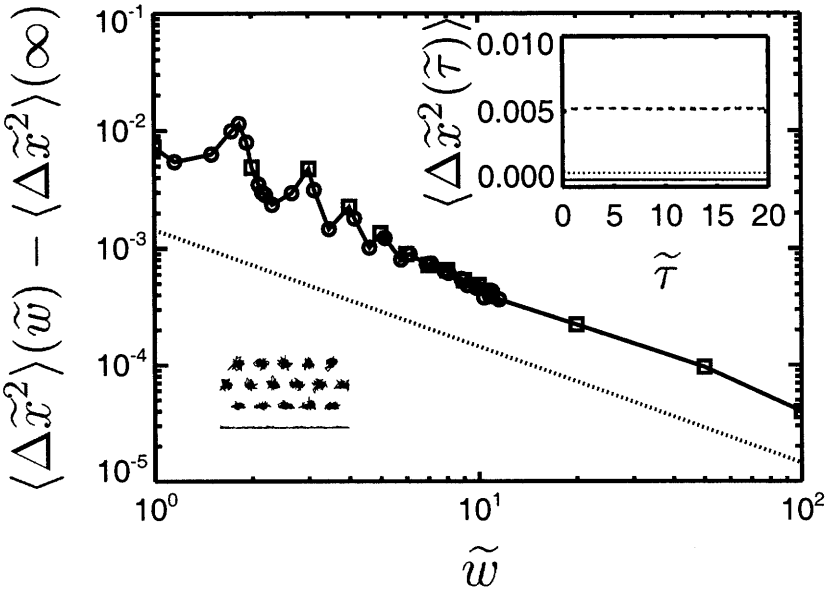

Fig. 3.4: *Plateau value of the mean squared displacement (MSD) of wall-colloids in the direction normal to the wall for selected dimensionless channel widths; square symbols correspond to integer channel widths and circle symbols correspond to non-integer channel widths. The value of* $\langle \Delta \widetilde{x}^2 \rangle (\infty)$ *is taken from an extrapolation of the simulation data. The dotted line is the approximation derived for the MSD [Equation 3.19] (without the constant term). Bottom left is a trace of the colloid motion near the wall in a dimensionless channel width of* $\widetilde{w} = 10$*, for a lag time of* $\widetilde{\tau} = 3.7$*, showing constrained motion at the wall. The top inset shows the MSD versus lag time for the three traces;* $\widetilde{w} = 3$ *(dashed line),* $\widetilde{w} = 10$ *(dotted line), and* $\widetilde{w} = 100$ *(solid line).*

scaling. After the integrations, the potentials become

$$\widetilde{U'}_{\text{near}}(\widetilde{x}, \widetilde{w}) = \frac{2\Gamma R \rho_L}{(\widetilde{c} - \widetilde{x})^2} \tag{3.9}$$

$$\widetilde{U'}_{\text{far}}(\widetilde{x}, \widetilde{w}) = 2\Gamma R^2 n \left(\frac{1}{2\widetilde{c} - \widetilde{x}} - \frac{1}{\widetilde{w} - \widetilde{x}} \right). \tag{3.10}$$

The dimensionless MSD in Figure 3.4 is much smaller than one for all channel widths and therefore, the potential can be expanded to first order near $\widetilde{x} = 0$ as

$$\widetilde{U'}(\widetilde{x}, \widetilde{w}) \approx A(\widetilde{w}, \widetilde{c}) + B(\widetilde{w}, \widetilde{c})\widetilde{x}, \tag{3.11}$$

where

$$A(\widetilde{w},\widetilde{c}) = \frac{2\Gamma R\rho_{\mathrm{L}}}{\widetilde{c}^2} + 2\Gamma R^2 n\left(\frac{1}{2\widetilde{c}} - \frac{1}{\widetilde{w}}\right) \tag{3.12}$$

$$B(\widetilde{w},\widetilde{c}) = \frac{4\Gamma R\rho_{\mathrm{L}}}{\widetilde{c}^3} + 2\Gamma R^2 n\left(\frac{1}{4\widetilde{c}^2} - \frac{1}{\widetilde{w}^2}\right). \tag{3.13}$$

The average MSD is given by the following expression

$$\langle\Delta\widetilde{x}^2\rangle(\widetilde{w},\widetilde{c}) = \langle(\widetilde{x}(\widetilde{\tau}) - \widetilde{x}(0))^2\rangle(\widetilde{w},\widetilde{c}). \tag{3.14}$$

In the long-time limit Equation 3.14 can be written as

$$\lim_{\widetilde{\tau}\to\infty}\langle\Delta\widetilde{x}^2\rangle(\widetilde{w},\widetilde{c}) = 2\langle\widetilde{x}^2\rangle(\widetilde{w},\widetilde{c}) - 2\langle\widetilde{x}\rangle^2(\widetilde{w},\widetilde{c}). \tag{3.15}$$

This expression can be written as the following integral

$$\lim_{\widetilde{\tau}\to\infty}\langle\Delta\widetilde{x}^2\rangle(\widetilde{w},\widetilde{c}) = 2\frac{\int_0^{\varepsilon}\widetilde{x}^2 e^{-A-B\widetilde{x}}\mathrm{d}\widetilde{x}}{\int_0^{\varepsilon} e^{-A-B\widetilde{x}}\mathrm{d}\widetilde{x}} - 2\left(\frac{\int_0^{\varepsilon}\widetilde{x}e^{-A-B\widetilde{x}}\mathrm{d}\widetilde{x}}{\int_0^{\varepsilon} e^{-A-B\widetilde{x}}\mathrm{d}\widetilde{x}}\right)^2. \tag{3.16}$$

Since the Boltzmann weighting goes to zero quickly as $\widetilde{x}$ increases, the limit (ε) of the integration can be taken to infinity. The average MSD displacement then becomes

$$\lim_{\widetilde{\tau}\to\infty}\langle\Delta\widetilde{x}^2\rangle(\widetilde{w},\widetilde{c}) = \frac{4}{B^2} - \frac{2}{B^2} = \frac{2}{B^2}. \tag{3.17}$$

From the density profiles in Figure 3.3 the position of the first peak away from the wall ($\widetilde{c}$) can be calculated as a function of the channel width. This dependence is shown in Figure 3.5 and is found to be

$$\widetilde{c} \approx 1.0 + \frac{1.0}{\widetilde{w}}. \tag{3.18}$$

Equation 3.18 implies that the separation between the row at the wall and the next row away is approximately equal to the lattice-line spacing in the unbounded 2D crystal (R) which is an intuitive result. The functional form of $\widetilde{c}$ is important in determining how the MSD behaves as a function of the channel width. Combining Equations 3.13, 3.17, and 3.18 and expanding in the limit of large $\widetilde{w}$ gives the approximate form for the average MSD as

$$\lim_{\widetilde{\tau}\to\infty}\langle\Delta\widetilde{x}^2\rangle(\widetilde{w},\widetilde{c}) \approx \frac{8}{\Gamma^2 R^2\left(Rn + 8\rho_{\mathrm{L}}\right)^2}\left(1 + \frac{Rn + 12\rho_{\mathrm{L}}}{Rn + 8\rho_{\mathrm{L}}}\frac{1}{\widetilde{w}}\right). \tag{3.19}$$

The result of this analysis is plotted as a dotted line in Figure 3.4 (without the constant term) and is seen to predict the correct scaling behavior. The quantitative error in the pre-factors is introduced by the many approximations made during the derivation of the MSD dependence on $\widetilde{w}$. Importantly, the derivation of the MSD dependence shows that the interactions of the wall-colloids with the colloids in their immediate vicinity (the neighboring row) are the dominant factor in determining the behavior of the MSD as a function of the channel width. The interactions with the colloids farther away give higher order corrections to the MSD scaling.

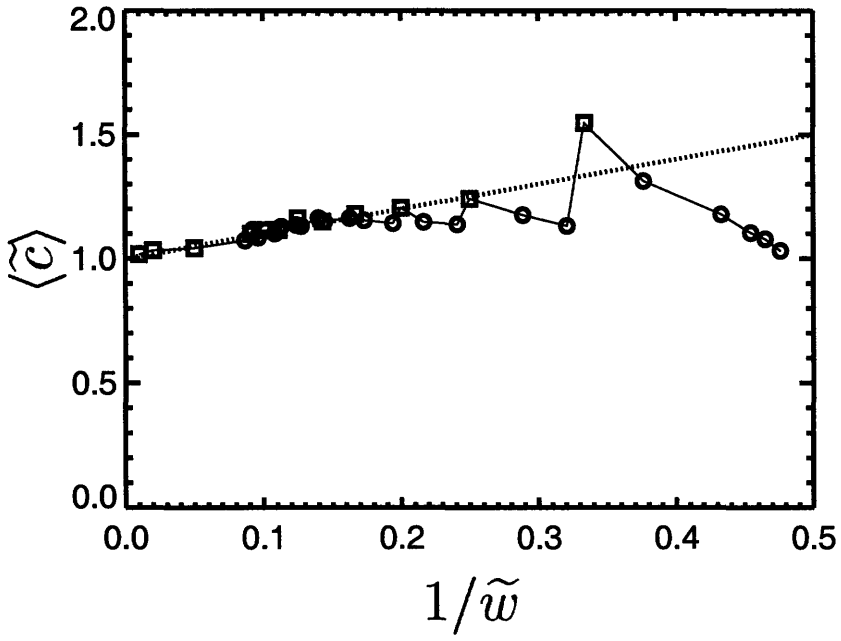

Fig. 3.5: *x position of the first peak in the density profile for selected dimensionless channel widths; square symbols correspond to integer channel widths and circle symbols correspond to non-integer channel widths. The dotted line is a linear fit to the data showing the functional form of* $\widetilde{c}$ *in the limit of large* $\widetilde{w}$.

The data in Figure 3.4 also show oscillations in the MSD as a function of the channel width. As in the case of the wall-spacing (Figure 3.2a) the oscillations decay after a channel width of $\sim$ 5. This implies that effects of the changes occurring in the center of the channel are being shielded from the wall colloids. There is a regular periodicity of the oscillations which is $\sim R$ implying that there are magic number channel widths and in this case the maxima in the MSD data occur at integer multiples of R for channel widths greater than 2.

Figure 3.6 shows the physical changes occurring in the structure that give rise to the first oscillation. For dimensionless channel widths less than $\sim$ 2 there are two rows of colloids, one on each wall. As the channel width is increased, the two rows of colloids have weaker interactions leading to an increase in the MSD plateau of the wall-colloids. Near a dimensionless channel width of 2, colloids begin to occupy the center of the channel. The repulsion due to the increased number of colloids occupying the center of the channel results in a decrease of the MSD of the wall-colloids. For a dimensionless channel width of 2.31 there is a well defined row in the center of the channel forcing the wall-colloids to remain near the wall, thus causing a minimum in the MSD at the wall. As the channel width is further increased, the center row begins to divide into two rows causing a very loose structure to exist in the center of the channel. This loose structure allows the colloids at the wall to fluctuate away more easily resulting in a maximum for the MSD at a dimensionless channel width of 3. Above the dimensionless channel width of 3, the rows in the center of the channel begin to form and become distinct and when $\widetilde{w} = 3.46$ there are two distinct rows in the bulk, both of which force their respective neighboring wall-colloids to remain near the wall. A similar process is repeated as the dimensionless channel width is increased from 3.46 to 4 (max MSD) to 4.62 (min MSD). The intermediate width of 4.15 shows a large amount of disorder in the bulk so it is surprising that a maximum in the MSD does not occur at this channel width. However, in this channel, the first rows in the bulk remained well defined and therefore do not allow the wall-colloids to fluctuate away from the walls. At a dimensionless channel width of 5 the row in the center of the channel again begins to broaden and the MSD at the walls passes through a maximum. However, in this case, the first row in from the wall is left relatively unchanged by this process and therefore the oscillations in the MSD of the wall-colloids are diminished for dimensionless channel widths greater than 5. In Figure 3.6 this effect is further illustrated by the examples of $\widetilde{w} = 4.15$ and 5.15 where it is evident that there is disorder in the center of the channel but the first rows in the bulk remain well defined.

Defect Structure

The analysis of the density profiles and the MSD at the walls leads to the observation that the structural changes that take place in the crystal as the channel width is increased are occurring predominantly in the bulk for large channels. The structural changes in the bulk in turn affect the properties of the wall-colloids. In order to further understand the effect of channel width on the structure of the 2D crystal, it is necessary to measure properties of the whole crystal, not just properties at the walls. One important measure of the structure of a 2D crystal is the defect concentration. For an unbounded system of repulsive dipoles in 2D the structure is purely hexagonal with each colloid having six neighbors. Defect sites in that crystal are defined as sites which have more or less than the usual six neighbors. For wall-colloids in a channel, a defect is defined as a colloid that would have more or less than six neighbors if the wall were not present. This translates to defects at the wall being defined as colloids with more or less than four neighbors since a wall-

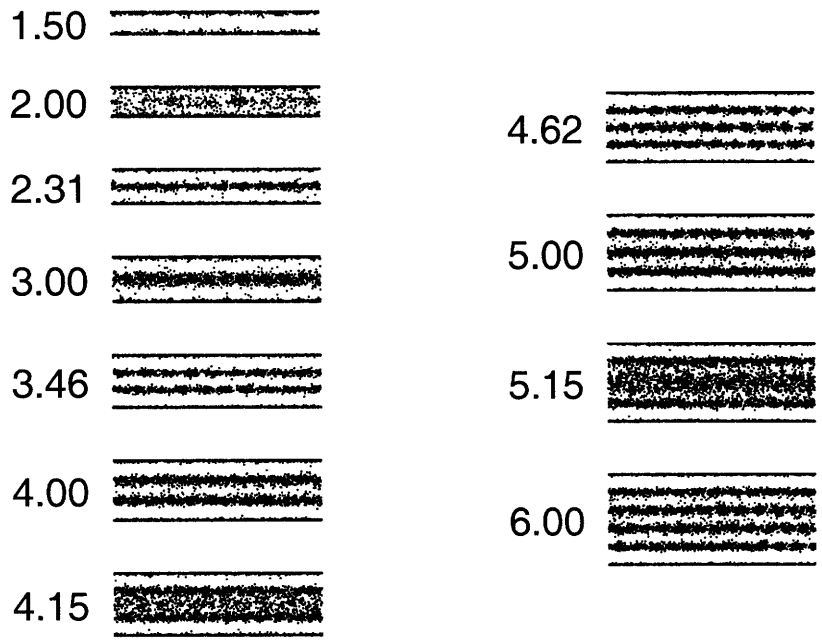

Fig. 3.6: *Density of colloids for selected dimensionless channel widths ($\widetilde{w} = 1.50$ to 6.00) for a total time of $\widetilde{\tau} = 37$ showing the oscillations between a loose and tight center row as the channel width is increased. Each point represents the position of a colloid and points were drawn every $\widetilde{\tau} = 0.37$.*

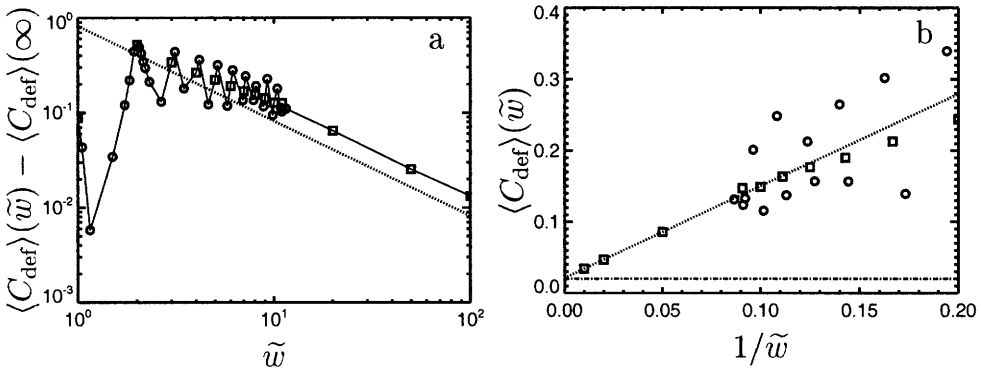

Fig. 3.7: *(a) Defect concentration for selected dimensionless channel widths; square symbols correspond to integer channel widths and circle symbols correspond to non-integer channel widths. The dotted line is the prediction given by Equation 3.24 (without the constant term). (b) The defect concentration approaches a constant as the channel width increases. The dash-dot line corresponds to the equilibrium defect concentration in the unbounded system at a dimensionless field strength of* $\Gamma = 16.13$.

colloid with four neighbors is equivalent to a non-defect site in the unbounded 2D case. This can be seen in the Delaunay triangle diagram in Figure 3.2b where the crystal is triangular and each wall colloid has four neighbors. For the non wall-colloids (bulk-colloids) in the channel system, defects are defined in the same way as they are in the unbounded 2D crystal. The concentration of defect sites can be used to determine the state of the system [80, 81], but here we are interested in using the defect concentration as a measure of how the channel system differs from the unbounded system.

The defect concentration as a function of channel width is shown in Figure 3.7a. Surprisingly, the defect concentration increases as the channel width is decreased. This is counter-intuitive because the channel geometry is shown to stabilize a layered structure near the walls as shown in the density profiles (Figure 3.3). These two observations are reconciled by noting that although the channel walls do impart a very nice layered structure near the walls, that structure is not perfectly hexagonal because the line-density of the colloids at the wall differs from that in the adjacent row. Therefore, the wall-spacing is not commensurate with the bulk crystal spacing and as a result defects occur near the walls. For the narrow channels, the wall-colloids comprise a large portion of the system and therefore their higher defect concentration dominates the overall defect concentration of the system.

The behavior of the defect concentration as a function of the channel width in Figure 3.7a is predicted by a simple argument. The concentration of defects is given by a bulk contribution and a wall contribution

$$C_{\rm def}(\widetilde{w}) = \frac{N_{\rm def}}{N} = \frac{N^{\rm b}_{\rm def}}{N^{\rm b}}\frac{N^{\rm b}}{N} + \frac{N^{\rm w}_{\rm def}}{N^{\rm w}}\frac{N^{\rm w}}{N}, \tag{3.20}$$

where N and $N_{\rm def}$ are the total number of colloids and defects in the system respectively. The parameters $N^{\rm b}$ and $N^{\rm w}$ are the number of bulk and wall colloids respectively. Again, the boundary

between the bulk region and the wall region is defined as a distance $R/2$ away from the walls. The ratios $N^{\mathrm{b}}_{\mathrm{def}}/N^{\mathrm{b}}$ and $N^{\mathrm{w}}_{\mathrm{def}}/N^{\mathrm{w}}$ can be approximated as constants equal to the unbounded system defect density and the semi-infinite wall-defect density respectively. The wall-defect structure is shown in Figure 3.8 (inset) where the defects along the walls are always accompanied by another defect in the first row of the bulk. Taking this into consideration, each wall-defect in the semi-infinite limit actually induces another defect in the bulk and therefore the semi-infinite wall-defect density must be doubled. Therefore, the total defect concentration is approximated as

$$C_{\mathrm{def}}(\widetilde{w}) \approx C^{\mathrm{b}}_{\mathrm{def}}(\infty)\frac{N^{\mathrm{b}}}{N} + 2C^{\mathrm{w}}_{\mathrm{def}}(\infty)\frac{N^{\mathrm{w}}}{N}. \tag{3.21}$$

Based upon the definition of the wall region, the two ratios in Equation 3.21 can be approximated as

$$\frac{N^{\mathrm{w}}}{N} \approx \frac{2\rho_{\mathrm{w}}}{nw} = \frac{2R}{0.83w} = \frac{2}{0.83\widetilde{w}} \tag{3.22}$$

$$\frac{N^{\mathrm{b}}}{N} \approx 1 - \frac{2}{0.83\widetilde{w}}. \tag{3.23}$$

The parameter ρ_{w} is the line density along the wall and is equal to $(0.83a)^{-1}$ (from Figure 3.2) for large channels. The factor of 2 comes from the two walls. Therefore the total concentration of defects is approximated as

$$C_{\mathrm{def}}(\widetilde{w}) \approx C^{\mathrm{b}}_{\mathrm{def}}(\infty) + \left(2C^{\mathrm{w}}_{\mathrm{def}}(\infty) - C^{\mathrm{b}}_{\mathrm{def}}(\infty)\right)\frac{2}{0.83\widetilde{w}}, \tag{3.24}$$

in the limit of large channels. The values of $C^{\mathrm{b}}_{\mathrm{def}}(\infty)$ and $C^{\mathrm{w}}_{\mathrm{def}}(\infty)$ were obtained by extrapolating the simulation data in the channels. This approximation (constant plus correction of order $\widetilde{w}^{-1}$) is seen as a dotted line in Figure 3.7a and additionally the total defect concentration is observed to approach the unbounded limit of 0.02 exactly as the channel width gets very large in Figure 3.7b. This observation implies that the defect properties of the channel system approach the unbounded system in the limit of large channels, as expected. Even for large channels however, there is still a large concentration of defects at the walls as seen in Figure 3.8. The concentration of wall-defects goes to a constant in the limit of large channels. The value that the wall-defect density approaches (0.18) is much larger than the value that the bulk-defect density approaches (0.02). The cause of this higher defect density can be seen in Figure 3.8 (inset) where there are stable dislocations along the length of the wall. In the unbounded system, a dislocation is defined as a pair of neighboring colloids with 5 and 7 neighbors respectively. Along the wall in the channel system, a dislocation is defined as a wall-colloid with 3 or 5 neighbors neighboring a bulk-colloid with 7 or 5 neighbors respectively. Along the wall, 18% of the total wall-colloids are part of a dislocation and are the cause of the higher density of defects at the wall. The dislocations along the walls are spaced evenly which is a consequence of the differing line-densities along the wall and in the first row. The different line-densities, force wall-colloids and their neighboring row to form dislocations at regular intervals in order to minimize the energy of interaction between these two rows.

The oscillations in defect concentration as a function of channel width decay much more slowly than the oscillations in the wall-spacing or MSD. The splitting of the center row into two rows as the channel width is increased causes a loose structure to form in the center of the channel and

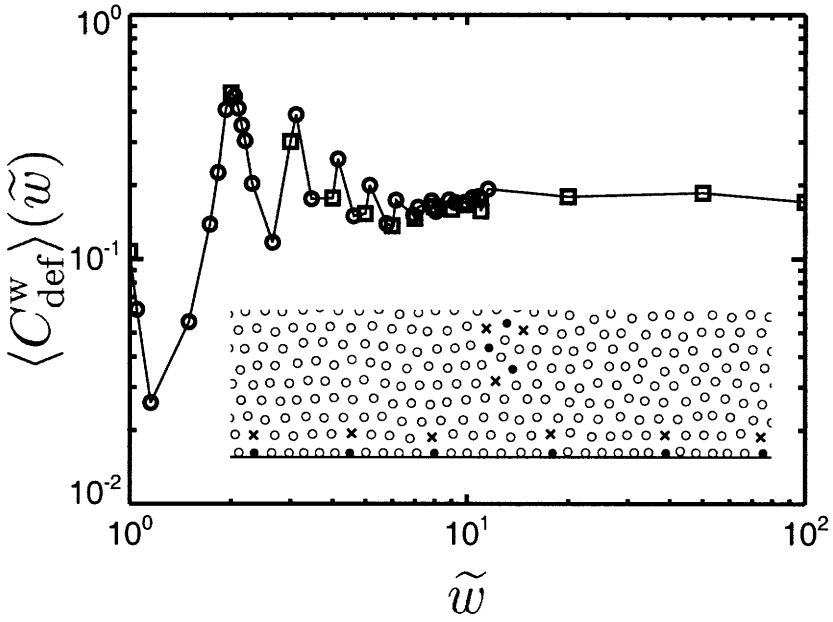

Fig. 3.8: *Defect concentration at the wall for selected dimensionless channel widths; square symbols correspond to integer channel widths and circle symbols correspond to non-integer channel widths. Inset is a snapshot near the wall for a dimensionless channel width of* 50 *showing coordination of nearest neighbors; open thin circles correspond to six-fold coordinated colloids (or four-fold if on a wall), closed circles correspond to five-fold coordinated colloids (or three-fold if on a wall), × symbols correspond to seven-fold coordinated colloids (or five-fold if on a wall).*

increases the defect concentration in the channel. When there are well defined rows in the center of the channel, the structure there is very regular and therefore the defect concentration in the channel is lower. As in the case of the wall-spacing and the MSD, the periodicity of the oscillations in the defect density is $\sim R$ but in this case the maxima and minima do not occur at integer multiples of R. The oscillations in defect density persist for large channels ($\widetilde{w} > 10$) indicating that the structure in the center of wide channels is still strongly influenced by the channel width. At the walls however, the oscillations in the wall-defect concentration decay by a channel with of ~ 5. The combination of these two observations leads to the conclusion that the large channel oscillations in total defect concentration are due to bulk contributions and not the walls. Therefore, the structural changes due to changing channel width are predominantly manifested in the center of the channel and the structure near the walls is influenced in a secondary manner. The results in this section indicate that defect concentration is a very sensitive measure of the effects of channel width on the crystal structure in the channel.

3.2.5 Dynamics in 2D Channels

In Sections 3.2.3 and 3.2.4 we characterized the equilibrium structures that form in these systems and we found that the colloids along the walls exhibit significantly different behavior from the colloids in the bulk. We performed an analysis of the colloids against the wall and found that they are highly localized and remain so over the duration of our simulations. Therefore, in this section we will focus on the dynamics of the bulk colloids. Again, a bulk colloid is defined as any colloid located at a distance greater than $R/2$ from the wall. *All of the results presented for $g_6(\widetilde{\tau})$ are given for the bulk colloids only.*

The bond-order correlation function is shown in Figure 3.9 for a variety of channel widths at two different field strengths. In Figure 3.9a $g_6(\widetilde{\tau})$ is shown for channels at a dimensionless field strength of 16.13, a value well into the solid phase for an unbounded system. For a channel width of 100, the $g_6(\widetilde{\tau})$ behavior is indistinguishable from the behavior in the unbounded system showing that the channel system approaches the unbounded system in the limit of large channels. As the channel width is made narrower the channel system becomes more disordered than the unbounded system at this dimensionless field strength [33]. This trend towards more disorder is non-monotonic and exhibits several oscillations as a function of channel width. An example of these oscillations is illustrated by the $g_6(\widetilde{\tau})$ behavior for the dimensionless channel widths 5 to 3 (g to a) in Figure 3.9a.

In Figure 3.9b, $g_6(\widetilde{\tau})$ is shown for channels at a dimensionless field strength of 12.41. This field strength is well into the liquid phase in the unbounded system where $g_6(\widetilde{\tau})$ decays exponentially to zero. In Figure 3.9b (and Figure 3.9c) at a dimensionless channel width of 100, the $g_6(\widetilde{\tau})$ curve begins to decay exponentially and is indistinguishable from the unbounded curve. However, at a dimensionless lag time of ~ 1, a plateau begins to develop and the curve deviates from the unbounded case. Eventually at a dimensionless lag time of ~ 50 the plateau begins to decay exponentially again. We will discuss this plateau in more detail shortly. As the dimensionless channel width is made narrower the channel system becomes more ordered than the unbounded system at this field strength. Again, the non-monotonic behavior in $g_6(\widetilde{\tau})$ is observed for this dimensionless field strength. In Figure 3.9b oscillations are shown for dimensionless channel widths 5 to 3 (g to a). However, in general as the channel width becomes wider the unbounded case is approached slowly as seen in Figure 3.9c where four $g_6(\widetilde{\tau})$ curves are shown for successively wider

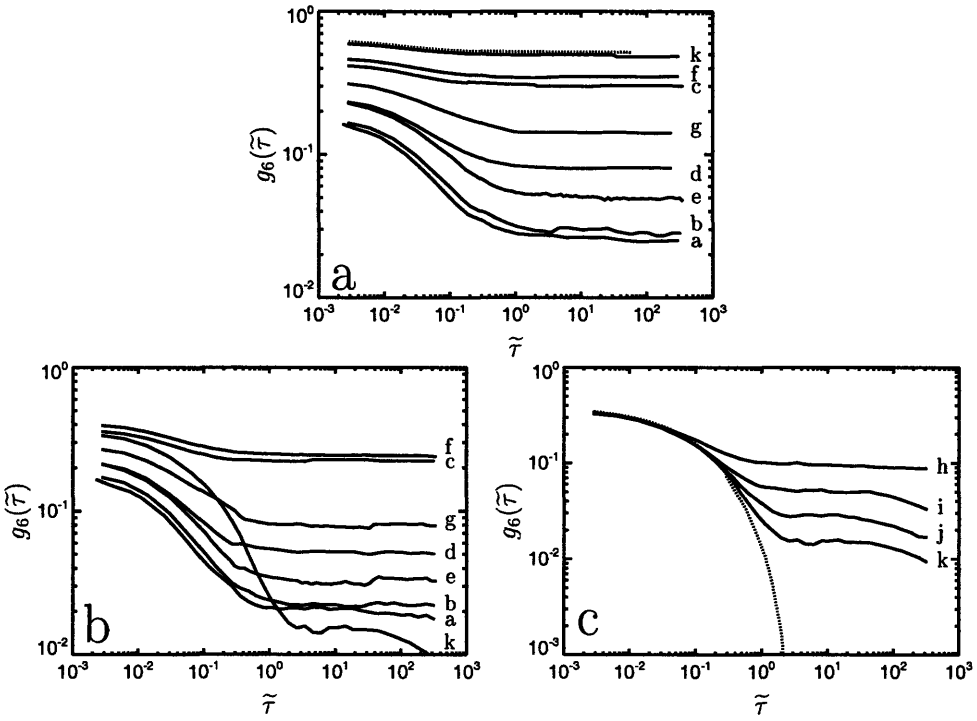

Fig. 3.9: *The bulk bond-order correlation function at a dimensionless field strength of (a)* $\Gamma = 16.13$, *(b)* $\Gamma = 12.41$ *for a variety of channel widths. (c) The bulk bond-order correlation function at a dimensionless field strength of* $\Gamma = 12.41$ *for large channel widths. The letters a, b, c, d, e, f, g, h, i, j, and k correspond to the dimensionless channel widths* 3, 3.12, 3.46, 4, 4.15, 4.62, 5, 10, 20, 50, *and* 100 *respectively. The dotted line corresponds to the unbounded system at a dimensionless field strength of (a)* $\Gamma = 16.13$ *and (c)* $\Gamma = 12.41$.

channels, 10, 20, 50 and 100 at a dimensionless field strength of 12.41. The second exponential decay of the plateau only becomes evident for channels with a dimensionless width $\widetilde{w} \geq 20$. The existence of this intermediate time plateau is a very interesting feature of this system and we offer below an explanation for its origin and subsequent decay.

Local Dynamics

The origin of the plateau is due to the presence of the parallel flat walls in the channel systems. The walls create a region of stable structure that extends away from the wall into the middle of the channel. We are interested in probing the local dynamics in these regions and therefore we chose to look at the bond-order correlation function in time for different sections of the channel. We analyzed $g_6(\widetilde{\tau})$ for strips of dimensionless width 2 along the length of the channel located at increasing distances from the walls. Therefore, the strip labelled 0-2 indicates the sections of the channel that are within a dimensionless distance of 2 from either wall. In our analysis, only colloids that remained in a given strip for the duration of the lag time were considered. Additionally, only bulk colloids were considered for this analysis (e.g. in the strip labelled 0-2, the colloids within a distance $R/2$ from the wall were not used in the analysis).

The results of this analysis are shown in Figure 3.10 for a dimensionless channel width of 100 at a dimensionless field strength of 12.41. In the regions nearest the wall (0-2 to 2-4) there is a very well defined plateau in $g_6(\widetilde{\tau})$ over all dimensionless lag times. As we move farther away from the walls (4-6 to 6-8) there is still a distinguishable plateau in $g_6(\widetilde{\tau})$ over all lag times but it is plagued by large statistical noise. The poor statistics are the result of the fact that the colloids in these sections do not remain in their respective sections for very long times. If we move even farther away from the wall (8-10 to 14-16) there is no longer a statistically distinguishable plateau in $g_6(\widetilde{\tau})$ and all of the curves fall on top of the curve for the unbounded system at this dimensionless field strength.

These results bring to light many interesting features of the dynamics in these systems. In the sections where there is a plateau in $g_6(\widetilde{\tau})$, it remains constant until the longest lag time for which we have statistics. Additionally, the value of this plateau is continuously decreasing as we move away from the wall until there is no longer a statistically significant plateau. This continuous decrease indicates that there is no well defined boundary between the "wall" region and the "bulk" region but rather there is a continuous transition from one to the other. This result is similar to the observations made by Segalman *et al.* [59] for a system of block copolymers confined in two dimensional channels. Teng *et al.* [57] also observed the decay of order as one moves away from the confining walls in a dusty plasma system. Additionally, in their results for $g_6(\widetilde{\tau})$ they observed a plateau for the sections near the walls, in good agreement with our results.

Now we address the issue of the subsequent decay in the plateau in large channels (Figure 3.9c) since no such decay is observed within the sections nearest the wall in Figure 3.10. The reason for the decay is actually related to the mobility of the colloids in the different regions of the channel. As mentioned previously, the statistics in Figure 3.10 for the sections 4-6 and 6-8 away from the wall become rather poor at long times due to this mobility. In Figure 3.11 we show trajectories for two colloids over four different dimensionless lag times in a dimensionless channel width of 100 at a dimensionless field strength of 12.41. For all of the lag times, the colloid against the wall remains very localized next to the wall but becomes increasingly mobile in the direction parallel to the wall. For a dimensionless lag time less than ~ 1 (Figure 3.11a) the colloid in the bulk is able to explore

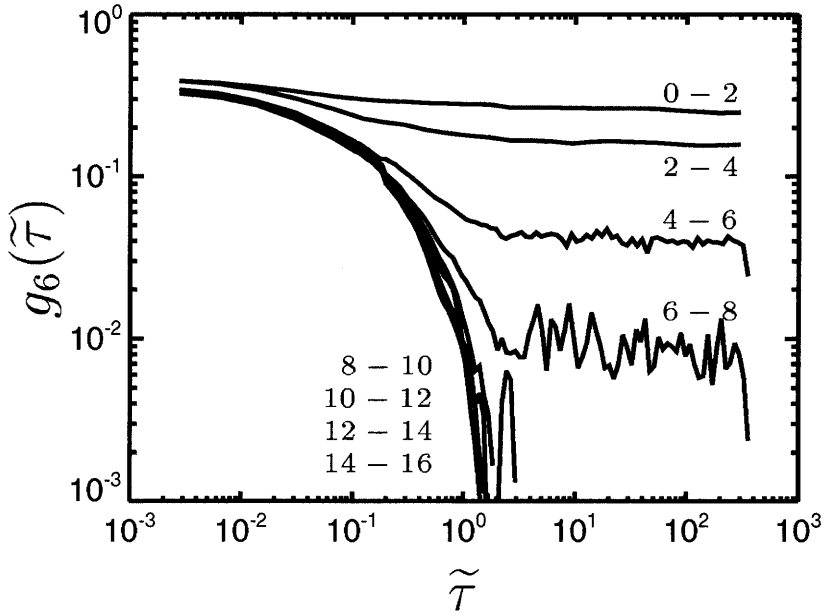

Fig. 3.10: *The local bond-order correlation function at a dimensionless field strength* $\Gamma = 12.41$ *and a dimensionless channel width* $\widetilde{w} = 100$. *The labels* $0-2$, $2-4$, *etc. refer to the dimensionless distance away from the wall where statistics were taken. The distances* $8-10$ *through* $14-16$ *away from the wall are statistically indistinguishable from one another and from the bond-order correlation function for the unbounded system at this field strength.*

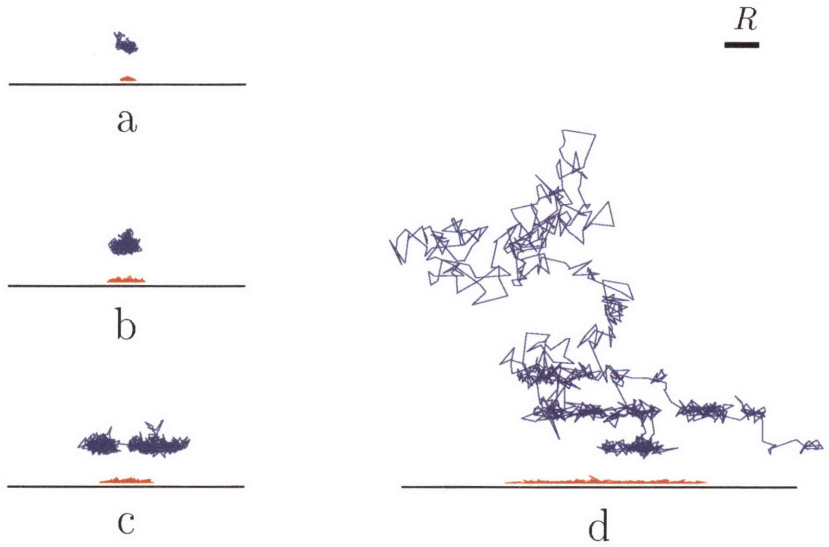

Fig. 3.11: *Trajectories for a bulk colloid (blue) and a neighboring wall colloid (red) over four different times at a dimensionless field strength of* $\Gamma = 12.41$ *in a channel of dimensionless width* $\widetilde{w} = 100$. *The total trajectory time is (a)* $\widetilde{\tau} = 0.373$, *(b)* $\widetilde{\tau} = 3.73$, *(c)* $\widetilde{\tau} = 37.3$, *and (d)* $\widetilde{\tau} = 373$. *The channel wall is drawn as a solid line.*

its local region without feeling the constraint of its neighboring colloids. This type of behavior is seen uniformly over the entire width of the channel and gives rise to the initial exponential decay in the bond-order correlation function. Over intermediate lag times (Figures 3.11b and c) that colloid completely explores its local environment but remains trapped in its respective region near the wall. Since the colloid remains trapped in this local region its orientation with respect to its neighbors remains well correlated in time and therefore a plateau develops in $g_6(\widetilde{\tau})$. Over very long lag times (Figure 3.11d) the bulk colloid is able to escape the region near the wall and make an excursion into the center of the channel. This excursion causes the correlation of the bond-order for this colloid to decay and therefore the plateau in $g_6(\widetilde{\tau})$ begins to decay for very long lag times.

Figures 3.10 and 3.11 illustrate that the structure in the different regions of the channel combined with the different dynamics in those regions give rise to the unusual behavior of the bond-order correlation function in time. The region closest to the wall is highly structured and the colloids there have low mobility while, at liquid-like field strengths, the regions far from the wall have less structure and high mobility. The exchange of colloids between these two regions of the channel is slow and therefore over intermediate times there is a plateau in $g_6(\widetilde{\tau})$ before the colloids near the wall can escape into the bulk. It is important to note that in Figure 3.9c the decay in the plateau is only seen for channels wider than ~ 20, matching well with what we have found in Figure 3.10 where we observed a persistent plateau in $g_6(\widetilde{\tau})$ out to a dimensionless distance of 8 from the walls. This means that, at this dimensionless field strength, in channels with a dimensionless width narrower than ~ 16 there are no regions where the $g_6(\widetilde{\tau})$ curve decays to zero and therefore in these channels we would expect the plateau to persist for all lag times.

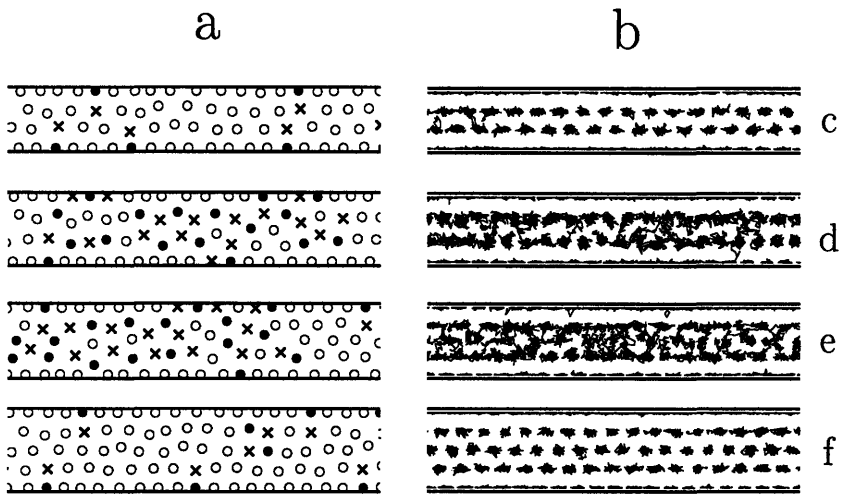

Fig. 3.12: *(a) Snapshots of equilibrium defect configurations at a dimensionless field strength of* $\Gamma = 16.13$ *for sections of dimensionless length 20, in four different channel widths c, d, e, and f corresponding to* $\widetilde{w} = 3.46$, 4, 4.15, *and* 4.62 *respectively (keeping consistent notation from the curves in Figure 3.9). Open thin circles correspond to six-fold coordinated colloids (or four-fold if on a wall), closed circles correspond to five-fold coordinated colloids (or three-fold if on a wall),* × *symbols correspond to seven-fold coordinated colloids (or five-fold if on a wall). (b) Trajectories of the colloids in that section of the channels for a dimensionless lag time of* $\widetilde{\tau} = 3.73$.

The behavior of the bond-order correlation function and the dynamics of the colloids in general are intimately related to the defects in these 2D systems [40, 37]. We have observed that the channel-like confinement gives rise to some very interesting defect properties [33] and we will now discuss in more detail how those defect properties affect the dynamics of the colloids in 2D channels.

Link Between Structure and Dynamics

It is well known that defects can give rise to increased mobility of the colloids in a solid 2D crystal. This point is illustrated for the channel systems in Figure 3.12. Figure 3.12a shows the defect structure for four different dimensionless channel widths (3.46, 4, 4.15, and 4.62) at a dimensionless field strength of 16.13. Again, in the channel systems, a bulk colloid is said to be a defect if it has more or less than six neighbors while a wall colloid is said to be a defect if it has more or less than four neighbors. It is quite evident that the defect concentration is larger for the intermediate channel widths of 4 and 4.15 than it is for the channel widths of 3.46 and 4.62. Additionally, it is important to note that even in the channels with a low concentration of defects (3.46 and 4.62) there are still regular dislocations along the wall [33]. Comparing the defect structures in Figure 3.12a with the trajectories shown in Figure 3.12b it is seen that the colloids in the channels with more defects are significantly more mobile than those in the channels with lower defect concentration.

Similar to the trajectories in Figure 3.11, the colloids along the wall remain highly localized even if there is significant mobility of the colloids in the bulk.

Again, the behavior (and the magnitude) of $g_6(\widetilde{\tau})$ is highly correlated to the defect structure of the 2D system. Therefore comparing the curves in Figure 3.9a for the same dimensionless channel widths as in Figure 3.12 we see that the oscillations in the trend of $g_6(\widetilde{\tau})$ as a function of channel width come about because of oscillations in the defect concentration. In the unbounded 2D system both the bond-order correlation function in time and information about the defects can be used to characterize the phase of the system and therefore we will apply a similar analysis to our 2D channel systems.

3.2.6 State-Diagram of Laterally Confined 2D Systems

As we have shown in Section 3.2.5, the channel system is quite heterogeneous with the regions near the wall having different behavior than the regions farther away from the wall. Additionally, there is no well defined boundary between these two regions and therefore it is very difficult to define a "phase" for the entire channel system. We can however produce a map of the properties of the system as a function of the independent thermodynamic variables controlling the system (Γ and $\widetilde{w}$). An example of this type of state diagram is shown in Figure 3.13 where we have mapped the bulk-defect concentration ($C_{\text{def}}^{\text{b}}$) as it is closely related to the dynamics of the 2D channel system. In Figure 3.13a we show the value of the bulk-defect concentration for each set of conditions that we simulated. In Figure 3.13b we show an interpolated continuous contour plot for the same data in order to more clearly illustrate the trends in the data. The most obvious characteristic of the state diagram in Figure 3.13 is the re-entrant behavior observed as a function of dimensionless channel width. The periodicity of the oscillations in the bulk-defect concentration as a function of channel width is $\sim R$. This observation suggests that the parallel channel walls cause a periodic destabilization of the crystal in the bulk as the channel width is decreased. We do not observe any re-entrant behavior as a function of dimensionless field strength, in contrast to systems confined in 2D circles or periodic 1D light fields [48, 49, 50, 54, 55, 56].

A state-diagram such as this is important in that it shows how sensitive the structures, and therefore dynamics, in 2D channel systems are to the geometric constraints imposed upon the system. The state-diagram presented here is quite general and similar trends occur for other properties of the 2D channel system such as the local orientational order parameter (Ψ_6) and even the value of the plateau in $g_6(\widetilde{\tau})$. Additionally, the re-entrant behavior as a function of the dimensionless channel width is an interesting characteristic that has not been observed in other 2D confining geometries.

As an example of the effect of Γ on the structure of the system we show density profiles for four different dimensionless channel widths in Figure 3.14. The four dimensionless channel widths in Figure 3.14 are the same as the four channels shown in Figure 3.12. For all of the dimensionless field strengths in Figure 3.14 there is a large magnitude peak in the density profiles occurring at the walls [33]. For low Γ systems (Figure 3.14a) there is not a significant qualitative difference between the density profiles for the four channels. However, as Γ is increased (Figures 3.14b and c) the density profiles for dimensionless channel widths 3.46 and 4.62 begin to appear strikingly different from the profiles for dimensionless channel widths 4 and 4.15. Sharp peaks in the density profiles appear across the channel for $\widetilde{w} = 3.46$ and 4.62 while for dimensionless channel widths of 4 and 4.15 the peaks are not as pronounced and there is less order across the channel.

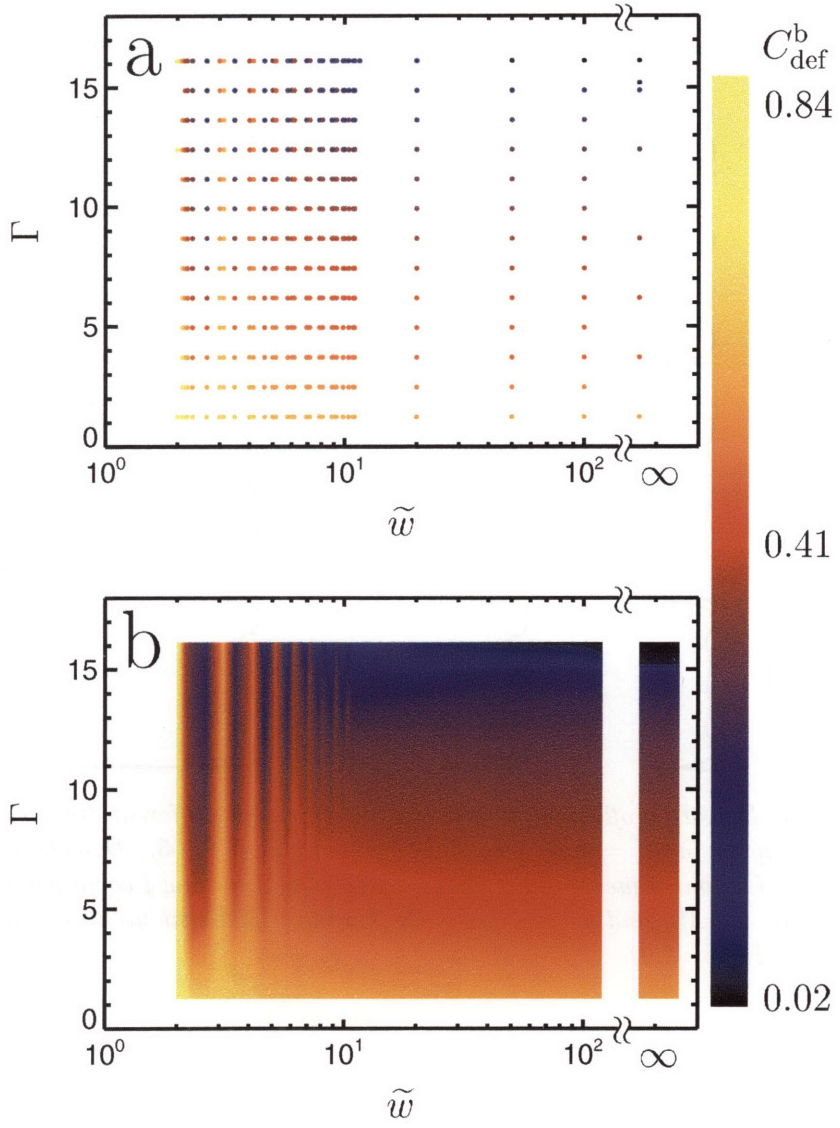

Fig. 3.13: *(a) Bulk defect concentration as a function of channel width and field strength. Light (yellow) indicates a high concentration of defects and dark (black) indicates a low concentration of defects. Each symbol designates a simulation result. (b) Continuum plot of bulk defect concentration as a function of channel width and field strength. Continuous contours have been interpolated along lines of constant defect concentration from the data in (a).*

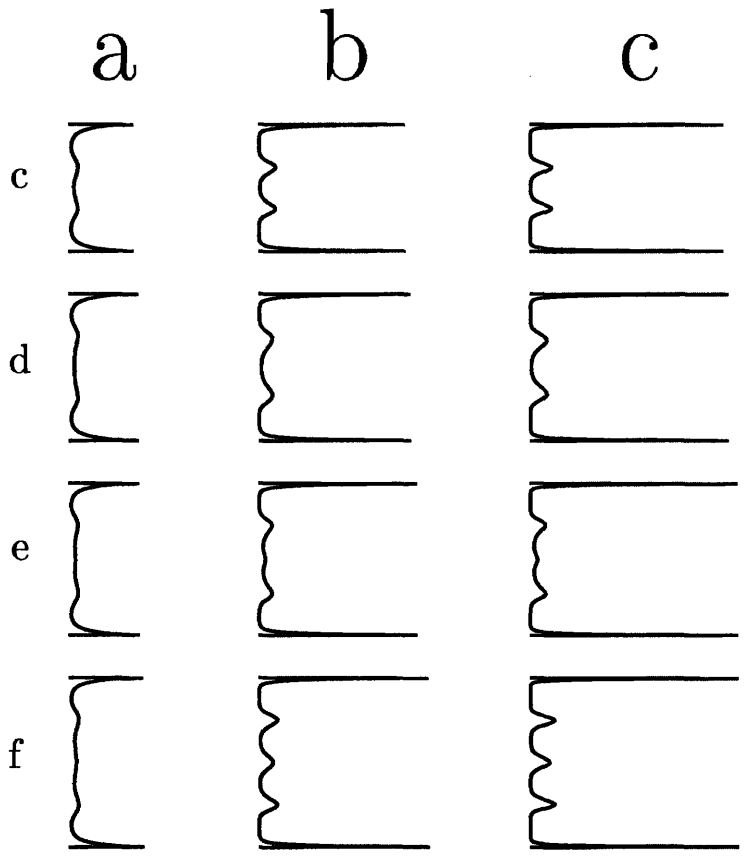

Fig. 3.14: *Density profiles across the channels for three different dimensionless field strengths (a)* $\Gamma = 2.48$, *(b)* $\Gamma = 8.69$, *(c)* $\Gamma = 13.65$. *Density profiles are given for four dimensionless channel widths c, d, e, and f corresponding to* $\widetilde{w} = 3.46$, 4, 4.15, *and* 4.62 *respectively (keeping consistent notation from the curves in Figure 3.9).*

Generality of re-entrant behavior for repulsive potentials

We have compared our results for the dipolar system with two other systems described here. The first system consists of colloids interacting via a r^{-6} potential defined as

$$U_{6ij}(r_{ij}) = \epsilon_6 \left(\frac{d}{r_{ij}}\right)^6. \tag{3.25}$$

Similar to the dipolar system, we define a dimensionless field strength Γ_6 as

$$\Gamma_6 = \frac{\epsilon_6}{k_B T} \left(\frac{d}{R}\right)^6, \tag{3.26}$$

where the length scale R is as defined for the dipolar system. The simulation details for the r^{-6} system are identical to those described in Section 3.2.1 and Chapter 2 for the dipolar system and $d \ll R$ so R is still the only important length scale.

The second system consists of hard-spheres confined in a 2D channel. The analogous term for the dimensionless field strength Γ_{HS} is defined for this system as [78]

$$\Gamma_{\mathrm{HS}} = nd^2, \tag{3.27}$$

where n is again the number density in the system. For the hard sphere system, the important length scale is now d so the dimensionless channel width for these systems is defined as the true width of the channel scaled by d. Additionally time is made dimensionless as $\widetilde{t} = t(k_{\mathrm{B}}T)/(\zeta d^2)$ for this system. The simulations of the hard sphere systems utilized the same dimensionless time step and total times as the dipole system. The algorithm developed by Heyes [27] was used to treat hard sphere interactions for this system.

Löwen [78] reports values for the solid-liquid phase transition for these two systems in the unbounded limit as $\Gamma_6^* = 5.33$ and $\Gamma_{\mathrm{HS}}^* = 0.887$ (where the asterisk refers to the phase transition point) giving us a reference for solid and liquid phases in these two systems. In Section 3.2.2 we showed that the phase transition in the dipolar system occurs in the range $\Gamma = 14.89 - 15.2$ so for this section we will take $\Gamma^* = 15.045$ for the dipolar system.

In Figure 3.15 we illustrate the general result of re-entrant behavior in 2D channel systems by showing data for bulk defect concentration as a function of dimensionless channel width for the three different types of 2D colloidal systems. In Figures 3.15a and b the dimensionless field strengths are such that the unbounded systems would be in the liquid phase while in Figure 3.15c the dimensionless field strengths are large so that the unbounded systems would be well into the solid phase. The curves in Figure 3.15 are equivalent to taking slices of constant Γ in Figure 3.13. The hard sphere results in Figures 3.15a and b were done for different fractions of Γ_{HS}^* than the respective simulations for the dipole and r^{-6} systems. This is because the hard sphere system becomes a gas if the number density is too low and therefore loses all structure. In Figure 3.15, as the interaction strength is increased, it is evident that the re-entrant behavior of the bulk defect concentration as a function of channel width becomes more pronounced for the dipolar and r^{-6} systems. For the hard sphere curves in Figures 3.15a and b this trend is evident as well. In Figure 3.15c the Γ_{HS} for the hard sphere system is large enough that there are hardly any defects in any of the channel widths but even this system still exhibits re-entrant behavior as a function of channel width. These results strongly suggest that the general form of the state-diagram shown in Figure 3.13 holds for 2D colloidal systems confined in hard-wall channels and interacting with repulsive potentials.

There are significant differences, however, between the three different types of colloidal systems. For instance, in Figure 3.15c the hard sphere system is nearly perfect due to the high number density while the other two systems still exhibit significant defect concentrations. A qualitative example of this difference between the systems is given in Figure 3.16 where we present snapshots of the defect structure in a section of a channel with dimensionless width 6.5 for the three different systems. The dimensionless field strengths in Figure 3.16 are $\Gamma = 1.13\Gamma^*$, $\Gamma_6 = 1.13\Gamma_6^*$, and $\Gamma_{\mathrm{HS}} = 1.13\Gamma_{\mathrm{HS}}^*$, all well into the solid phase for the unbounded systems. It is evident that the three systems have significantly different defect distributions. The dipolar system shows the regular dislocations along the wall that have been reported previously [33], while the other two systems exhibit no such regular

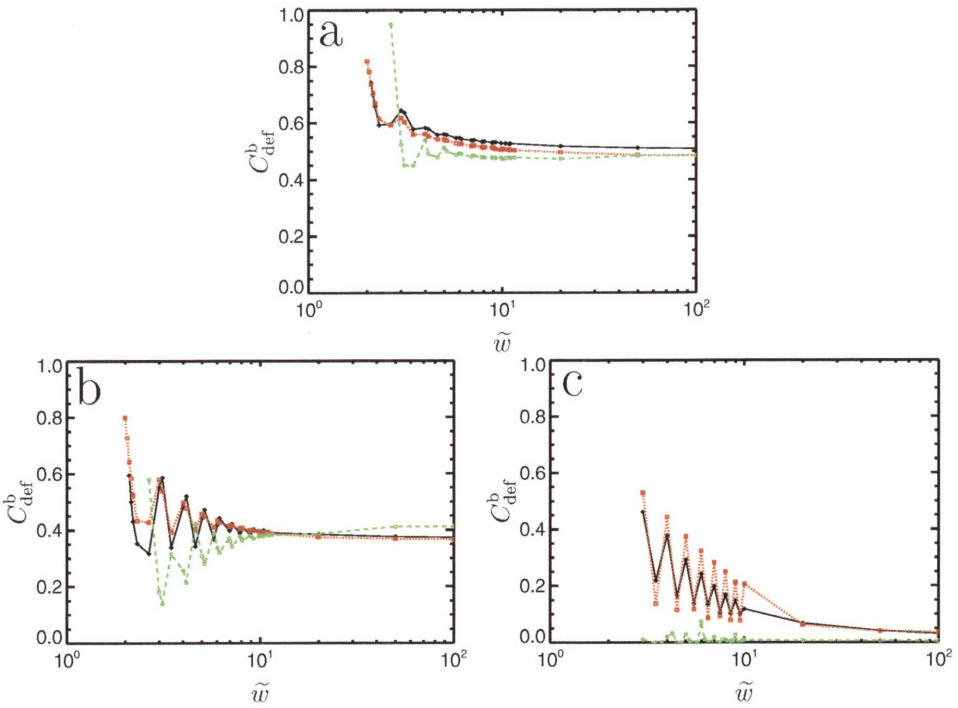

Fig. 3.15: *Concentration of defects in the bulk as a function of dimensionless channel width at three different dimensionless field strengths (a)* $\Gamma = 0.16\Gamma^*$, $\Gamma_6 = 0.16\Gamma^*_6$, $\Gamma_{HS} = 0.79\Gamma^*_{HS}$ *(unbounded liquid phase) (b)* $\Gamma = 0.58\Gamma^*$, $\Gamma_6 = 0.58\Gamma^*_6$, $\Gamma_{HS} = 0.9\Gamma^*_{HS}$ *(unbounded liquid phase) (c)* $\Gamma = 1.13\Gamma^*$, $\Gamma_6 = 1.13\Gamma^*_6$, $\Gamma_{HS} = 1.13\Gamma^*_{HS}$ *(unbounded solid phase). The (black) solid lines correspond to the dipolar system* (r^{-3})*, the (red) dotted lines correspond to the* r^{-6} *system, and the (green) dashed lines correspond to the hard sphere system.*

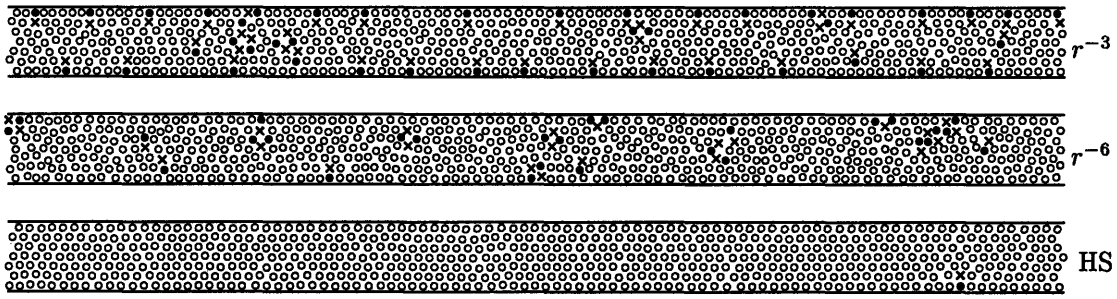

Fig. 3.16: *Snapshots of equilibrium defect configurations in channels with a dimensionless width of* $\widetilde{w} = 6.5$ *and a dimensionless field strength of* $\Gamma = 1.13\Gamma^*$, $\Gamma_6 = 1.13\Gamma_6^*$, $\Gamma_{HS} = 1.13\Gamma_{HS}^*$. *Each snapshot shows a section of dimensionless length* 100 *(total dimensionless channel length is* 170*). Open thin circles correspond to six-fold coordinated colloids (or four-fold if on a wall), closed circles correspond to five-fold coordinated colloids (or three-fold if on a wall),* × *symbols correspond to seven-fold coordinated colloids (or five-fold if on a wall). The channel walls are shown as solid lines.*

defects along the walls. Rather, in the r^{-6} system, the defects are found in small clusters that are distributed along the length of the channel. In the hard sphere system there are very few, short lived, pairs of dislocations showing evidence of the extreme ordering mentioned above.

3.3 Experiments on 2D MR Colloids

The 2D MR colloid system was also studied experimentally as a model for the self-assembly of MR fluids in microfluidic geometries. The experimental study of this system will have tremendous impact on the choices of materials and dimensions for real microfluidic devices utilizing self-assembled MR fluids as structural components.

3.3.1 Experimental Procedures

Using soft-lithography [82] we fabricated poly-dimethylsiloxane (PDMS) channels 40μm tall and 40, 80, and 200μm wide. These channels were treated with an oxygen plasma and bonded to a thin sheet of PDMS such that the two ends of the channel remained open. The channel was filled with a solution of paramagnetic colloidal spheres (2.8μm carboxylated DynaBeads® M-270, Dynal) suspended in 5.0× TBE buffer (0.17M ionic strength) to screen the electrostatic repulsion between the colloids. At this ionic strength the Debye length is ~1nm. The colloids have a magnetic susceptibility of 1 (given by manufacturer) [83] and a specific gravity of 1.6 causing them to sediment in the z-direction due to gravity to the bottom of the channel, forming a monolayer in the x-y plane with out of plane thermal fluctuations less than ~ 80nm. The open ends of the microchannel were then sealed using Vaseline® and the entire channel system was submerged in TBE buffer inside a sealed chamber with dimensions of ~ 2cm × 2cm × 2cm in order to prevent evaporation and pressure driven flows within the channel. The cell was placed inside an electromagnetic coil (25mm

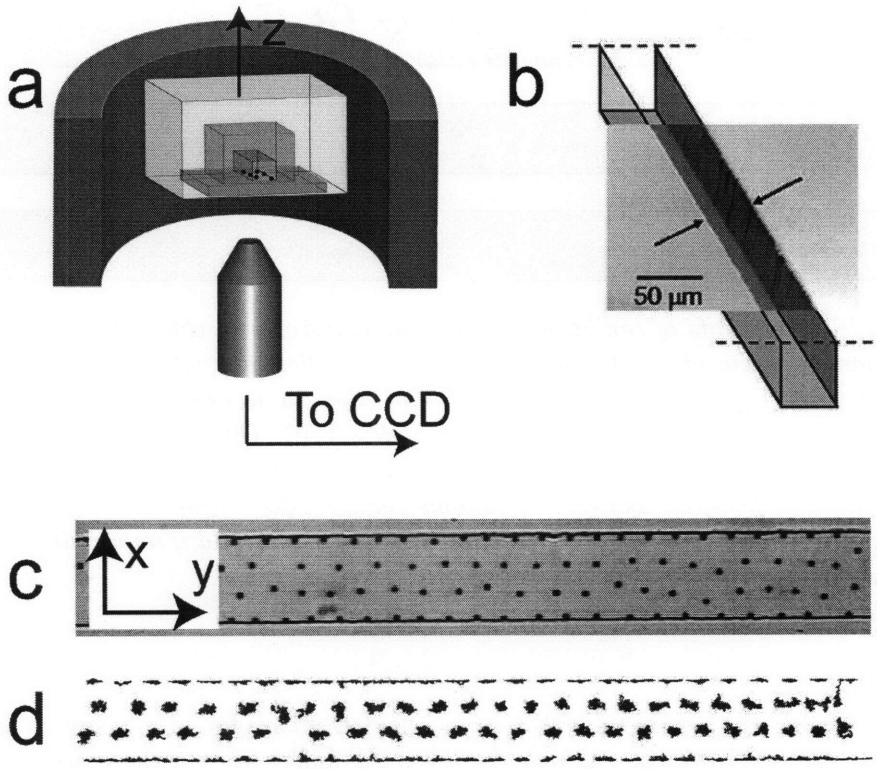

Fig. 3.17: *(a) Schematic of the experimental setup (not to scale). An end view of the channel is shown with the shaded regions being PDMS. The beads sediment in the z-direction to the bottom of the channel. The entire channel system is submerged in TBE buffer inside a chamber and placed into the center of the magnetic coil. The system is observed from underneath with the microscope objective (20×) and the images are captured with a CCD camera and sent to the computer for analysis. (b) SEM image of the PDMS channel before it is sealed. The opening shown will be the bottom of the well once the channel is sealed with a thin sheet of PDMS. The arrows indicate the location of the walls of the channel. (c) Characteristic image obtained during an experiment. The channel width is* $40\mu m$ *and the dimensionless channel width is* 3.44. *(d) Trace of the positions of the colloids in (c) for a dimensionless time of* 0.65.

inner diameter) such that the channel was located in the center of the coil thus causing the system to experience a uniform magnetic field in the z-direction (normal to the monolayer of colloids). The magnetic field was calibrated using an axial Hall probe and Gauss-meter (SYPRIS) and found to be uniform within a circle of radius 1cm in the center of the coil. The uniform field induced dipole moments in the colloids causing them to experience purely repulsive interactions [73]. The magnetic coil was placed on an inverted microscope (Axiovert 40 CFL, Zeiss) and image stacks of the system were captured using a CCD camera (KPM1A, Hitachi). A schematic of the experimental

setup is shown in Figure 3.17a and an SEM image of one of the PDMS channels (before bonding) is shown in Figure 3.17b. An example of an experimental image is shown in Figure 3.17c. The image stacks were analyzed off-line using custom programs [84, 85] written in the IDL language (Research Systems, Boulder CO) allowing us to assemble trajectories for the colloids such as the one shown in Figure 3.17d.

The dimensionless channel width $\widetilde{w}$ was defined as the real channel width divided by R. Using the current in the magnetic coil and the number density of colloids in the system as free parameters, we were able to explore a large section of the $\Gamma - \widetilde{w}$ phase space. We varied the dimensionless width of the channels between experiments by changing n, keeping $d \ll R$ for all of the channel widths. We performed experiments for a dimensionless field strength of $\Gamma \sim 12 \pm 1$ (in the liquid phase in the unbounded system [40, 86, 34]). The precise value of Γ could only be measured after an accurate value for n was obtained, during the off-line analysis of the experiment, and therefore during an experiment we aimed for $\Gamma \sim 12$.

After filling the channel with magnetic colloids, allowing them to sediment, and estimating n for a given system, the magnetic field was turned on and the system was equilibrated for several tens of dimensionless times. We measured the free diffusion coefficient of the colloids along the surface to be $\sim 52\%$ of the calculated Stokes diffusion coefficient ($D_0 = k_B T/\zeta$). Time was made dimensionless with the time for a colloid to freely diffuse one unit length along the PDMS surface [$\widetilde{t} = t(0.52 k_B T)/(\zeta R^2)$]. After equilibration, 1000 images were taken over a dimensionless time of ~ 15 and used to analyze the structural and dynamical properties of the system. By repeating several experiments at fixed conditions and obtaining identical results each time, we ensured that the size of the system and the time over which statistics were taken was sufficiently large to represent the equilibrium state of the system. The calculated properties were then compared with results from BD simulations performed as previously described. These simulations do not have any fitted parameters as all of the physical properties in the experiments were known a priori (or measured) for the beads, coil, and channels.

3.3.2 Structural Oscillations

As stated previously, the most characteristic global property of the structure in this system is the layering of the colloids parallel to the channel walls [57, 33]. This layering is illustrated in the density profiles shown in Figure 3.18 from the experimental system (dotted lines) and from BD simulations (gray solid lines). For all of the channel widths there is very good agreement between the simulation results and the experimental results. Slight differences arise at the walls of the channel where the experimental peak heights show some variance with respect to each other and the simulation results. In the PDMS channels the walls are not perfectly planar (Figure 3.17b) and this roughness gives rise to the differences in the peak heights that we observe experimentally.

In order to accurately and quantitatively capture the effects of the rough walls in the density profiles generated from our BD simulations, we obtained an estimate for the standard deviation of the wall position from our experiments and used that information to approximate "rough walls" during the post processing of the simulations. A schematic of this process is presented in Figure 3.19. The experimental distribution of the wall position was determined by tracing the position of each wall colloid for the duration of the 1000 frames and taking the outer most x-position (normal to the wall) as the location of the wall in the vicinity of that colloid. We were then able to assemble a distribution of wall positions for the channel. For a typical experiment the wall position was

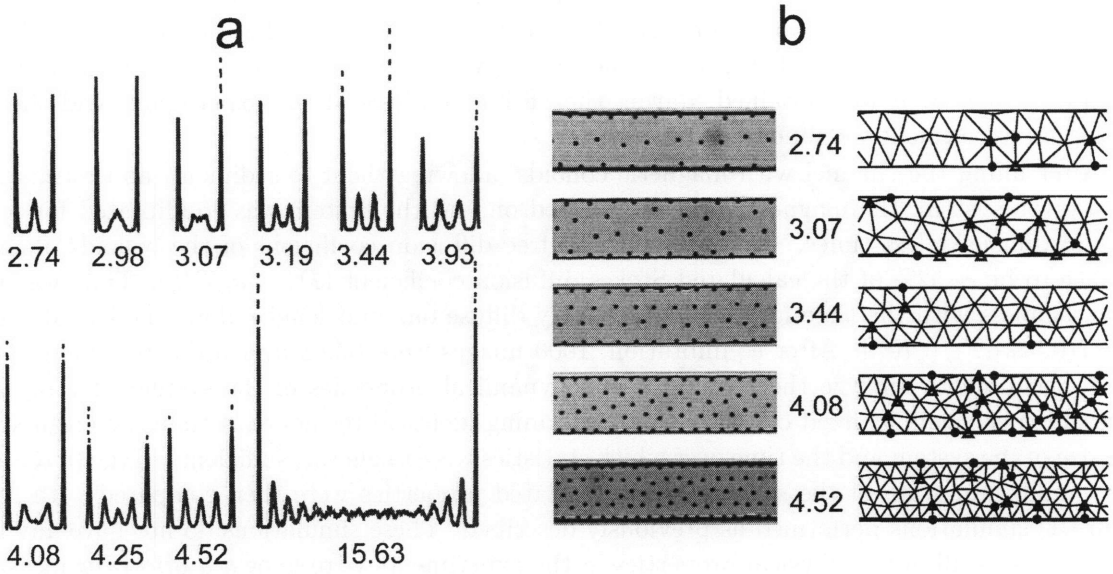

Fig. 3.18: *(a) Density profiles across the channels for ten different dimensionless channel widths* 2.74, 2.98 3.07, 3.19, 3.44, 3.93, 4.08, 4.25, 4.52, *and* 15.63. *The gray solid curve corresponds to the predictions from BD simulations and the dotted black curves correspond to the density profile measured experimentally. (b) Snapshots of the experimental system and Delaunay triangulations for five different dimensionless channel widths* 2.74, 3.07, 3.44, 4.08, *and* 4.52. *All of the channels shown have a true width of* $40\mu m$. *Open triangles are seven-coordinated colloids (five-coordinated if next to the wall) and closed circles are five-coordinated colloids (three-coordinated if next to the wall).*

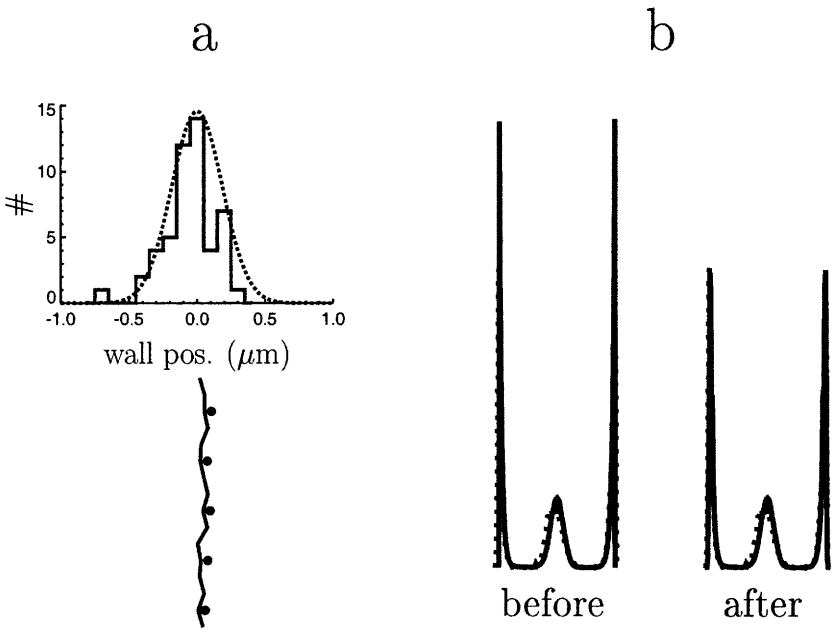

Fig. 3.19: *(a) Top: The distribution of wall positions for a dimensionless channel width of* 2.74 *is shown as the gray histogram and the gaussian curve with the same mean and standard deviation as the histogram is shown as a dotted black line. Bottom: Schematic of one channel wall illustrating the roughness and how the wall colloids can be used to probe that roughness. (b) Comparison of experimental (dotted black) and simulation (solid gray) density profiles for a dimensionless channel width of* 2.74 *before and after the simulation data have been corrected for wall roughness.*

measured to have standard deviation of $\sim 0.3\mu$m. In post-processing the simulation results, a random gaussian variable was added to the x-position of the wall colloids with the same standard deviation as measured from the experiment. Even with the presence of rough walls however, both the experiments and the simulations exhibit very large peaks at the walls indicating the high degree of localization that occurs at the hard-wall.

Another important property to note is the periodic broadening and sharpening of the peaks in the center of the channel as the channel width is increased (Figure 3.18a). This behavior implies that there are structural changes occurring in the center of the channel as a function of the dimensionless channel width. In order to study in more detail these structural changes, we used the experimental images to perform a Delaunay triangulation on the positions of the colloids to determine the nearest neighbors and the locations of the defect sites in the channel as shown in Figure 3.18b. A colloid was considered a defect if it had more or less than six neighbors. Again, in the case of flat walls, we have to treat the colloids at the walls differently than those in the bulk and therefore, we define the wall colloids as any colloid located within a distance of $R/2$ from the wall. Recall, wall colloids are considered to be defects if they have more or less than four neighbors. The results in Figure 3.18b

show clearly that the structure in the narrow channels is oscillating between order and disorder (low and high defect concentrations) as the channel width is increased.

A similar set of structural transitions has been noted previously for hard sphere systems confined in thin slits (3D systems) [87, 88]. However, in the case of hard spheres in thin slits, the structural transitions are the result of geometric constraints upon the packing of the spheres resulting in transitions from one type of solid crystal structure to another. The 3D system can transition from a triangular to square lattice and back as the thin gap height is increased [87]. In the case of repulsive dipoles confined in 2D channels, the system remains in a triangular lattice at all channel widths but the lattice lines alternate between straight (parallel to the walls) and buckled as the channel width is increased. Additionally, in the 2D channel system, the structural transitions are intimately tied to changing dynamics in the system.

For the largest channel shown in Figure 3.18a the layering near the walls is seen to give way to an isotropic (liquid) structure in the center of the channel for this dimensionless field strength. This feature strongly resembles the structure of a hard sphere fluid near a flat hard wall. In the case of hard spheres, the wall can act as a nucleation site for a perfect, layered, crystal to form out of the fluid phase [64]. However, in the case of repulsive dipoles in 2D next to a hard wall this is not exactly what happens. The long-ranged nature of the colloidal interaction combined with the presence of a hard wall leads to a higher concentration of colloids along the wall than in the bulk for large channels [33]. This concentration difference causes the appearance of dislocations along the wall, as seen in Figure 3.20c, resulting in a seemingly contradictory response of this system to the presence of a flat hard wall. In Figures 3.18a and 3.20b the dimensionless channel width 15.63 clearly exhibits a more crystalized (layered) state near the walls but we show that although the wall assists in the natural formation of a crystal it also induces regularly spaced defects in that crystal. Furthermore, as seen in Figure 3.20c, the first layer in the bulk corrects the structure and the dislocations along the wall no longer strongly affect the structure of the rest of the system. This experimental result is consistent with the simulation results discussed earlier in this chapter.

The appearance of dislocations along the wall is an interesting phenomenon seen in different forms in other systems. The large channel limit in hard-wall channels is essentially equivalent to a hard circular confinement with infinite radius. Kong et. al. [53] showed that large 2D clusters confined in hard-wall circles exhibit a high number of defects along the confining boundary. More recently de Villeneuve et. al. [63] studied a 2D slice of a 3D hard-sphere colloidal system near a spherical impurity, using confocal microscopy. The spherical impurity created a convex boundary in the 2D slice. In this case they observed grain boundaries emanating radially outward from the circular boundary similar to the regularly spaced dislocations observed in our 2D hard-wall channel system. However there are significant differences between these three examples. In the large 2D clusters as well as the convex boundary case, the defects along the confining boundary are attributed to the bending of the lattice while in our system the lattice does not need to bend at the boundary. Additionally, in the case of the convex boundary, the defects continue to radiate out into the bulk as grain boundaries while in our system they are terminated after the first layer in the bulk.

3.3.3 Structure and Dynamics

Having located the defect sites in our system we were also able to calculate the average concentration of defects for a given set of conditions. The results for the total and wall concentration of defects are

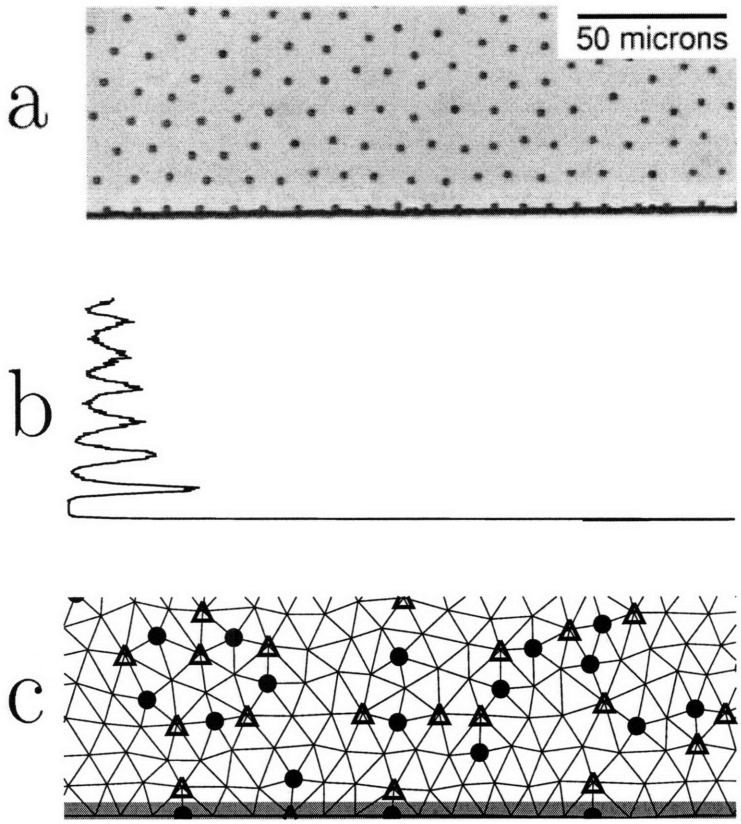

Fig. 3.20: *(a) Experimental image for a section of a channel with* $\widetilde{w} = 15.63$ *showing the structure near the wall. (b) Density profile in the section of the channel shown in (a). (c) Delaunay triangulation for the section of the channel shown in (a). The shaded region at the bottom represents the "wall-region" (a distance less than* $R/2$ *from the wall). Open triangles are seven-coordinated colloids (five-coordinated if in the wall region) and closed circles are five-coordinated colloids (three-coordinated if in the wall region).*

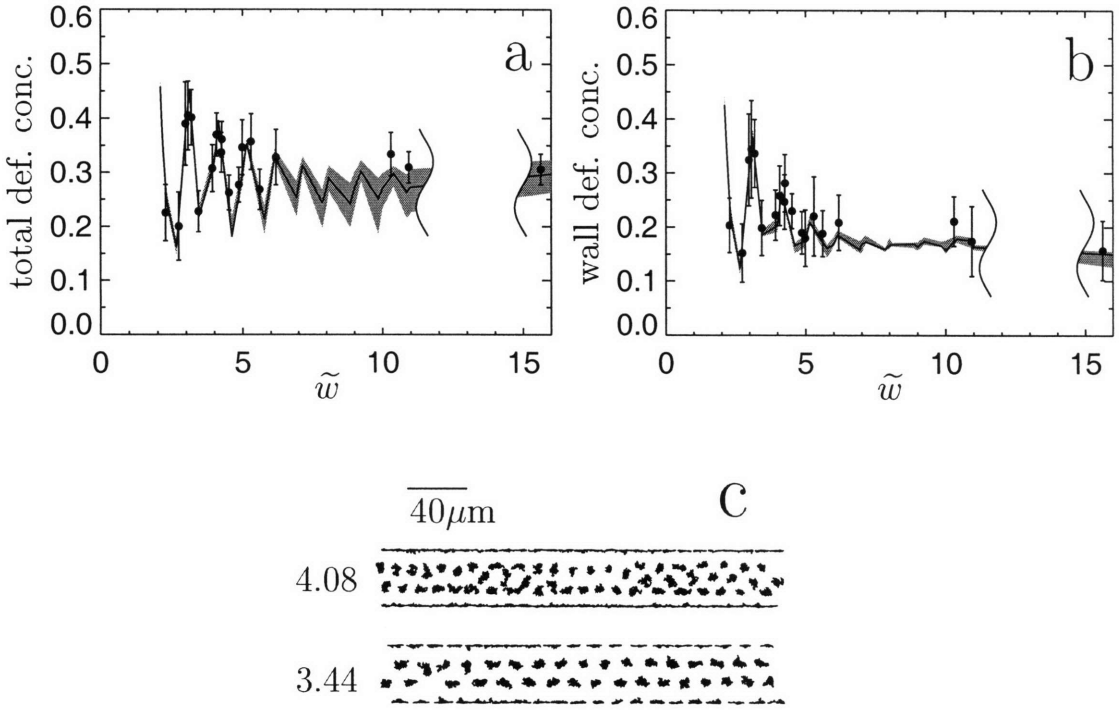

Fig. 3.21: *Defect concentration as a function of dimensionless channel width at a dimensionless field strength of* 12 ± 1 *for (a) the channel as a whole and (b) the wall region. The solid line represents the simulation results for* $\Gamma = 12$ *with the shaded region representing the range of defect concentrations for* $\Gamma = 12 \pm 1$. *The closed circles represent the experimental data. (c) Colloid trajectories in two different channel widths (*4.08 *and* 3.44*) at* $\Gamma = 12 \pm 1$ *for a dimensionless time of* 0.65.

shown in Figures 3.21a and b respectively. We observed very pronounced oscillating behavior in the total defect concentration (Fig. 3.21a) in our experimental system. We note that for very narrow channels, the total defect concentration follows closely with that of the wall defect concentration since most of the colloids in the system are wall colloids. However, above a dimensionless channel width of ~ 5 the wall behavior begins to deviate from that of the total defect concentration. As predicted [33], in the large channel limit, the wall defect concentration goes to a constant value not equal to zero due to the presence of stable dislocations along the wall.

The defect concentration is intimately tied to the dynamics of the system and therefore the dynamical behavior of the system also oscillates as a function of dimensionless channel width. In Fig. 3.21c the two traces shown are for a peak (4.08) and valley (3.44) in the defect concentration curve shown in Fig. 3.21a. The channel with the higher defect concentration (4.08) exhibits more liquid-like dynamics, with some of the colloids more easily able to diffuse away from their original positions in a short time. For the lower defect concentration (3.44) the colloidal crystal appears to be more solid-like with the colloids remaining on their original lattice sites.

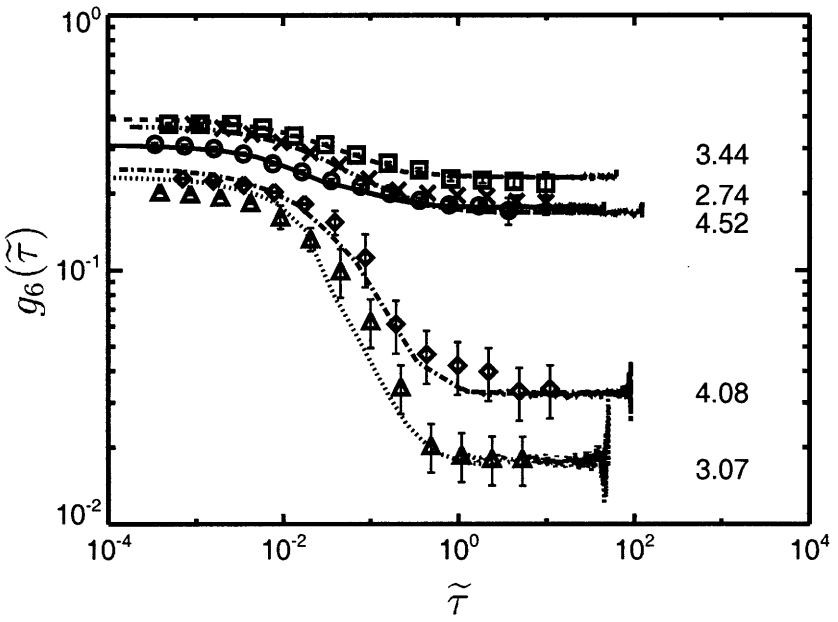

Fig. 3.22: *Bulk bond-order correlation function as a function of time for five different dimensionless channel widths* 2.74 *(solid line and circle symbols),* 3.07 *(dotted line and triangle symbols),* 3.44 *(dashed line and square symbols),* 4.08 *(dash-dot line and diamond symbols), and* 4.52 *(dash-triple-dot line and* $\times$ *symbols). The lines represent results from BD simulations and the symbols are experimental results.*

A more quantitative measure of the dynamics in the system is the bond-order correlation function in time ($g_6(\widetilde{\tau})$). In the 2D channel system, the behavior of $g_6(\widetilde{\tau})$ for the colloids in the bulk (a distance greater than $R/2$ from the wall) can be used as a measure of the state of the system [34]. In Figure 3.22 we show $g_6(\widetilde{\tau})$ data for the five dimensionless channel widths shown in Figure 3.18b from both simulations and experiments. As the dimensionless channel width is increased from 2.74 to 4.52 the $g_6(\widetilde{\tau})$ behavior of the system oscillates between a solid like constant for $\widetilde{w} = 2.74$, 3.44, and 4.52 and a liquid like decay for $\widetilde{w} = 3.07$ and 4.08. All of the curves in Figure 3.22 show the characteristic intermediate-time plateau in $g_6(\widetilde{\tau})$ that is expected for thin channels but they illustrate the re-entrant behavior of the system, transitioning from liquid-like to solid-like and back as the channel width is increased [34]. Previous authors have theoretically predicted similar re-entrant behavior for another 2D system (in parabolic confinement) [60] but this is the first experimental observation of re-entrant behavior as a function of confining geometry for 2D repulsive colloidal systems.

Contrary to these results are the observations for colloids confined in 2D circles [48, 49] where re-entrant behavior is reported as a function of the dimensionless field strength. In Figure 3.23 we show that there is no such re-entrant behavior as a function of dimensionless field strength in this system. However, we do note that the behavior of the system as a function of dimensionless field strength is strongly dependent upon the dimensionless width of the channel. For $\widetilde{w} = 3.07$,

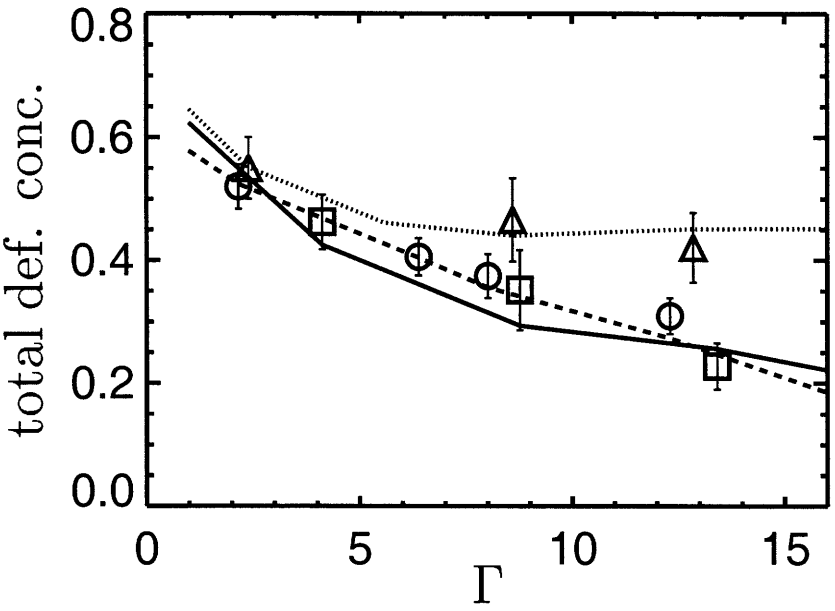

Fig. 3.23: *The total defect concentration as a function of* Γ *for three different dimensionless channel widths* 3.07 *(triangles),* 3.41 *(squares), and* 10.93 *(circles). The lines represent simulation results for* $\widetilde{w} = 3.07$ *(dotted line),* 3.41 *(solid line), and* 10.93 *(dashed line).*

increasing Γ does not greatly affect the concentration of defects in the system while for $\widetilde{w} = 3.41$ the concentration of defects decreases significantly as Γ is increased. For wider channels such as $\widetilde{w} = 10.93$, increasing Γ causes a decrease in the total defect concentration because, as mentioned previously, the large channels have a bulk region that behaves more like the unbounded system (without walls).

3.4 Summary

An analysis has been presented of the structure and dynamics in a system of repulsive dipoles confined in 2D channels. The application of parallel planar walls to the system of 2D dipoles results in unique and sometimes surprising properties. This system has not been explored in the literature and it is important in further understanding the effects of confinement on colloidal systems.

The alignment of the crystal in the direction of the walls is expected for any confined colloidal system, however the large magnitude of the wall-peaks in the density profile is a unique property of the long-ranged nature of the particle interactions. The spreading of the peaks in the center of the channel, for channel widths not commensurate with the natural crystal, indicates a loss of structure in that region. The defect concentration and local bond-orientational order in the channel confirm that the local structure is disrupted in these channels. The oscillations in all of the structural properties indicate that the crystal in the 2D channel system can be altered by slight changes in the channel width. This is a very important observation for any application that is

highly dependent on the type of structure in the channel. Additionally, the slow approach ($\widetilde{w}^{-1}$) of the system properties to their unbounded values indicate that channel-like confinement, even fairly large channels, drastically changes the structural properties of the 2D dipolar crystal. The same properties of MR colloids confined in 2D channels were observed in both simulations and experiments indicating that the BD simulations are capable of reproducing realistic results for this system.

The structural analysis of the dipole system in 2D channels shows many similarities to other studies of confined 2D systems. Wall-induced layering is observed in this system analogous to the layering observed in the dusty-plasma study [57] and the shell structure in circular confinements [49, 89, 51, 90, 52]. However, in the case of repulsive magnetic dipoles there is a higher density and localization at the walls in the 2D channel system than in the dusty plasma system. Extreme localization of the wall-particles has been observed in hard circular confinement studies with long ranged repulsive interactions [89]. However, the increased localization as a function of the channel width is an important observation in this study in that it shows how the addition of walls continues to influence the behavior of the system, even for large channel widths. In the experimental systems, where the channel walls appeared rough on the length-scale of a colloid diameter, the extreme localization of colloids at the walls was also observed and affected the structure and dynamics of the rest of the system.

Similar to the dusty plasma study, order-disorder transitions were observed in the channel by observing the alternate sharpening and broadening of the density peaks as the channel width was increased. However, in the case of the dipole interactions, the wall-peak actually increases in magnitude as the channel width is increased due to the long-ranged nature of the inter-particle interactions and the presence of the hard wall. Also, the sharpening and broadening of the peaks only occurs near the center of the channel in the case of dipolar interactions indicating that the structure of the crystal in the center of the channel changes significantly with only slight changes in the channel width. The oscillations in the structural properties as a function of the channel width occur with a regular period $\sim R$ indicating that there are certain regular intervals of channel widths (magic numbers) that are commensurate with the natural structure of dipolar particles in 2D channels. These magic numbers do not occur at integer multiples of R, as expected, but are influenced by such system properties as the high density at the walls. This observation is important in that it indicates that there is an appropriate, yet complex, methodology for predicting the structures that will form in the channel system.

We have compared the dynamical properties of these systems to the case of an unbounded 2D system. We have performed careful simulations of the unbounded system in an attempt to determine over which range of dimensionless field strengths the solid-liquid phase transition occurs. We were able to determine that the phase transition occurs in a narrow range of dimensionless field strengths (between 14.89 and 15.2) but we were unable to converge our simulations of the unbounded system between these two dimensionless field strengths. Experimentally, a hexatic phase has been observed in this system [39, 40, 41] indicating that it may be possible to observe this type of phase in a simulation with an extremely large number of colloids.

We perturbed this 2D unbounded system by introducing parallel hard walls to create a channel-like geometry. In the channel systems we observed dynamics that differed significantly from the unbounded system in both our simulations and experiments. We observed the existence of a plateau in the bond-order correlation function due to the stabilizing presence of a hard wall. We also observed that the channel systems exhibited strikingly different local structure and dynamics in

the regions near the wall and farther away from the walls causing both the onset and the subsequent decay of the plateau in the bond-order correlation function in large channels at lower dimensionless field strengths. The heterogeneity of the channel systems was shown by calculating the bond-order correlation function in different sections of the channel. We observed a decay in the correlation function as we moved away from the walls in our channel systems. This observation is consistent with studies performed on spherical block copolymers confined in very wide 2D channels [59]. However, combining this observation with our analysis of the local dynamics of the colloids leads to an explanation of the anomalous form of the $g_6(\widetilde{\tau})$ curves seen in this 2D channel system.

The dynamics in 2D colloidal systems are strongly linked to the defect properties of those systems and we showed this to be true for the 2D channel systems as well. We have presented a state-diagram for dipoles confined in a 2D channel system as a function of dimensionless field strength and dimensionless channel width that summarizes the behavior of these systems. The qualitative aspects of the state-diagram are applicable to any order parameter of the 2D channel system as they are all linked to the structure and dynamics. The exact nature of the simulation state-diagram was further validated by direct comparison to our experimental results for the 2D channel system. Additionally, by simulating systems with sharper repulsive potentials we have shown that the general form of the state-diagram presented here (with re-entrant behavior) can be considered universal for colloids in 2D hard-wall channels interacting with repulsive potentials.

We have observed re-entrant behavior in the properties of the dipolar system as a function of the geometry of the system, not the dimensionless field strength. This finding is similar to the re-entrant behavior observed in other simulation studies of colloids confined in 2D channels [60] demonstrating that, qualitatively, this behavior can be seen for a variety of colloidal interactions as well as confining potentials. Despite the qualitative similarities however, there are important differences between the hard wall confinement presented here and the parabolic confinement studied previously. These differences have been discussed extensively in the case of 2D circular geometries [89, 48, 50, 53]. An example of an important difference between these two types of confinement is that the average density of colloids remains constant when the external field strength is decreased in hard wall systems while in systems with parabolic confinement the average density of colloids increases with decreased external field strength. As a result of these distinctions, hard wall systems and parabolic systems can behave quite differently, even in the case of channels. An example of this difference in behavior is the unusual structural transition from four rows to three rows and then back to four rows as the interaction strength between colloids was increased in parabolic channel-like confinement [60]. No such structural transition is observed in the case of hard wall confinement. However, as mentioned previously, both systems do exhibit re-entrant behavior.

We did not observe any re-entrant behavior as a function of dimensionless field strength in either our simulation or experimental results but the re-entrant behavior as a function of the dimensionless channel width implies that the structural properties and therefore the dynamics of these self-assembled colloidal systems in microfluidic geometries are very sensitive to the confinement geometry itself. This will have impact upon many applications where both the structure and mobility of the self-assembled colloids are important considerations in the application design. Additionally, it illustrates the many effects that confinement can have upon the self-assembly process of colloidal systems.

3.5 Outlook

The specifics of the self-assembly next to the hard-wall have been discussed in this work and we have shown that although the wall does induce an ordered layered structure in this system, it also causes defects to form along the wall disrupting the natural lattice. This is an example where confining boundaries are used to both promote stability and disrupt natural structure in a single colloidal system.

Looking forward into the future, the next step that this research can take is to investigate more closely the properties of the dislocations that arise along the walls in the 2D hard-wall channels for repulsive dipoles. We have determined that one of the causes of the interesting structural and dynamical behavior in 2D channel systems is the different crystal structure that exists next to the walls in these systems. This study will be important to elucidate the physics behind this observation. The energetics of the 2D colloidal crystal in hard-wall channels are an important property that will help to explain why the dislocations arise for dipoles but not for r^{-6} potentials. Additionally, the nature of the dynamics of the dislocation glide along the walls will be an important property for understanding in more detail how the dynamics of the 2D crystal are affected by the introduction of parallel hard walls with a dimensionless width of $\widetilde{w}$. From a practical standpoint, once we fully understand the origin and effects of the dislocations along the walls, we can design microfluidic devices to either utilize the presence of the dislocations or to suppress their formation.

CHAPTER 4

Thin Slit Systems

The confined self-assembly of induced dipoles such as the kind found in magnetorheological (MR) fluids has been of great interest for many years from both a fundamental science standpoint and from a practical application standpoint [91, 10, 3, 92]. The confinement of MR fluids can cause drastic changes in the nature of the structures that form under the application of an external magnetic field [10, 93]. Recently, the self-assembled structures formed by MR fluids under the application of an external magnetic field have been used as structural components in microfluidic devices to perform size-dependent separation of DNA molecules [3, 92]. In these devices, a low volume fraction MR fluid is self-assembled in a slit-like microchannel by the application of a uniform external magnetic field directed normal to the thin-slit. The self-assembled structure formed by the MR fluid in this geometry resembles an array of column-like clusters spanning the height of the channel. The spacing between these columns (or the pore-size in the channel) is an important parameter for characterizing the efficacy of the DNA separation.

4.1 Background

Columns can form in thin-slit channels when the volume fraction of MR colloids is less than about 0.1 and the external magnetic field strength is strong enough to overcome the Brownian motion of the colloids [94, 91, 10, 8]. There has been much research done to measure and model how the spacing between the column structures in thin-slits depends upon the thickness of the slit. The

experimental investigations have been performed in thin-slits with thicknesses ranging from ~ 10 to 1000's of colloid diameters [94, 91, 10, 93, 8]. The theoretical investigations into this system have generally been performed at infinite external field strength (or zero temperature) [94, 95, 96]. All of the experiments and theoretical studies performed on this system have concluded that there is a power-law dependence on the spacing between columns as a function of the thickness of the thin-slit [94, 91, 10, 93, 95, 96]. However, there has been much disagreement about the exact value of the power-law. A survey of the literature can convince one that it is generally agreed that the power-law in thin-slits with a thickness of ~ 10 to 100's of colloid diameters is ~ 0.4 and as the slit-thickness is increased to several 1000's of colloid diameters the power-law transitions to ~ 0.6 [94, 91, 10, 95]. All of the above results are generally applicable as long as the external magnetic field is large enough to overcome Brownian motion. However, as the magnitude of the external magnetic field approaches infinity, there is theoretical evidence that there should be in fact only a single power law dictating the spacing between columns as a function of the slit-thickness [96].

It is well known that as the external magnetic field is slowly increased from zero to a large value, bulk field responsive fluids such as MR fluids undergo several structural transitions [97, 98, 8, 99]. The first transition is from a gas of Brownian colloids to randomly distributed chains of colloids aligned in the field direction. This aggregation into chains is known as head-to-tail aggregation. As the field is further increased, the chains of colloids begin to aggregate laterally in order to form clusters of zipped chains. This secondary aggregation is known as zippering. Likewise, in confined MR fluid self-assembly the same transitions can occur as the external field magnitude is increased. These transitions are illustrated in Fig. 4.1 where we show a schematic of the evolution of the MR fluid structure from a randomly dispersed state (left) to the lowest energy state (right) in two different slit-thicknesses. In the top of Fig. 4.1 the lowest energy structure on the right consists of chains spanning the height of the thin-slit and therefore only head-to-tail aggregation is necessary to form these structures. In the bottom of Fig. 4.1 the system must undergo both the head-to-tail aggregation and the zippering transitions. However, because of the confinement in a thin-slit, the energy barriers associated with the zippering of chains of MR colloids can be large, thus preventing the system from reaching the lowest energy state. We will show that one needs to take into account not only the lowest energy state of the thin-slit system but also the energy barriers associated with achieving that state in order to fully understand the self-assembly of MR fluids confined in thin-slits.

The characteristic length-scales in microfluidic devices are ever-shrinking and therefore it is likely that the thickness of the channels used for DNA separations will continue to shrink down to the fundamental limit of a single MR colloid diameter. In the extreme case where the thickness of the channel is equivalent to a single colloid diameter, the MR colloids will self-assemble in truly two-dimensional (2D) channels. As of yet, the self-assembly of dilute MR fluids in such extreme confinement has not been studied. Some work has been done to study the self-assembly of concentrated MR fluids (> 0.2 volume fraction) under this extreme confinement but the structures that form at such high concentrations are not column-like [11]. Some of the infinite field theoretical models mentioned previously can be extended down into the range where the slit-thickness is less than 10 colloid diameters but, as we will show, these models do not tell the whole story of the self-assembly in thin-slits.

In this work we use Brownian dynamics simulations to study the self-assembly of dilute MR fluids under confinement in thin-slits. We are interested in studying the phase space that is practical for the microfluidic DNA separation devices mentioned previously, namely volume fractions < 0.1

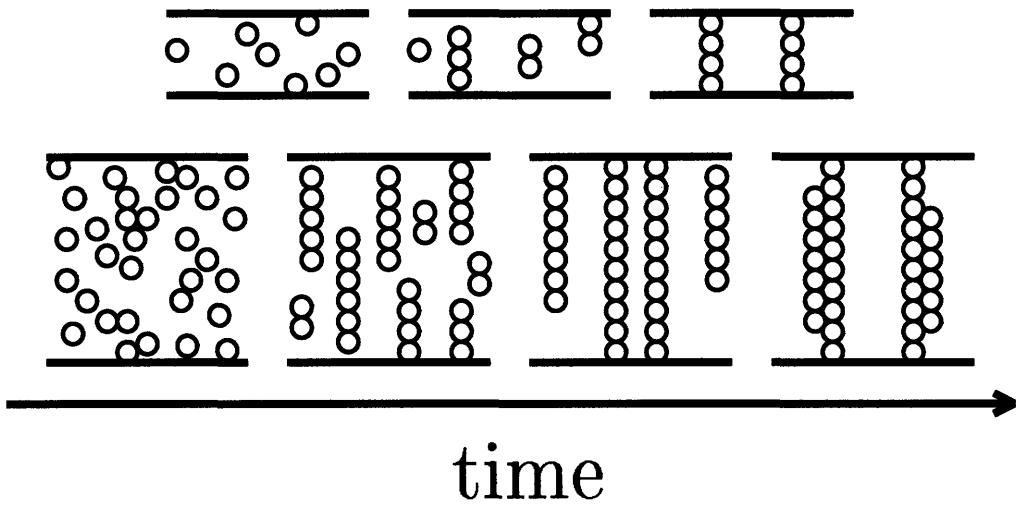

Fig. 4.1: *Top: Schematic of the self-assembly of an MR fluid confined in a thin-slit with a thickness equal to* 4 *colloid diameters. At time zero the MR fluid is a gas-like Brownian suspension and as the external field is slowly ramped the colloids aggregate head-to-tail in order to form chains spanning the height of the thin-slit. Bottom: Schematic of the self-assembly of an MR fluid confined in a thin-slit with a thickness equal to* 10 *colloid diameters. At time zero the MR fluid is a gas of Brownian colloids and as the external field is slowly ramped the colloids first aggregate head-to-tail in order to form chains and then undergo a secondary zippering transition in order to reach the lowest energy state. There can be significant energy barriers to the zippering transition.*

and external fields that are sufficiently large to cause structure formation but small enough that they can be experimentally realized. We observed that there is a cross-over from truly 2D behavior to the 3D behavior observed in the experimental systems mentioned above. We explain the mechanism of the cross-over in these systems and discuss the details of the structure in the systems when the slit-thickness is < 5 colloid diameters. We propose a model for predicting the properties (structure and dynamics) of the self-assembled MR fluids in the case of extreme confinement.

4.2 Simulation Details

We used the Brownian dynamics (BD) simulation technique to model the self-assembly of the MR fluid in thin-slits [24, 33, 34]. The dimensionless equation of motion for this system was derived in Chapter 2 (Equation 2.10). The equation of motion was integrated forward in time using a simple Euler integration scheme. At the end of a time-step, hard sphere overlaps were treated with the Displacement Algorithm (Chapter 2). This procedure was performed for all overlaps, between two colloids and between colloids and hard walls [33, 34], and was iterated until all overlaps in the system were removed.

The boundary conditions of the simulations in this work were periodic in the x- and y-directions and hard-walls in the z-direction. The uniform external magnetic field was directed in the z-direction (normal to the thin-slit) causing the MR colloids to self-assemble into column structures spanning the height of the thin-slit. Simulations were performed for the self-assembly of five different volume fractions of MR fluid (ϕ =0.01, 0.03, 0.04, 0.05, and 0.07) in thin-slits ranging in thickness from $1d$ to $30d$ (or dimensionless thickness of $\widetilde{L} = 1$ to 30). The simulations were done in boxes with dimensionless lengths of 60, 35, 35, 30, and 30 in the x- and y-directions for the volume fractions 0.01, 0.03, 0.04, 0.05, and 0.07 respectively. Therefore, the number of colloids in the simulations (N) ranged from 69 to 3,610 depending upon $\widetilde{L}$ and ϕ.

A dimensionless time-step of $\Delta\widetilde{t} = 10^{-4}$ was used with time made dimensionless as $\widetilde{t} = t\left(k_{\mathrm{B}}T\right) / \left(\zeta d^2\right)$ where $\left(\zeta d^2\right) / \left(k_{\mathrm{B}}T\right)$ is the time necessary for an MR colloid to freely diffuse a distance equal to its diameter. A dimensionless cutoff for the dipole-dipole interaction of 20 was used along with a linked-list binning algorithm [25] where the bin sizes were slightly larger than the cutoff value. Therefore, only interactions between colloids separated by a distance less than the cutoff were considered. The simulations were started from a random configuration and the external magnetic field strength was ramped continuously from $\lambda = 0$ to $\lambda = 50$ over a dimensionless time of 100 after which it was held constant at $\lambda = 50$. Ramping the external magnetic field over a longer time did not change the final properties measured in the simulations. We tracked the spacing between the columns (or clusters) formed by the MR colloids until it remained constant for a dimensionless time of at least 100 before we began to collect statistics. All of the simulations were determined to be converged in system-size, time-step, cutoff for the dipole-dipole interaction, and ramp-time for the external magnetic field. For each set of conditions $(\phi, \widetilde{L})$, six separate trajectories were simulated (all from different starting configurations) in order to obtain a reasonable average for the physical properties of the structure and dynamics in these systems. An example of an equilibration curve for $\widetilde{L} = 5$ and $\phi = 0.01$ is shown in Fig. 4.2. Schematics of the initial and final states of the system are shown as insets in Fig. 4.2.

The average spacing between clusters was calculated in the following manner as illustrated in Fig. 4.3. Starting with a snapshot of the system configuration (Fig. 4.3 left), the $(\widetilde{x}, \widetilde{y})$ position of the center of mass was calculated for each continuously connected cluster of MR colloids resulting

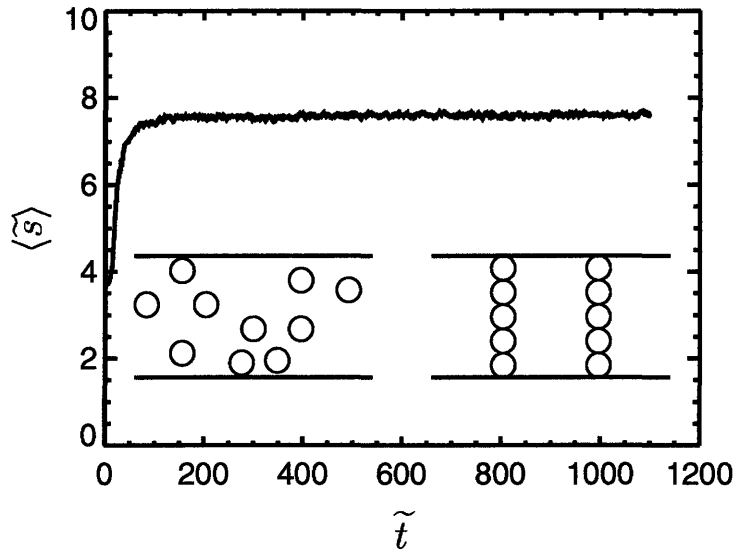

Fig. 4.2: *The average dimensionless spacing between clusters* ($\langle\widetilde{s}\rangle$) *versus dimensionless time for a typical simulation* ($\widetilde{L} = 5$) *where the dimensionless external magnetic field is ramped from* $\lambda = 0$ *to* $\lambda = 50$ *over a dimensionless time of* 100 *and then held constant at* 50 *until the system reaches steady-state. The inset on the left shows a typical random starting configuration and the inset on the right is an example of the final, steady-state structure.*

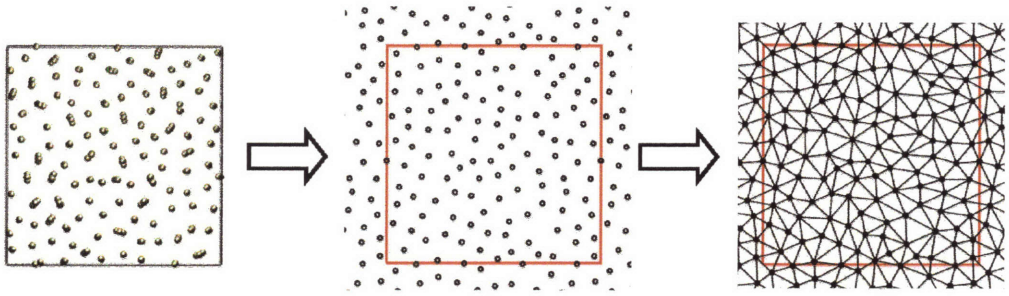

Fig. 4.3: *Left: Top view of the simulation box. Middle: 2D projection of the centers of mass of all the clusters in the simulation box. The red line represents the periodic boundaries of the simulation box. Right: Delaunay triangulation of the 2D projection showing the nearest neighbors of all of the clusters in the simulation box from which the average spacing can be calculated.*

in a 2D projection of the thin-slit system in the x-y plane (Fig. 4.3 middle). MR colloids were considered to be connected if they were in hard-sphere contact. A Delaunay triangulation was performed on the 2D projection in order to determine the nearest neighbors of each cluster (Fig. 4.3 right). The average distance between clusters was then calculated as the average distance between nearest neighbor clusters.

4.3 Transition from 2D to 3D

As mentioned above, the previous work on the self-assembly of MR fluids in thin-slits under the application of a uniform external magnetic field normal to the thin-slit has all been done in slits with dimensionless thicknesses ranging from $\widetilde{L} \sim 10$ to 1000's. We are interested in probing the properties of self-assembled MR fluids under much tighter confinement ($\widetilde{L} = 1$ to 30) as there are many interesting properties of these systems that have not been observed in the previous work. In Fig. 4.4 we present our simulation results (circle symbols) for the average dimensionless spacing between clusters as a function of the dimensionless slit-thickness for $\phi = 0.04$. We compare our simulation results to the experimental results of Liu *et al.* [10] (triangle symbols) for the same system. The dashed (horizontal) line in Fig. 4.4 represents the spacing between colloids at this volume fraction for a purely 2D system. This spacing is defined as [33]

$$\langle \widetilde{s} \rangle_{2D} \equiv \sqrt{\frac{\pi}{2\phi_A\sqrt{3}}} = \sqrt{\frac{\pi}{3\phi\sqrt{3}}} \tag{4.1}$$

where ϕ_A is the area fraction of colloids which, for a monolayer of colloids, is related to ϕ as $\phi_A = 1.5\phi$. The dotted (power-law) line in Fig. 4.4 is the empirical power-law that Liu *et al.* found to best fit their data in the range $\widetilde{L} \lesssim 200$ and is given by

$$\langle \widetilde{s} \rangle = 2.058\widetilde{L}^{0.37} \tag{4.2}$$

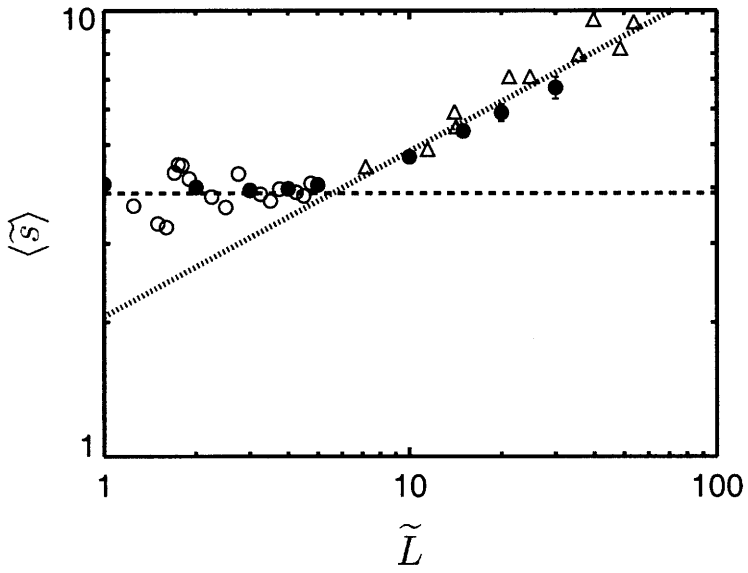

Fig. 4.4: *Dimensionless spacing between clusters as a function of dimensionless slit-thickness for* $\phi = 0.04$. *The simulation data are shown as circles (closed circles are integer values of* $\widetilde{L}$*). The simulations were performed at* $\lambda = 50$. *The experimental data of Liu* et al. *[10] (performed at* $\lambda = 166$*) are shown as open triangles. The dashed line is the spacing for a 2D system at the same* ϕ *given by Equation 4.1 and the dotted line is the empirical power-law given by Equation 4.2 that Liu* et al. *fit to their experimental data.*

The spacing in our simulations follows very closely the spacings from the experimental work of Liu *et al.* [10] for dimensionless slit-thicknesses > 10. However, there are two interesting features of the data shown in Fig. 4.4; the deviation from the empirical power law for slit-thickness < 10 and the large oscillations in the spacing between clusters as a function of the slit-thickness for extremely thin slits ($\widetilde{L} \leq 5$). The deviation from the power law is expected intuitively but the details have not been previously explored. The large oscillations that occur in the dimensionless spacing for extremely thin slits will be discussed shortly.

In discussing the deviation from the power-law behavior, we are in essence discussing the transition from 3D to 2D behavior in these systems. For this discussion it will be useful to relate the cluster spacing to the average cluster size in the system. Using simple geometric arguments we can relate the average cluster size in the thin-slit system to the average cluster spacing as shown in Fig. 4.5. We define the average cluster size as $\langle c \rangle = N/N_c$ where N_c is the number of clusters in the system. If we assume that the clusters all have a dimensionless circular cross sectional area $\widetilde{A}_c$ and are arranged in a triangular lattice with dimensionless spacing $\widetilde{s}$ as shown in the inset of Fig. 4.5 then the area fraction of clusters is equal to the area fraction in a triangular lattice

$$\phi_A \equiv \frac{N_c \widetilde{A}_c}{\widetilde{A}} = \frac{\frac{1}{2}\widetilde{A}_c}{\frac{\sqrt{3}}{4}\widetilde{s}^2} \tag{4.3}$$

where $\widetilde{A}$ is the dimensionless area of the x-y plane. Using the definition of the volume fraction

$$\phi \equiv \frac{N\pi}{6\widetilde{A}\widetilde{L}} \tag{4.4}$$

we can first substitute the definition for the average cluster size ($\langle c \rangle = N/N_c$) into Equation 4.4 for N and then we can further substitute for the ratio $N_c/\widetilde{A}$ from Equation 4.3. Making these two substitutions into Equation 4.4 and re-arranging we arrive at the relationship between the average spacing between clusters as a function of the average cluster size

$$\langle \widetilde{s} \rangle = \sqrt{\frac{\pi}{3\phi\sqrt{3}} \frac{\langle c \rangle}{\widetilde{L}}} \tag{4.5}$$

which is plotted as the dashed line in Fig. 4.5.

When $\widetilde{L} = \langle c \rangle$ Equation 4.5 reduces to Equation 4.1, the value for the dimensionless spacing in the 2D system. This means that if the clusters are simply chains with a single colloid width spanning the height of the thin-slit, the average spacing between those chains should be equal to $\langle \widetilde{s} \rangle_{2D}$. We independently measured the average dimensionless spacing between clusters and the average cluster size in our simulations for all ϕ and plotted them in Fig. 4.5. The relationship between average spacing and the cluster size is very well predicted by Equation 4.5. In our BD simulations we have access to the properties of the individual clusters (arrangement and number of colloids within a cluster) which are not easily accessible in experimental systems so we can relate changes in the average spacing between clusters to specific changes in the properties of the clusters themselves. In the experimental work, only general shape properties of the clusters have been used to explain the spacing behavior as a function of slit-thickness [91, 10]. The relationship between cluster properties and average spacing (Equation 4.5) will become important in later discussions of

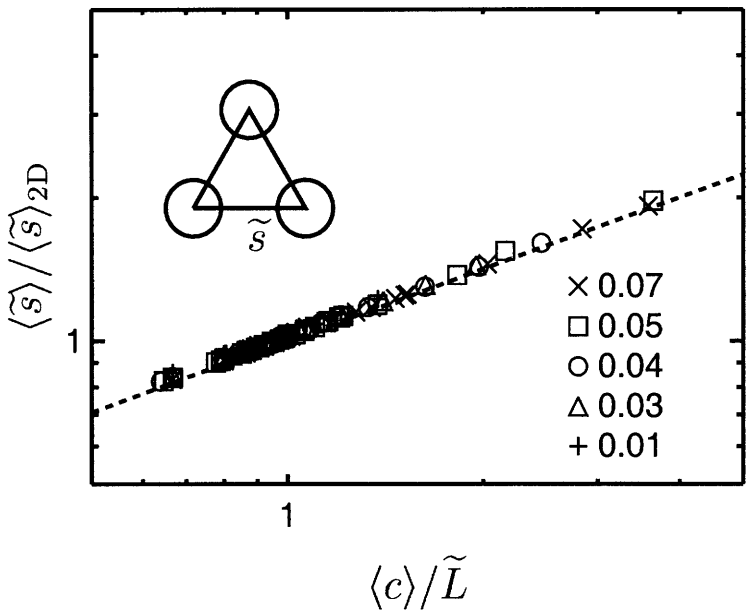

Fig. 4.5: *Average spacing between clusters as a function of the average cluster size in the system. Data for five different volume fractions are presented. The dashed line is the prediction given by Equation 4.5 and the inset is a schematic top-view of a triangular arrangement of clusters with circular cross-sections.*

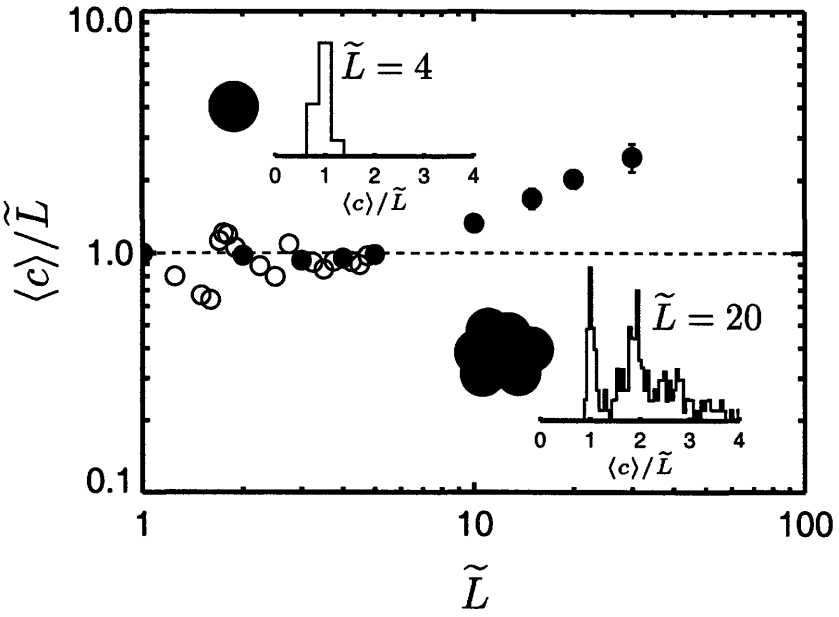

Fig. 4.6: *Average cluster size as a function of dimensionless slit-thickness for* $\phi = 0.04$. *The solid circles represent integer values of the dimensionless slit-thickness* $\widetilde{L}$. *The horizontal dashed line represents the case where the clusters are single colloid width chains spanning the slit-thickness. The top inset is a histogram of the distribution of cluster sizes in a thin-slit with* $\widetilde{L} = 4$ *along with a top-view image of a characteristic cluster under these conditions. The bottom inset is a histogram of the distribution of cluster sizes in a thin-slit with* $\widetilde{L} = 20$ *along with a top-view image of a characteristic cluster containing zipped chains.*

spacing as a function of slit-thickness and volume fraction.

For instance, the cross-over in the behavior of the dimensionless spacing from 2D to 3D as shown in Fig. 4.4 is directly related to the more complex clustering occurring as the slit-thickness is increased. This point is illustrated in Fig. 4.6 where it is evident that the cross-over in the spacing between clusters is directly correlated with the cross-over from clusters which are single chains spanning the height of the thin-slit ($\langle c \rangle / \widetilde{L} = 1$) to clusters containing several "zipped" chains. Recall that zipped chains are chains of MR colloids directed in the external field direction which have aggregated laterally to form larger clusters [99]. For a dimensionless slit-thickness of 4 (Fig. 4.6 top inset) most of the clusters are chains containing 4 colloids spanning the height of the thin-slit ($\langle c \rangle / \widetilde{L} = 1$). For a dimensionless slit-thickness of 20 (Fig. 4.6 bottom inset) there is a bimodal distribution of cluster types. There is a distinct peak at $\langle c \rangle / \widetilde{L} = 1$ implying that a significant fraction of the clusters are single chains spanning the height of the thin-slit while there is another, much broader, peak representing clusters consisting of several zipped chains. Again, in Fig. 4.6 oscillations occur in the average cluster size as a function of the slit-thickness for $\widetilde{L} \leq 5$ which will be discussed shortly.

There have been several models created to describe both the spacing between clusters and

the cluster sizes themselves as a function of the slit-thickness in these systems [94, 10, 96]. The model developed by Grasselli *et al.* [94] assumes the clusters are ellipsoids spanning the height of the thin-slit and containing enough colloids so that there is a distinct surface and bulk for each cluster. This assumption breaks down for thin-slits where $\widetilde{L} \lesssim 30$ since the clusters under such confinement only contain a hand-full of colloids and are quite discrete in nature. Similarly the model developed by Liu *et al.* [10] assumes cylindrical clusters spanning the height of the thin-slit and again containing distinct surface regions and bulk regions. Therefore this model also breaks down for $\widetilde{L} \lesssim 30$ since it relies on a continuum description of the clusters. The model developed by Gross [96] considers discrete colloids arranged in clusters with either body-centered-tetragonal (bct) or face-centered-cubic (fcc) internal structures at infinite field strength.

The Gross model calculates the infinite-field lowest-energy configuration of the colloids in the system for each slit-thickness. Using Equation 4.5, the average cluster-size predicted by the Gross model can be translated into an average spacing between clusters. The prediction for the average spacing as a function of slit-thickness from the Gross model is shown in Fig. 4.7 dotted line along with our simulation results. The Gross model only makes predictions for integer values of $\widetilde{L}$ and therefore we will concentrate for now on those slit-thicknesses (filled circles in Figs. 4.4, 4.6, and 4.7). For $\widetilde{L} \leq 4$ the lowest energy state of the system as predicted by the Gross model consists of clusters with $\langle c \rangle = \widetilde{L}$. Our simulation results match the predictions of the Gross model for the integer values of $\widetilde{L}$ in this range. However, for $\widetilde{L} \geq 5$ there are significant deviations between our simulation results (as well as experimental results [10] shown in Fig. 4.4) and the predictions by the Gross model for the lowest energy state. When we quench our simulations to zero-temperature, we find that the energy in the system is higher than the energy for the configurations predicted by the Gross model. This implies that our simulations (and the experimental results [10]) are indeed in meta-stable states and and do not reach the ground state configurations.

The discrepancy in power-laws was noted by Gross who offered the following postulate for why experimental observations of spacing versus slit-thickness do not match the predictions from his theoretical, infinite-field, model. Gross conjectured that for low volume fractions and high external field strengths the energy barriers for chain aggregation (zippering) may not be able to be overcome over laboratory time scales and therefore many of the experimental results for the thin-slit system were possibly trapped in states that do not correspond to the ground state at infinite external magnetic field [96]. This comment has the potential to explain the behavior that has been observed experimentally [10] and that we have observed in our simulations but it has not been elaborated upon in satisfying detail in the literature. *We will now show that the presence of energy barriers can dictate many of the properties of self-assembled MR fluids in thin-slits where* $\widetilde{L} \leq 30$.

4.3.1 Energy Barriers to Chain Aggregation

Two rigid chains of MR colloids aligned parallel to one another interact with an energy $\widetilde{U}_c(\widetilde{r})$ that has the general form shown in Fig. 4.8a [9]. The energy curve consists of two parts (Fig. 4.8a inset). The attractive energy well on the left can exist if the chains have a net attraction once they have zipped and the approach energy on the right exists for all parallel chains as they approach one another laterally. For large $\widetilde{r}$ all parallel chains have a repulsive interaction and as they approach each other that repulsion increases (the maximum in Fig. 4.8a). If the chains are "uniformly parallel", meaning that they are of the same length and are not shifted vertically with respect to one another, then their interaction is always repulsive and there is no "zipped" energy-well.

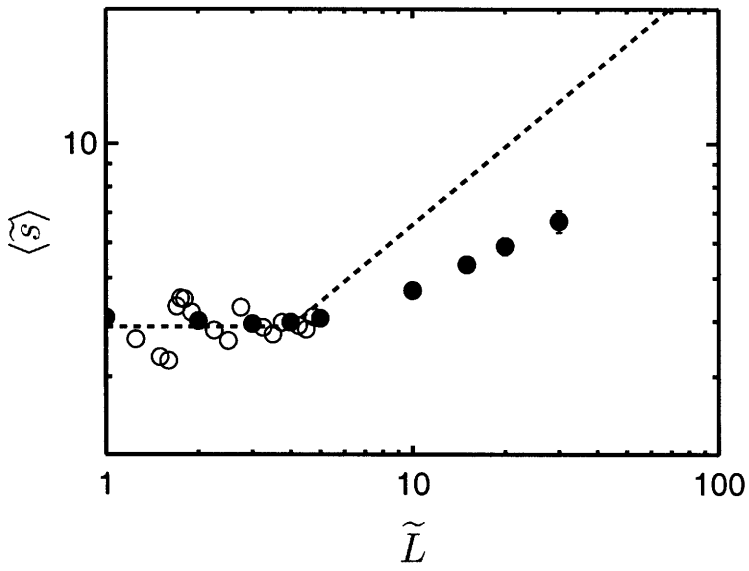

Fig. 4.7: *Average dimensionless spacing as a function of dimensionless slit-thickness. The dashed line is the spacing predicted by the Gross model [96]. The closed symbols represent integer values of* $\widetilde{L}$.

However, if the chains are shifted with respect to one another or are of different lengths then there can be a "zipped" energy-well in their interaction energy. In fact, if the two chains are small enough such that they can undergo head-to-tail aggregation as illustrated in Fig. 4.8b, then there exists a path for their aggregation with little or no energy barrier at all. Therefore, head-to-tail aggregation between individual MR colloids or short chains can readily occur in the thin-slit system as long as it is geometrically feasible. The vertical line on the left hand side of the energy curve in Fig. 4.8a represents the hard-sphere excluded volume potential when two chains are completely aggregated. Increasing the dimensionless external magnetic field strength λ will cause the maximum and minimum in Fig. 4.8a to increase in magnitude. The exact form of $\widetilde{U}_c(\widetilde{r})$ can be calculated for any two rigid chains by simply summing the dipole-dipole interactions between all of the colloids in the two chains.

The discussion of the energy barriers is relevant to the results presented in Fig. 4.7. When $\widetilde{L} \leq 4$ the lowest energy state of the system as predicted by the Gross model is single colloid width chains spanning the height of the thin-slit. As illustrated in Fig. 4.8b, the head-to-tail aggregation necessary to form the single chains does not involve any significant energy barrier and therefore the system is not kinetically limited from reaching the lowest energy state. For $\widetilde{L} \geq 5$ the lowest energy state of the system as predicted by the Gross model consists of clusters containing zipped chains. However, in Fig. 4.8a we illustrate that the zippering of chains involves energy barriers which have to be overcome in order to form the larger clusters predicted by the Gross model. As mentioned previously, this idea has been postulated in the literature [96, 9] but a more quantitative analysis will be presented here. We have developed a simple model to quantify the energy barriers to zippering under the extreme confinement studied in this work. Our model attempts to calculate

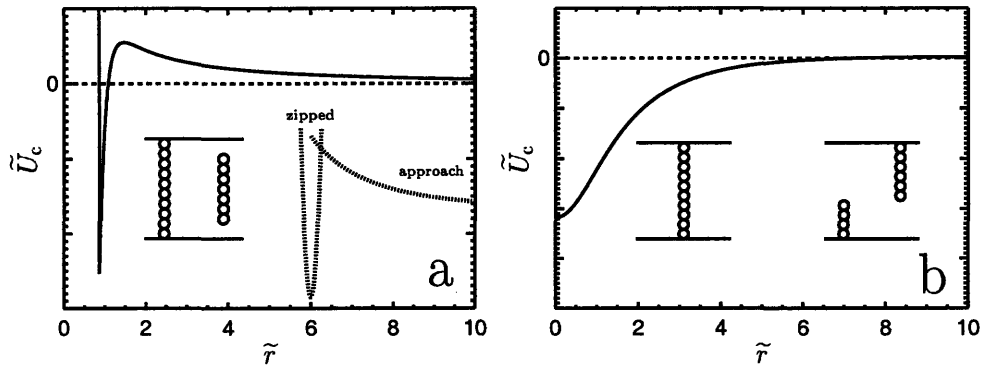

Fig. 4.8: *(a) The general form of the interaction energy between two chains of MR colloids (in arbitrary units) as a function of their separation distance. The right inset illustrates the two parts of the energy curve, the approach energy and the zipped energy. The left inset illustrates the configuration of chains undergoing zippering. (b) The form of the interaction energy between two short chains which are able to undergo head-to-tail aggregation. The inset illustrates the configuration of the two short chains before (right) and after (left) head-to-tail aggregation.*

the potential energy barriers to aggregation for various global constraints (N, $\widetilde{L}$, and ϕ) in order to determine when the thin-slit system is kinetically limited from reaching the lowest-energy state as predicted by the Gross model. Our model differs from previous attempts to model the energy barriers to zippering [9] in that we include the effects of volume fraction which physically accounts for additional net attraction forces between chains, due to the surrounding chains, which must be added to the simple picture presented in Fig. 4.8.

4.3.2 Model

In the real thin-slit system, we have a fixed number of colloids N in a box with a fixed height $\widetilde{L}$ and a fixed volume fraction ϕ such that the ratio N/ϕ is also fixed. Recall that $N = N_c\langle c\rangle$ so the previous fixed ratio can be written as $N_c\langle c\rangle/\phi$. Therefore fixing $\widetilde{L}$, N_c, and $\langle c\rangle/\phi$ is tantamount to fixing N, $\widetilde{L}$, and ϕ. Furthermore, the ratio $\langle c\rangle/(\widetilde{L}\phi)$ is fixed and therefore $\langle\widetilde{s}\rangle$ is fixed for a given value of $\widetilde{L}$. We find that fixing N_c and $\langle\widetilde{s}\rangle$ for a given $\widetilde{L}$ leads to more useful conclusions from our model.

Therefore, consider a periodic one dimensional system of N_c rigid chains aligned with the external field and interacting with dimensionless energy $\widetilde{U}_c(\widetilde{r})$ (made dimensionless with k_BT). For simplicity, the chains only interact with their two nearest neighbors along the line and the entire system is under the global constraints mentioned above such that

$$\sum_i n_i \equiv N_c \tag{4.6}$$

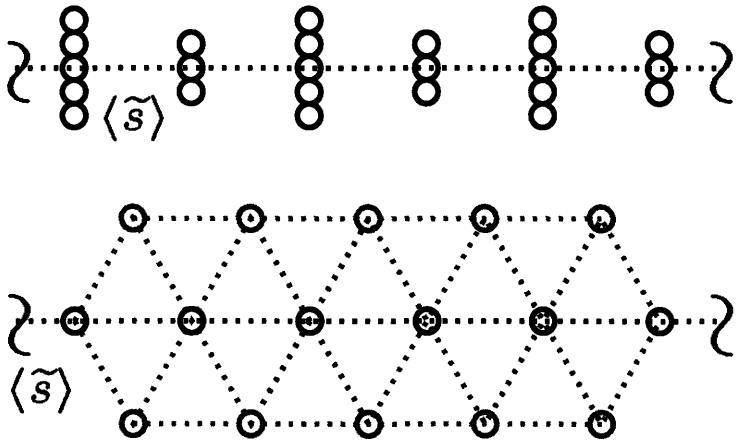

Fig. 4.9: *Top: A side view of the one-dimensional periodic line where the neighbor-pairs of clusters are all identical. Bottom: Top-down view of a hexagonal arrangement of chains in a thin-slit where the lattice spacing is* $\langle\widetilde{s}\rangle$. *The model considers the highlighted lattice vector (considered to be a one-dimensional periodic line).*

and

$$\sum_i n_i \widetilde{r}_i \equiv N_c \langle\widetilde{s}\rangle \tag{4.7}$$

where n_i is the number of pairs of neighboring chains with separation $\widetilde{r}_i$. The motivation for this model is illustrated in Fig. 4.9 where we observe that the top-down view of the thin-slit system looks like a hexagonal lattice in the ideal case with spacing between clusters given by $\langle\widetilde{s}\rangle$. The lattice vectors in this simplified picture can therefore be considered the one dimensional periodic system we are modelling.

The Boltzmann weighted probability of having a set of separations $\mathbf{n} = \{n_0, n_1, \ldots\}$ in our model is

$$\omega(\mathbf{n}) = \frac{N_c!}{n_0! n_1! \ldots} e^{-\widetilde{U}_c^{\text{tot}}} \tag{4.8}$$

where $\widetilde{U}_c^{\text{tot}}$ is defined as

$$\widetilde{U}_c^{\text{tot}} \equiv \sum_i n_i \widetilde{U}_c(\widetilde{r}_i). \tag{4.9}$$

We want to find the set of separations that maximize the probability given in Equation 4.8 under the constraints given by Equations 4.6 and 4.7. Using Lagrange multipliers we write the maximization function as

$$\frac{\partial}{\partial n_i}\left[\ln\left(\frac{N_c!}{\prod_i n_i!}\right) - \sum_i n_i \widetilde{U}_c(\widetilde{r}_i) - \alpha \sum_i n_i - \beta \sum_i n_i \widetilde{r}_i\right] = 0. \tag{4.10}$$

Solving Equation 4.10 using Stirling's approximation for the first term on the LHS we are left

with the result

$$n_i^* = Ce^{-\left[\widetilde{U}_c(\widetilde{r}_i)+\beta\widetilde{r}_i\right]} \tag{4.11}$$

where the constant C comes from the first Lagrange multiplier (α) and is found by applying the first constraint (Equation 4.6). Substituting in for the constant term we find

$$n_i^* = \frac{N_c e^{-(\widetilde{U}_c(\widetilde{r}_i)+\beta\widetilde{r}_i)}}{\sum_i e^{-(\widetilde{U}_c(\widetilde{r}_i)+\beta\widetilde{r}_i)}}. \tag{4.12}$$

Applying the second constraint and substituting Equation 4.5 for $\langle\widetilde{s}\rangle$ we can solve for the Lagrange multiplier β with

$$\frac{\int \widetilde{r}e^{-(\widetilde{U}_c(\widetilde{r})+\beta\widetilde{r})}d\widetilde{r}}{\int e^{-(\widetilde{U}_c(\widetilde{r})+\beta\widetilde{r})}d\widetilde{r}} = \sqrt{\frac{\pi}{3\phi\sqrt{3}}\frac{\langle c\rangle}{\widetilde{L}}} \tag{4.13}$$

where we have replaced the sums over i with integrals over the separation distance $\widetilde{r}$. Equation 4.13 can be solved numerically for β once we specify $\widetilde{U}_c(\widetilde{r})$, ϕ, $\langle c\rangle$, and $\widetilde{L}$. More importantly, in this model the probability that two chains will be separated by a distance $\widetilde{r}$ is given by

$$P(\widetilde{r}) = \frac{e^{-\left[\widetilde{U}_c(\widetilde{r})+\beta\widetilde{r}\right]}}{\int e^{-\left[\widetilde{U}_c(\widetilde{r})+\beta\widetilde{r}\right]}} \tag{4.14}$$

meaning that the dimensionless potential energy between two neighboring chains is equivalent to $\widetilde{U}_c(\widetilde{r}) + \beta\widetilde{r}$.

Again, the general form of the interaction between two rigid chains undergoing a zippering aggregation is shown in Fig. 4.8a. Recall that the specific form of $\widetilde{U}_c(\widetilde{r})$ depends upon the two types of chains and λ. If we take the part of the function $\widetilde{U}_c(\widetilde{r})$ that lies to the right of the maximum, we can calculate β for a specific system given ϕ, $\langle c\rangle$, and $\widetilde{L}$ using Equation 4.13. Furthermore, we can then use β to calculate the potential energy between two neighboring chains ($\widetilde{U}_c(\widetilde{r}) + \beta\widetilde{r}$). An example of the potential energy between a rigid chain of 10 MR colloids and rigid chains of different lengths (N_{small}) in a thin-slit with $\widetilde{L} = 10$ is shown in Fig. 4.10a. The volume fraction of the MR fluid in this case was taken to be 0.04 and the dimensionless field strength was $\lambda = 50$. The two interacting chains were assumed to be aligned in the vertical direction along the centerline of the thin-slit but shifted such that they can undergo a zippering aggregation as illustrated in Fig. 4.10b (insets). The curves in Fig. 4.10a illustrate the effect that β has upon the interaction between two chains in this model. Physically, β is the parameter that takes into account the presence of other chains in the system. For instance, if the two test chains in Fig. 4.10a move far away from one another, the energy $\widetilde{U}_c(\widetilde{r})+\beta\widetilde{r}$ actually increases because they are moving closer to the other chains in the system (i.e. they increase the total energy in the system). Therefore, the value of β will depend upon the volume fraction in the system and the types of chains for which the interaction energy is being calculated.

The idea of a volume fraction dependence upon the interaction between chains has been speculated before by Mohebi et al. [9]. In their work, the authors define a separation distance between chains called an escape distance below which two chains will zipper and above which the two chains will repel one another. They allude to the fact that as the volume fraction is increased, chains will be in closer proximity to one another and therefore more likely to enter the escape distance of their neighboring chains. However, this effect has not been quantified in the literature and here we

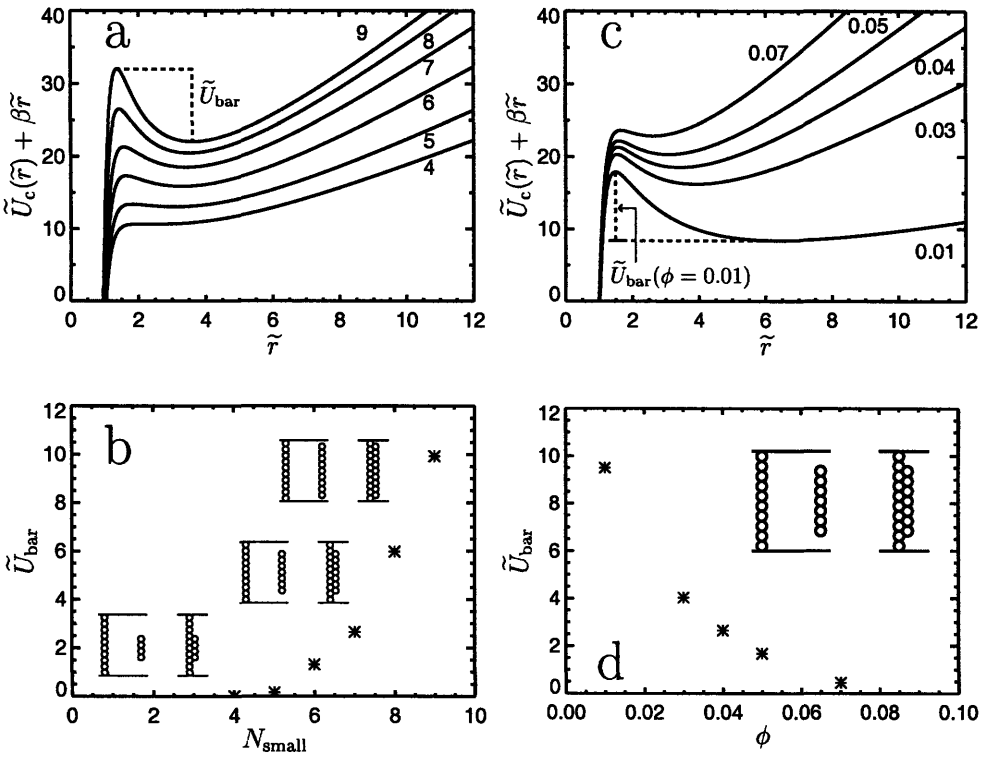

Fig. 4.10: *(a) The dimensionless potential energy between neighboring chains of length* 10 *and* N_{small} *for six different small chain lengths (*$N_{small} = 9$, 8, 7, 6, 5, *and* 4 *from top to bottom) at a dimensionless field strength of* $\lambda = 50$ *in a dimensionless slit-thickness of* $\widetilde{L} = 10$. *The potential energy barrier to aggregation is shown for* $N_{small} = 9$. *(b) The dimensionless energy barrier to aggregation as a function of* N_{small} *at a volume fraction of* 0.04 *and a dimensionless field strength of* 50. *Insets are illustrations of the systems presented in this figure before aggregation (left) and after aggregation (right) for* $N_{small} = 9$, 7, *and* 4 *from top to bottom. (c) The dimensionless potential energy between neighboring chains of length* 10 *and* 7 *for five different volume fractions (*0.07, 0.05, 0.04, 0.03, *and* 0.01 *from top to bottom) at a dimensionless field strength of* $\lambda = 50$ *in a dimensionless slit-thickness of* $\widetilde{L} = 10$. *The potential energy barrier to aggregation is shown for* $\phi = 0.01$. *(d) The dimensionless energy barrier to aggregation as a function of volume fraction for a chain of length* 10 *and a chain of length* 7. *Inset is an illustration of the system presented in this figure before aggregation (left) and after aggregation (right).*

present a quantitative analysis of the volume fraction dependence.

The curves in Fig. 4.10a show a local energy minimum near a dimensionless separation of ~ 4 which increases in magnitude as N_{small} is increased. In order for two chains to zipper (have a dimensionless separation distance < 1) they must pass through the transition state in their interaction energy (the maxima near $\widetilde{r} \sim 1.5$ in Fig. 4.10a) before reaching the aggregated state. The difference between the local energy minimum and the transition state energy is the energy barrier to aggregation $\widetilde{U}_{\text{bar}}$. In Fig. 4.10a the energy of the transition state as a function of N_{small} is increasing faster than the local energy minimum and therefore the energy barrier to aggregation increases with N_{small}. When $\widetilde{U}_{\text{bar}} \sim 1$ two chains can zipper relatively easily by diffusion. In Fig. 4.10b we see that for a small chain length $N_{\text{small}} \leq 6$ the dimensionless energy barrier to aggregation is $\lesssim 1$ implying that the two chains can easily undergo the zippering aggregation. This means that for a given $\widetilde{L}$, ϕ, and λ there can be a critical small chain length (N^*_{small}) such that for any chain smaller than N^*_{small} it is energetically likely that it will zipper with a chain of length $N_{\text{big}} = \widetilde{L}$.

In Fig. 4.10c we show the dimensionless potential energy between a chain of length 10 and a chain of length 7 at several different volume fractions in a dimensionless slit-thickness of 10 with $\lambda = 50$. This illustrates the effect that the volume fraction has upon the interaction between neighboring chains since increasing the volume fraction causes the energy barrier to aggregation to decrease. By increasing the volume fraction, the chains are forced to be closer together. This closer proximity means that they have less freedom to diffuse away from their neighbors and therefore β will be larger. The larger value of β causes the local minima in Fig. 4.10c to increase much faster than the the local maximum (transition state energy) and therefore the energy barrier to aggregation is reduced with increased volume fraction. As a result, the ability for two chains to undergo a zippering aggregation depends heavily upon the volume fraction in the system as shown in Fig. 4.10d where the energy barrier shrinks significantly as ϕ is increased.

We are interested in knowing when zippering aggregation barriers are small as a function of the slit-thickness for the thin-slit system and therefore, we applied our model to the following problem. For a fixed slit thickness, we calculated the energy barriers for the zippering of one rigid chain which spanned the height of the thin-slit ($N_{\text{big}} = \widetilde{L}$) and another rigid chain with a length $1 \leq N_{\text{small}} \leq \widetilde{L} - 1$. The vertical position of the small chain was determined as

$$\begin{aligned} &\text{if } N_{\text{big}} - N_{\text{small}} \text{ is even: } \widetilde{z}_{\text{small}} = \frac{\widetilde{L}}{2} - 0.5 \\ &\text{if } N_{\text{big}} - N_{\text{small}} \text{ is odd: } \widetilde{z}_{\text{small}} = \frac{\widetilde{L}}{2} \end{aligned} \tag{4.15}$$

where $\widetilde{z}_{\text{small}}$ is defined as

$$\widetilde{z}_{\text{small}} \equiv \frac{1}{N_{\text{small}}} \sum_{i}^{N_{\text{small}}} \widetilde{z}_i. \tag{4.16}$$

In Fig. 4.11 we show for several different ϕ the value of N_{small} where the dimensionless aggregation energy barrier to zippering becomes ≤ 1 as a function of $\widetilde{L}$ (or N_{big}). For any slit-thickness $\widetilde{L}$ and volume fraction ϕ a chain spanning the height of the thin-slit can zipper with any other chain of length $N_{\text{small}} \leq N^*_{\text{small}}$ where N^*_{small} is the critical small-chain length shown in Fig. 4.11.

Scaling the lengths in Fig. 4.11 by the characteristic dimensionless length-scale $\langle \widetilde{s} \rangle_{2D}$ causes all

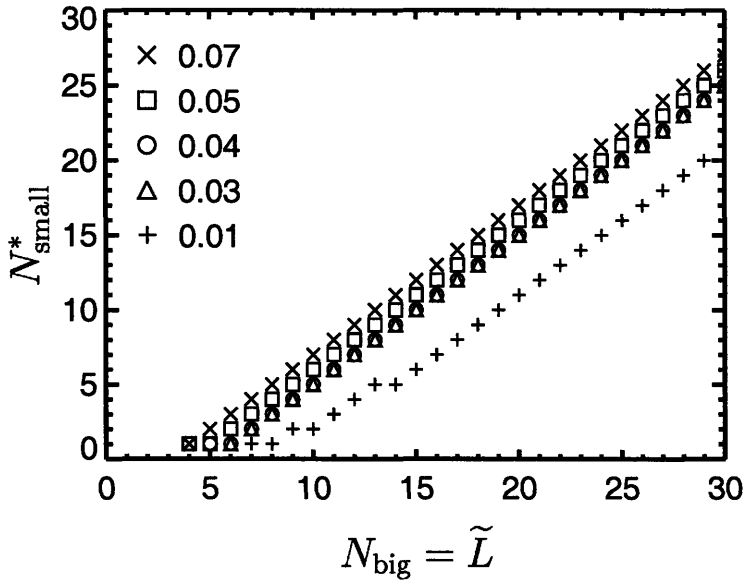

Fig. 4.11: *Critical small-chain length as a function of dimensionless slit-thickness for five different volume fractions at a dimensionless field strength of* $\lambda = 50$.

of the critical small-chain length curves ($N^*_{\text{small}}(\widetilde{L})$) to collapse onto a single master curve as shown in Fig. 4.12. This is a very important result as it indicates that there is a self-similar behavior of the thin-slit system when the slit-thickness is scaled by $\sqrt{\phi}$. Additionally, for our simple model, this result indicates that zippering aggregation can only occur when $\widetilde{L}/\langle\widetilde{s}\rangle_{2D} \gtrsim 1.2$. Consequently, if the lowest energy state of the thin-slit system contains clusters with zipped chains, then that state may not be able to be achieved if the energy barriers to zippering are too high. We expect that the dimensionless slit-thickness where the system will depart from 2D behavior should be affected by the energy barriers to zippering and from our model we find that the departure slit-thickness will be proportional to $\sqrt{\phi}$ (as predicted by the collapse in Fig. 4.12).

In Fig. 4.13 we present the dimensionless spacing between clusters as a function of the dimensionless slit-thickness for integer slit-thicknesses only. In Fig. 4.13a, the departure point of the cluster spacing from 2D behavior depends upon ϕ. Scaling both the dimensionless slit-thickness and the dimensionless spacing between clusters by the 2D spacing ($\langle\widetilde{s}\rangle_{2D}$) in Fig. 4.13b we show that the dimensionless slit-thickness where the system departs from 2D behavior is indeed proportional to $\sqrt{\phi}$ and occurs when $\widetilde{L}/\langle\widetilde{s}\rangle_{2D} \gtrsim 1.2$ (the vertical dotted line segment in Fig. 4.13b). To further emphasize the importance of this scaling in volume fraction we show in the inset of Fig. 4.13b the collapse of the cluster-spacing curves if we take the ϕ scaling predicted by the Gross model [96]. In Fig. 4.7 the lowest-energy model shows an abrupt departure from 2D behavior at $\widetilde{L} \geq 4$ for $\phi = 0.04$. Based on the lowest-energy model, the departure point from 2D behavior should be proportional to $\phi^{0.122}$ however, it is shown by the poor collapse in the inset of Fig. 4.13b that the departure point does not depend solely upon the lowest energy state but that energy barriers to aggregation are of great importance.

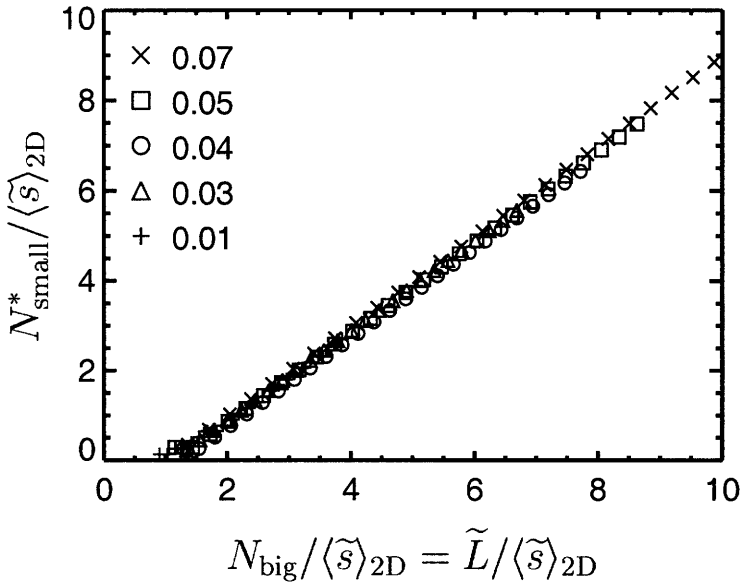

Fig. 4.12: *Scaled critical small-chain length as a function of dimensionless slit-thickness scaled by the 2D spacing for five different volume fractions at a dimensionless field strength of* $\lambda = 50$.

Not only does the model presented here predict the departure from 2D behavior but it also appears in Fig. 4.13b to explain the behavior of the system after the departure as well. Figure 4.12 shows the self-similar nature of the aggregation of chains in a simple model system. For the thin-slit system, consider a scaled slit-thickness of $\widetilde{L}/\langle\widetilde{s}\rangle_{2D}$ in the range where zippering is energetically feasible (greater than 1.2). At any volume fraction, the scaled lengths of the chains that can zipper with a chain of length $\widetilde{L}$ are the same. This means that the average cluster size will also scale with $\langle\widetilde{s}\rangle_{2D}$ and therefore the spacing between clusters will not have a volume fraction dependence. Thus, all of the scaled spacing curves in Fig. 4.13b collapse for the range of slit-thicknesses studied here.

The volume fraction dependence is further illustrated in Fig. 4.14 where we show top-down views of the clusters in a dimensionless slit-thickness of 10 at four different volume fractions. The distribution of cluster sizes for each of the four cases is also presented in Fig. 4.14 showing the increased fraction of zipped clusters as the volume fraction is increased. The left most peak in the cluster distributions is for a cluster size of 10 and the broader peak that appears in the distributions for larger volume fractions is for clusters of zipped chains.

4.3.3 Time-scales for Zippering

The dimensionless first passage time for a rigid Brownian chain of N_{small} colloids diffusing in a 1D dimensionless potential energy landscape $\widetilde{U}_{\text{ls}}$ (where U_{ls} is made dimensionless with $k_{\text{B}}T$) to

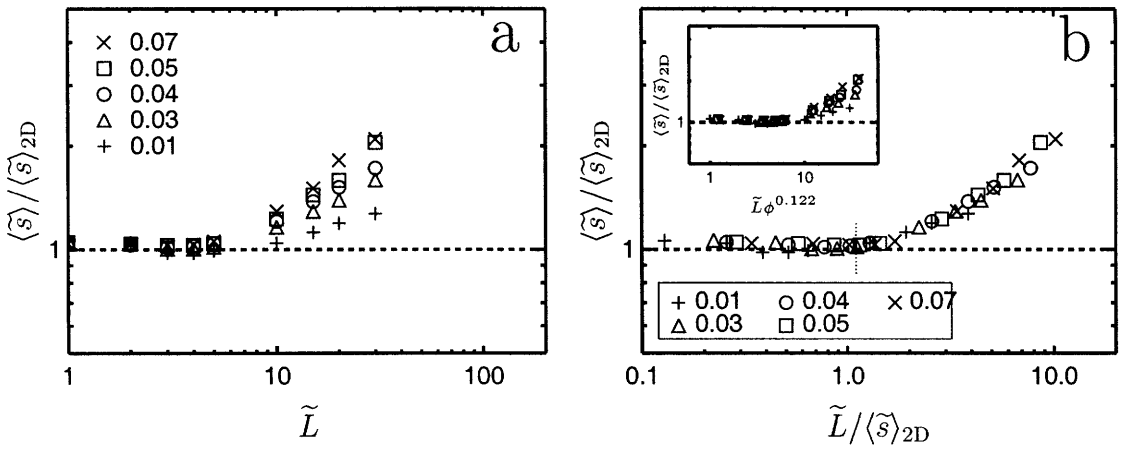

Fig. 4.13: *(a) The average dimensionless spacing between clusters (scaled by the 2D spacing) for five different volume fractions as a function of the dimensionless slit-thickness for integer values of $\widetilde{L}$ only. (b) The average dimensionless spacing between clusters (scaled by the 2D spacing) as a function of the dimensionless slit-thickness (also scaled by the 2D spacing) for five different volume fractions. The horizontal dashed lines are the 2D spacing. The vertical dotted line segment in (b) denotes the point at which our model predicts the dimensionless spacing will deviate from 2D behavior. The inset in (b) shows the average dimensionless spacing between clusters (scaled by the 2D spacing) as a function of the dimensionless slit-thickness scaled as predicted by the Gross model [96].*

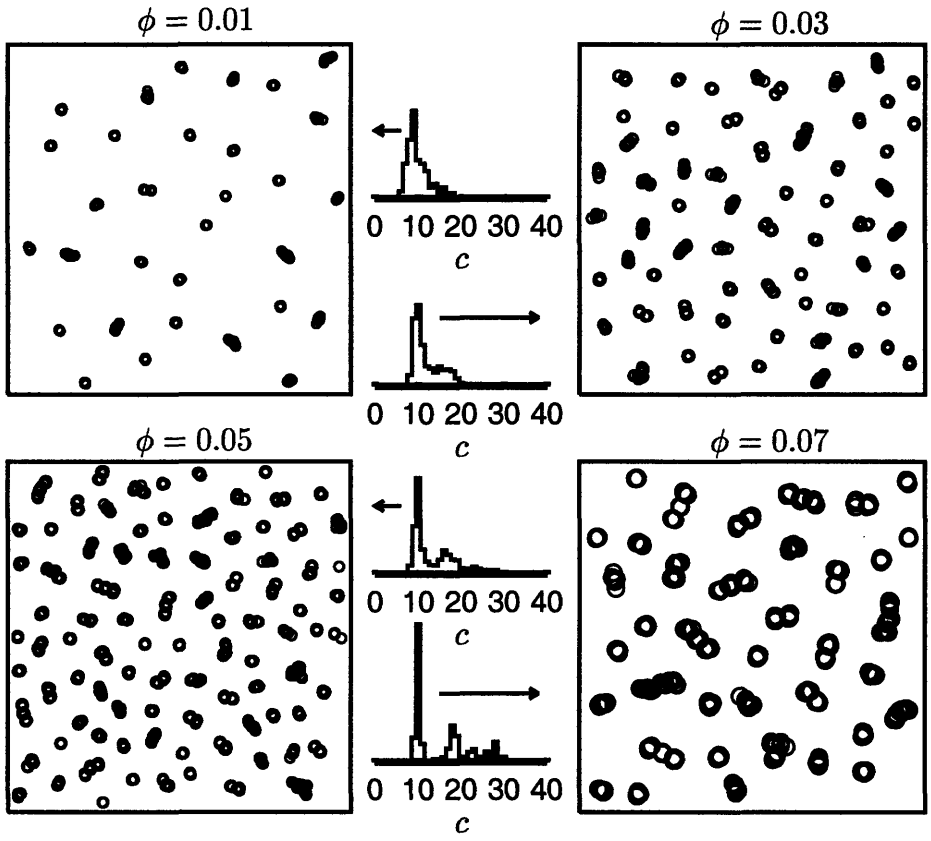

Fig. 4.14: *Top-down views of the thin-slit system for four different volume fractions in a dimensionless slit-thickness of* 10 *at a dimensionless field strength of* 50. *The cluster-size distributions are shown along the center for volume fractions of* 0.01, 0.03, 0.05, *and* 0.07 *(from top to bottom). The fraction of clusters containing zipped chains increases as the volume fraction is increased.*

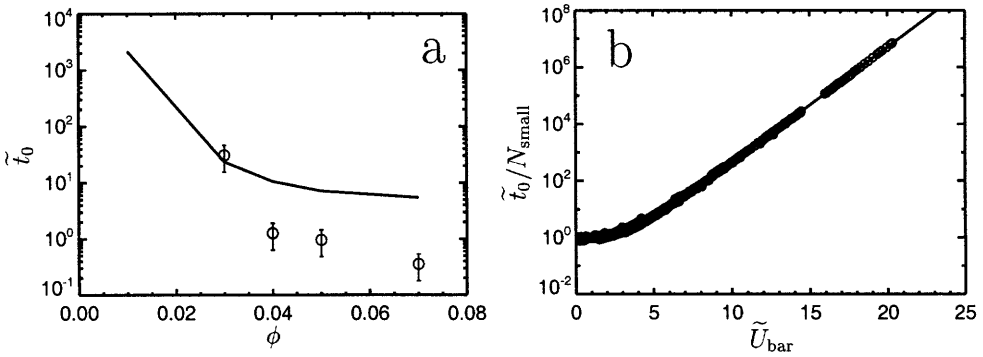

Fig. 4.15: *(a) Mean dimensionless aggregation time as a function of ϕ for a chain of 7 MR colloids to undergo a zippering aggregation with a chain of 10 MR colloids in a dimensionless slit-thickness of 10 and a dimensionless external field strength of 50. The solid line is the theoretical prediction given by Equation 4.17 and the circles are the results from BD simulations. (b) Calculated dimensionless aggregation time (Equation 4.17) as a function of the dimensionless energy barrier for $2 \leq N_{big} \leq 30$ and $1 \leq N_{small} < N_{big}$ at $\lambda = 50$. The solid line is an empirical fit to the data given by $\widetilde{t}_0/N_{small} = 1 + 0.036e^{0.937\widetilde{U}_{bar}}$.*

overcome a dimensionless energy barrier located at position $\widetilde{x}_0$ is given by [100]

$$\widetilde{t}_0 = \frac{N_{\text{small}}}{\langle \widetilde{s} \rangle_{\text{2D}}^2} \int_0^{\widetilde{x}_0} e^{-\widetilde{U}_{\text{ls}}(\widetilde{x})} \left\{ \int_{\widetilde{x}}^{\widetilde{x}_0} e^{\widetilde{U}_{\text{ls}}(\widetilde{y})} \mathrm{d}\widetilde{y} \right\} \mathrm{d}\widetilde{x} \tag{4.17}$$

where time is made dimensionless with $(\zeta \langle \widetilde{s} \rangle_{\text{2D}}^2 d^2)/(k_{\text{B}}T)$ since $\langle \widetilde{s} \rangle_{\text{2D}}$ is the important dimensionless length scale in this problem. For the example shown in Fig. 4.10c we can solve Equation 4.17 numerically for each of the five volume fractions in order to estimate the time for the two chains to aggregate. In Fig. 4.15a we show the solution to Equation 4.17 (solid line) as a function of ϕ along with the mean times for aggregation for simple BD simulations. The simple BD simulations consisted of 8 chains of MR colloids, 7 of which contained 10 colloids and the 8th containing 7 colloids. The chains were started on a hexagonal lattice, oriented in the field-direction (z-direction), and confined between hard walls inside a simulation box with dimensionless height $\widetilde{L} = 10$. The simulation box had periodic boundary conditions in the other two cartesian directions and the dimensionless lengths of the periodic dimensions were equal and determined by the volume fraction. The system was simulated using our BD algorithm until the small chain aggregated with one of the larger chains. This procedure was repeated 100 times and the mean time for aggregation was thus calculated.

As shown in Fig. 4.15a, our simple model for the energy between chains as a function of chain-length, field strength, and volume fraction is able to qualitatively predict the fact that there are orders of magnitude increases in the timescales for zippering as the volume fraction is decreased. For the case presented in Fig. 4.15a, the energy barriers to aggregation are given in Fig 4.10d. For the higher volume fraction cases the chains in the simple simulations zip together much faster than

predicted by the model due to the fluctuations of the colloids within the chains [98, 101]. When the colloids in a chain are able to fluctuate then the barrier to the zippering aggregation can be reduced and therefore the time for aggregation is also reduced. However, the timescales for aggregation found in our simple BD simulations for this particular case still show orders of magnitude increases as the volume fraction decreases (and therefore the energy barrier to aggregation increases). In fact, for the case of $\phi = 0.01$ we were not able to observe even a single aggregation event for chains of length 7 and 10 in our simple BD simulations when simulating out to dimensionless times of 150,000.

In Fig. 4.15b we show the timescales for zippering as a function of the energy barrier as predicted by our model for dimensionless slit-thicknesses ranging from 2 to 30 and $\lambda = 50$. The data for all of the volume fractions fall onto a single master curve given by $\widetilde{t}_0/N_{\text{small}} = 1 + 0.036e^{0.937\widetilde{U}_{\text{bar}}}$ which is plotted as a solid line in Fig. 4.15b. The exponential increase in the aggregation time as a function of energy barriers indicates how the presence of energy barriers to zippering can cause the structure of self-assembled MR fluids in certain thin slits to be unable to reach the lowest energy state.

4.3.4 Discussion

The results presented in this section illuminate several important features of self-assembly of dilute MR fluids confined in extremely thin-slits. Most notably, we have studied the transition from truly 2D behavior to 3D behavior of the structure in the system, manifested in the spacing between clusters. This cross-over in the structural properties has not been addressed in previous work. When we extrapolate the models previously developed down to the extremely small slit-thicknesses studied in this work we find that a new understanding is needed in order to explain the trends that we observe. We have introduced a simple model for the energy of interaction between chains of MR colloids taking into account the volume fraction of the MR fluid. This model is the first to quantitatively address the effect of volume fraction upon the energy barriers to aggregation for dilute MR fluids in thin-slits. We have used the model to predict the transition point from 2D behavior to 3D behavior in the thin-slit system. In particular, the transition is correlated with the ability of the chains to begin aggregating laterally into larger column-like clusters. Our model is able to predict, as a function of volume fraction, at which dimensionless slit-thickness this aggregation becomes kinetically feasible. Additionally, in agreement with previous work [10] we find that the 3D behavior of the spacing between clusters follows a power-law. Furthermore, our model explains the volume fraction dependence of the self-assembled structures in thin-slits when $\widetilde{L} \leq 30$. This represents the first quantitative analysis of the transition from 2D to 3D behavior for dilute MR fluids self-assembling in the thin-slit system.

We have attempted to use the model for the energy barriers to aggregation in order to predict the timescales for zippering of chains in the thin-slit system. We found qualitative agreement between the predicted timescales and our BD simulations for this aggregation process in that the timescales increase by orders of magnitude as the volume fraction is decreased. The dimensionless timescale for aggregation from our model for a chain of length 7 to zipper with a chain of length 10 at $\phi = 0.03$ and $\lambda = 50$ is $\widetilde{t}_0 \sim 23.5$. The dimensionless energy barrier to aggregation in this case is ~ 4. For 1μm colloids in water, this translates to a real time of ~ 10.4 minutes. By comparison, if the short chain length were 8 instead of 7 then the dimensionless energy barrier would be ~ 7.8 and the dimensionless timescale for aggregation would be $\widetilde{t}_0 \sim 525$ or 6.7 hours. During the process of slowly ramping the external field, many short chains will first form with different lengths (Fig. 4.1)

and in order to reach the lowest energy state of zipped clusters, those short chains must aggregate laterally. The timescale of this process will be dominated by the slowest aggregation step which, as we have shown, can be prohibitively long. This point supports the contention that real experimental studies of self-assembly in thin-slits can be kinetically trapped in metastable states that only change over extremely long time scales.

4.4 Quasi 2D Thin-Slits

In Fig. 4.4 the spacing between clusters oscillates as a function of slit-thickness for extremely thin slits ($\widetilde{L} \leq 5$). The structure of concentrated MR fluids ($\phi = 0.2$) has been shown to oscillate between disorder and labyrinth structures in extremely thin-slits [11] but the self-assembly of dilute MR fluids has not been previously investigated. In Fig. 4.16 we show the spacing between clusters as a function of slit-thickness for all five volume fractions. Schematics of the types of clusters that form in three different slit-thicknesses are shown as well. Based on observations of the cluster types in these systems, we have determined that the oscillations in spacing with increasing $\widetilde{L}$ are due to geometric effects in the case of declining spacing or energetically favorable re-arrangement of the cluster types in the case of increasing spacing. In 2D ($\widetilde{L} = 1$) the colloids experience purely repulsive interactions and the spacing is determined simply by geometry [33, 34]. As the slit-thickness increases, the colloids still experience repulsive interactions for $\widetilde{L} < 1 + \sqrt{1/3}$ and therefore the clusters will remain just single colloids. In order to maintain a constant volume fraction of MR colloids the clusters must be closer to one another, hence the decrease in spacing. Once the slit-thickness becomes large enough $\widetilde{L} \sim 1.75$ the MR colloids can have attractive interactions and can therefore begin to form clusters larger than a single colloid. As mentioned previously, the spacing is proportional to $\sqrt{\langle c \rangle / \widetilde{L}}$ and therefore the spacing increases sharply as more large clusters are formed. This process is repeated between each integer value of $\widetilde{L}$.

We have shown in Fig. 4.5 that the spacing between clusters is related to the average cluster size in the thin-slit system and therefore it is useful to be able to predict the types of clusters that form as a function of slit-thickness. None of the current studies in the literature are able to model the extremely thin slits studied here. Therefore, we developed a zero-temperature model similar in nature to the Gross model [96] but applicable to the case of extremely thin slits. Our model consists of three possible types of clusters arranged on a hexagonal lattice with a spacing defined by the average cluster size as shown in Fig. 4.17. We chose three types of clusters in order to limit the degrees of freedom in our model such that we were able to easily find a solution. The three types of clusters (A, B, and C) vary depending upon the slit-thickness as shown on the left in Fig. 4.17. For instance, when $1 \leq \widetilde{L} < 2$ the clusters A, B, and C are a "singlet", "doublet", and "triplet" arranged as shown in Fig. 4.17. The intra-cluster arrangement of colloids was chosen such that it minimized the intra-cluster energy per colloid. Intra-cluster energy is determined by summing all of the interaction energies between MR colloids within a cluster and dividing by the number of colloids in the cluster.

Using the model as outlined, we varied the concentrations of clusters (ϕ_A, ϕ_B, ϕ_C) in order to minimize the total energy per colloid. The cluster concentration was defined as $\phi_i \equiv N_i / N_{\text{clust}}$ where N_i is the total number of clusters of type i and N_{clust} is the total number of clusters. The

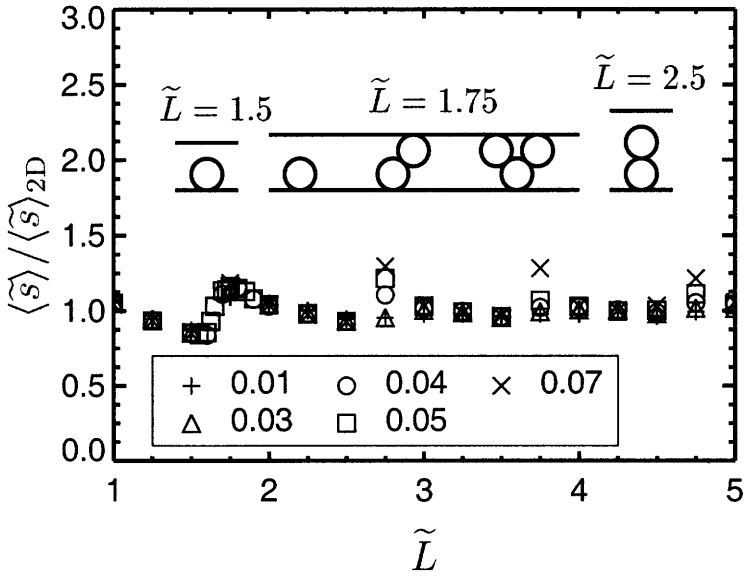

Fig. 4.16: *Average dimensionless spacing normalized by the 2D spacing as a function of dimensionless slit-thickness for five different volume fractions* ($\phi =$ 0.01, 0.03, 0.04, 0.05, 0.07) *at a dimensionless field strength of* $\lambda = 50$. *The types of clusters observed in our simulations are shown for three dimensionless slit-thicknesses* (1.5, 1.75, *and* 2.5) *as insets.*

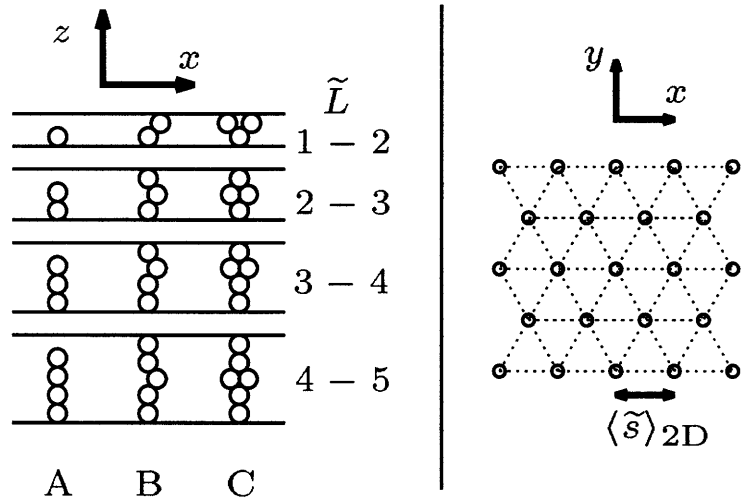

Fig. 4.17: *Left: A schematic of the possible types of clusters for each range of dimensionless slit-thicknesses considered. Right: A schematic of the hexagonal lattice of clusters with lattice spacing* $\langle\widetilde{s}\rangle_{2D}$. *Any of the clusters on the lattice can be of type A, B, or C.*

total energy per colloid was defined as

$$\frac{\widetilde{U}_{\text{tot}}}{N} = \frac{\widetilde{U}_{\text{tot}}^{\text{intra}}}{N} + \frac{\widetilde{U}_{\text{tot}}^{\text{inter}}}{N} \tag{4.18}$$

where $\widetilde{U}_{\text{tot}}^{\text{intra}}/N$ and $\widetilde{U}_{\text{tot}}^{\text{inter}}/N$ are the total intra- and inter-cluster energies per colloid respectively. The total intra-cluster energy per colloid is defined as

$$\frac{\widetilde{U}_{\text{tot}}^{\text{intra}}}{N} = \frac{N_{\text{A}}\widetilde{U}_{\text{A}}^{\text{intra}} + N_{\text{B}}\widetilde{U}_{\text{B}}^{\text{intra}} + N_{\text{C}}\widetilde{U}_{\text{C}}^{\text{intra}}}{N_{\text{A}}n_{\text{A}} + N_{\text{B}}n_{\text{B}} + N_{\text{C}}n_{\text{C}}} \tag{4.19}$$

where n_i is the number of MR colloids in a cluster of type i and $\widetilde{U}_i^{\text{intra}}$ is calculated, as mentioned, by summing all of the interaction energies between the colloids in a cluster of type i. The total inter-cluster energy is defined as

$$\frac{\widetilde{U}_{\text{tot}}^{\text{inter}}}{N} = \frac{1}{2}\frac{\sum_i^{\text{A,B,C}}\sum_j^{\text{A,B,C}}\phi_i\phi_j\widetilde{U}_{ij}^{\text{inter}}}{\phi_{\text{A}}n_{\text{A}} + \phi_{\text{B}}n_{\text{B}} + \phi_{\text{C}}n_{\text{C}}} \tag{4.20}$$

and the energy $\widetilde{U}_{ij}^{\text{inter}}$ is defined as

$$\widetilde{U}_{ij}^{\text{inter}} = \sum_{\text{lat}}\left\langle \widetilde{U}_{ij}^{\text{clust}}(\widetilde{r}_{\text{lat}})\right\rangle \tag{4.21}$$

where the sum is over all the lattice sites and the term $\widetilde{U}_{ij}^{\text{clust}}(\widetilde{r}_{\text{lat}})$ denotes the energy between a cluster of type i and a cluster of type j separated by a distance $\widetilde{r}_{\text{lat}}$. The dimensionless distance $\widetilde{r}_{\text{lat}}$ is determined by both the characteristic spacing $\langle\widetilde{s}\rangle_{\text{2D}}$ and the specific lattice site. The $\langle\rangle$ brackets denote an angle-averaged energy meaning we allow the two clusters to rotate with respect to one another keeping their center-of-mass separation equal to $\widetilde{r}_{\text{lat}}$ and take their average interaction energy. We summed over a large enough lattice such that increasing the number of sites did not change the results.

Once we have found the distribution of cluster concentrations (ϕ_{A}, ϕ_{B}, ϕ_{C}) that minimizes the energy per colloid for a given $\widetilde{L}$, λ, and ϕ we can calculate the average cluster size and therefore the average spacing between clusters. In Fig. 4.18 we show the normalized average spacing between clusters as a function of dimensionless slit-thickness for all five volume fractions from both our simulations (symbols) and our zero-temperature model (dashed lines). The curves are shifted for ease of viewing. The predictions from our model match well with the simulation results for most slit-thicknesses. In particular, the model correctly predicts the magnitude and locations of the oscillations in the spacing as a function of the slit-thickness. However, in some instances, there is disagreement between our model and the simulation results due to the following sources. Either our model does not contain enough detail (cluster types) or the lowest energy state is unreachable over reasonable simulation time-scales due to energy barriers.

We illustrate the sources of disagreement between our model and the simulation results in Fig. 4.19. In Fig. 4.19a we show as dotted lines the cluster-size distributions predicted by our model for all ϕ for two dimensionless slit-thicknesses. The actual cluster-size distributions from our BD simulations are shown as solid lines. The left set of distributions is for a dimensionless slit-thickness of 2.75 and the right set of distributions is for a dimensionless slit-thickness of 3.75. Recall

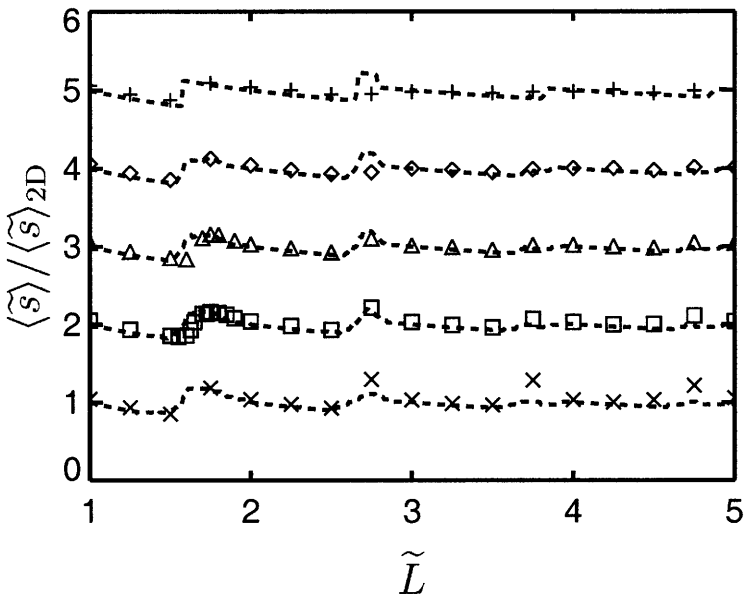

Fig. 4.18: *Normalized dimensionless spacing as a function of slit-thickness for* $\phi = 0.01$, 0.03, 0.04, 0.05, *and* 0.07 *(from top to bottom) for* $\lambda = 50$. *The curves are shifted by* 1 *with respect to one another for ease of viewing. The dashed lines are the predictions from the zero-temperature model for each* ϕ.

that our model only allows for three types of clusters in each slit-thickness but the BD results for $\phi = 0.07$ show that there are in fact more, larger, cluster types. This is an example of a case where our model does not contain enough detail to accurately predict the cluster-size distribution and therefore the spacing between clusters. A point of interest resulting from this observation is that our simulation results are consistent with previous work done on the self-assembly of concentrated MR fluids under extreme confinement where the authors observed labyrinth structures in dimensionless slit-thicknesses of 3.8 [11]. The large clusters in our simulations are the precursors to the labyrinth structures observed for more concentrated MR fluids as illustrated in Fig. 4.19d. In the top-down view of the thin-slit system when $\phi = 0.07$ and $\widetilde{L} = 3.75$ the clusters are arranged in a configuration that can easily lead to the labyrinth structures observed in this slit-thickness with more concentrated MR fluids.

For $\widetilde{L} = 3.75$ and $\phi \leq 0.04$ the model does well in predicting the cluster-size distributions. However, in the case of $\widetilde{L} = 2.75$ for the same range of ϕ the cluster-sizes predicted by the model are not observed in the simulations. The cause of this discrepancy is shown in Fig. 4.19b where we show the energy of interaction between two doublets in a slit with dimensionless thickness of 2.75 at a dimensionless field strength of $\lambda = 50$. The dotted line represents the maximum interaction energy between the two clusters when they are configured as shown in the inset. The gray area represents the possible energy states between the two clusters as measured in BD simulations and the solid line is the average interaction energy also taken from the BD simulations. Taking the average interaction energy measured in the BD simulations, we calculated β and therefore the

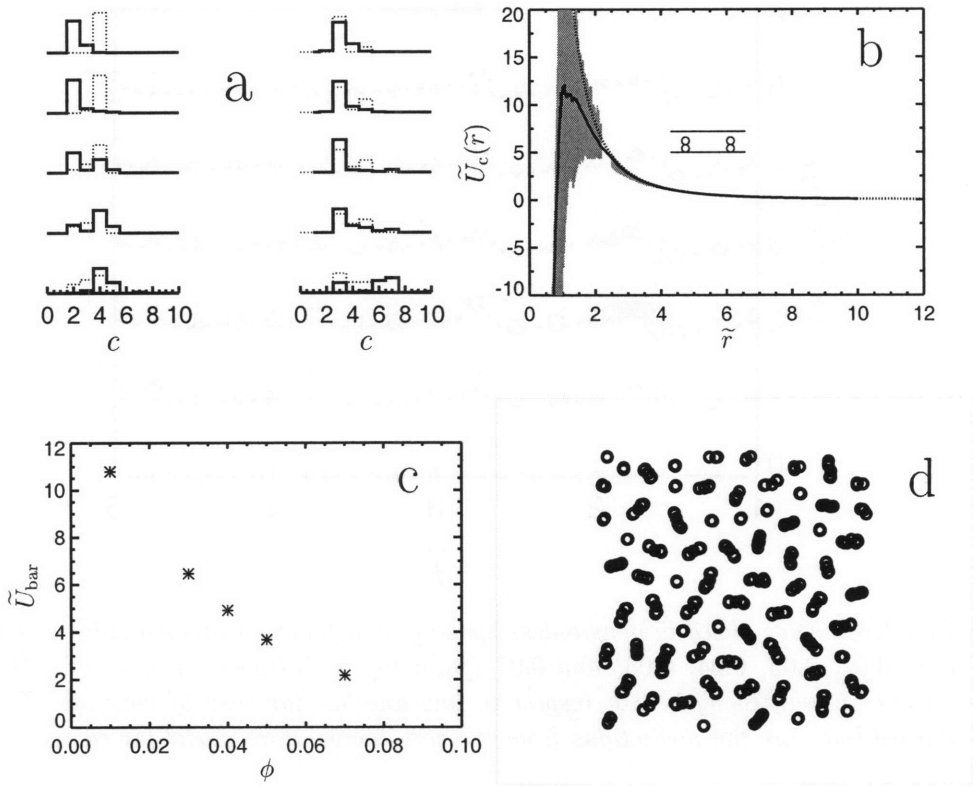

Fig. 4.19: *(a) Cluster size distributions for* $\widetilde{L} = 2.75$ *(left) and* $\widetilde{L} = 3.75$ *(right). From top to bottom the distributions are for* $\phi = 0.01$, 0.03, 0.04, 0.05, *and* 0.07. *The dotted lines are the predictions from the zero-temperature model and the solid lines are from the BD simulations. (b) The energy of interaction between two doublets in a dimensionless slit-thickness of* 2.75 *with* $\lambda = 50$. *The dotted line is the analytical interaction energy for the the configuration shown in the inset. The gray area represents the energies of interaction between doublets observed in the BD simulations and the solid line is the average interaction energy as a function of separation distance observed in the BD simulations. (c) The dimensionless energy barriers to aggregation for doublets as a function of volume fraction in a slit of dimensionless thickness* $\widetilde{L} = 2.75$ *and* $\lambda = 50$. *(d) Top-down view of the self-assembled structure when* $\widetilde{L} = 3.75$, $\phi = 0.07$, *and* $\lambda = 50$ *showing the precursor to the labyrinth structure.*

energy barriers to zippering in this case. The resulting energy barriers are plotted in Fig. 4.19c where it is clear that the energy barriers to zippering are large (several k_BT) for small ϕ indicating that the aggregation times are quite large for these systems.

Despite the sensitive slit-thicknesses where our zero-temperature model disagrees with the simulations due to the presence of energy barriers to zippering, it generally does a good job of predicting the spacing between clusters for slit-thicknesses $1 < \widetilde{L} < 5$ when $0.01 \leq \phi \leq 0.07$. Furthermore,

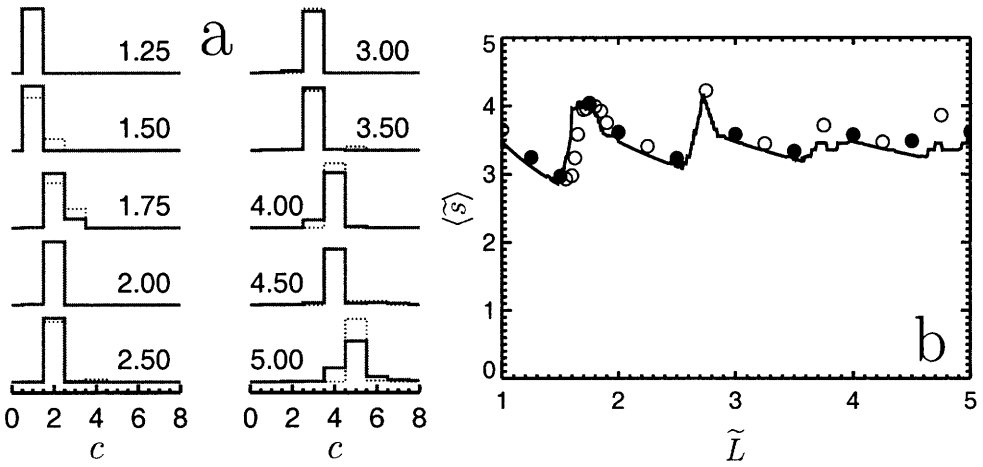

Fig. 4.20: *(a) Cluster size distributions for $\phi = 0.05$ in a variety of dimensionless slit-thicknesses. The gray solid line is the distribution observed in the BD simulations and the dotted black line is the prediction from the zero-temperature model. (b) The average spacing between clusters as a function of dimensionless slit-thickness for $\phi = 0.05$. The solid line is the prediction from the zero-temperature model and the symbols are the simulation results. The closed symbols denote the slit-thicknesses presented in (a).*

it correctly predicts the magnitude of the oscillations in spacing as well as the decay in the oscillations as the slit-thickness is increased. The cause of the oscillations (geometric effects and re-arrangement of the cluster types) is confirmed by both the model and the simulation results. In Fig. 4.20 we show the predictions for the cluster distributions and spacing between clusters for a volume fraction of $\phi = 0.05$. In Fig. 4.20b, the oscillations in spacing are quite obvious and the zero temperature model clearly predicts the spacings observed in our BD simulations. Additionally, in Fig. 4.20a the cluster distributions predicted by the model are also found in the simulations. The oscillations are shown to be correlated with the changes in the cluster distributions. For instance as $\widetilde{L}$ increases from 2.5 to 3 the cluster-size changes from 2 to 3 and as a result the spacing between clusters increases. From $\widetilde{L} = 3$ to 3.5 the cluster-size remains constant and therefore the spacing decreases as a result of the geometric constraint due to the constant volume fraction.

4.5 Summary

As the length scales in microfluidic devices utilizing self-assembled MR fluids shrink, new scalings and models are needed to describe the properties of both the self-assembly and the structures that form in these devices. The previous work on self-assembly of MR fluids in thin-slits has not addressed this increasingly important range of phase space where the slits are extremely thin and the MR fluid is dilute. We have shown that the self-assembled structures in extremely thin slits undergo a cross-over in their properties from a purely 2D system to the 3D behavior observed previously [10, 96, 94]. We have shown that this cross-over is due to the increased "clustering" of

the MR fluid colloids. The cross-over is strongly influenced by the energy barriers associated with the zippering aggregation of chains of MR colloids under the extreme confinement induced by the thin-slit. It has been postulated that the energetics of the zippering aggregation are important in the self-assembly of MR fluids under confinement in a thin-slit but this point has not been quantitatively analyzed in the literature [96, 9]. We introduced a model for the energetics of the zippering aggregation and showed how the cross-over in behavior from 2D to 3D depends upon the volume fraction of the MR fluid. Using the model for aggregation, we were able to predict the time-scales for two chains to aggregate given ϕ, $\widetilde{L}$, and λ. This result leads to the observation that, in certain instances, it is unfeasible for aggregation of chains to occur even though thermodynamics predicts that the aggregated state is the lowest-energy state [96].

For dimensionless slit-thicknesses ranging from 1 to 5, we have shown that discrete properties of the clusters are very important for determining the spacing between clusters. By simply changing the slit thickness slightly, the spacing between clusters can drastically change due to the energetically favorable re-arrangement of cluster types in the system. We introduced a new zero-temperature model for the distribution of cluster types in extremely thin-slits in order to predict the spacing between clusters as a function of slit-thickness. Our model is able to quantitatively predict the spacing between clusters in the range $1 \leq \widetilde{L} \leq 5$ with some notable exceptions. The sources of the disagreement between our zero-temperature thermodynamic model and the BD simulations again arise from barriers to aggregation or the lack of sufficient detail in the model. In the highest volume fraction case $\phi = 0.07$ we see that very large clusters can form when the dimensionless slit thickness is between integer values. This observation is consistent with a previous study on the self-assembly of concentrated MR fluids in extremely thin slits [11]. The large clusters in these cases are precursors to the labyrinth structure that can form if the MR fluid is concentrated enough.

4.6 Outlook

Energy barriers appear in many systems in nature and are often important in determining whether a system can reach its lowest energy state. In thin-slits the energy barriers to "zippering" have been shown to be quite important in determining the structure of dilute MR fluids under the application of a uniform magnetic field for dimensionless slit-thicknesses $\widetilde{L} < 30$. We note that they are probably also very important for determining the structure of MR fluids in much thicker slits as evidenced by the discrepancy between results presented in the theoretical and experimental literature [96, 10, 94, 91, 8, 98]. The energy barriers in these thicker slits have not, however, been quantitatively analyzed in the literature due to the much larger complexity involved.

CHAPTER 5

Self-Assembly Under Flow

The self-assembly of MR fluids under the application of pressure driven flow and an external magnetic field involves mechanisms that are not seen in the absence of flow. From a basic science standpoint, the effects that flow can have upon the self-assembly process are important for understanding structure formation under these conditions. In particular, the flow can affect the nature of the interactions between MR colloids and, in addition, it can affect the kinetics of structure formation and the final structure that forms. Many applications utilizing MR fluids require the fluid to flow through channels under the application of pressure [102]. Therefore, a study of the self-assembly of MR fluids under these conditions is of great importance.

5.1 Background

For many years the flow behavior of MR and ER fluids has been studied both experimentally [103, 104, 105, 106, 107] and in simulations [108, 109, 110]. It has been determined that MR fluids generally behave as a Bingham fluid for concentrated suspensions [103]. The yield stress of the fluid has been shown to depend upon the magnitude of the external magnetic field [6, 103]. This yield stress has been attributed to the formation of structures in the MR fluid when the external magnetic field is applied. Most of the experimental and simulation studies have been performed upon systems in steady or oscillatory shear flow [108, 111] and only recently has attention been paid to pressure driven flow [110, 106, 107].

Recent studies on the pressure driven flow of concentrated MR fluids have investigated both the microstructure as well as the rheological properties of the fluids [110, 106, 107]. The structural assessments have focused upon the general evolution of the system to its final steady-state configuration. The authors have found that both the structure and the rheological properties of concentrated MR fluids under pressure driven flow depend upon the boundary conditions and the orientation of the external magnetic field. However, none of the studies have addressed the specific mechanisms of the formation of chains in dilute MR fluids under the application of pressure driven flow.

There have been a number of studies of the self-assembly of chains in dilute MR fluids in rotating magnetic fields [112, 113, 114, 115]. These studies have focused on the forces acting upon a chain of MR colloids when it is immersed in a viscous fluid under the application of a rotating external magnetic field. The authors have found that the types of structures that form depend upon the balance of viscous and magnetic forces. The dimensionless parameter relating the viscous and magnetic forces is the Mason number [116, 104, 114]. However, in this case the flow forces arise not due to external pressure gradients but because of the viscous drag on the chain as it is rotated through the fluid.

The kinetics of self-assembly in dilute MR fluids have been well studied in the quiescent case (the absence of bulk fluid flow) [117]. It has been established that the fluid self-assembles into chains which grow in length as a power-law in time. The forces at work in the growth of the chain are the magnetic forces which must overcome the Brownian motion of the colloids. The growth of chains under the application of pressure driven flow should follow some of the same mechanisms as found in the quiescent case but as we will show there are multiple mechanisms involved when flow is applied.

The fact that many applications utilizing MR fluids involve pressure driven flow through microchannels implies that there is a definite need for understanding structure formation in dilute MR fluids under these conditions. Here we present a simulation study of the self-assembly of a dilute MR fluid experiencing pressure driven flow through a rectangular microchannel under the application of a uniform external magnetic field.

5.2 Simulation Details

In this work, we studied a dilute MR fluid in a rectangular thin-slit microchannel with periodic boundaries in the y-direction and flat hard walls in the x and z-directions. The simulation box had a dimensionless size of $10 \times 100 \times 100$ where lengths were made dimensionless with the colloid diameter d. The uniform external magnetic field was directed in the z-direction and the pressure driven flow down the channel was in the y-direction. A schematic of the coordinate system for these simulations is shown in Fig. 5.1.

The Poiseuille flow in this study imposed a velocity $\mathbf{V}(\mathbf{r}_i(t))$ on a colloid located at $\mathbf{r}_i$ given by

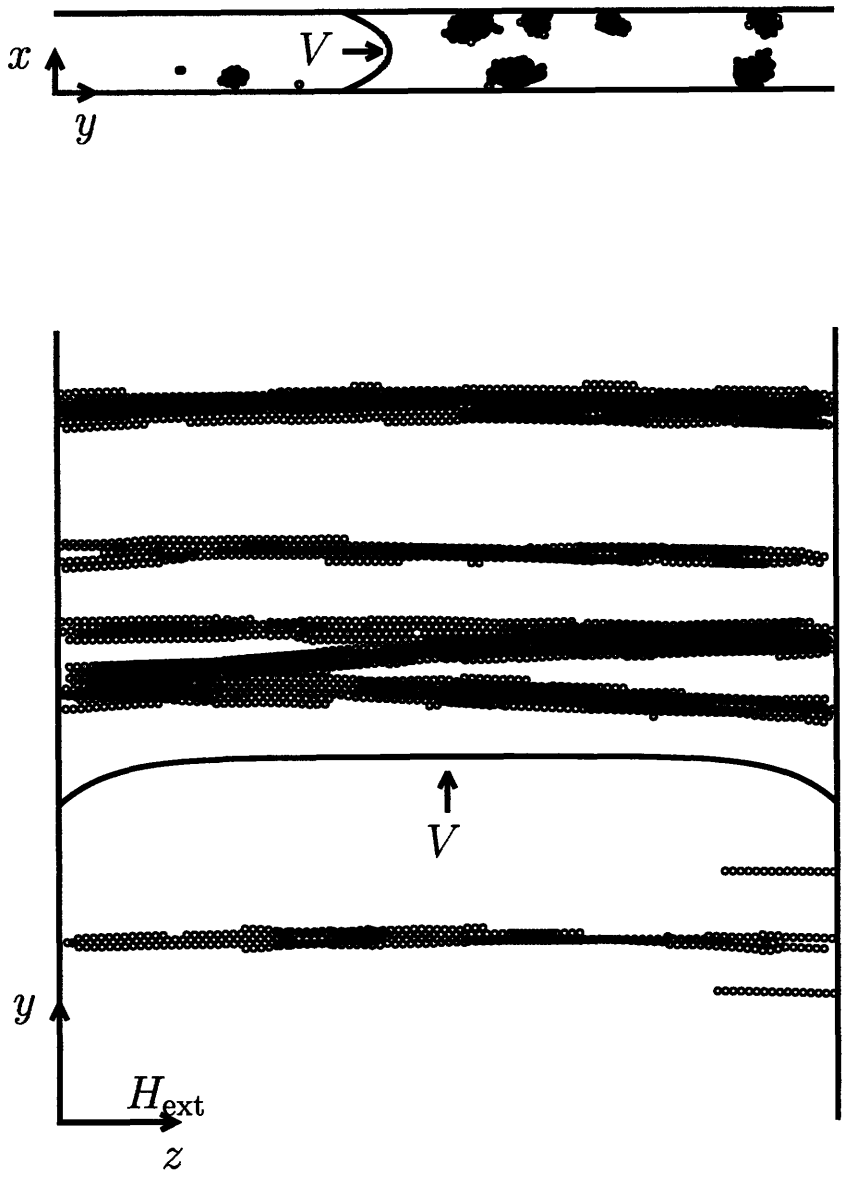

Fig. 5.1: *Schematic of the system for studying the self-assembly of dilute MR fluids under the application of pressure driven flow. There are hard walls in the z-direction and the x-direction and the y-direction has periodic boundary conditions. The flow is in the y-direction and the uniform external magnetic field is in the z-direction. The MR colloids form structures that span the channel in the z-direction and are convected in the y-direction. Top: Cross-section of the channel in the x-y plane where the positive z-direction is into the page. Bottom: Cross-section of the channel in the y-z plane where the positive x-direction is into the page.*

the expression [118]

$$\mathbf{V}(\mathbf{r}_i(t)) = 6v_{\text{avg}} \left[\begin{array}{l} \left(\dfrac{\mathbf{r}_i(t)\cdot\mathbf{e_x}}{L} - \dfrac{(\mathbf{r}_i(t)\cdot\mathbf{e_x})^2}{L^2} \right) \\ -\displaystyle\sum_{n=0}^{\infty} \frac{(-1)^n}{\lambda_n^3} e^{-\lambda_n(\mathbf{r}_i(t)\cdot\mathbf{e_z})/L} \cos\left(\lambda_n \frac{\mathbf{r}_i(t)\cdot\mathbf{e_x} - L/2}{L} \right) \\ -\displaystyle\sum_{n=0}^{\infty} \frac{(-1)^n}{\lambda_n^3} e^{-\lambda_n(W-\mathbf{r}_i(t)\cdot\mathbf{e_z})/L} \cos\left(\lambda_n \frac{\mathbf{r}_i(t)\cdot\mathbf{e_x} - L/2}{L} \right) \end{array} \right] \mathbf{e_y}, \tag{5.1}$$

where $L = 10d$ is the height of the channel in the x-direction, $W = 100d$ is the width of the channel in the z-direction, v_{avg} is the average bulk fluid velocity in the y-direction, and λ_n is given by

$$\lambda_n \equiv \left(n + \frac{1}{2} \right) \pi. \tag{5.2}$$

The form of the velocity profile is shown in Fig. 5.1 for both the x-y plane (top) and in the y-z plane (bottom) along the centerline of the channel in the z- and x-directions respectively. We have assumed that the presence of the colloids in the fluid does not disturb the velocity profile given by Equation 5.1 and we have neglected the hydrodynamic interactions between the colloids and the hard-walls. This method has been used successfully in the literature to simulate the self-assembly of field-responsive fluids in flow [119].

The MR colloids were modeled as hard spheres with an induced point dipole at their centers. Again, the interaction energy between two MR colloids U_{ij} is given by Equation 1.10. *In this study we have assumed a large magnitude external magnetic field ($\lambda \gg 1$) and a large magnitude average velocity ($Pe \gg 1$, where Pe is the Peclet number) such that we can neglect the thermal motion of the MR colloids.* The equation of motion for a single colloid in our system was thus given by

$$\mathrm{d}\mathbf{r}_i(t) \simeq \mathbf{V}(\mathbf{r}_i(t))\mathrm{d}t + \frac{1}{\zeta} \sum_{i \neq j}^{N} -\nabla U_{ij} \mathrm{d}t, \tag{5.3}$$

where the inertia of the colloids is neglected and, for simplicity, we neglect the hydrodynamic interactions between colloids. The parameter ζ is the Stokes drag coefficient on a single colloid. For this system, we have made lengths dimensionless with the colloid diameter d and times have been made dimensionless as $\widetilde{t} = t(3U_0)/(2d^2\zeta)$ where $(2d^2\zeta)/(3U_0)$ is the time it takes a colloid to move a distance d due to its magnetic interaction with another colloid. The parameter U_0 is the natural energy scale for this system defined as $U_0 \equiv -U_{ij}(d,0) = \pi\mu_0 d^3\chi^2 H_{\text{ext}}^2/72$ which is the magnitude of the energy between two touching colloids aligned head to tail. Using this set of length, time, and energy scales Equation 5.3 is re-written in dimensionless form as

$$\mathrm{d}\widetilde{\mathbf{r}}_i(\widetilde{t}) \simeq \mathrm{Ma}\widetilde{\mathbf{V}}(\widetilde{\mathbf{r}}_i(\widetilde{t}))\mathrm{d}\widetilde{t} + \frac{2}{3} \sum_{i \neq j}^{N} -\widetilde{\nabla}\widetilde{U}_{ij} \mathrm{d}\widetilde{t} \tag{5.4}$$

where the Mason number (Ma) for this system is defined as

$$\mathrm{Ma} \equiv \frac{2d\zeta v_{\mathrm{avg}}}{3U_0} = \frac{144\eta v_{\mathrm{avg}}}{d\mu_0\chi^2 H_{\mathrm{ext}}^2}. \tag{5.5}$$

At a time of zero, the MR colloids were placed in the simulation box at random positions. In this study, we investigated the self-assembly of an MR fluid with a volume fraction of $\phi = 0.025$ and therefore the number of colloids in our simulations was 4,775. The simulation was integrated forward in time using the simple Euler integration scheme with a defined Ma. At the end of a time step, hard sphere overlaps were removed using the Displacement Algorithm described in Chapter 2. The dimensionless time step used in these simulations was $\Delta\widetilde{t} = 0.01$ and a dimensionless cutoff distance of 27 was used for the magnetic interactions. Since we have neglected Brownian motion in this study, the simulations were deterministic meaning that the results of a single simulation did not have statistical noise but instead were determined by the Mason number and the starting configuration of the colloids. Therefore, we performed six simulations with different starting configurations at every Ma in order to ensure a good statistical sampling of the system. All of the starting configurations gave qualitatively indistinguishable results.

5.3 Cluster Growth

The kinetics of aggregation in dilute MR fluids have been characterized in the case of no flow by tracking the average cluster-size as a function of time [117]. Typically, the aggregation of the MR colloids in a dilute MR fluid occurs head-to-tail and therefore long chains of colloids form in time. The cluster-size grows with a power-law dependence on time in the no-flow case of diffusion limited aggregation [117]. In Fig. 5.2 we show the average cluster-size as a function of dimensionless time in our system for five different values of Ma. The average cluster-size is defined as $\langle c \rangle \equiv N/N_{\mathrm{c}}$ where N is the number of colloids in our simulations and N_{c} is the number of clusters. A cluster is defined as a continuously connected group of colloids where two colloids are considered to be connected if they are in hard-sphere contact.

In Fig. 5.2 several interesting observations can be made. At short times ($\widetilde{t} < 10$) the behavior of the system (as far as growth-rate of clusters) is independent of Ma. For longer times, as Ma is increased from 0.0 to 1.0, the growth-rate increases implying that the formation of clusters occurs at an increased rate for higher Ma. However, for Ma=1.0 at long dimensionless times ($\widetilde{t} > 400$) the power-law of the growth-rate shrinks to near zero and the average cluster-size remains constant. The growth-rate of clusters for Ma=0.001 is indistinguishable from the growth-rate at Ma=0.0 over the range of dimensionless times shown in Fig. 5.2. The mechanisms and behavior inherent in these three important observations will be discussed in the following section.

5.3.1 Modes of Aggregation

The formation of a connection between two colloids can occur head-to-tail as mentioned or, in the case of "zipped" chains, can occur laterally. These two types of connections, vertical and horizontal respectively, are illustrated in Fig. 5.3. Two colloids are considered to be in vertical contact if they are touching and the angle made by the vector connecting their centers and the external field vector is $\theta \leq 30$ or $\theta \geq 150$ [9]. Likewise, two colloids are in horizontal contact if they are touching and $30 < \theta < 150$ [9].

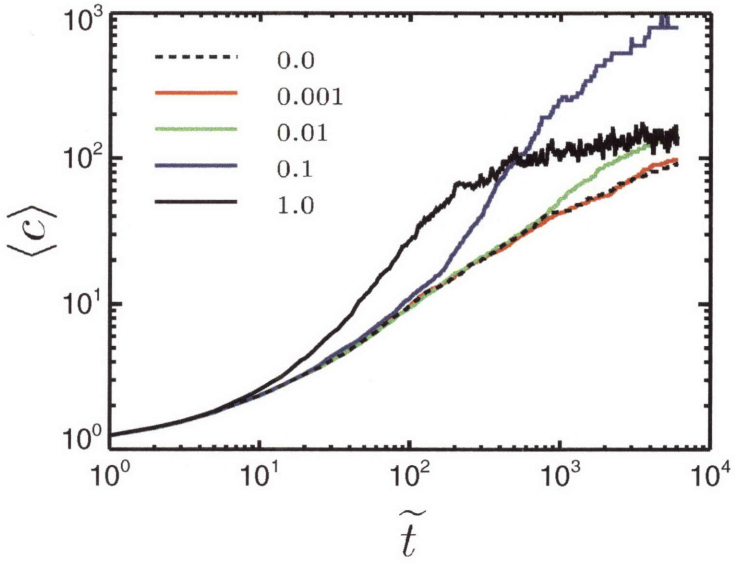

Fig. 5.2: *Average cluster size as a function of dimensionless time for an MR fluid with* $\phi = 0.025$ *at five different values of Ma. The black dashed line represents the cluster growth-rate when there is no bulk-flow.*

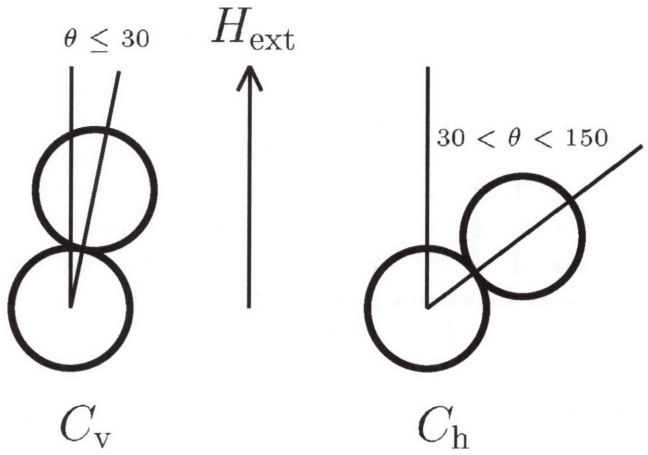

Fig. 5.3: *Left: A connection is considered vertical if* $\theta \leq 30$ *or* $\theta \geq 150$. *Right: A connection is considered horizontal if* $30 < \theta < 150$.

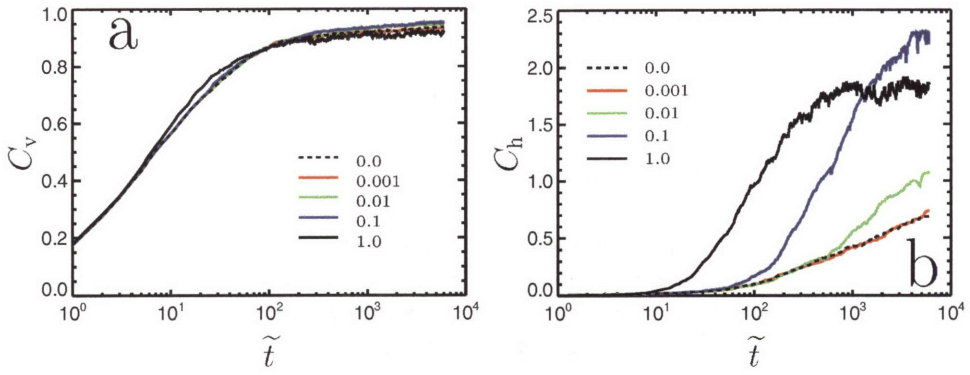

Fig. 5.4: *(a) Vertical connectivity as a function of dimensionless time for five different values of Ma. (b) Horizontal connectivity as a function of dimensionless time for five different values of Ma. The black dashed lines represent the connectivity growth-rate when there is no bulk-flow.*

The vertical connectivity is defined as

$$C_{\mathrm{v}} = \frac{N_{\mathrm{v}}}{N-1} \tag{5.6}$$

where N_{v} is the number of vertical connections in the system. The parameter C_{v} can vary between 0 and 1. The horizontal connectivity is defined as

$$C_{\mathrm{h}} = \frac{N_{\mathrm{h}}}{N-1} \tag{5.7}$$

where N_{h} is the number of horizontal connections in the system. The parameter C_{h} can vary between 0 and 3. These two parameters, C_{v} and C_{h}, will prove important in understanding the mechanisms of aggregation under the application of pressure driven flow. In Fig. 5.4 we show the vertical and horizontal connectivity as a function of time for the same five Mason numbers shown in Fig. 5.2. The connectivity behavior illuminates the aggregation mechanisms leading to the behavior observed in Fig. 5.2. For instance, the vertical connectivity as a function of time is fairly independent of Ma. This implies that vertical connections are formed in this system at the same rate regardless of the flow velocity (v_{avg}). This is in contrast to the experimental study of Brunet et al. [120] who studied the growth-rate of a chain of MR colloids when the external magnetic field and the flow were in the same direction. In this study the authors found that the chain growth, by vertical connections, was dependent upon the flow rate of the bulk fluid.

At long times ($\widetilde{t} > 200$), the vertical connectivity reaches a plateau as almost all of the possible vertical connections have been made by this time. In contrast, the horizontal connectivity (Fig. 5.4b) remains at a value of zero for $\widetilde{t} \lesssim 10$ at all values of Ma. At longer times, the growth-rate of the horizontal connectivity depends upon Ma in the same manner as the cluster-size, increasing rates for increasing Ma. The plateau in the horizontal connectivity only occurs for Ma=1.0 over the range of dimensionless times shown in Fig. 5.4, similar to the cluster-size as a function of time.

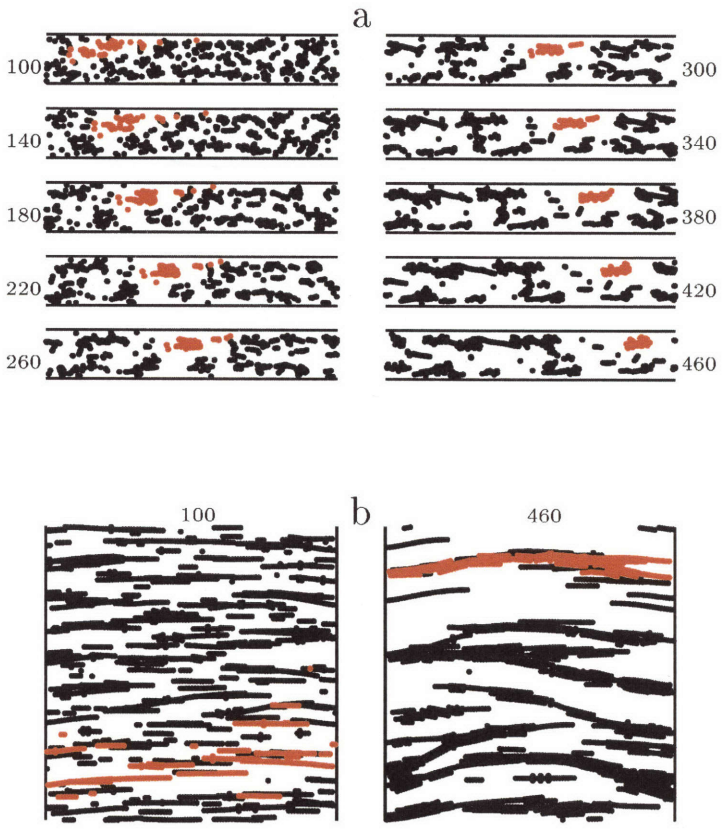

Fig. 5.5: *(a) Snapshots in time of the configuration of colloids in the x-y plane at* $Ma = 0.1$*. The flow is parabolic from left to right and the external magnetic field is directed into the page. (b) Top-view snapshots of the thin-slit channel in the y-z plane for the first and last times shown in (a). The flow direction is upwards and the magnetic field is directed left to right. The colloids marked in red evolve from a set of dispersed chains into a single cluster over dimensionless time shown in the snapshots.*

Again, the connectivity growth-rates for Ma=0.001 are indistinguishable from the growth-rates at Ma=0.0 over the range of dimensionless times shown in Fig. 5.4.

The combination of the horizontal and vertical connectivity data help to explain the salient features in Fig. 5.2. At short times, there are only vertical connections being made and they are

independent of the bulk fluid velocity. Therefore, for all values of Ma, the cluster growth-rate is identical. However, at intermediate times the horizontal connectivity becomes non-zero and the fluid velocity becomes important. This increase in horizontal connectivity is a secondary process driven by the interactions between co-flowing chains of MR colloids. The mechanism of the growth of the horizontal connectivity is due to the zippering of chains flowing past one another and is illustrated in Fig. 5.5. Recall from Fig. 5.1 (top) that the pressure driven flow profile in the x-y plane is parabolic. Therefore, chains at different x-positions in the channel experience different bulk fluid velocities. In Fig. 5.5 we show several snapshots in time of the x-y plane at Ma=0.1. As the dimensionless time increases from 100 to 460 the chains marked in red in Fig. 5.5 flow past one another, aggregating to form the large cluster depicted in the snapshot at $\widetilde{t} = 460$.

When two chains pass one another in the bulk flow, if they are close enough together and their relative velocities are small enough they can aggregate laterally creating several horizontal connections. This "shear assisted aggregation" should therefore depend upon the average velocity in the system. In Figs. 5.2 and 5.4b the horizontal aggregation is clearly dependent upon the flow rate in the system. Contrary to the vertical connections, this mechanism is similar to the work of Brunet et al. [120] where the ratio of the magnetic attraction to the shear forces (relative velocity) dictates whether or not a flowing colloid can aggregate with the chain of MR colloids. The fact that lateral aggregation is dependent upon the flow rate in this system as opposed to head-to-tail aggregation in the work of Brunet et al. has to do with the different orientations of the external magnetic field and the flow velocity (orthogonal versus parallel).

The two timescales for the formation of clusters are further illustrated for Ma=0.1 in Fig. 5.6 where we show several top-view snapshots of the configuration of colloids in the microchannel. For $\widetilde{t} \leq 50$ (Figs. 5.6a to c) only the vertical connectivity is increasing and therefore the cluster formation is only occurring head-to-tail. In Fig. 5.6d at $\widetilde{t} = 100$ the system consists of many single chains of MR colloids that have only begun to aggregate laterally. At the later time of $\widetilde{t} = 1000$ in Fig. 5.6e, more chains have aggregated laterally and therefore the average cluster-size is increased. At very long dimensionless times such as $\widetilde{t} = 5000$ in Fig. 5.6f, the larger clusters continue to aggregate laterally, increasing both the horizontal connectivity and the average cluster-size.

The plateau that occurs in both the average cluster-size and the horizontal connectivity for Ma=1.0 is due to the following mechanism. Larger values of Ma physically imply stronger flow forces versus the magnetic forces in the system. We have shown that chains of MR colloids will form in this system regardless of the flow rate for the range of Ma we have studied. As a secondary process those chains will aggregate laterally to form larger clusters. However, if the flow forces are so strong that they can shear clusters apart then the system reaches a steady-state where clusters are constantly forming and breaking due to the competing effects of the magnetic forces and the flow forces. A similar effect has been observed in the case of rotating chains of MR colloids when the frequency of the rotating magnetic field is increased above a certain threshold [112].

This steady-state region is the cause of the plateaus for Ma=1.0 in Figs. 5.2 and 5.4b. The steady-state is further illustrated in Fig. 5.7 where top-view snapshots of the microchannel are shown for Ma=1.0 at the same dimensionless times as those in Fig. 5.6. This series of snapshots shows some qualitative similarities and differences compared with those in Fig. 5.6. For $\widetilde{t} \leq 10$ the two sets of snapshots look very similar for Ma=0.1 and Ma=1.0. However, for $\widetilde{t} \geq 50$ the horizontal connectivity begins to increase for Ma=1.0 and the snapshots in Figs. 5.7c to f look very different from those in Figs. 5.6c to f. At long times, the clusters that form for Ma=1.0 can not span the width of the channel in the z-direction as they do for the Ma=0.1 case. In Fig. 5.1 (bottom), the

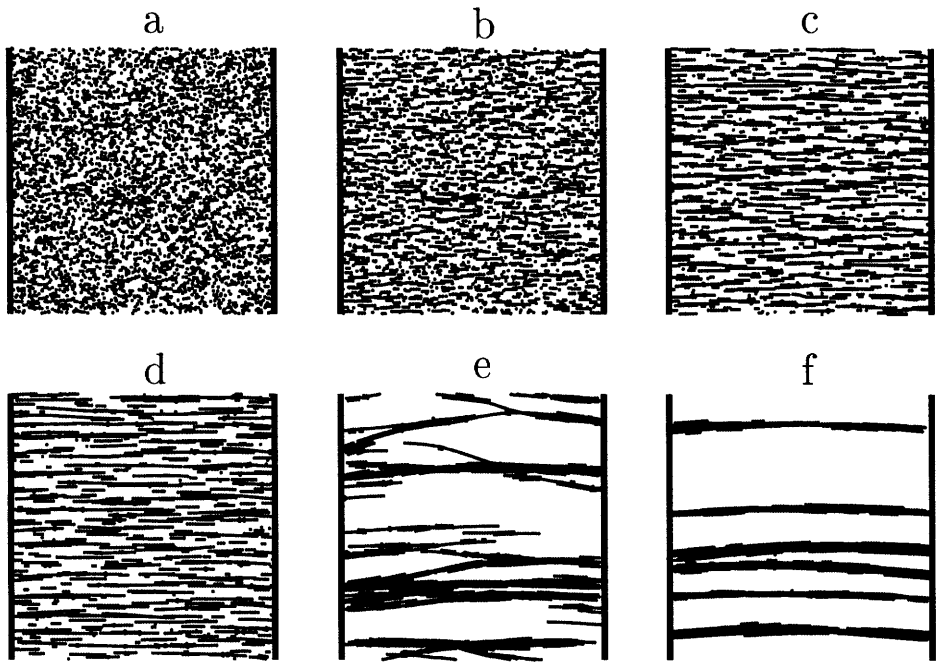

Fig. 5.6: *Snapshots of the microchannel in the y-z plane for a system with* $Ma = 0.1$ *at dimensionless times of (a)* $\widetilde{t} = 1$, *(b)* $\widetilde{t} = 10$, *(c)* $\widetilde{t} = 50$, *(d)* $\widetilde{t} = 100$, *(e)* $\widetilde{t} = 1000$, *and (f)* $\widetilde{t} = 5000$. *The channel walls in the z-direction are depicted as solid lines.*

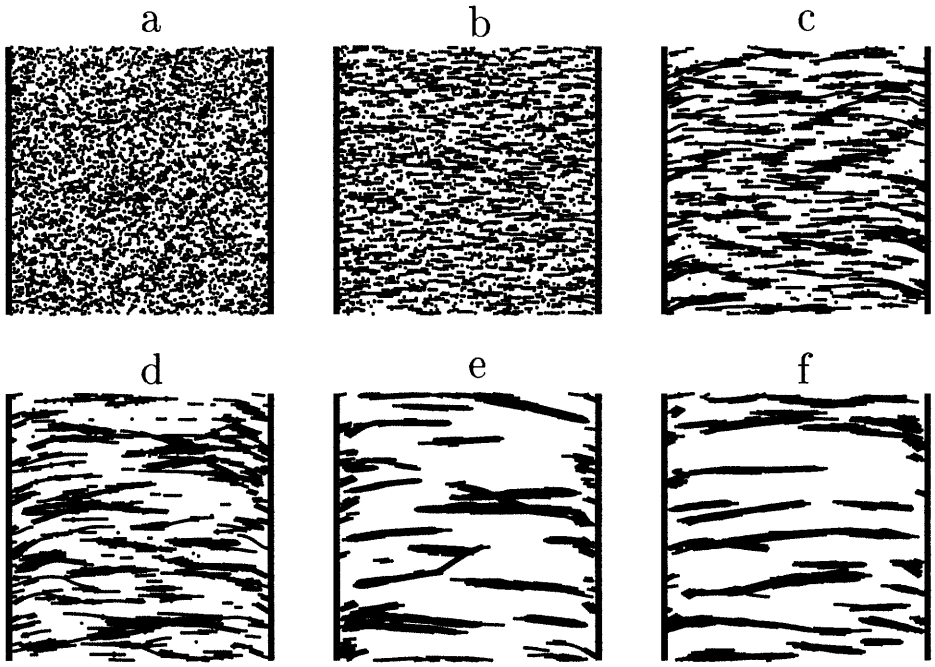

Fig. 5.7: *Snapshots of the microchannel in the y-z plane for a system with* $Ma = 1.0$ *at dimensionless times of (a)* $\widetilde{t} = 1$, *(b)* $\widetilde{t} = 10$, *(c)* $\widetilde{t} = 50$, *(d)* $\widetilde{t} = 100$, *(e)* $\widetilde{t} = 1000$, *and (f)* $\widetilde{t} = 5000$. *The channel walls in the z-direction are depicted as solid lines.*

velocity profile in the y-z plane has large gradients near the walls. These gradients in the velocity profile cause the clusters to experience shear forces along their length. When the shear forces are small they just cause the steady configuration of the clusters to appear bent in the flow direction (Fig. 5.6f). However, if the shear forces are large enough to break the clusters apart then the "shear induced breaking" leads to the steady-state configuration depicted in Figs. 5.7e and f. In these two snapshots, separated by significant lengths of time, the qualitative nature of the clusters in the system does not change, implying steady-state due to shear induced breaking of the clusters.

Due to the periodic boundary conditions in the flow direction and the finite number of colloids N, as time approaches infinity we expect that for lower values of Ma ($\text{Ma} \leq 0.1$) there should also be a plateau in the cluster-size and horizontal connectivity as a function of time, albeit due to a different mechanism than the one just described. For the lower Mason numbers, eventually all of the colloids will be incorporated into a few large clusters that do not break apart under the pressure induced flow, therefore causing a plateau in the cluster-size as a function of time. This process clearly has not occurred by a dimensionless time of 6000 since the average cluster-size is still increasing in the system with $\text{Ma} \leq 0.1$ (Fig. 5.2).

The value of Ma where shear induced breaking was found to be significant was $\text{Ma} \geq 0.25$. This result is shown in Fig. 5.8 where we plot the average cluster-size at a dimensionless time of $\widetilde{t} = 6000$ as a function of Ma. Clearly, for $\text{Ma} \leq 0.075$ the average cluster-size increases as a

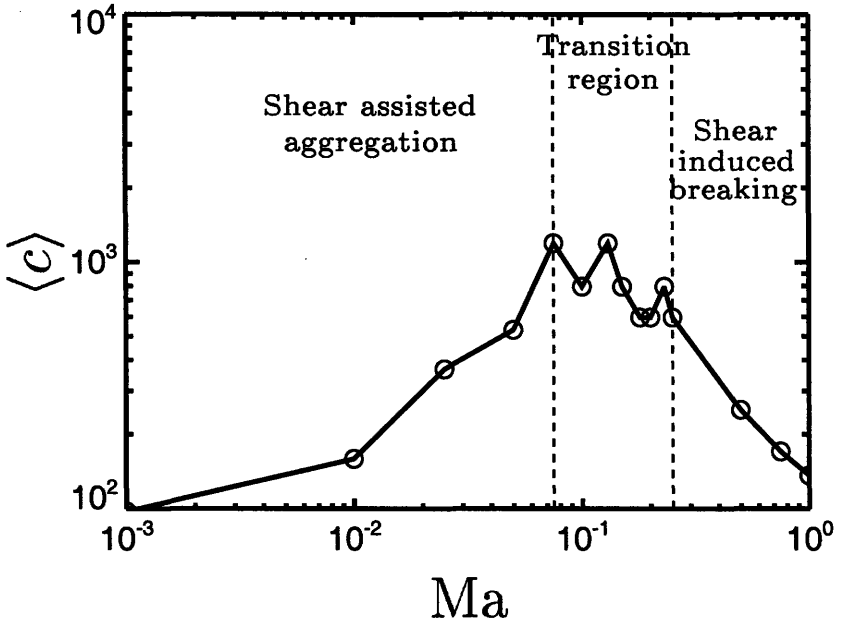

Fig. 5.8: *Average cluster-size as a function of Ma at a dimensionless time of* $\widetilde{t} = 6000$. *The solid line connects the symbols and is only to guide the eye. The shear assisted aggregation, transition region, and shear induced breaking ranges are separated by the vertical dashed lines.*

function of Ma. This is consistent with the observation that chains aggregate laterally by zippering when they flow past one another (Fig. 5.5). The higher the Mason number, the more frequently chains will pass each other and be given the opportunity to aggregate laterally. For $\text{Ma} \geq 0.25$ the average cluster-size decreases as a function of Ma. This too is consistent with the description of shear induced breaking causing a steady-state cluster-size where large aggregates can not exist due to the strong flow forces present in the system. When $0.075 < \text{Ma} < 0.25$ the average cluster-size remains constant as a function of Ma in Fig. 5.8. This range of Mason numbers is the transition region between the shear assisted aggregation and the shear induced breaking regions at low and high Ma respectively.

5.3.2 Flow Rate Dependence

In the shear assisted aggregation regime the growth-rate of the horizontal connectivity was shown in Fig. 5.4b to depend upon the flow rate in the system. This is further illustrated in Fig. 5.9a where the horizontal connectivity as a function of time is plotted for a range of Ma in the shear assisted aggregation and transition regions. The important phenomenon in shear assisted aggregation is the change in velocity from zero at the walls to its maximum value at the center of the channel in the x-direction. If we therefore scale the dimensionless time with this shear rate (or multiply $\widetilde{t}$ by $3\text{Ma}/\widetilde{L}$) then we can capture the flow rate dependence of the shear assisted aggregation. The multiple $3\widetilde{t}\text{Ma}/\widetilde{L}$ is simply a re-scaling of time such that $\widetilde{t}^* = 3\widetilde{t}\text{Ma}/\widetilde{L} = (1.5v_{\text{avg}})/(L/2)t$. In

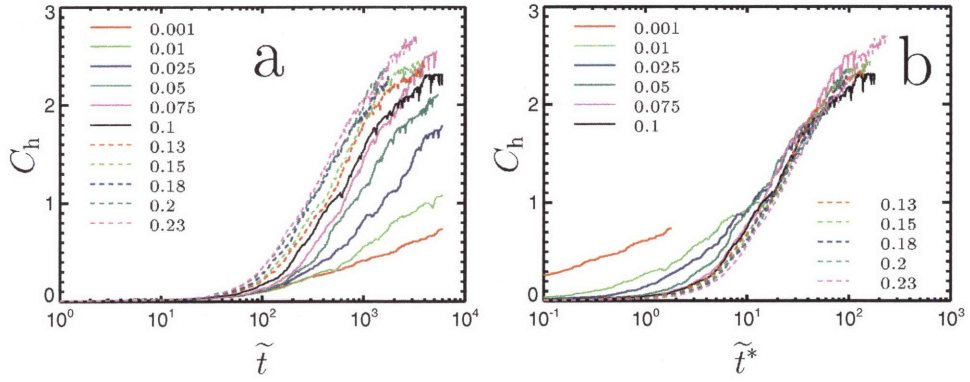

Fig. 5.9: *(a) Horizontal connectivity as a function of dimensionless time for a variety of Mason numbers in the shear assisted aggregation and transition regions. (b) Horizontal connectivity as a function of scaled dimensionless time where* $\widetilde{t}^* = 3\widetilde{t}Ma/\widetilde{L} = (1.5v_{avg})/(L/2)t$ *for the same values of Ma from (a).*

Fig. 5.9 we show how the dimensionless time $\widetilde{t}^*$ is able to capture the flow rate dependence of the horizontal connectivity growth in the shear assisted aggregation and transition regimes. The collapse of the curves in Fig. 5.9b implies that the growth of the horizontal connectivity depends linearly on the average velocity of the bulk fluid in this system.

The growth behavior of the horizontal connectivity in the shear induced breaking region is also dependent upon the flow rate. In Fig. 5.10a we show the horizontal connectivity as a function of dimensionless time for values of Ma in the shear induced breaking region. Again, if we scale the dimensionless time in order to take account of the flow rate dependence, we see that the horizontal connectivity curves in the shear induced breaking region also collapse (Fig. 5.10b). This implies that the horizontal connectivity behavior of the system is also linearly proportional to the average velocity of the bulk fluid in the shear induced breaking region. The curves in Fig. 5.10b have also been normalized by the plateau value of the horizontal connectivity C_h^* in order to show their self-similar nature.

5.4 Discussion

We have shown that the self-assembly of MR fluids under pressure driven flow in a thin-slit microchannel with a uniform external magnetic field directed orthogonal to the flow direction is a two-step process in time. At short times, the MR colloids attract each other head-to-tail and form chain-like aggregates and the rate of formation is independent of the flow rate. The chains that form are convected down the channel and because of the parabolic nature of the Poiseuille flow in the x-direction, chains can experience different velocities. As the chains flow past one another, they aggregate laterally to form larger clusters in a process that is highly dependent upon the bulk fluid flow rate. This shear assisted aggregation occurs for $Ma \lesssim 0.1$. The existence of two de-coupled time scales for the structure formation process in this system implies that the curves in Fig. 5.2 can not be collapsed using a single scaling. At short times, the magnetic time scale is important

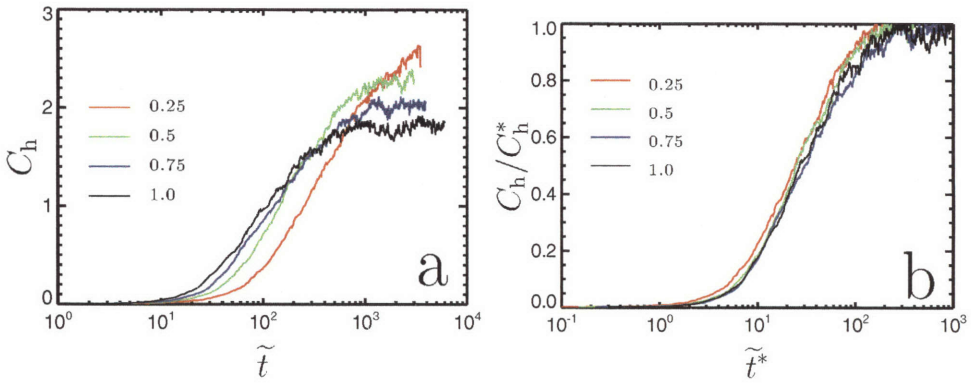

Fig. 5.10: *(a) Horizontal connectivity as a function of dimensionless time for a variety of Mason numbers in the shear induced breaking region. (b) Normalized horizontal connectivity as a function of scaled dimensionless time where* $\widetilde{t}^* = 3\widetilde{t}Ma/\widetilde{L} = (1.5v_{avg})/(L/2)t$ *for the same values of Ma from (a).*

but at longer times, the flow time scale dominates.

At large values of Ma, the clusters that form can not span the width of the channel in the field direction because of the large shear rates near the walls. The fluid flow in these cases acts to break the clusters apart resulting in a steady-state average cluster-size that decreases with increasing Ma. This shear induced breaking region occurs for Ma $\gtrsim 0.25$. In between the shear assisted aggregation and shear induced breaking regions, the system is in a transition region where the long-time average cluster-size is not dependent upon the flow rate of the bulk fluid.

Our results are similar to some of the previous work done on self-assembly of MR fluids in flow. As in the case of Brunet et al. [120] we have found that aggregation of MR colloids in the flow direction depends upon the flow rate in the system. In our case this corresponds to lateral aggregation of chains while in their work, the chains and flow were oriented in the same direction so the aggregation of the colloids was head-to-tail. Additionally, we have found that above a threshold value of Ma ≈ 0.25 the clusters will break due to the high shear rates present in the system. This is similar to the results for chains of MR colloids subjected to a rotating magnetic field where there is a threshold frequency for the external field (corresponding to a threshold value of Ma) above which the chain of colloids will break due to shear forces [112].

5.5 Outlook

A point that has not been made in this chapter is the following. One could conceivably perform a force balance on a cluster spanning the width of the channel in order to determine its steady-state shape in the pressure driven flow and at which flow rate it is expected to break apart. This would elucidate some of the physics of the transition from shear assisted aggregation to shear induced breaking of the clusters. Another point of interest is illustrated in Fig. 5.1 (top) where the few large clusters are seen to repel one another such that they flow only along the bottom and top surfaces of the thin-slit channel. This repulsion was discussed in Chapter 4 and therefore the

configuration in Fig. 5.1 is not surprising. However, it is well known that concentrated colloidal suspensions will undergo shear induced migration away from regions of high shear [121]. This shear induced migration is due to the hydrodynamic interactions between the colloids and between the colloids and the wall. This mechanism is absent in the simulations presented here and therefore it is not possible to observe shear induced migration with the simulation technique of this chapter. However, even though the MR fluid we have studied is dilute ($\phi = 0.025$) the clusters are locally concentrated areas of colloids and therefore might be subject to shear induced migration. If this effect is important, it would work to counteract the magnetic repulsion causing the clusters to be pressed against the two walls in the y-z plane. This is a point of some interest which could be investigated further in the future.

CHAPTER 6

Pattern Assisted Cell Sorting

One unique property of MR fluids as structural components in microfluidic devices is their ability to be dynamic in nature. When exposed to an external force in addition to an external magnetic field, the structures can move while still maintaining their integrity. This can be a very useful property when designing microfluidic applications utilizing MR fluids as structural components. We present here an example of an application for MR fluid structures under the application of pressure driven flow in a microfluidic device. This work was done in collaboration with Daniel C. Pregibon.

6.1 Background

In recent years, the drive to develop microfluidic technologies for performing lab scale procedures has increased immensely [3, 4, 122]. Many of these new technologies utilize field responsive fluids as an integral structural component of the microfluidic devices [18, 123, 3, 19]. This promising area of research brings together the microstructures formed by field responsive fluids with the small scale geometries of microfluidic channels to create a new class of lab-on-chip technologies.

The microstructure of MR fluids have been well studied both experimentally [124, 99] and with simulations [97, 8]. The general result of all of these studies is that under the application of a uniform external magnetic field, MR fluids self-assemble into chain like structures aligned in the direction of the external field. As mentioned in Chapter 4, depending upon the volume fraction of colloids in the MR fluid, the chains can coalesce to form larger scale "labyrinth" structures (at high

volume fractions) or "column-like" structures (at low volume fractions). The confinement of MR fluids in microfluidic geometries has also been well studied [10, 11, 34, 35]. Confinement in the field direction helps to dictate the types of structures that will form (labyrinth versus columns) [10, 11] and confinement in one or two dimensions orthogonal to the external field determines the nature of the inter-cluster structure. The influence of confinement upon the structure can be useful for many microfluidic applications.

The isolation and separation of cells is of particular importance in the effort to develop microfluidic diagnostic and therapeutic tools. In particular, cancer therapies, pre-implantation diagnostics, and studies in basic cell science all rely upon the ability to isolate and separate cells of interest. Current approaches to cellular separations include flow cytometry [125, 126, 127, 128], surface affinity chromatography [129, 130], electrophoretic fractionation [131, 132], optical sorting [133], and immunomagnetic separations [134, 135, 136]. Immunomagnetic cell sorting has become very popular in the field due to its relative simplicity, low cost, and high specificity.

The immunomagnetic separation technique traditionally consists of a separate incubation step followed by the separation step. In the incubation step, a heterogeneous cell population is incubated with magnetic colloids decorated with an antibody that binds specifically to the surface marker of a target cellular phenotype. The separation is then performed by subjecting the cell-colloid mixture to a magnetic field gradient in either a batch or continuous fashion in order to separate the cells bound to the magnetic colloids [134, 135, 136, 137, 138]. The incubation step required in this assay, limits the true "continuous" operation of such devices. Even more importantly, the extended incubation time required (typically 15 to 30 minutes) may alter the physiology of the cells causing the results to be inaccurate. Therefore, there is a great need for an immunomagnetic cell separation device that combines the incubation (cell binding) and separation into a single step, thus improving both the speed and accuracy of chip-based diagnostic tools.

When exposed to an external magnetic field paramagnetic colloids will experience interactions due to their induced dipole moments. These interactions are responsible for structure formation in MR fluids and in the case of the immunomagnetic assays mentioned above the interactions will cause the magnetic colloids to form chains in the field direction. We propose here a new method for manipulating immunomagnetic colloids to achieve cell binding and sorting in a single microfluidic process. The method we present is based upon similar physics to those demonstrated by Inglis et al. [21], but has several advantages over the previous work. In particular, we propose to "guide" chains of paramagnetic colloids along magnetic rails that have been fixed to the bottom surface of a microfluidic channel [139]. The general scheme is presented in Fig. 6.1 where the magnetic chains, cell mixture, and buffer are introduced to the microfluidic device separately and exposed to a uniform magnetic field normal to the bottom surface of the channel. The driving force for motion of the three streams down the channel is pressure driven flow. Due to the laminar flow, the three streams will only mix by diffusion under normal circumstances. However, the presence of the magnetic rails causes the chains of magnetic colloids to traverse the stream with the cell mixture where they can then capture the cells of interest and proceed to the clean buffer stream. This procedure has the advantage of being able to perform the separation in a single step with no batch incubation step required prior to the separation. As we will show, our method has the added advantage of "column arrest" where we can hold the chain of magnetic colloids fixed on the rail as the bulk fluid phase flows past thus increasing the amount of time that a chain can spend in contact with any of the three streams.

In order to characterize this system, we investigated the motion of a free-moving chain of

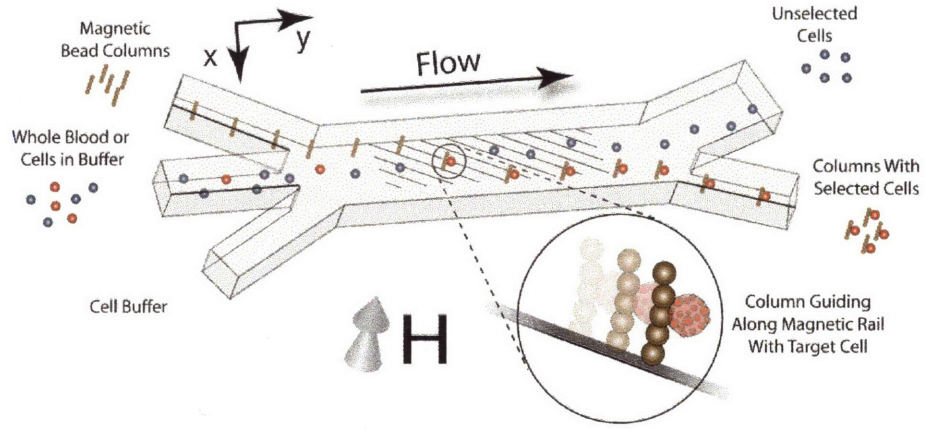

Fig. 6.1: *General scheme for magnetic pattern assisted cell sorting. Three streams are introduced into the microfluidic channel on the left hand side. As they co-flow down the channel the selected cells are captured and separated from the general population by magnetic chains traversing the width of the channel with the aid of patterned rails.*

magnetic colloids flowing in a thin-slit microfluidic channel past a single rail patterned to the bottom of the channel. The uniform external magnetic field was directed normal to the bottom surface of the channel causing the chain to align in the field direction. We varied the external magnetic field strength, bulk fluid velocity, and slit-thickness in order to determine their effects upon the behavior of the system. Additionally, we investigated the use of discrete colloid rails consisting of a line of magnetic colloids fixed on the bottom surface of the channel versus continuous rails consisting of a continuous strip of magnetic material fixed to the bottom surface of the channel. We determined that the operation of the device depends upon the type of rail, the slit-thickness, and the ratio of the magnetic field to the flow velocity.

6.2 Simulation Details

The system studied consisted of short chains of MR colloids interacting with a single "rail" of paramagnetic material patterned on the bottom surface of a thin slit microchannel. A uniform external magnetic field was applied in the z-direction (normal to the surface containing the rail) and a Poiseuille flow was applied in the y-direction. The thin slit simulation box consisted of hard walls in the z-direction and periodic boundary conditions in the x and y-directions. The rail was either modeled as a line of discrete MR colloids fixed to the bottom surface or as a continuous line of magnetic material with the same line-density of dipoles as the discrete rail case. Both of these cases are described below.

The bulk Poiseuille flow imposed a velocity $\mathbf{V}(\mathbf{r}_i(t))$ on a colloid located at $\mathbf{r}_i$ given by the expression

$$\mathbf{V}(\mathbf{r}_i(t)) = 6v_{\text{avg}}\left[\frac{\mathbf{r}_i(t)\cdot\mathbf{e_z}}{L} - \left(\frac{\mathbf{r}_i(t)\cdot\mathbf{e_z}}{L}\right)^2\right]\mathbf{e_y}, \tag{6.1}$$

where L is the height of the thin slit in the z-direction, $\mathbf{e_z}$ is the unit vector in the z-direction, and v_{avg} is the average velocity of the bulk fluid flow in the y-direction.

The MR colloids were modeled as hard spheres of diameter d with an induced point dipole at their centers. The interaction energy between two MR colloids U_{ij} is given by Equation 1.10. *In our model, we assume a large magnitude external magnetic field and a large Peclet number flow such that we can neglect the thermal motion of the MR colloids.* The equation of motion for a single colloid in our system was thus given by

$$\mathrm{d}\mathbf{r}_i(t) \simeq \mathbf{V}(\mathbf{r}_i(t))\mathrm{d}t + \frac{1}{\zeta}\left[\sum_{i\neq j}^{N} -\boldsymbol{\nabla}U_{ij} - \boldsymbol{\nabla}U_i^{\text{rail}}\right]\mathrm{d}t, \tag{6.2}$$

where the inertia of the colloids is neglected and, for simplicity, we neglect the hydrodynamic interactions between MR colloids. The parameter ζ is the drag coefficient on a single colloid, $-\boldsymbol{\nabla}U_{ij}$ is the force on colloid i due to its magnetic interaction with colloid j, and $-\boldsymbol{\nabla}U_i^{\text{rail}}$ is the force on colloid i due to its magnetic interaction with the rail. The form of U_i^{rail} will be discussed shortly.

In this system, lengths are made dimensionless as $\widetilde{r} = r/d$ and times are made dimensionless as $\widetilde{t} = v_{\text{avg}}t/d$ where d/v_{avg} is the time it takes for a colloid to convect a distance d due to the imposed flow v_{avg}. This timescale differs from the one introduced in Chapter 5 but is more useful for this study because we will only consider cases with non-zero v_{avg}. The natural energy scale for this system is defined as $U_0 \equiv -U_{ij}(d,0) = \pi\mu_0 d^3\chi^2 H_{\text{ext}}^2/72$ which is the magnitude of the energy between two touching colloids aligned head to tail. Taking this set of length, time, and energy scales Equation 6.2 is re-written in dimensionless form as

$$\mathrm{d}\widetilde{\mathbf{r}}_i(\widetilde{t}) \simeq \widetilde{\mathbf{V}}(\widetilde{\mathbf{r}}_i(\widetilde{t}))\mathrm{d}\widetilde{t} + \frac{2}{3\text{Ma}}\left[\sum_{i\neq j}^{N} -\widetilde{\boldsymbol{\nabla}}\widetilde{U}_{ij} - \widetilde{\boldsymbol{\nabla}}\widetilde{U}_i^{\text{rail}}\right]\mathrm{d}\widetilde{t}. \tag{6.3}$$

The dimensionless parameter in the second term on the RHS of Equation 6.3 is called the Mason number (Ma) and is a ratio of the flow forces to the magnetic forces in the system. The Mason number has been defined with different proportionality factors in the literature [116, 104, 114] but it is always the ratio of viscous forces to magnetic forces. In this study the Mason number is defined as

$$\text{Ma} \equiv \frac{2\zeta v_{\text{avg}}}{3U_0/d} = \frac{144\eta v_{\text{avg}}}{d\mu_0\chi^2 H_{\text{ext}}^2}. \tag{6.4}$$

The dimensionless size of the simulation box was set at $100 \times 500 \times \widetilde{L}$ and the initial conditions for each simulation were as follows. The magnetic rail was placed on the bottom surface of the channel such that it intersected the dimensionless coordinates $(1, 20, 0.5)$ and made an angle θ_{r} with respect to the x-axis. A chain of MR colloids aligned in the z-direction and containing N colloids, where $2 \leq N \leq \widetilde{L}$, was placed at the dimensionless coordinates $(50\cos\theta_{\text{r}} + 1, 10, 0.5)$ such that the bottom colloid in the chain was touching the bottom surface of the slit and it was located, in the x-direction, at the center of the rail.

Discrete rails. In the discrete case, the rail consisted of 100 MR colloids of diameter d stamped in a line to the bottom of the channel. The first colloid in the rail was located at the dimensionless coordinates $(1, 20, 0.5)$ and each subsequent colloid was located at the dimensionless positions $(1 +$

$(n-1)\cos\theta_r, 20 + (n-1)\sin\theta_r, 0.5)$. In this case, the colloids in the rail were identical to the colloids in the short chain and therefore the energy of interaction between colloid i in the short chain and the rail is simply

$$U_i^{\text{rail}}(\mathbf{r}_i) = \frac{\pi\mu_0 d^6\chi^2 H_{\text{ext}}^2}{144}\sum_{n=1}^{100}\frac{1-3\cos^2\theta_{in}}{r_{in}^3}. \tag{6.5}$$

Continuous rails. In the continuous case, the rail was modeled as an infinite line of paramagnetic material with an effective "line density" of dipoles equal to m/d due to the external magnetic field, where m is the dipole moment of a single MR colloid given by $m = (\pi d^3\chi H_{\text{ext}})/6$. As mentioned previously, the line of paramagnetic material was located in the dimensionless plane $\widetilde{z} = 0.5$. The energy of interaction between colloid i in the short chain and the continuous rail is given by

$$U_i^{\text{rail}}(\hat{\mathbf{r}}_i, \hat{\theta}_i) = \frac{\pi\mu_0 d^3\chi^2 H_{\text{ext}}^2}{144}\left(\frac{1-2\cos^2\hat{\theta}_i}{\hat{r}_i^2}\right), \tag{6.6}$$

where $\hat{r}_i$ is the dimensionless scalar magnitude of the shortest vector connecting colloid i and the rail defined as

$$\begin{aligned}\hat{\mathbf{r}}_i = &\left[\widetilde{x}_i - \frac{\widetilde{x}_i + \widetilde{y}_i\tan\theta_r + \tan\theta_r(\tan\theta_r - 20)}{1+\tan^2\theta_r}\right]\mathbf{e_x}\\ &+\left[\widetilde{y}_i - \frac{\tan\theta_r(\widetilde{x}_i + \widetilde{y}_i\tan\theta_r) + (\tan\theta_r - 20)}{1+\tan^2\theta_r}\right]\mathbf{e_y}\\ &+[\widetilde{z}_i - 1/2]\,\mathbf{e_z}\end{aligned} \tag{6.7}$$

and $\hat{\theta}_i$ is the angle made by the vector $\hat{\mathbf{r}}_i$ and the external field vector ($\mathbf{e_z}$).

After placing all of the colloids in the appropriate positions and defining Ma and θ_r for the system, the equation of motion was integrated forward in time using the Euler integration scheme. At the end of a time step, hard sphere overlaps were removed by using the Displacement Algorithm described in Chapter 2. The dimensionless time step used in these simulations was $\Delta\widetilde{t} = 0.01\text{Ma}$ ensuring that the displacement of a colloid during a time step was only a small fraction of d. Since we have neglected Brownian motion in this study, the simulations were deterministic meaning that the results of a single simulation did not have statistical noise but instead were determined by the system parameters ($\widetilde{L}$, θ_r, Ma). Therefore, only a single simulation was performed for each set of parameters.

6.3 Discrete Rails

Using lithographic techniques, one can affix a line of magnetic colloids to the bottom surface of a microfluidic channel [139]. In the case of our cell separation device, this line of magnetic colloids forms the discrete rail as in the case described above. When we consider the free chain of magnetic colloids to be of length $N = \widetilde{L}$ such that it spans the height of the thin-slit channel then we have observed that there are four general modes of behavior for the interaction between the chain and the patterned discrete rail. The chain of colloids can guide parallel to the rail without touching it (Guiding I), stick to the rail without moving (Sticking), guide along the rail by physically contacting

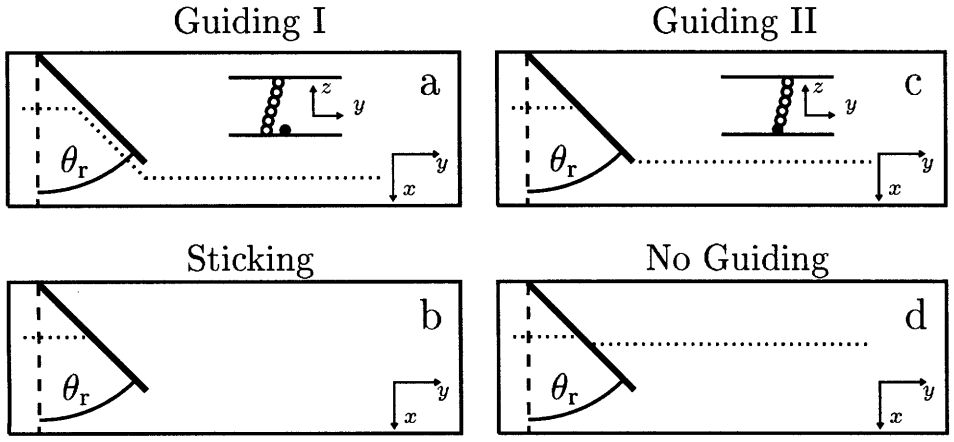

Fig. 6.2: *Four different modes of behavior for a chain of magnetic colloids flowing in the y-direction from left to right. (a) In the Guiding I mode, the chain guides parallel to the rail without touching it. The inset shows the configuration of the chain (open circles) and the rail (closed circle) in the Guiding I mode. (b) In the Sticking mode, the chain does not move along the rail but remains arrested as the bulk fluid flows past. (c) In the Guiding II mode, the chain mounts the rail and guides along the rail in physical contact. The inset shows the configuration of the chain (open circles) and the rail (closed circle) in the Guiding II mode. In the Guiding II mode, the chain can lose the bottom-most colloid when it mounts the rail thus the illustration in the inset only contains five magnetic colloids. (d) In the No Guiding mode, the chain does not remain in sustained contact with the rail but instead flows by without guiding.*

it (Guiding II), or be weakly affected by the presence of the rail and simply flow past it without guiding (No Guiding). The four different behaviors are illustrated in Fig. 6.2.

In the Guiding I mode (Fig. 6.2a), the bottom colloid in the chain feels a repulsive force from the rail that is much stronger than the flow force. The attractive interactions between the colloids in the chain cause it to remain connected in the z-direction and therefore it can not move past the rail. In this mode, the chain remains upstream of the rail and guides parallel to the rail without touching it (Fig. 6.2a inset). In the Sticking mode, the flow force experienced by the chain is able to overcome the repulsion between the rail and the bottom colloid in the chain causing the chain to mount the rail. During this mounting process, the chain can lose it's bottom colloid as illustrated in Fig. 6.3. Once the chain has mounted the rail, it experiences a complex potential energy landscape along the rail. This potential energy landscape arises from the anisotropic interactions between MR colloids. When the chain is directly between two of the colloids in the discrete rail it is in a local minimum of the potential energy and in order to proceed along the rail, the flow forces must be able to overcome the energy barriers.

This point is further illustrated in Fig. 6.3b where the chain experiences a portion of the flow force along the rail from left to right. If the flow force is not strong enough to overcome the potential energy barriers associated with moving along the rail then the chain will remain in the Sticking

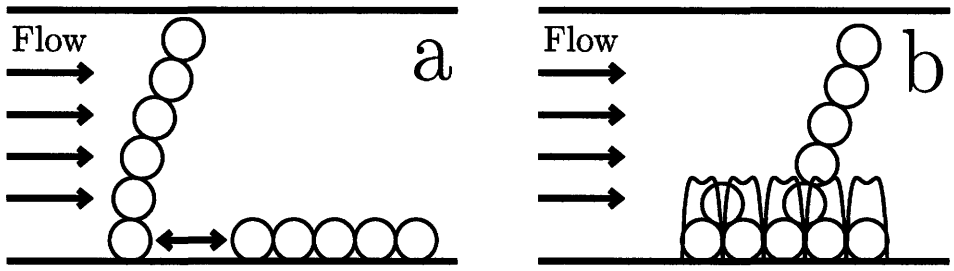

Fig. 6.3: *(a) An illustration of the forces acting upon the chain of magnetic colloids in the vicinity of the rail. The bottom colloid experiences a repulsion from the rail while the chain as a whole feels a driving force towards the rail from the bulk fluid flow. (b) When the chain has mounted the rail typically it loses it's bottom colloid in order to sit on top of the rail and still span the height of the microchannel. The chain feels the driving force due to the fluid flow but must overcome the potential energy barriers associated with moving along the rail. The form of the energy barriers is shown by the solid line.*

mode. If the flow forces are strong enough, then the chain will guide while in contact with the rail in the Guiding II mode. If the flow force is stronger still, then the chain breaks away from the rail and continues to flow down the channel without guiding. This is the No Guiding mode mentioned above. We have determined in which regions of phase space (Ma, $\widetilde{L}$, and θ_r) the different modes will dominate the behavior of the chain of magnetic colloids in this system. The trajectories of the chains (such as shown in Fig. 6.2) were used to determine the mode of behavior for a chain under a given set of conditions.

The phase diagram for the four modes of behavior when the chain of magnetic colloids spans the height of the channel is shown in Fig. 6.4 for three different dimensionless channel heights. The behavior of the chain is seen to depend upon the Mason Number (Ma), the channel height ($\widetilde{L}$), and the angle of the rail (θ_r). When the rail angle is very small ($\theta_r \leq 10$) the rail is almost perpendicular to the flow direction and therefore there is no range of Ma where the chain will guide in contact with the rail (Guiding II). The chain may be in the Guiding I mode for a very small range of Ma but otherwise it either sticks on the rail or does not guide at all. As the angle of the rail is increased ($10 < \theta_r \leq 65$) there are significant ranges of Ma where the chain can be in any of the four modes. The Guiding II region continues to grow over this range of rail angles and the Sticking region shrinks. For large rail angles ($\theta_r > 65$) the rail is almost parallel to the flow direction and the Guiding II region is the dominant region in Fig. 6.4. The Guiding I region also grows significantly over this range of rail angles but shows an additional dependence on the number of colloids in the chain. This indicates that the parameters NMa and θ_r do not uniquely define the behavior of the system at the Guiding I boundary.

6.3.1 Predicting the Phase Boundaries

Using simple force balances, we can predict where the boundaries will occur between the different modes of behavior in this system. For instance the boundary between the No Guiding mode and

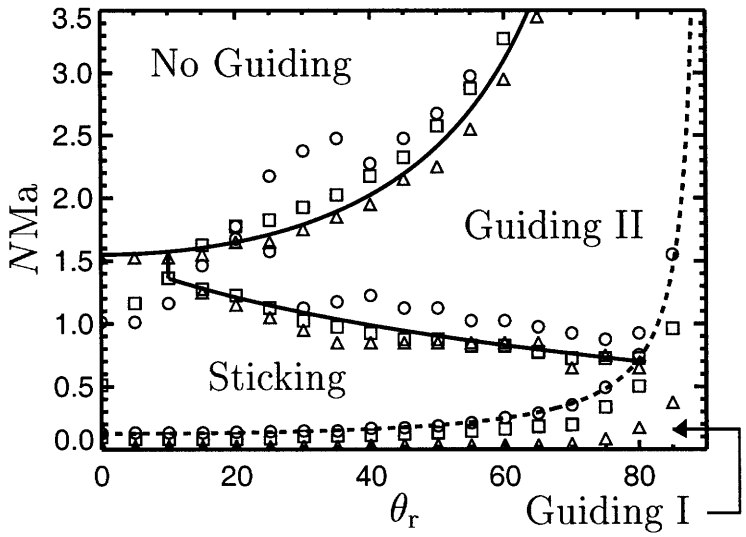

Fig. 6.4: *The phase diagram for the interaction between a chain of N magnetic colloids spanning the height of the microchannel and a discrete magnetic rail fixed to the bottom of the channel. The mode of interaction depends upon the chain length, rail angle, and ratio of flow to magnetic forces (Ma). The solid lines are the phase boundary predictions given by Equations 6.10 and 6.14 for the No Guiding/Guiding II and Guiding II/Sticking boundaries respectively. The dashed line is to guide the eye for the Guiding I/Sticking transition and has the form* $NMa = 0.125/\cos\theta_r$.

the Guiding II mode should occur when the flow forces perpendicular to the rail are larger than the magnetic forces attracting the chain to the rail. The path of a chain over the rail in the No Guiding mode is shown in Fig. 6.5 for three different rail angles θ_r. At all three angles, the chain leaves the rail by pulling off of the down stream edge of the rail. The flow forces perpendicular to the rail can be written as

$$F_{\perp}^{\text{Flow}} \propto N v_{\text{avg}} \zeta \cos\theta_r \tag{6.8}$$

since the bulk flow acts upon all of the colloids in the chain. The dominant magnetic force due to the rail is upon the colloid touching the rail since the magnetic force between two MR colloids decays with separation distance to the fourth power (Equation 2.5). Therefore the magnetic force on the chain due to the rail can be written as

$$F_{\perp}^{\text{Mag}} \propto (U_0/d) \tag{6.9}$$

Equating the expressions given in Equations 6.8 and 6.9 results in the following expression

$$N\frac{v_{\text{avg}}\zeta}{U_0/d} \propto N\text{Ma} = \frac{C_{\perp}}{\cos\theta_r} \tag{6.10}$$

where $C_{\perp}$ is an O(1) proportionality constant for this case. When $F_{\perp}^{\text{Flow}}$ and $F_{\perp}^{\text{Mag}}$ are approximately equal the chain will transition from the Guiding II mode to the No Guiding mode. We have found in our simulations that $C_{\perp}$ equals 1.55 for the Guiding II to No Guiding transition. This constant was determined by simulating the case $\theta_r = 0$ such that the entire flow force is opposed by the magnetic forces. The prediction given by Equation 6.10 is plotted as a solid line in Fig. 6.4.

Likewise, the phase boundary between the Sticking mode and the Guiding II mode should occur when the flow forces parallel to the rail are large enough to overcome the potential energy barriers to moving along the rail shown in Fig. 6.3b. The path of a chain along the rail in the Guiding II mode is shown in Fig. 6.5 for three different rail angles θ_r. When guiding along the rail, the chain hops from one potential energy well to another by passing over the intervening colloid. The resistance to guiding in this case will depend upon the detailed interactions between the bottom colloid in the chain and the two colloids on the rail between which it sits before hopping. A schematic of the geometry in this case is shown in Fig. 6.6 for a top-view (x-y plane - normal to the thin-slit) and a side-view (perpendicular to the rail). The position of the center of the bottom colloid in the chain is denoted by the filled circle in Fig. 6.6 and its position relative to the next "downstream" colloid in the rail is denoted by r, θ, and ϕ in spherical coordinates. The bottom colloid in the chain is constrained to be in contact with the downstream rail colloid and its force in the r direction is exactly countered by the hard-sphere repulsion.

In the case of the Sticking/Guiding II transition, the motion of the chain along the rail is quite complicated as it depends upon not only the magnetic and flow forces but also steric forces due to the hard-sphere repulsion. However, the boundary between these two regimes should be some combination of the two extreme limits $\theta_r \to 0$ and $\theta_r \to 90$. When $\theta_r \to 0$ the flow force is completely perpendicular to the rail and therefore it should be balanced by the magnetic forces perpendicular to the rail. We have already shown the form of that force balance in Equation 6.10. When $\theta_r \to 90$, the flow forces are entirely perpendicular to the rail. However, a portion of the flow force is normal to the downstream rail colloid's surface and is therefore cancelled by the hard-sphere

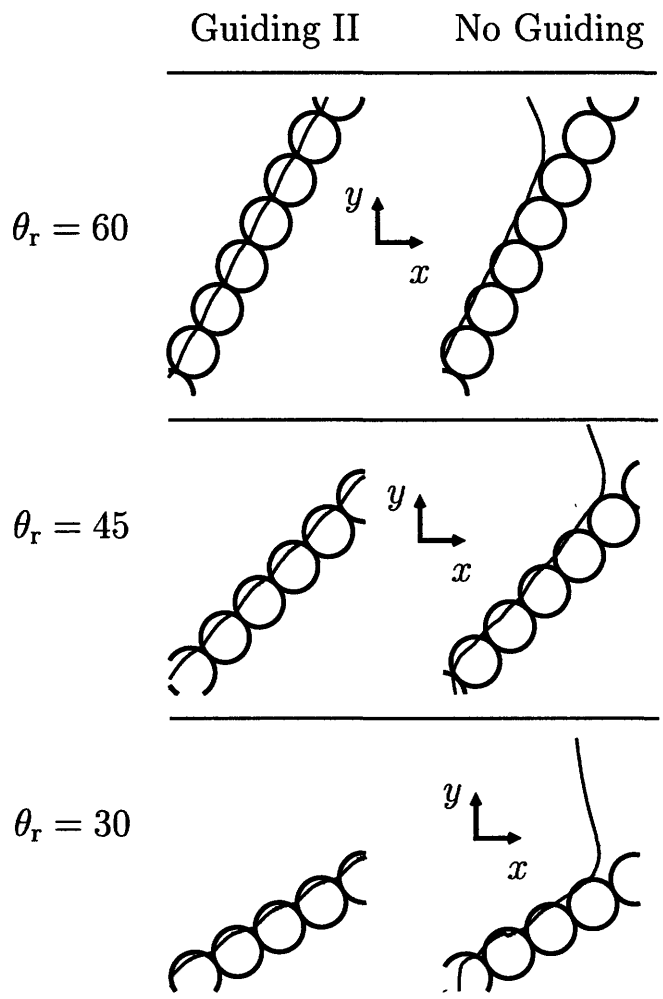

Fig. 6.5: *Trajectories of the chain along the rail in the Guiding II and No Guiding modes for three different rail angles. The colloids in the rail are depicted as circles and the trajectory of the chain is shown as a solid line.*

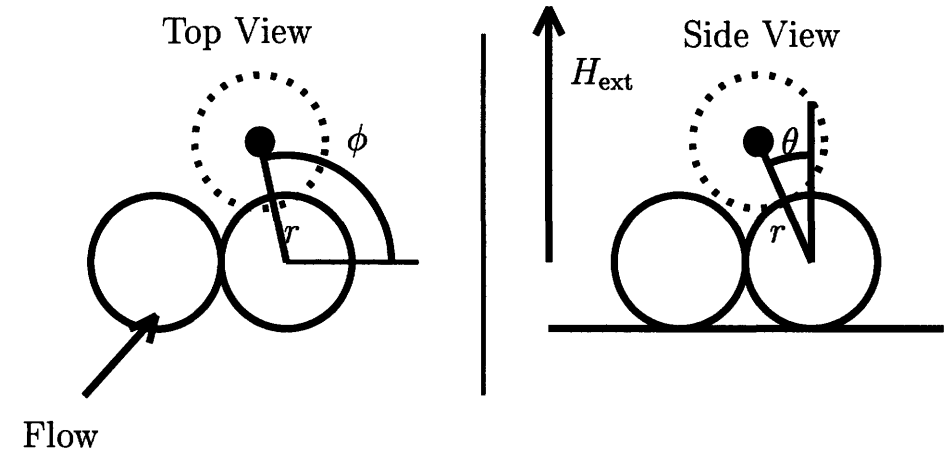

Fig. 6.6: *An exaggerated schematic of the local coordinate system between the chain and the discrete rail. The position of the center of the bottom colloid in the chain is denoted by the filled circle surrounded by a dashed circle. The local spherical coordinates are shown for this configuration. Left is a top-view of the system and right is a side view. The flow direction and external field directions are shown with solid arrows.*

repulsion. The appropriate force balance when $\theta_r \to 90$ is in the θ-direction as defined in Fig. 6.6. When $\theta_r \to 90$ the angle $\phi = 180$. For this specific case, the magnetic forces in the θ-direction are given by

$$F_\theta^{\text{Mag}} \approx \frac{U_0}{d}\left(4.125\cos\theta + 1.875\cos 3\theta - 6\cos\theta\sin\theta\right). \tag{6.11}$$

Likewise, the flow forces in the θ-direction can be written as

$$F_\theta^{\text{Flow}} \propto N v_{\text{avg}}\zeta\cos\theta\left(\sin\phi\cos\theta_r + \cos\phi\sin\theta_r\right) \tag{6.12}$$

Therefore, equating the two forces in Equations 6.11 and 6.12 yields the force balance in the θ-direction

$$N\frac{v_{\text{avg}}\zeta}{U_0/d} \propto N\text{Ma} \approx \left[\frac{2.25 + 3.75\left(2\cos^2\theta - 1\right) - 6\sin\theta}{\sin\theta_r}\right] \tag{6.13}$$

The energy landscape in Fig. 6.3b is very steep when the chain is between two rail colloids. In other words, the motion in the direction down the rail is very constrained. Therefore, the angle θ in Equation 6.13 is fairly constant since it depends upon the ability of the chain to move down the rail.

As mentioned, the boundary between Sticking and Guiding II is a combination of the behavior of the system in the two extreme limits of rail angle. Expressing the boundary as a linear combination gives

$$N\text{Ma} \approx \left(\frac{90 - \theta_r}{90}\right)\frac{C_\perp}{\cos\theta_r} + \left(\frac{\theta_r}{90}\right)\frac{C_\theta}{\sin\theta_r} \tag{6.14}$$

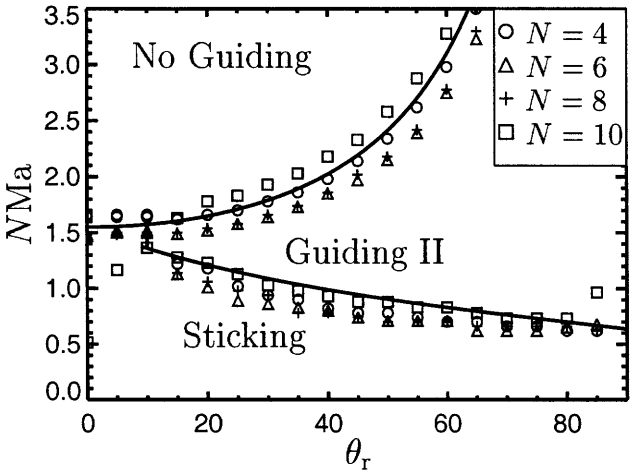

Fig. 6.7: *The phase diagram for the interaction between a chain of N magnetic colloids where $N \leq \widetilde{L}$ and a discrete magnetic rail fixed to the bottom of the channel. The dimensionless channel height was* 10 *for this case. The solid lines are the predictions given by Equations 6.10 and 6.14 for the No Guiding/Guiding II and Guiding II/Sticking boundaries respectively.*

where $C_\perp$ and C_θ are proportionality constants. In our simulations, we find that $C_\perp = 1.93$ and $C_\theta = -0.59$ by matching the behavior of the system at the two limits $\theta_r = 0$ and $\theta_r = 90$. We already showed that $N\mathrm{Ma} = 1.55$ at the limit where $\theta_r = 0$ (for the Guiding II/No Guiding transition) and by performing a simulation for $\theta_r = 90$ we find that $N\mathrm{Ma} = 0.64$ in that limit.

The force balance for the boundary between the Guiding I mode and the Sticking mode is even more complicated than the other two phase boundaries and is not self-similar as a function of the chain length. In Fig 6.4 it appears that the Guiding I mode disappears asymptotically as the chain length is increased. Therefore, we only show the form of the boundary to guide the eye in Fig 6.4. However, the predictions for the phase boundaries given by Equations 6.10 and 6.14 are seen to be quite accurate in Fig. 6.4. They are able to predict not only the shape and location of the phase boundary but also the chain-length dependence. This is further illustrated in Fig. 6.7 where we show the phase diagram for chains of height 4, 6, 8, and 10 interacting with the discrete rail in a channel with $\widetilde{L} = 10$. This figure emphasizes the fact that the chain length is the important length scale in determining the phase boundaries.

A feature that is conspicuously absent from Fig. 6.7 is the Guiding I mode that exists for the case of $N = \widetilde{L}$. When the chain length is smaller than the channel height, the repulsion on the bottom colloid due to the presence of the rail causes the short chain to elevate in the z-direction in order to reduce that repulsive energy. The elevation of the short chain allows it to mount the rail even at very low values of Ma so for $N < \widetilde{L}$ the Guiding I mode can not exist. This elevation is not possible when the chain spans the height of the microchannel and therefore at low Ma, the Guiding I mode exists for $N = \widetilde{L}$.

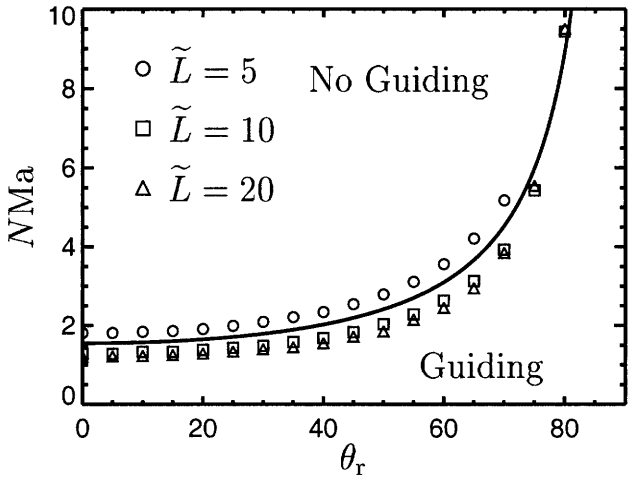

Fig. 6.8: *The phase diagram for the interaction between a chain of N magnetic colloids spanning the height of the microchannel $\widetilde{L}$ and a continuous magnetic rail fixed to the bottom of the channel. The solid line is the prediction given by Equation 6.10.*

6.4 Continuous Rails

The system presented by Inglis et al. [21] consisted of continuous rails on which cells coated with magnetic nanoparticles could guide. In the separation scheme that we have presented, the presence of a continuous rail leads to the two modes of behavior shown in Fig. 6.8. Most notably, there is no Sticking mode in the continuous rail case since the potential energy landscape shown in Fig. 6.3b does not exist for continuous rails. The absence of the Sticking mode causes the Guiding I and Guiding II regions of the phase diagram to merge and therefore the only two modes are Guiding and No Guiding. This is similar to the observations of Inglis et al. where they observe guiding when the magnetic forces are large and no guiding when the flow forces are large. Again the transition from the No Guiding mode to the Guiding mode is due to the balance of forces perpendicular to the rail given by Equation 6.10. This force balance was also presented by Inglis et al. [21].

6.5 Discussion

The four modes of behavior present in the discrete rail case create a distinct advantage over the two modes available in the continuous rail case. In particular, the ability to transition back and forth between the Sticking mode and one of the Guiding modes can be useful for the cell separation scheme presented in this work. As mentioned, the incubation of the heterogeneous cell solution with the magnetic beads is usually the rate limiting step in immunomagnetic separations. However, in our scheme one could take advantage of the different modes of behavior in order to efficiently perform the incubation in a continuous manner.

For instance, the three streams in Fig. 6.1 can be introduced to the microchannel as shown with $\theta_r = 45°$ and $\mathcal{N}\text{Ma} = 1.5$. The external magnetic field could then be oscillated such that $\mathcal{N}$Ma

changes from 1.5 to 0.5 with a defined frequency. This oscillation of the external magnetic field would cause the chains to alternatively guide and stop with the same frequency as the external field. Therefore, the chains would "march" along the rails, moving across the three flowing streams and pausing when the external field is high. When the chains are paused in the stream containing the heterogeneous mixture of cells then they will be able to capture the cells of interest as they flow by. The oscillation frequency of the external field could be adjusted such that the chains will, on average, spend enough time in the stream containing the cells to ensure an optimum effective incubation period. Operated in this manner, the device we propose would be the first continuous-flow immunomagnetic cell separation process performed on a microfluidic scale.

We have presented here an application that utilizes the self-assembled structures found in MR fluids as dynamic structures in a microfluidic device. The idea for the pattern assisted cell separation device presented in this chapter can have an important impact upon this area of microfluidics since it is a simple scheme that does not require extensive fabrication or precise magnetic field gradients. Furthermore, it allows one to perform separations of biological entities in a continuous fashion, incorporating an effective incubation step into the separation process and thus removing the need for a time-intensive batch incubation.

The device proposed by Inglis et al. [21] is similar in nature to the one proposed here but it uses continuous rails and therefore does not support the Sticking mode present in our device. As a result, the Inglis device requires an incubation of the cell mixture and the magnetic nanoparticles in a batch process before the separation step. The Sticking mode is critical in that it allows the chains to be temporarily trapped in the stream containing the cell mixture in order to capture the cells of interest.

6.6 Outlook

In the near future, a set of proof of principle experiments must be done with discrete rails as outlined in this work. The technologies to construct the device proposed here already exist in the literature and therefore the ideas presented can be verified in a real cell separation device. In particular, we must show that we can apply the phase diagram we have found in our simulations in order to "march" the chains along the rails to perform the continuous immunomagnetic cell separation proposed in Section 6.5.

CHAPTER 7

Conclusions and Outlook

In this thesis we have presented a series of studies that merge the areas of microfluidics and MR fluids. This is a timely union of these two technologies as new microfluidic applications are being developed that utilize the self-assembling properties of MR fluids [4]. We have systematically investigated the effects that confinement in microfluidic geometries has upon the structure and dynamics of self-assembled MR fluids. The work done here will have a broad impact upon the design and ultimate use of MR fluids as structural components in microfluidic devices.

7.1 Two Dimensional Systems

We began in Chapter 3 by investigating a model system consisting of MR fluid confined in a plane with an external magnetic field directed normal to that plane. The MR fluid in this system formed a monolayer of colloids interacting with purely repulsive dipolar interactions. This system has been of interest for many years as a model for 2D crystallization and melting [87]. We performed the largest BD simulations to date of unbounded 2D dipole system (14, 784 colloids) in order to determine the external field strength at which the solid-liquid phase transition occurs [34]. We were able to determine upper and lower bounds for the phase transition region providing a very narrow window of external field strengths over which it occurs. Our results were consistent with, albeit more precise than, previous simulation work on the same system.

In addition to the unbounded system, we fully characterized the structure and dynamics of MR fluids confined in 2D channels with parallel hard walls [33, 34, 35]. We found that the dimensionless

channel width plays a crucial role in determining the structure and state of the system. We mapped out the state of the system as a function of external field strength and channel width and discovered that the system exhibits re-entrant behavior as a function of channel width but not external field strength. The behavior of the 2D channel system oscillates back and forth between solid-like and liquid-like states as the channel width is increased. This represents the first time such an observation has been made as a function of the geometry of the system. Previous work had found re-entrant behavior of the system as a function of external field strength for MR fluids confined in 2D circles [49]. Additionally, we were able to show that the re-entrant behavior as a function of channel width was not unique to the dipolar interaction but in fact is general for repulsive interactions between colloids confined in 2D hard-wall channels.

Another property of MR colloids in the 2D channel system that we observed was the regular defect structure along the hard-walls. Free dislocations arose along the hard-walls in this system due to the energetically favorable arrangement of colloids consisting of a higher density along the walls. The presence of these defects gives rise to many of the structural properties observed for MR fluids under this confinement. However for other repulsive interactions the dislocations along the wall were not observed indicating that the energetics in these systems do not favor that structure. Therefore the general property of re-entrant behavior for repulsive colloids in 2D channels does not rely upon the presence of free dislocations along the walls.

All of the results found in our BD simulations for MR fluids in 2D hard-wall channels were confirmed experimentally [35]. We performed a series of experiments with paramagnetic colloids in a monolayer confined between parallel hard walls and subjected to a uniform external magnetic field. The results from these experiments confirmed exactly the observations from our BD simulations and allowed us to verify that the structure of MR fluids under this extreme confinement is well-modeled with our BD technique.

7.2 Thin Slit Systems

Another technologically relevant geometry for the confinement of MR fluids is a thin-slit microchannel. In Chapter 4 we investigated the self-assembly of dilute MR fluids confined in thin-slits with a uniform external magnetic field directed normal to the confining planes. In particular, we characterized the spacing between the clusters that form as a function of the slit-thickness and volume fraction of the MR fluid. This property of the system is crucial to the DNA separation devices that utilize self-assembled MR fluids in thin-slits [4]. We showed quantitative agreement between our BD simulations and previous experimental work on the same system [10]. The previous work only considered slit-thicknesses larger than tens of colloid diameters but due to advances in microfluidic technology, the sizes of microchannels can now range down to a single colloid diameter. Our simulations represent the first investigation of self-assembly of dilute MR fluids in such extremely thin slits (less than five colloid diameters in thickness).

We showed that there is a cross-over in the behavior of the spacing between clusters as the slit-thickness is reduced. The details of the cross-over were shown to be highly dependent upon the energy barriers to lateral aggregation of MR colloids confined in thin-slits. We introduced a model to predict when the energy barriers to aggregation become significant as a function of the volume fraction of MR fluid and the slit-thickness. This model was the first to include the effects of volume fraction on the energetics of aggregation and we were able to show that indeed it plays an important role in determining when the barriers to aggregation become important. We were

able, for the first time, to quantitatively explain the volume fraction dependence of the cross-over in behavior as the slit-thickness is reduced. Our model also helps to explain why real MR fluid systems in thin-slits can not reach their theoretically predicted ground states [96].

In the extremely thin slits (less than five colloid diameters) we observed that the spacing between clusters oscillates as a function of slit-thickness. This was the first observation of its kind for dilute MR fluids although a similar oscillating behavior has been observed for very concentrated MR fluids [11]. We introduced a quantitative model for the ground states of the MR fluid clusters under such extreme confinement and showed that it was able to predict the oscillations in spacing. We showed that for most slit-thicknesses in this range, the system reached the ground state configuration of clusters but in some cases the energy barriers to aggregation were again too large to reach the ground state.

The study of the thin-slit system is of great importance for understanding the self-assembled MR fluid structures that will form in microfluidic devices. Using the results of this study, one can tailor the geometry of a microfluidic channel in order to achieve a desired pore size between the MR fluid structures. Additionally, this study introduced a quantitative model of the energy barriers to aggregation that exist in the thin-slit system which will aid in understanding the dynamic response of MR fluids to an external magnetic field under such confining conditions.

7.3 MR Fluids and Flow

Taking our experiences in modelling the behavior of MR fluid structures in microfluidic geometries, in Chapter 5 we investigated, more generally, the self-assembly of MR fluids under the application of pressure driven flow. We chose to study the technologically relevant geometry of a thin-slit microchannel with an aspect ratio of 10:1. In our study, the external magnetic field was directed perpendicular to the flow direction along the wide-axis of the thin-slit. This study is relevant as many applications utilizing MR fluids require the fluids to flow under the application of pressure through microfluidic channels [102].

Using simulations, we were able to show the important processes taking place during self-assembly in pressure driven flow. Head-to-tail aggregation of MR colloids was shown to occur at the same rate, independent of the fluid flow rate, for all of the flow rates studied. In contrast, the lateral aggregation of chains of MR colloids depended heavily upon the flow rate and we found that there were two important regions of flow rate affecting this aggregation process. At lower flow rates the shear assisted aggregation regime dominated where the non-uniform nature of the flow profile in the plane normal to the thin-slit assisted chains in aggregating laterally. At higher flow rates the shear induced breaking regime dominated due to the non-uniform flow profile parallel to the thin-slit. This velocity profile acts along the length of the clusters that form and near the side walls, where the gradient of the profile is large, the clusters shear apart in this regime. The mechanisms elucidated by this study are important for understanding and predicting the response times of MR fluids to the application of an external magnetic field in the presence of bulk fluid flow. Additionally, this study has provided a prediction for the mechanism of how MR fluid structures will fail under the application of pressure driven flow and at which flow rates that failure will occur.

In Chapter 6 we introduced an idea for a cell separation device that utilizes MR fluids as structural components that can move under the application of bulk fluid flow. The design of this device was done in collaboration with Daniel C. Pregibon. This immunomagnetic separation device idea would be the first continuous device able to perform all of the steps in a cell separation.

The device consists of "rails" of paramagnetic colloids fixed to the bottom surface of a thin-slit microchannel which are capable of guiding a free vertical chain of paramagnetic colloids along the rail. The paramagnetic colloids in the chain are decorated with an antibody that binds specifically to the surface markers of cells of interest. As the chain guides along the rail, it can capture cells as they flow past and then drag them into a clean buffer stream for separation farther downstream.

We characterized, using simulations, the operational range of the device and showed the different modes in which it can be run. In addition, we presented theoretical predictions for the boundaries between the different modes of operation and showed how those predictions match with the simulation results. We compared the operation of this device with a previous application in the literature [21] in order to show the added functionality present in our device. At present, the device presented in Chapter 6 is the first microfluidic example capable of performing a continuous immunomagnetic cell separation.

7.4 Future Work

In the future there are many exciting directions this research can take. One area of considerable interest is to investigate further the properties of 2D colloidal crystals with repulsive dipolar interactions near hard-walls. We have shown that regular free dislocations arise along the walls in 2D channels but we have not studied the properties of these dislocations. Specifically, one could study the timescales associated with their diffusion along the wall and the frequency with which they form and annihilate. Additionally, a more rigorous understanding of the energetics leading to their formation would be very interesting from a basic physics standpoint.

In thin-slits, experimental exploration of the extremely thin slit regime (less than five colloid diameters) would illustrate how useful the oscillating spacing (or pore size) between MR fluid clusters can be for DNA separations. Additionally, the ideas presented in Chapter 4 for the energy of interaction between two chains of MR colloids at a fixed volume fraction and slit-thickness could be extended to the range of slit-thicknesses studied experimentally in the literature [10]. There is still a discrepancy in the literature between the cluster spacings observed experimentally [10] and the ground state cluster spacings predicted by theory [96]. This discrepancy is most likely due to the presence of energy barriers to aggregation of clusters (larger than single chains) but it has not been shown quantitatively for the larger slit-thicknesses (greater than 100 colloid diameters).

The results for MR fluids self-assembling in flow presented in Chapter 5 should be compared to experimental results. In particular, it should be determined how important shear induced migration is in this system, how important is the channel geometry (both size and aspect ratio), and how do the results depend upon the volume fraction of the MR fluid. Another point of interest would be to develop a model for predicting the steady-state shape of the clusters under the application of pressure driven flow. Additionally, the cell sorting device presented in Chapter 6 could be fabricated and tested to determine if the theoretical predictions in this thesis hold true for a physical device. The technology exists in the literature to fabricate the device and therefore it should be considered for the sake of introducing the first continuous immunomagnetic cell separation device.

We have pointed out several directions that this research can take in the immediate future. Undoubtedly, farther into the future, these questions and many more will be addressed. The idea of utilizing MR fluids as structural components in microfluidic devices is blossoming into a wide-ranging field with many interesting scientific and application oriented problems. This thesis will serve as a guide for undertaking and solving these problems.

Appendix A

Tips and Tricks

This appendix contains detailed descriptions of many useful tools that were used during the process of the research in this Thesis. An overview of the Brownian dynamics (BD) algorithm is given along with detailed descriptions of the more unique features. The important "post-processing" routines used for calculating properties of the simulated systems are also listed with descriptions. Additionally, experimental tips are given for performing experiments on the self-assembly of MR fluids in microfluidic channels

A.1 Brownian Dynamics Algorithm

The general form of the BD code is shown in Fig. A.1. Each subroutine presented in Fig. A.1 will be described in more detail in this section.

initialize.f This subroutine initializes the random number generator and any lookup tables that might be necessary. The random number generator was developed in [24] and is given on pages 308-309. The necessary lookup tables could be for the flow profile as well as the hard-wall equations given in Chapter 2.

placement.f There are many different ways to place the colloids inside the simulation box. The two most useful starting configurations are a random starting configuration where the colloids are placed using randomly generated positions or a previous simulation's ending configuration. If

```
main.f [reads input file and calls simulation]
    simulation.f [integrates equation of motion]
        initialize.f [initializes random number generator]
        placement.f [places the colloids in the simulation box as instructed
                     in the input file]
        headermovieprint.f [prints the input parameters into the output
                            file]
        movieprint.f [prints the initial configuration of colloids into the
                      output file]
        for i=1,final_time
            zeromove.f [sets the "move" vectors to zero]
            if (field_on) then
                newlist.f [bins the colloids based on their positions]
                interactions.f [calculates the magnetic interactions
                                between colloids and updates the
                                "move" vectors]
            endif
            if (flow_on) then
                flow.f [calculates the force on the colloids due to bulk
                        fluid flow and updates the "move" vectors]
            endif
            if (brown_on) then
                brownian.f [calculates the Brownian force on the
                            colloids and updates the "move" vectors]
            endif
            makemove.f [adds the "move" vectors to the positions of
                        the colloids]
            period.f [enforces periodic boundary constraints if any]
            newlist.f [bins the colloids based on their positions]
            hardsphere.f [enforces the hard sphere constraint]
            period.f [enforces periodic boundary constraints if any]
            if (sample_time) then
                movieprint.f [prints the current configuration of
                              colloids into the output file]
            endif
        continue
```

Fig. A.1: *Pseudo code description of the BD algorithm used for the research in this thesis.*

the colloids are placed randomly then after each colloid is placed we must check to ensure that it hasn't overlapped with any of the other colloids in the system.

headermovieprint.f This subroutine simply prints a copy of the input file as the first lines of the output file. In the output file, the lines printed by this subroutine are preceded with a # sign which acts as a comment symbol.

movieprint.f The position vectors are sent to this subroutine so that they can be printed to the output file. The output file is in the "xyz" format which has the following form (after the comment lines printed in headermovieprint.f). The number of colloids is printed on its own line followed by a comment line which contains the time of the snapshot. Then N lines are printed (one for each colloid) formatted as

type x-position y-position z-position

zeromove.f This subroutine simply takes in the move vectors (the vectors that give the displacement for each colloid) and sets them to zero in preparation for the next time-step in the loop.

newlist.f The colloids are binned into a linked list set of bins as described in [25] on page 552.

interactions.f The magnetic interactions between all of the colloids are calculated. We loop through the bins that are created in newlist.f and calculate the interactions between each colloid in a bin and each other colloid in that bin and half of the neighboring bins. While looping through all of the bins, we check to enforce the periodic boundary conditions (check to see if a neighboring bin exists as a periodic reflection) and the hard-wall conditions (check to see if a bin is next to a hard wall so it has no neighbors on that side). The interactions between the colloids are calculated using the force equation (Equation 2.5) in Chapter 2 and the displacements due to the magnetic interactions are added to the move vectors.

flow.f The flow forces are calculated based upon the positions of the colloids (without HI) and the displacements are added to the move vectors. The flow force can have an analytical form or can be a numerical lookup table that was generated in initialize.f.

brownian.f The displacement due to Brownian motion is added to the move vectors by generating three random numbers (one in each cartesian direction) for each colloid in the system.

makemove.f The move vectors are simply added to the position vectors in order to step the positions of the colloids forward in time.

period.f The periodic boundary conditions are enforced by looping through all the colloids and checking if their positions are outside the simulation box. If the colloids are outside the simulation box in one of the periodic directions, their position is replaced by the periodic image that is inside the simulation box.

hardsphere.f The hard-sphere and hard-wall constraints are enforced by this subroutine. First, all of the move vectors are re-zeroed and then all of the bins along the hard walls are checked for colloids that overlap with the wall. If there are colloids overlapped with the hard-walls, they are displaced according to the rules given in Section 2.2.1 for the Displacement Algorithm. We then loop through all of the bins in the same manner as described for interactions.f and calculate the hard-sphere interactions between all of the colloids. The displacements due to the hard sphere interactions [27] are added to the move vectors and after all of the interactions have been calculated,

the colloid positions are updated with the move vectors. If none of the colloids were found to be overlapped, then we exit the subroutine. Otherwise, the subroutine is repeated until all overlaps are removed.

A.2 Post-processing

The output file from the simulations contains a series of configuration snapshots in time for the simulation system. In order to analyze the system, we must be able to calculate useful properties using the output file. Generally, we have written many post-processing codes that read in the output file into a set of position vectors one frame at a time and calculate properties such as density profiles (**calcdens.f**), connectivity (**calcconn.f**), cluster properties (**calcclust.f**), etc. For the special case of calculating the nearest neighbors in 2D, we have developed another set of codes described below.

A.2.1 Delaunay Triangulation

The output file is re-formatted (using **makepositions.f**) into a file with two columns containing the following lines

Nframes	Nframes	
Nparts	Nparts	
xside	yside	
dt	dt	
x-pos	y-pos	(N×Nframes lines)
time between frames	time between frames	

This file is then read into IDL (using **format_pos.pro**) as an array p(2,Nframes,N) containing the x- and y-positions of the colloids in every frame. The IDL procedure **createtri.pro** is then used to create a file containing all of the position and nearest neighbor information for the colloids in every frame.

createtri.pro Takes as input the array p(2,Nframes,N) and a sample frequency (freq). This procedure, loops through the frames (with the frequency defined by the user) and runs the built in IDL procedure **triangulate.pro** on the x- and y-positions of the colloids in each frame. The command line for running **triangulate.pro** is

```
triangulate,x,y,tr,conn=c
```

where the vector c contains the nearest neighbors for each colloid in the system for one frame. For more information on the triangulate procedure, the IDL Reference Guide should be consulted. The

procedure **createtri.pro** then writes to an output file. The first six lines of the output file contain Nparts, Nframes, Nsamp, xside, yside, and freq where Nsamp=Nframes/freq. After the first six lines, the procedure prints the following lines for each frame that has been sampled. One line is printed containing the length of the vector c. The vector c is then printed followed by N lines containing the x- and y-positions of the colloids in the frame.

The output file from **createtri.pro** is then used as input for post-processing scripts to calculate the bond-order correlation function (**boot.f**), defect density (**countdef.f**), and spacing between clusters (**calcspace.f**). Additionally, the outputs from the Delaunay triangulation (tr and c) can be used to plot the 2D structure of the colloids in the system using **plottri.pro** and **colortri.pro** respectively.

All of the codes presented in this appendix are given in their full form in Appendices B and C.

A.3 Experimental Tricks

During the course of designing and performing the experiments in this thesis, we learned many valuable lessons about what works and what does not work. In this section, we give a few of the lessons learned in order to aid in performing this research in the future.

A.3.1 Colloid Preparation

The paramagnetic colloids used in this research were purchased from Dynal (Dynabeads). The magnetic properties quoted in the documentation sent with the colloids are not always accurate and the best source for up to date information is to call Dynal. Generally, two types of colloids were used in this research, epoxy coated and carboxylated. The epoxy coated colloids have no surface charge and are shipped in deionized (DI) water. In order to prevent sticking and aggregation in experiments, we found that a 0.02 wt% solution of Triton X-100 surfactant should be used as the carrier fluid. In order to exchange the carrier fluid we placed our sample of Dynabeads over a household magnet in order to concentrate the colloids at the bottom of the vial. A pipette was then used to remove the supernate and replace the same volume with the surfactant solution. This "washing" procedure was repeated three times to ensure a complete exchange of the carrier fluid. Likewise for the carboxylated colloids, they are shipped in DI water. In the case of charged colloids, we have found that a buffer solution (5× TBE) is the best carrier fluid. The TBE usually contains many salt crystals and it must be filtered with a 0.2μm filter before being used as a carrier fluid for the colloids. After filtering, the same washing procedure is applied using TBE instead of surfactant solution.

We have found that the colloid solutions do not have a long life when kept outside the refrigerator. After a week or two, the colloids will aggregate and/or the TBE will crystalize in the vial and the colloid solution will not be useful any longer. The best remedy for this is to make a fresh colloid solution for each set of experiments to be performed. The colloids (as received from Dynal) will keep indefinitely in the refrigerator and therefore it is best to start each set of experiments with a freshly washed sample of colloids.

A.3.2 Channel Preparation

Just as important as having a freshly washed sample of colloids is having a clean microchannel environment in which to perform experiments. We have found that the best method for producing

clean channels with uniform surface properties is to use PDMS for all four sides of the channel. To make a thin sheet of PDMS (the eventual bottom surface of the channel) we pour 10g of the PDMS solution into a clean petri dish. The PDMS must be degassed and contain no bubbles in order to produce a smooth surface when cured.

To assemble the channels, the following procedure is used. A glass cover-slip is cleaned with DI water and ethanol to remove any dust particles. A rectangle is cut out of the thin PDMS and placed, clean-face-up, on the glass cover-slip. Meanwhile, the appropriate channel is cut out from the mold of the master template and any reservoirs (access holes) are cut as well. The two pieces, cover-slip with thin PDMS and channel (face up) are placed into the oxygen plasma chamber and exposed to an oxygen plasma for 15 seconds. The channel is then placed face down onto the thin PDMS in order to create a four-walled all-PDMS microchannel. The oxygen plasma causes the PDMS surfaces to have a negative charge which, when coupled with the carboxylated Dynabeads, prevents the colloids from sticking to the surfaces of the channel.

In the case of the 2D channel studies, the experiments must remain stable for up to 24 hours and therefore a secondary enclosure was created to keep the entire channel system submerged in TBE (Chapter 3). Without the secondary enclosure, evaporation and permeation of the carrier fluid would cause a net flow in the system [140], thus disrupting the dynamics of the colloids themselves. This secondary enclosure was simply created with cover-slips for the top and bottom and thick PDMS walls on the sides. The bottom cover-slip of the enclosure served the same purpose as the cover-slip mentioned above and therefore the thin PDMS was placed directly on the bottom surface of the enclosure.

A.3.3 Tracking Colloids

In order to track the positions of the colloids during an experiment, special tracking procedures were used as described in [85]. Generally, a movie of the experiment was recorded on digital video tape and after the experiment was completed, several stacks of images were taken from the movie with a fixed interval of time between the images. The positions of the colloids were then located in each image and a tracking algorithm was used to track individual colloids in time through the stack of images.

There were many difficulties in accurately tracking the positions of the colloids due to optical interference from the channel walls. We minimized the interference due to the presence of the walls in the following manner. A single image was produced by averaging all of the images in the stack. In this image, the walls are the only non-moving part of the system so the colloid positions are blurred out and only an image of the walls is left. We then subtracted the image of the walls from each image in the stack in order to remove the interference from the walls. This procedure only worked well when the images in the stack were separated by long enough times that the colloids moved significantly between each frame.

Another trick that we learned while performing the experiments was the following. During the tracking procedure, it is much easier to track if one feeds the initial positions of the colloids (in the first frame) into the tracking algorithm. Since the colloids do not move very far (relative to the inter-colloid distance) and they are separated by large distances, inputting the initial positions helps to remove false tracks that may occur due to noise in the images.

Appendix B

Brownian Dynamics Code

This appendix contains the Fortran codes used for the BD simulations in this thesis. The general descriptions of these codes are given in Appendix A.

B.1 input

```
Numparts       = 1000
Nfixed         = 0
FinalTime      = 50
Timestep       = 0.0001
StartFrame     = 1
StartConfig    = rand
Nseed          = 68046503
Geometry       = 50 50 30
HSCut          = 5.5
StartField     = 50
StopField      = 50
Periodicity    = .true. .true. .true.
Dimensionality = .true. .true. .true.
PulseField     = .false.
```

```
PulseON         = 0
PulseOFF        = 0
MagCut          = 10
MagStartTime    = 0
Vavg            = 0
Movie           = movie.xyz
SampleNum       = 1000
END
```

B.2 main.f

```
      program main

      implicit none
      integer n, Tfinal, nseed, pon, poff
      integer ftime, sframe, nfixed, nsamp
      double precision dt, xside, yside, zside, lambda, mbinsize
      double precision hbinsize, lambdao, G
      character*32 input,scratch,moviefile,sconf
      logical perx, pery, perz, xdim, ydim, zdim, pulse


      scratch = 'Beginning'
      input = 'Reading input ...'
      write(*,*) scratch
      write(*,*) input

      open (unit=3, file='./input', status='old')
 5    read(3,*) input
      backspace(unit=3)
      if(input.eq."Numparts") then
         read(3,*) input, scratch, n
      elseif(input.eq."Nfixed") then
         read(3,*) input, scratch, nfixed
      elseif(input.eq."FinalTime") then
         read(3,*) input, scratch, Tfinal
      elseif(input.eq."Timestep") then
         read(3,*) input, scratch, dt
      elseif(input.eq."StartFrame") then
         read(3,*) input, scratch, sframe
      elseif(input.eq."StartConfig") then
         read(3,*) input, scratch, sconf
      elseif(input.eq."Nseed") then
         read(3,*) input, scratch, nseed
      elseif(input.eq."Geometry") then
         read(3,*) input, scratch, xside, yside, zside
      elseif(input.eq."HSCut") then
         read(3,*) input, scratch, hbinsize
      elseif(input.eq."StartField") then
         read(3,*) input, scratch, lambdao
      elseif(input.eq."StopField") then
         read(3,*) input, scratch, lambda
      elseif(input.eq."PulseField") then
```

```
      read(3,*) input, scratch, pulse
    elseif(input.eq."PulseON") then
      read(3,*) input, scratch, pon
    elseif(input.eq."PulseOFF") then
      read(3,*) input, scratch, poff
    elseif(input.eq."MagCut") then
      read(3,*) input, scratch, mbinsize
    elseif(input.eq."MagStartTime") then
      read(3,*) input, scratch, ftime
    elseif(input.eq."#") then
      read(3,*) input
    elseif(input.eq."Periodicity") then
      read(3,*) input, scratch, perx, pery, perz
    elseif(input.eq."Movie") then
      read(3,*) input, scratch, moviefile
    elseif(input.eq."Dimensionality") then
      read(3,*) input, scratch, xdim, ydim, zdim
    elseif(input.eq."Vavg") then
      read(3,*) input, scratch, G
    elseif(input.eq."SampleNum") then
      read(3,*) input, scratch, nsamp
    elseif(input.eq."END") then
      goto 15
    else
      write(*,*) "The variable ",input," is formatted"
      write(*,*) "incorrectly in the input file"
      stop
    endif
    goto 5

15  close(unit=3)

    call simulation (dt,xside,yside,zside,n,lambda,mbinsize,
   +     hbinsize,Tfinal,ftime,nseed,perx,pery,perz,xdim,ydim,
   +     zdim,moviefile,lambdao,sframe,G,nfixed,sconf,pulse,pon,
   +     poff,nsamp)
    end
```

B.3 simulation.f

```
    subroutine simulation(dt,xside,yside,zside,n,lambda,mbinsize,
   +     hbinsize,Tfinal,ftime,nseed,perx,pery,perz,xdim,ydim,
   +     zdim,moviefile,lambdao,sframe,G,nfixed,sconf,pulse,pon,poff,
   +     nsamp)

    implicit none
    integer time,Tfinal, nseed, ftime,sframe
    integer n, mxbinnum, mybinnum, mzbinnum, pon, poff
    integer hxbinnum, hybinnum, hzbinnum,nfixed,nsamp
    integer hoc(0:10000000), ll(n), on, off, counter
    double precision xside, yside, zside, x(n), y(n), z(n), dt
    double precision hbinsize, lambdao
    double precision xmove(n), ymove(n), zmove(n)
    double precision Bmult, lambda, mbinsize, G
    double precision mxbinsize, mybinsize, mzbinsize, Q
```

```
      double precision hxbinsize, hybinsize, hzbinsize
      logical perx, pery, perz, xdim, ydim, zdim, pulse
      character*32 moviefile, sconf

*/*** Constants ***********
      open(unit=9,file=moviefile,status='new')

      time = 0
      mxbinnum = IDINT(xside/mbinsize)
      if(mxbinnum.eq.0) mxbinnum=1
      mybinnum = IDINT(yside/mbinsize)
      if(mybinnum.eq.0) mybinnum=1
      mzbinnum = IDINT(zside/mbinsize)
      if(mzbinnum.eq.0) mzbinnum=1
      mxbinsize = xside/dble(mxbinnum)
      mybinsize = yside/dble(mybinnum)
      mzbinsize = zside/dble(mzbinnum)
      hxbinnum = IDINT(xside/hbinsize)
      if(hxbinnum.eq.0) hxbinnum=1
      hybinnum = IDINT(yside/hbinsize)
      if(hybinnum.eq.0) hybinnum=1
      hzbinnum = IDINT(zside/hbinsize)
      if(hzbinnum.eq.0) hzbinnum=1
      hxbinsize = xside/dble(hxbinnum)
      hybinsize = yside/dble(hybinnum)
      hzbinsize = zside/dble(hzbinnum)
      if(mxbinnum*mybinnum*mzbinnum.gt.10000000)
     + write(*,*) 'Too many magnetic bins'
      if(hxbinnum*hybinnum*hzbinnum.gt.10000000)
     + write(*,*) 'Too many hardsphere bins'
      Bmult = sqrt(24.0d0*dt)
      Q = 0.0d0
      on=0
      off=1
      counter=0
*/************************
      call initialize(nseed)
      call placement (xside, yside, zside, x, y, z, n,xdim,ydim,zdim,
     +     sframe,nfixed,sconf,perx,pery,perz)
      write (*,*) "All Placed"
      call headermovieprint(9,dt,xside,yside,zside,n,lambda,mbinsize,
     +     hbinsize,Tfinal,ftime,nseed,perx,pery,perz,xdim,ydim,
     +     zdim,moviefile,lambdao,sframe,G,nfixed,sconf,pulse,pon,
     +     poff,nsamp)
      call movieprint (9,n,x,y,z,time,xside,yside,zside,0,nfixed)

*/*** Main body of simulation ****

      do 40 time=1,Tfinal
*/*** Forces *****
         if (time.gt.ftime) then
            counter=counter+1
            if(pulse) then
               if(off.eq.1.and.counter.eq.poff) then
                  Q = 3.0d0/2.0d0*((lambda-lambdao)/dble(Tfinal-ftime)*
```

```
     +                  dble(time-ftime)+lambdao)
                     off=0
                     on=1
                     counter=0
                  elseif(on.eq.1.and.counter.eq.pon) then
                     Q=0.0d0
                     off=1
                     on=0
                     counter=0
                  endif
               else
                  on=1
                  Q = 3.0d0/2.0d0*((lambda-lambdao)/dble(Tfinal-ftime)*
     +                dble(time-ftime)+lambdao)
               endif
            endif
            call zeromove(n,xmove,ymove,zmove)
            if(on.eq.1) then
               call newlist(n,x,y,z,hoc,ll,mxbinsize,
     +              mybinsize,mzbinsize,mxbinnum,mybinnum,mzbinnum)
               call interactions(xside,yside,zside,x,y,z,dt,mxbinnum,
     +              mybinnum,mzbinnum,n,perx,pery,perz,hoc,ll,
     +              Q,mbinsize,xmove,ymove,zmove,mxbinsize,
     +              mybinsize,mzbinsize)
            endif
            call flow(n,dt,x,G,xside,ymove)
            call brownian (n,xmove,ymove,zmove,xdim,ydim,zdim,Bmult)
            call makemove (n,x,y,z,xdim,ydim,zdim,xmove,ymove,zmove,nfixed)
*/***************

*/**** Constraints *****
            call period(n,x,y,z,xside,yside,zside,perx,pery,perz)
            call newlist(n,x,y,z,hoc,ll,hxbinsize,
     +           hybinsize,hzbinsize,hxbinnum,hybinnum,hzbinnum)
            call hardsphere (xside,yside,zside,x,y,z,hxbinnum,hybinnum,
     +           hzbinnum,n,perx,pery,perz,hoc,ll,xdim,ydim,zdim,nfixed,
     +           hxbinsize,hybinsize,hzbinsize)
            call period(n,x,y,z,xside,yside,zside,perx,pery,perz)
*/*********************
            if(Tfinal.gt.nsamp) then
               if(MOD(time,Tfinal/nsamp).eq.0) then
                  call movieprint (9,n,x,y,z,time,xside,yside,zside,on,
     +                             nfixed)
               endif
            else
               call movieprint(9,n,x,y,z,time,xside,yside,zside,on,nfixed)
            endif

 40      continue

         close(unit=9)
         end
```

B.4 initialize.f

```
      subroutine initialize(nseed)

      implicit none
      integer nseed

      call ranils(nseed)

*/****************************************************************
*/     Can also hard code any lookup tables that might be needed.
*/     For instance, to calculate the flow force on a particle
*/     located at a certain position, it might be faster to have a
*/     look up table and interpolate rather than calculating the
*/     force on the fly.
*/****************************************************************

      return
      end
```

B.5 ranils.f

```
      subroutine ranils(iseed)

      parameter (IN=2147483563,IK=40014,IQ=53668,IR=12211,NTAB=32)
      integer IV(NTAB)
      common /RANBLS/ IDUM,IDUM2,IY,IV

      IDUM=iseed+123456789
      IDUM2=IDUM

      do 10 J=NTAB+8,1,-1
         K=IDUM/IQ
         IDUM=IK*(IDUM-K*IQ)-K*IR
         if(IDUM.lt.0) IDUM=IDUM+IN
         if(J.le.NTAB) IV(J)=IDUM
 10   continue

      IY=IV(1)
      return
      end
```

B.6 placement.f

```
      subroutine placement (xside,yside,zside,x,y,z,n,xdim,ydim,
     +     zdim,sframe,nfixed,sconf,xper,yper,zper)

      implicit none
      integer sframe,rand,nfixed
      integer n,i,k,j,nx,ny,latt
      integer Nparts,time,crds
      double precision x(n),y(n),z(n),xside,yside,zside
      double precision spacing,volfrac,rnflt,PI
      parameter (PI=3.14159d0)
      logical xdim,ydim,zdim,done,xper,yper,zper
      character*32 type,junk,sconf
```

```
      rand=0
      latt=0
      crds=0
      if (sconf.eq."rand") then
         rand = 1
      elseif(sconf.eq."latt") then
         latt = 1
      elseif(sconf.eq."coords") then
         crds = 1
      else
         write(*,*) 'Bad starting configuration input'
         stop
      endif

      if (rand.eq.1) then
         do 13 i=1,nfixed
*/*************************************************************
*/     Some block of code to place the fixed colloids at their
*/     positions as defined by the problem
*/*************************************************************
 13      continue
         do 15 i=nfixed+1,n
 5          x(i) = rnflt()*xside
            y(i) = rnflt()*yside
            z(i) = rnflt()*zside
            if(.not.xdim) x(i) = xside/2.0d0
            if(.not.ydim) y(i) = yside/2.0d0
            if(.not.zdim) z(i) = zside/2.0d0
            call checkplace (x,y,z,n,i,done,xside,yside,zside,
     +           xper,yper,zper)
            if (.not.done) goto 5
 15      continue
      endif

      if (latt.eq.1) then
         volfrac = dble(n)*PI*0.25d0/(xside*yside)
         spacing = sqrt(PI/(2.0d0*sqrt(3.0d0)*volfrac))
         nx = idint(xside/spacing)
         ny = idint(yside/(spacing*sqrt(3.0d0)*0.5d0))+1
         k = 0
         write(*,*) 'Spacing = ',spacing
         write(*,*) 'Placing ',nx,' x ', ny, ' array'
         do 25 i=1,nx
            do 30 j=1,ny
               k=k+1
               if(MOD(j,2).eq.0) then
                  x(k) = dble(i-1)*spacing+spacing/2.0d0+0.5d0
               else
                  x(k) = dble(i-1)*spacing+0.5d0
               endif
               y(k) = dble(j-1)*spacing*sqrt(3.0d0)*0.5d0+0.5d0
               z(k) = zside/2.0d0
 30         continue
 25      continue
      endif
```

```
      if (crds.eq.1) then
         open(unit=1,file='coords',status='old')
 3       read(1,*) junk
         if (junk.eq.'#') goto 3
         backspace(unit=1)
         read(1,*) Nparts
         backspace(unit=1)
         do 20 i=1,sframe
            read(1,*)
            read(1,*) time
            do 40 j=1,Nparts
           if (i.eq.sframe) then
                 read(1,*) type, x(j), y(j), z(j)
              else
                 read(1,*) type
              endif
 40         continue
 20       continue
      endif

      return
      end
```

B.7 checkplace.f

```
      subroutine checkplace (x,y,z,n,j,done,xside,yside,zside,
     +     xper,yper,zper)

      implicit none
      integer i, n, k, j
      double precision x(n), y(n), z(n)
      double precision diffsq, xside, yside, zside
      logical done,xper,yper,zper

      if (j.gt.1) then
         k = j - 1
         done = .true.
         do 15 i=1,k
            diffsq = (x(j)-x(i))*(x(j)-x(i))+(y(j)-y(i))*(y(j)-y(i))
     +              +(z(j)-z(i))*(z(j)-z(i))
            if (diffsq.lt.1.0d0) then
               done = .false.
            end if
 15       continue
      else
         done = .true.
      end if

*/*************************************************************
*/     This code is for flat walls.  If the walls are not flat then
*/     the code must be modified to include the functional form of
*/     the walls.
*/*************************************************************
      if(.not.xper) then
```

```
      if(x(j).lt.0.5d0.or.x(j).gt.xside-0.5d0) done=.false.
    endif
    if(.not.yper) then
      if(y(j).lt.0.5d0.or.y(j).gt.yside-0.5d0) done=.false.
    endif
    if(.not.zper) then
      if(z(j).lt.0.5d0.or.z(j).gt.zside-0.5d0) done=.false.
    endif

    return
    end
```

B.8 headermovieprint.f

```
      subroutine headermovieprint(unit,dt,xside,yside,zside,n,lambda,
     +     mbinsize,hbinsize,Tfinal,ftime,nseed,perx,pery,perz,xdim,
     +     ydim,zdim,moviefile,lambdao,sframe,G,nfixed,sconf,pulse,pon,
     +     poff,nsamp)

      implicit none
      integer unit, n, Tfinal, ftime, nseed,sframe,nfixed
      integer pon, poff, nsamp
      double precision dt, xside, yside, zside,G
      double precision lambda, mbinsize, hbinsize, lambdao
      logical perx, pery, perz, xdim, ydim, zdim,pulse
      character*32 moviefile,sconf

1     format(' # Timestep        = ',f9.7)
2     format(' # Geometry        = ',f10.4,f10.4,f10.4)
3     format(' # HSCut           = ',f10.4)
4     format(' # StartField      = ',f10.4)
5     format(' # StopField       = ',f10.4)
6     format(' # MagCut          = ',f10.4)
7     format(' # Vavg            = ',f10.4)

      write (unit,*) '# Numparts        = ', n
      write (unit,*) '# Nfixed          = ', nfixed
      write (unit,*) '# FinalTime       = ', Tfinal
      write (unit,1) dt
      write (unit,*) '# StartFrame      = ', sframe
      write (unit,*) '# StartConfig     = ', sconf
      write (unit,*) '# Nseed           = ', nseed
      write (unit,2) xside, yside, zside
      write (unit,3) hbinsize
      write (unit,*) '# Periodicity     = ', perx, pery, perz
      write (unit,*) '# Dimensionality = ', xdim, ydim, zdim
      write (unit,4) lambdao
      write (unit,5) lambda
      write (unit,*) '# PulseField      = ', pulse
      write (unit,*) '# PulseON         = ', pon
      write (unit,*) '# PulseOFF        = ', poff
      write (unit,6) mbinsize
      write (unit,*) '# MagStartTime    = ', ftime
      write (unit,7) G
      write (unit,*) '# Movie           = ', moviefile
```

```
      write (unit,*) '# SampleNum        = ', nsamp

      return
      end
```

B.9 movieprint.f

```
      subroutine movieprint (unit,n,x,y,z,time,xside,yside,zside,on,
     +     nfixed)

      integer i, n, unit, time,on, nfixed
      double precision x(n), y(n), z(n)
      double precision xside, yside, zside

      write (unit,*) n
      write(unit,78) time, xside, yside, zside, on

 78   format(i8,' fs x= ',f9.3,' y= ',f9.3,' z= ',f9.3,
     +     ' field= ',i2)

      do 7 i=1,n
         if (i.le.nfixed) then
            write (unit,5) x(i),y(i),z(i)
 5          format('C',2x,f9.3,2x,f9.3,2x,f9.3)
         else
            write (unit,6) x(i),y(i),z(i)
 6          format('N',2x,f9.3,2x,f9.3,2x,f9.3)
         endif
 7    continue


      return
      end
```

B.10 zeromove.f

```
      subroutine zeromove(n,xmove,ymove,zmove)

      implicit none

      integer i, n
      double precision xmove(n), ymove(n), zmove(n)


      do 4 i=1,n
         xmove(i) = 0.0d0
         ymove(i) = 0.0d0
         zmove(i) = 0.0d0
 4    continue

      return

      end
```

B.11 newlist.f

```
      subroutine newlist (n, x, y, z, hoc, ll ,rnx,rny,rnz,ncellx,
     +     ncelly,ncellz)

      implicit none
      integer n, i, ncellx, ncelly, ncellz, ncell3, hoc(0:10000000)
      integer icelx, icely, icelz, icel, ll(n)
      double precision x(n), y(n), z(n)
      double precision rnx, rny, rnz

      ncell3 = ncellx*ncelly*ncellz

      do 5 icel=0,ncell3-1
         hoc(icel) = 0
 5    continue


      do 10 i=1,n
         icelx = idint(dint(x(i)/rnx))
         icely = idint(dint(y(i)/rny))
         icelz = idint(dint(z(i)/rnz))
         if ((icelx.ge.ncellx).or.(icely.ge.ncelly).or.
     +        (icelz.ge.ncellz).or.(icelx.lt.0).or.
     +        (icely.lt.0).or.(icelz.lt.0)) then
           write(*,*) "Particles are outside the box!!!",
     +                  i,x(i),y(i),z(i)
         endif
         icel = icelx + ncellx*icely + ncellx*ncelly*icelz
         ll(i) = hoc(icel)
         hoc(icel) = i
 10   continue

      return
      end
```

B.12 interactions.f

```
      subroutine interactions (xside,yside,zside,x,y,z,dt,ncellx,
     +     ncelly,ncellz,n,perx,pery,perz,hoc,ll,
     +     Q,mbinsize,xmove,ymove,zmove,rnx,rny,rnz)

      implicit none

      integer i, n, hoc(0:10000000), ll(n), ncellx, ncelly, ncellz
      integer icelx, icely, icelz, pid
      double precision xside,yside,zside,x(n),xmove(n),dt,z(n),zmove(n)
      double precision y(n), ymove(n), Q, mbinsize, rnx, rny, rnz
      logical perx, pery, perz

      do 3 i=1,n
         icelx = idint(dint(x(i)/rnx))
         icely = idint(dint(y(i)/rny))
         icelz = idint(dint(z(i)/rnz))
         pid=i
         call mbins (icelx,icely,icelz,ncellx,ncelly,ncellz,hoc,
     +        ll,n,perx,pery,perz,x,y,z,xside,yside,
```

```
     +          zside ,xmove,ymove,zmove,dt ,Q, mbinsize , pid )
 3    continue

      return
      end
```

B.13 mbins.f

```
      subroutine mbins (icelx ,icely ,icelz ,ncellx ,ncelly ,ncellz ,hoc,ll ,n,
     +      perx , pery , perz ,x,y,z,xside ,yside ,zside ,xmove,ymove,
     +      zmove,dt ,Q, mbinsize , pid )


      implicit none
      integer icelx , ncellx , icely , ncelly , icelz , ncellz , n, pid
      integer hoc(0:10000000), ll(n), i, dx, dy, dz, xch, ych, zch
      integer dumicelx , dumicely , dumicelz , jcel , j, skip
      double precision x(n), y(n), z(n), xside , yside , zside
      double precision xmove(n), ymove(n), zmove(n)
      double precision xi , yi , zi , xmovei , ymovei , zmovei
      double precision xmovej , ymovej , zmovej
      double precision dt, Q, mbinsize
      double precision xmult , ymult , zmult , sqdist , sqcutoff
      double precision dumx, dumy, dumz
      logical perx , pery , perz

      sqcutoff = mbinsize*mbinsize
      i=pid
      skip = 0
      do 53 dx=icelx+1,icelx,-1
         xmult = 0.0d0
         dumicelx = dx
         call wallcheck (dumicelx ,ncellx ,perx ,xmult ,skip)
         xch=1
         if(dx.eq.icelx) xch=0
         if (skip.eq.0) then
            do 52 dy = icely-1,icely+1
               if(dx.eq.icelx .and. dy.eq.icely-1) skip=1
               ymult = 0.0d0
               dumicely = dy
               call wallcheck (dumicely ,ncelly ,pery ,ymult ,skip)
               ych=1
               if(dy.eq.icely) ych=0
               if (skip.eq.0) then
                  do 51 dz = icelz-1,icelz+1
                     if((dx.eq.icelx).and.(dy.eq.icely)
     +                    .and.(dz.eq.icelz-1)) then
                        skip = 1
                     endif
                     zmult = 0.0d0
                     dumicelz = dz
                     call wallcheck (dumicelz ,ncellz ,perz ,zmult ,skip)
                     zch=1
                     if(dz.eq.icelz) zch=0
                     if(skip.eq.0) then
```

```
                    jcel = dumicelx+ncellx*dumicely+
     +                   ncellx*ncelly*dumicelz
                    j = hoc(jcel)
 50                 if(j.ne.0) then
                       if (j.ne.i) then
                          dumx = x(j) + xside * xmult
                          dumy = y(j) + yside * ymult
                          dumz = z(j) + zside * zmult
                          sqdist = (x(i)-dumx)*(x(i)-dumx)+
     +                        (y(i)-dumy)*(y(i)-dumy)+
     +                        (z(i)-dumz)*(z(i)-dumz)
                          if (sqdist.lt.sqcutoff) then
                             xmovei = xmove(i)
                             ymovei = ymove(i)
                             zmovei = zmove(i)
                             xi = x(i)
                             yi = y(i)
                             zi = z(i)
                             xmovej = xmove(j)
                             ymovej = ymove(j)
                             zmovej = zmove(j)
                             call magnetic (sqdist,xi,yi,zi,
     +                           dumx,dumy,dumz,
     +                           xmovei,ymovei,zmovei,
     +                           xmovej,ymovej,zmovej,dt,Q,
     +                           xch,ych,zch)
                             xmove(i) = xmovei
                             ymove(i) = ymovei
                             zmove(i) = zmovei
                             xmove(j) = xmovej
                             ymove(j) = ymovej
                             zmove(j) = zmovej
                          endif
                       endif
                       j=ll(j)
                       goto 50
                    endif
                 endif
                 skip = 0
 51           continue
           endif
           skip = 0
 52     continue
        endif
        skip = 0
 53  continue
     return
     end
```

B.14 wallcheck.f

```
     subroutine wallcheck (dumcell, ncell, per, mult, skip)

     implicit none
     integer dumcell, ncell, skip
```

```
      double precision mult
      logical per


      if(dumcell.gt.ncell-1) then
         if(per) then
            dumcell = dumcell - ncell
            mult = 1.0d0
         else
            skip = 1
         endif
      elseif(dumcell.lt.0) then
         if(per) then
            dumcell = dumcell + ncell
            mult = -1.0d0
         else
            skip = 1
         endif
      endif

      return
      end
```

B.15 magnetic.f

```
      subroutine magnetic (sqdist,xi,yi,zi,xj,yj,zj,xmovei,
     +     ymovei,zmovei,xmovej,ymovej,zmovej,
     +     dt,Q,xch,ych,zch)

      implicit none

      integer xch,ych,zch
      double precision sqdist, xi, xj, yi, yj, zi, zj
      double precision xmovei, xmovej, ymovei, ymovej, zmovei, zmovej
      double precision xcomp, ycomp, zcomp, dt, Q

      xcomp = -Q/((sqrt(sqdist))**5)*
     +     (xi-xj)*((5.0d0*(zi-zj)*
     +     (zi-zj)/sqdist)-1.0d0)*dt
      ycomp = -Q/((sqrt(sqdist))**5)*
     +     (yi-yj)*((5.0d0*(zi-zj)*
     +     (zi-zj)/sqdist)-1.0d0)*dt
      zcomp = -Q/((sqrt(sqdist))**5)*
     +     (zi-zj)*((5.0d0*(zi-zj)*
     +     (zi-zj)/sqdist)-3.0d0)*dt

      xmovei = xmovei+xcomp
      ymovei = ymovei+ycomp
      zmovei = zmovei+zcomp

      if(xch.ne.0.or.ych.ne.0.or.zch.ne.0) then
         xmovej = xmovej-xcomp
         ymovej = ymovej-ycomp
         zmovej = zmovej-zcomp
```

```
      endif

      return
      end
```

B.16 flow.f

```
      subroutine flow(n,dt,x,G,xside,ymove)

      implicit none

      integer n, i
      double precision xside
      double precision x(n)
      double precision ymove(n)
      double precision G, dt

      do 5 i=1,n
*/*****************************************************
*/     Insert the block of code that calculates the flow
*/     profile for your geometry.  This flow profile is
*/     parabolic in the x-direction with flow in the
*/     y-direction.
*/*****************************************************
        ymove(i)=ymove(i)+G*dt*(x(i)-x(i)*x(i)/xside)
 5    continue

      return
      end
```

B.17 brownian.f

```
      subroutine brownian (n,xmove,ymove,zmove,xdim,ydim,zdim,mult)

      implicit none
      integer n, i
      double precision xmove(n), ymove(n), zmove(n), rnflt
      double precision mult
      logical xdim, ydim, zdim

      do 15 i=1,n
            if (xdim) xmove(i) = xmove(i) + (rnflt()-0.5d0)*mult
            if (ydim) ymove(i) = ymove(i) + (rnflt()-0.5d0)*mult
            if (zdim) zmove(i) = zmove(i) + (rnflt()-0.5d0)*mult
 15   continue

      return
      end
```

B.18 rnflt.f

```
      double precision function rnflt()

      parameter (IN1=2147483563,IK1=40014,IQ1=53668,IR1=12211)
      parameter (IN2=2147483399,IK2=40692,IQ2=52774,IR2=3791)
```

```
      parameter (NTAB=32,AN=1./IN1,INM1=IN1-1,NDIV=1+INM1/NTAB)
      integer IV(NTAB)
      common /RANBLS/ IDUM,IDUM2,IY,IV

      K = IDUM/IQ1
      IDUM = IK1*(IDUM-K*IQ1)-K*IR1

      if(IDUM.lt.0) IDUM=IDUM+IN1

      K = IDUM2/IQ2
      IDUM2 = IK2*(IDUM2-K*IQ2)-K*IR2

      if(IDUM2.lt.0) IDUM2=IDUM2+IN2

      J=1+IY/NDIV
      IY=IV(J)-IDUM2
      IV(J)=IDUM
      if(IY.lt.1) IY=IY+INM1
      rnflt = dble(AN*IY)

      return
      end
```

B.19 makemove.f

```
      subroutine makemove(n,x,y,z,xdim,ydim,zdim,xmove,ymove,zmove,
     +     nfixed)

      implicit none

      integer i, n, nfixed
      double precision x(n), y(n), z(n)
      double precision xmove(n), ymove(n), zmove(n)
      logical xdim, ydim, zdim

      do 103 i=1,n
         if(.not.xdim) xmove(i) = 0.0d0
         if(.not.ydim) ymove(i) = 0.0d0
         if(.not.zdim) zmove(i) = 0.0d0
         if(i.le.nfixed) then
            xmove(i) = 0.0d0
            ymove(i) = 0.0d0
            zmove(i) = 0.0d0
         endif
         x(i) = x(i) + xmove(i)
         y(i) = y(i) + ymove(i)
         z(i) = z(i) + zmove(i)
         if(abs(xmove(i)).gt.0.25d0.or.abs(ymove(i)).gt.0.25d0
     +        .or.abs(zmove(i)).gt.0.25d0)
     +        write(*,*) 'Big move ',i,xmove(i),ymove(i),zmove(i)
  103 continue

      return
      end
```

B.20 period.f

```
      subroutine period(n,x,y,z,xside,yside,zside,perx,pery,perz)

      implicit none

      integer n, i
      double precision x(n), y(n), z(n)
      double precision xside, yside, zside
      logical perx, pery, perz

      if (perx.or.pery.or.perz) then
         do 5 i=1,n
            if (perx) then
               if (x(i).gt.xside) x(i)=x(i)-xside
               if (x(i).lt.0.0d0) x(i)=x(i)+xside
            endif
            if (pery) then
               if (y(i).gt.yside) y(i)=y(i)-yside
               if (y(i).lt.0.0d0) y(i)=y(i)+yside
            endif
            if (perz) then
               if (z(i).gt.zside) z(i)=z(i)-zside
               if (z(i).lt.0.0d0) z(i)=z(i)+zside
            endif
 5       continue
      endif

      return
      end
```

B.21 hardsphere.f

```
      subroutine hardsphere (xside,yside,zside,x,y,z,ncellx,
     +     ncelly,ncellz,n,perx,pery,perz,hoc,ll,xdim,ydim,zdim,nfixed,
     +     rnx,rny,rnz)

      implicit none

      integer i, n, hoc(0:10000000), ll(n), ncellx, ncelly, ncellz
      integer icelx, icely, icelz, pid
      integer done, count, nfixed
      double precision xside,yside,zside,x(n),xmove(n),z(n),zmove(n)
      double precision y(n), ymove(n), rnx, rny, rnz
      logical perx, pery, perz, xdim, ydim, zdim

      done = 0
      count = 1
 1    if (done.eq.0) then
         if (MOD(count,100).eq.0) write(*,*) 'HS count = ',count
         count = count + 1
         done = 1
         do 3 i=1,n
            xmove(i) = 0.0d0
            ymove(i) = 0.0d0
```

```
            zmove(i) = 0.0d0
 3        continue
          call wallexvol(xside,yside,zside,n,x,y,z,perx,pery,perz,hoc,ll,
     +         ncellx,ncelly,ncellz)

          do 32 i=1,n
             icelx = idint(dint(x(i)/rnx))
             icely = idint(dint(y(i)/rny))
             icelz = idint(dint(z(i)/rnz))
             pid=i
             call hbins (icelx,icely,icelz,ncellx,ncelly,ncellz,
     +            hoc,ll,n,perx,pery,perz,x,y,z,xside,yside,zside,
     +            xmove,ymove,zmove,done,nfixed,pid)
 32       continue

          do 103 i=1,n
             if(.not.xdim) xmove(i) = 0.0d0
             if(.not.ydim) ymove(i) = 0.0d0
             if(.not.zdim) zmove(i) = 0.0d0
             x(i) = x(i) + xmove(i)
             y(i) = y(i) + ymove(i)
             z(i) = z(i) + zmove(i)
 103      continue
          goto 1
       endif
       return
       end
```

B.22 wallexvol.f

```
       subroutine wallexvol (xside,yside,zside,n,x,y,z,perx,
      +     pery,perz,hoc,ll,ncellx,ncelly,ncellz)

       implicit none
       integer n,i,ncell3,icel,jcel,hoc(0:10000000),ll(n)
       integer ncellx,ncelly,ncellz
       double precision x(n), y(n), z(n)
       double precision xside,yside,zside
       logical perx, pery, perz

       ncell3 = ncellx*ncelly*ncellz
*/*************************************************************
*/     The code in here is only for flat walls.  If you want
*/     to incorporate walls that are not flat, you must insert
*/     the functional forms of the walls below
*/*************************************************************


       if (.not.perx) then
          do 10 icel=0,ncell3-1,ncellx
             i=hoc(icel)
 15          if (i.ne.0) then
                if(x(i).lt.0.5d0) x(i) = 0.5d0
                i=ll(i)
                goto 15
```

```
            endif
10        continue

          do 20 icel=ncellx-1,ncell3-1,ncellx
             i=hoc(icel)
25           if (i.ne.0) then
                if(x(i).gt.xside-0.5d0) x(i) = xside-0.5d0
                i=ll(i)
                goto 25
             endif
20        continue
       endif

       if (.not.pery) then
          do 30 icel=0,ncell3-1,ncellx*ncelly
             do 31 jcel=icel,icel+ncellx-1
                i=hoc(jcel)
35              if (i.ne.0) then
                   if(y(i).lt.0.5d0) y(i) = 0.5d0
                   i=ll(i)
                   goto 35
                endif
31           continue
30        continue

          do 40 icel=(ncelly-1)*ncellx,ncell3-1,ncellx*ncelly
             do 41 jcel=icel,icel+ncellx-1
                i=hoc(jcel)
45              if (i.ne.0) then
                   if(y(i).gt.yside-0.5d0) y(i) = yside - 0.5d0
                   i=ll(i)
                   goto 45
                endif
41           continue
40        continue
       endif

       if (.not.perz) then
          do 50 icel=0,(ncellx*ncelly)-1
             i=hoc(icel)
55           if (i.ne.0) then
                if(z(i).lt.0.5d0) z(i) = 0.5d0
                i=ll(i)
                goto 55
             endif
50        continue

          do 60 icel=ncell3-(ncellx*ncelly),ncell3-1
             i=hoc(icel)
65           if (i.ne.0) then
                if(z(i).gt.zside-0.5d0) z(i) = zside-0.5d0
                i=ll(i)
                goto 65
             endif
60        continue
```

```
      endif


      return
      end
```

B.23 hbins.f

```
      subroutine hbins (icelx,icely,icelz,ncellx,ncelly,ncellz,hoc,ll,n,
     +     perx,pery,perz,x,y,z,xside,yside,zside,xmove,ymove,
     +     zmove,done,nfixed,pid)


      implicit none
      integer icelx, ncellx, icely, ncelly, icelz, ncellz, n
      integer hoc(0:10000000), ll(n), i, dx, dy, dz
      integer dumicelx, dumicely, dumicelz, jcel, j, skip
      integer done, nfixed, pid, xch, ych, zch
      double precision x(n), y(n), z(n), xside, yside, zside
      double precision xmove(n), ymove(n), zmove(n)
      double precision xi, yi, zi, xmovei, ymovei, zmovei
      double precision xmovej, ymovej, zmovej
      double precision xmult, ymult, zmult, sqdist
      double precision dumx, dumy, dumz
      logical perx, pery, perz

      i=pid
      skip = 0
      do 53 dx=icelx+1,icelx,-1
         xmult = 0.0d0
         dumicelx = dx
         call wallcheck (dumicelx,ncellx,perx,xmult,skip)
         xch=1
         if(dx.eq.icelx) xch=0
         if (skip.eq.0) then
            do 52 dy = icely-1,icely+1
               if(dx.eq.icelx .and. dy.eq.icely-1) skip=1
               ymult = 0.0d0
               dumicely = dy
               call wallcheck (dumicely,ncelly,pery,ymult,skip)
               ych=1
               if(dy.eq.icely) ych=0
               if (skip.eq.0) then
                  do 51 dz = icelz-1,icelz+1
                     if((dx.eq.icelx).and.(dy.eq.icely)
     +                    .and.(dz.eq.icelz-1)) then
                        skip = 1
                     endif
                     zmult = 0.0d0
                     dumicelz = dz
                     call wallcheck (dumicelz,ncellz,perz,zmult,skip)
                     zch=1
                     if(dz.eq.icelz) zch=0
                     if(skip.eq.0) then
                        jcel = dumicelx+ncellx*dumicely+
```

```
     +                        ncellx*ncelly*dumicelz
                          j = hoc(jcel)
 50                       if(j.ne.0) then
                             if (j.ne.i) then
                                dumx = x(j) + xside * xmult
                                dumy = y(j) + yside * ymult
                                dumz = z(j) + zside * zmult
                                sqdist = (x(i)-dumx)*(x(i)-dumx)+
     +                               (y(i)-dumy)*(y(i)-dumy)+
     +                               (z(i)-dumz)*(z(i)-dumz)
                                if (sqdist.lt.0.99d0) then
                                   done = 0
                                   xmovei = xmove(i)
                                   ymovei = ymove(i)
                                   zmovei = zmove(i)
                                   xi = x(i)
                                   yi = y(i)
                                   zi = z(i)
                                   xmovej = xmove(j)
                                   ymovej = ymove(j)
                                   zmovej = zmove(j)
                                   call HSexvol (sqdist,xi,yi,zi,
     +                                 dumx,dumy,dumz,
     +                                 xmovei,ymovei,zmovei,
     +                                 xmovej,ymovej,zmovej,nfixed,
     +                                 i,j,xch,ych,zch)
                                   xmove(i) = xmovei
                                   ymove(i) = ymovei
                                   zmove(i) = zmovei
                                   xmove(j) = xmovej
                                   ymove(j) = ymovej
                                   zmove(j) = zmovej
                                endif
                             endif
                             j=ll(j)
                             goto 50
                          endif
                       endif
                       skip = 0
 51                 continue
                    endif
                    skip = 0
 52              continue
                 endif
                 skip = 0
 53           continue
              return
              end
```

B.24 HSexvol.f

```
      subroutine HSexvol (sqdist,xi,yi,zi,xj,yj,zj,xmovei,ymovei,
     +     zmovei,xmovej,ymovej,zmovej,nfixed,i,j,xch,ych,zch)
```

```
      implicit none

      integer nfixed, i, j, xch, ych, zch
      double precision sqdist, xi, xj, yi, yj, zi, zj, dist
      double precision xmovei, xmovej, ymovei, ymovej, zmovei, zmovej
      double precision rmove, xcomp, ycomp, zcomp


      dist = sqrt(sqdist)
      rmove = 0.5d0*(dist-1.0d0)
      xcomp = rmove*(xi-xj)/dist
      ycomp = rmove*(yi-yj)/dist
      zcomp = rmove*(zi-zj)/dist


      if(i.gt.nfixed.and.j.gt.nfixed) then
         xmovei = xmovei-xcomp
         ymovei = ymovei-ycomp
         zmovei = zmovei-zcomp
      elseif(i.gt.nfixed.and.j.le.nfixed) then
         xmovei = xmovei-xcomp-xcomp
         ymovei = ymovei-ycomp-ycomp
         zmovei = zmovei-zcomp-zcomp
      endif

      if(xch.ne.0.or.ych.ne.0.or.zch.ne.0) then
         if(i.gt.nfixed.and.j.gt.nfixed) then
            xmovej = xmovej+xcomp
            ymovej = ymovej+ycomp
            zmovej = zmovej+zcomp
         elseif(i.le.nfixed.and.j.gt.nfixed) then
            xmovej = xmovej+xcomp+xcomp
            ymovej = ymovej+ycomp+ycomp
            zmovej = zmovej+zcomp+zcomp
         endif
      endif

      return
      end
```

Appendix C

Post-processing Codes

The following Fortran and IDL codes are used to calculate properties of the simulated systems using the output file from the BD code.

C.1 calcdens.f

```
      program calcdens

*/*********************************************
*/     Program to calculate the density profile of
*/     colloids in 2D channels
*/*********************************************

      implicit none

      integer Nparts, i, p, Nframes, index, bin, bad, nbins
      parameter (index=50000)
      double precision x, xside, yside
      double precision slicewidthw, slicewidth, dist
      double precision dens(index)
      double precision rho, PI
      character*32 tpe
```

```
      Nframes = 1001
      slicewidthw = 0.1d0

      bad=0
      do 2 i=1,index
         dens(i) = 0.0d0
2     continue
      open(unit=10,file='movie.xyz',status='old')
3     read(10,*) tpe
      if (tpe.eq.'#') goto 3
      backspace(unit=10)
      read(10,*) Nparts
      read(10,*) i, tpe, tpe, xside, tpe, yside
      rho = dble(Nparts)/((xside-1.0d0)*yside)
      nbins = IDINT((xside-1.0d0)/slicewidthw)
      if(nbins.gt.index) then
         bad=1
         goto 73
      endif
      slicewidth = (xside-1.0d0-2.0d0*slicewidthw)/(nbins-2)
      backspace(unit=10)
      backspace(unit=10)
      do 4 i=1,Nframes
         read(10,*)
         read(10,*)
         do 5 p=1,Nparts
            read(10,*) tpe, x
            if(x.lt.0.5d0+slicewidthw) then
               bin = 1
            elseif (x.gt.xside-0.5d0-slicewidthw) then
               bin = nbins
            else
               bin = IDINT((x-0.5d0-slicewidthw)/slicewidth)+2
               if (bin.eq.nbins) write(*,*) 'nbins'
            endif
            dens(bin) = dens(bin)+1.0d0
5        continue
4     continue
      close(unit=10)

      open (unit=13,file='density',status='new')
      tot = 0
      write(13,*) 0, 0
      do 8 i=1,nbins
         if(i.eq.1) then
            dist = slicewidthw/2.0d0
         elseif (i.eq.nbins) then
            dist = xside-1.0d0-slicewidthw/2.0d0
         else
            dist=slicewidth*(DBLE(i)-1.5d0)+slicewidthw
         endif
         dens(i)=dens(i)/(dble(Nframes))
         if(i.eq.1.or.i.eq.nbins) then
            dens(i)=dens(i)/(yside*slicewidthw)
         else
```

```
            dens(i)=dens(i)/(slicewidth*yside)
         endif
         dens(i)=dens(i)/rho
         write(13,*) dist,dens(i)
 8    continue
      write(13,*) xside-1.0d0, 0
      close(unit=13)

 73   if(bad.eq.1) write(*,*) 'Need to increase index'

      end
```

C.2 calcconn.f

```
      program calcconn

*/***********************************************
*/     Program for calculating the connectivity of
*/     the simulated system
*/***********************************************

      implicit none
      integer Nparts, i, j, k, Nframes
      integer time, index, bad
      parameter (index=50000)
      double precision x(index), y(index), z(index), dt
      double precision hconn, vconn, zside
      double precision xside, yside, xsep, ysep, zsep
      double precision hsep
      character*32 tpe, tpe2
      logical xper, yper, zper


      xper=.true.
      yper=.true.
      zper=.false.
      Nframes = 1001


      bad=0
      do 6 j=1,index
         x(j) = 0.0d0
         y(j) = 0.0d0
         z(j) = 0.0d0
 6    continue
      open(unit=10,file='movie.xyz',status='old')
      open(unit=11,file='connectivity',status='new')
 3    read(10,*) tpe, tpe2
      if (tpe.eq.'#') then
         if (tpe2.eq.'Numparts') then
            backspace(unit=10)
            read(10,*) tpe, tpe2, tpe, Nparts
         elseif(tpe2.eq.'Timestep') then
            backspace(unit=10)
            read(10,*) tpe, tpe2, tpe, dt
```

```
         elseif(tpe2.eq.'Geometry') then
            backspace(unit=10)
            read(10,*) tpe, tpe2, tpe, xside, yside, zside
         endif
         goto 3
      endif
      backspace(unit=10)
      backspace(unit=10)

      if(Nparts.gt.index) then
         bad=1
         goto 73
      endif
      do 20 k=1,Nframes
         read(10,*)
         read(10,*) time
         do 25 j=1,Nparts
            read(10,*) tpe, x(j), y(j), z(j)
25       continue
         hconn=0.0d0
         vconn=0.0d0
         do 30 i=1,Nparts-1
            do 35 j=i+1,Nparts
               xsep=abs(x(j)-x(i))
               ysep=abs(y(j)-y(i))
               zsep=abs(z(j)-z(i))
               if(xper.and.xsep.gt.xside/2.0d0) xsep=xside-xsep
               if(yper.and.ysep.gt.yside/2.0d0) ysep=yside-ysep
               if(zper.and.zsep.gt.zside/2.0d0) zsep=zside-zsep
               if(sqrt(xsep*xsep+ysep*ysep+zsep*zsep).lt.1.05d0) then
                  hsep=sqrt(xsep*xsep+ysep*ysep)
                  if(hsep/zsep.lt.0.57735d0) then
                     vconn=vconn+1.0d0
                  else
                     hconn=hconn+1.0d0
                  endif
               endif
35          continue
30       continue
         hconn=hconn/dble(Nparts-1)
         vconn=vconn/dble(Nparts-1)
         write(11,*) dble(time)*dt,hconn,vconn
20    continue
      close(unit=10)
      close(unit=11)

73    if(bad.eq.1) write(*,*) 'Need to increase index'
      end
```

C.3 calcclust.f

```
      program calcclust

*/*************************************************
*/     Program to calculate the clusters in the system.
```

```
*/     Outputs a file "flatmovie" containing the x-
*/     and y-positions of the clusters (2D projection).
*/     Also outputs a file "clustersize" containing the
*/     cluster size distribution in the simulation. The
*/     file "clustvst" contains the average cluster
*/     size in the system versus time.
*/*****************************************************

      implicit none
      integer index1, cmax
      parameter (index1=10000)
      parameter (cmax=300)
      integer Nframes, Nparts, ll(index1,12), counter, bad
      integer time, nn(index1), i, j, k, frame
      integer found(index1), newmemb, ind, cl(cmax)
      integer csize(cmax), totcount
      double precision dt, xside, yside, zside
      double precision dist, zsep, xsep, ysep
      double precision x(index1), y(index1), z(index1)
      double precision xcol, ycol, tempx, tempy
      character*32 tpe, tpe2
      logical xper, yper, zper

      xper=.true.
      yper=.true.
      zper=.false.
      Nframes = 1001

      bad=0
      do 2 i=1,cmax
         csize(i)=0
 2    continue
      open(unit=10,file='movie.xyz',status='old')
      open(unit=11,file='flatmovie',status='new')
      open(unit=13,file='clustvst',status='new')
 3    read(10,*) tpe, tpe2
      if (tpe.eq.'#') then
         if (tpe2.eq.'Numparts') then
            backspace(unit=10)
            read(10,*) tpe, tpe2, tpe, Nparts
            write(11,*) '# Numparts      = ',Nparts
         elseif(tpe2.eq.'Timestep') then
            backspace(unit=10)
            read(10,*) tpe, tpe2, tpe, dt
            write(11,*) '# Timestep      = ',dt
         elseif(tpe2.eq.'Geometry') then
            backspace(unit=10)
            read(10,*) tpe, tpe2, tpe, xside, yside, zside
            write(11,*) '# Geometry      = `, xside, yside, zside
         endif
         goto 3
      endif
      backspace(unit=10)
      backspace(unit=10)
      if(Nparts.gt.index1) then
```

```
      bad=1
      goto 73
   endif
   totcount=0
   do 20 frame=1,Nframes
      do 25 j=1,Nparts
         do 26 i=1,12
            ll(j,i)=0
26       continue
         nn(j)=0
         found(j)=0
25    continue
      read(10,*)
      read(10,*) time
      write(11,*) Nparts
      write(11,*) time, ' fs'
      do 30 j=1,Nparts
         read(10,*) tpe, x(j), y(j), z(j)
30    continue
      do 35 i=1,Nparts
         counter=0
         do 40 j=1,Nparts
            if(i.ne.j) then
               xsep=abs(x(i)-x(j))
               ysep=abs(y(i)-y(j))
               zsep=abs(z(i)-z(j))
               if(xper.and.xsep.gt.xside/2.0d0) xsep=xside-xsep
               if(yper.and.ysep.gt.yside/2.0d0) ysep=yside-ysep
               if(zper.and.zsep.gt.zside/2.0d0) zsep=zside-zsep
               dist=sqrt(xsep*xsep+ysep*ysep+zsep*zsep)
               if(dist.lt.1.05d0) then
                  counter=counter+1
                  ll(i,counter)=j
               endif
            endif
40       continue
         nn(i)=counter
35    continue
      do 45 i=1,Nparts
         xcol=-100.0d0
         ycol=-100.0d0
         do 47 j=1,cmax
            cl(j)=0
47       continue
         if(found(i).eq.0) then
            totcount=totcount+1
            found(i)=1
            counter=1
            ind=1
            cl(counter)=i
            newmemb=1
99          if(ind.le.counter.or.newmemb.eq.1) then
               newmemb=0
               do 50 k=1,nn(cl(ind))
                  j=ll(cl(ind),k)
```

```
                    if(found(j).eq.0) then
                       newmemb=1
                       found(j)=1
                       counter=counter+1
                       cl(counter)=j
                    endif
50               continue
                 ind=ind+1
                 goto 99
              endif
              xcol=x(i)
              ycol=y(i)
              do 55 k=2,counter
                 j=cl(k)
                 tempx=x(j)
                 tempy=y(j)
                 if(xcol-tempx.gt.xside/2.0d0) then
                    tempx=tempx+xside
                 elseif(xcol-tempx.lt.-xside/2.0d0) then
                    tempx=tempx-xside
                 endif
                 if(ycol-tempy.gt.yside/2.0d0) then
                    tempy=tempy+yside
                 elseif(ycol-tempy.lt.-yside/2.0d0) then
                    tempy=tempy-yside
                 endif
                 xcol=(xcol*dble(k-1)+tempx)/dble(k)
                 ycol=(ycol*dble(k-1)+tempy)/dble(k)
55            continue
              if(counter.gt.cmax) then
                 bad=2
                 goto 73
              endif
              csize(counter)=csize(counter)+1
           endif
555        format('C',2x,f9.3,2x,f9.3,2x,f9.3)
           write(11,555) xcol, ycol, 0.0d0
45      continue
        counter=0
        do 83 i=1,cmax
           if(csize(i).ne.0) counter=counter+1
83      continue
        write(13,*) dble(time)*dt,dble(Nparts)/dble(counter)
20    continue
      close(unit=10)
      close(unit=11)
      close(unit=13)
      open(unit=12,file='clustersize',status='new')
      do 80 i=1,cmax
         write(12,*) i, dble(csize(i))/dble(totcount)
80    continue
      close(unit=12)

73    if(bad.eq.1) write(*,*) 'Need to increase index1'
      if(bad.eq.2) write(*,*) 'Need to increase cmax'
```

```
      end
```

C.4 makepositions.f

```
      program makepositions

*/***********************************************
*/     Reformats the file movie.xyz into a form
*/     that can be read in by format_pos.pro
*/***********************************************

      implicit none

      integer Nparts, i, p, Nframes, time, timeold
      double precision x, y, z, xside, yside, zside, dt
      character*32 tpe, tpe2

      Nframes = 1001


      open(unit=10,file='movie.xyz',status='old')
      open(unit=11,file='positions',status='new')
 3    read(10,*) tpe, tpe2
      if (tpe.eq.'#') then
         if (tpe2.eq.'Numparts') then
            backspace(unit=10)
            read(10,*) tpe, tpe2, tpe, Nparts
         elseif(tpe2.eq.'Timestep') then
            backspace(unit=10)
            read(10,*) tpe, tpe2, tpe, dt
         elseif(tpe2.eq.'Geometry') then
            backspace(unit=10)
            read(10,*) tpe, tpe2, tpe, xside, yside, zside
         endif
         goto 3
      endif
      backspace(unit=10)
      backspace(unit=10)
      write(11,*) Nframes, Nframes
      write(11,*) Nparts, Nparts
      write(11,*) xside, yside
      write(11,*) dt, dt
      time = 0
      do 4 i=1,Nframes
         timeold=time
         read(10,*) time
         read(10,*) time
         do 5 p=1,Nparts
            read(10,*) tpe, x, y, z
            write(11,*) x, y
 5       continue
 4    continue
      write(11,*) time-timeold, time-timeold
      close(unit=10)
```

```
    close(unit=11)
    end
```

C.5 format_pos.pro

```
function format_pos, file, per=per

;*****************************************
;    Program to read in the x-y coordinates
;    from a simulation into IDL
;*****************************************

t=read_ascii(file)
a=t.field1
nframes=a(0,0)
nparts=a(0,1)
xside=a(0,2)
yside=a(1,2)
dt=a(0,3)
interval=a(0,nframes*nparts+4)

if(keyword_set(per)) then begin
    traj=fltarr(2,nframes,4*nparts)
endif else begin
    traj=fltarr(2,nframes,nparts)
endelse

for j=0,nframes-1 do begin
    ind = long(j)*long(nparts)+4
    traj(0,j,0:nparts-1)=a(0,ind:ind+long(nparts-1))
    traj(1,j,0:nparts-1)=a(1,ind:ind+long(nparts-1))

    if(keyword_set(per)) then begin
        traj(0,j,nparts:2*nparts-1)=a(0,ind:ind+long(nparts-1))+xside
        traj(1,j,nparts:2*nparts-1)=a(1,ind:ind+long(nparts-1))

        traj(0,j,2*nparts:3*nparts-1)=a(0,ind:ind+long(nparts-1))
        traj(1,j,2*nparts:3*nparts-1)=a(1,ind:ind+long(nparts-1))+yside

        traj(0,j,3*nparts:4*nparts-1)=a(0,ind:ind+long(nparts-1))+xside
        traj(1,j,3*nparts:4*nparts-1)=a(1,ind:ind+long(nparts-1))+yside
    endif
endfor

openw,1,'datafile'
if(keyword_set(per)) then begin
    printf,1,4*nparts
endif else begin
    printf,1,nparts
endelse
printf,1,nframes
printf,1,xside
printf,1,yside
printf,1,dt
printf,1,interval
```

```
close,1

return,traj

end
```

C.6 createtri.pro

```
pro createtri,traj,mult

;***********************************
;    Program to calculate a Delaunay
;    triangulation of a set of points
;    in 2D.
;***********************************

t=read_ascii('datafile')
a=t.field1

nparts=a(0)
nframes=a(1)
g=ceil(nframes/mult)
xside=a(2)
yside=a(3)

openw,1,'triangles'
printf,1,fix(nparts)
printf,1,fix(nframes)
printf,1,g
printf,1,xside
printf,1,yside
printf,1,mult

for frame=0,nframes-1,mult do begin
    xx=traj(0,frame,*)
    yy=traj(1,frame,*)
    w=where(xx(*) ge -10.)
    x=xx(w)
    w=where(yy(*) ge -10.)
    y=yy(w)
    triangulate,x,y,tr,conn=c
    n=n_elements(c)
    printf,1,n
    for i=long(0),long(n-1) do begin
        printf,1,c(i)
    endfor
    for i=long(0),long(n_elements(x)-1) do begin
        printf,1,x(i),y(i)
    endfor
    for i=long(n_elements(x)),long(nparts-1) do begin
    printf,1,-100.,-100.
    endfor
endfor
close,1
end
```

C.7 boot.f

```
      program boot

*/*********************************************
*/     Program for calculating the g6(t) in the
*/     bulk region of 2D channels
*/*********************************************

      implicit none

      integer ind1, ind2
      parameter (ind1=201)
      parameter (ind2=109999)
      integer Nparts, i, ind, n, sze, nframe
      integer k, frame, j, indi, indio, ind2io, shortcount
      integer ind2i, count(0:ind2), c(0:ind1,0:ind2)
      integer bulk, bad
      double precision x(0:ind1,0:ind2), y(0:ind1,0:ind2),xside,yside
      double precision psioim, psiore, dt
      double precision psire, psiim, psitotre(0:ind2)
      double precision psitotim(0:ind2), angle, dist
      double precision xsep, ysep, interval, interval2
      double precision psitempre, psitempim
      double precision rho, lenscl, lenscl2, PI
      parameter (PI=3.141592654d0)


      bad=0
      open(unit=9,file='datafile',status='old')
      read(9,*)
      read(9,*)
      read(9,*) xside
      read(9,*) yside
      read(9,*) dt
      read(9,*) interval
      close(unit=9)
      do 5 i=0,ind2
         do 10 j=0,ind1
            x(j,i) = 0.0d0
            y(j,i) = 0.0d0
            c(j,i) = 0
10       continue
         count(i) = 0
         psitotre(i) = 0.0d0
         psitotim(i) = 0.0d0
5     continue

      open(unit=10,file='triangles',status='old')
      read(10,*) Nparts
      read(10,*)
      read(10,*) n
      read(10,*) xside
      read(10,*) yside
      read(10,*) interval2
```

```
      rho = dble(Nparts)/(xside-1.0d0)/yside
      lenscl = 1.0d0/sqrt(2.0d0*rho/sqrt(3.0d0))
      lenscl2 = lenscl*lenscl
      if(n.gt.ind1) then
         bad=1
         goto 73
      endif
      do 15 frame=0,n-1
         read(10,*) sze
         if(sze.gt.ind2) then
            bad=2
            goto 73
         endif
         do 20 j=0,sze-1
            read(10,*) ind
            c(frame,j) = ind
20       continue
         do 25 j=0,Nparts-1
            read(10,*) x(frame,j), y(frame,j)
25       continue
15    continue
      close(unit=10)

      do 30 frame=0,n-2
         do 35 nframe=frame,n-1
            ind=nframe-frame
            psitempre = 0.0d0
            psitempim = 0.0d0
            do 40 i=0,Nparts-1
               bulk=1
               if(y(frame,i).lt.2.0d0*lenscl.or.
     +              y(frame,i).gt.yside-2.0d0*lenscl.or.
     +              y(nframe,i).lt.2.0d0*lenscl.or.
     +              y(nframe,i).gt.yside-2.0d0*lenscl) then
                  bulk = 0
               endif
               if(x(frame,i).lt.lenscl/2.0d0+0.5d0.or.
     +              x(frame,i).gt.xside-lenscl/2.0d0-0.5d0.or.
     +              x(nframe,i).lt.lenscl/2.0d0+0.5d0.or.
     +              x(nframe,i).gt.xside-lenscl/2.0d0-0.5d0) then
                  bulk = 0
               endif
               if(bulk.ne.0) then
                  count(ind)=count(ind)+1
                  indio=c(frame,i)
                  ind2io=c(frame,i+1)-1
                  psiore = 0.0d0
                  psioim = 0.0d0
                  shortcount=0
                  do 55 k=indio,ind2io
                     if(c(frame,k).ne.i) then
                        xsep=x(frame,c(frame,k))-x(frame,i)
                        ysep=y(frame,c(frame,k))-y(frame,i)
                        dist=sqrt(xsep*xsep+ysep*ysep)
                        angle=acos(xsep/dist)
```

```
                        if(ysep.lt.0.0d0) then
                           angle=2.0d0*PI-angle
                        endif
                        angle=angle*6.0d0
                        psiore=psiore+cos(angle)
                        psioim=psioim+sin(angle)
                        shortcount=shortcount+1
                     endif
55                continue
                  psiore=psiore/dble(shortcount)
                  psioim=psioim/dble(shortcount)

                  ind2i=c(nframe,i+1)-1
                  indi=c(nframe,i)
                  shortcount=0
                  psire = 0.0d0
                  psiim = 0.0d0
                  do 75 k=indi,ind2i
                     if(c(nframe,k).ne.i) then
                        xsep=x(nframe,c(nframe,k))-x(nframe,i)
                        ysep=y(nframe,c(nframe,k))-y(nframe,i)
                        dist=sqrt(xsep*xsep+ysep*ysep)
                        angle=acos(xsep/dist)
                        if(ysep.lt.0.0d0) then
                           angle=2.0d0*PI-angle
                        endif
                        angle=angle*6.0d0
                        psire=psire+cos(angle)
                        psiim=psiim+sin(angle)
                        shortcount=shortcount+1
                     endif
75                continue
                  psire=psire/dble(shortcount)
                  psiim=psiim/dble(shortcount)
                  psitempre=psitempre+(psiore*psire+psioim*psiim)
                  psitempim=psitempim+(psiore*psiim-psioim*psire)
               endif
40          continue
            psitotre(ind) = psitotre(ind) + psitempre
            psitotim(ind) = psitotim(ind) + psitempim
35       continue
30    continue

      open(unit=11,file='bulk-g6oft',status='new')
      do 85 k=0,n-1
         psitotre(k)=psitotre(k)/dble(count(k))
         psitotim(k)=psitotim(k)/dble(count(k))
         write(11,*) dble(k)*dt*interval*interval2/lenscl2,
     +        psitotre(k),count(k)
85    continue
      close(unit=11)


73    if(bad.eq.1) write(*,*) 'Need to increase ind1'
      if(bad.eq.2) write(*,*) 'Need to increase ind2'
```

```
      end
```

C.8 countdef.f

```
      program countdef

*/***********************************************
*/     Program for calculating the concentration
*/     of defects in the 2D channel system
*/***********************************************

      implicit none

      integer index
      parameter (index=200000)
      integer Nparts, i, ind, n, sze
      integer k, frame, j, indj, shortcount
      integer ind2j, c(0:index)
      integer totcount,wtotcount,midcount,highcount,lowcount,btotcount
      integer blowcount, bad
      integer wlowcount, whighcount,bhighcount
      double precision x(0:index), y(0:index), xside
      double precision dt, slicewidth, yside
      double precision interval, interval2

      bad=0
      open(unit=9,file='datafile',status='old')
      read(9,*)
      read(9,*)
      read(9,*) xside
      read(9,*) yside
      read(9,*) dt
      read(9,*) interval
      close(unit=9)

      open(unit=10,file='triangles',status='old')
      read(10,*) Nparts
      read(10,*)
      read(10,*) n
      read(10,*) xside
      read(10,*) yside
      read(10,*) interval2

      slicewidth = 0.5d0*sqrt(sqrt(3.0d0)/(2.0d0*
     +            (dble(Nparts)/(xside-1.0d0)/yside)))

      open(unit=11,file='defects',status='new')
      open(unit=12,file='wall-defects',status='new')
      open(unit=13,file='bulk-defects',status='new')
      do 15 frame=0,n-1
         do 5 i=0,index
            x(i) = 0.0d0
            y(i) = 0.0d0
            c(i) = 0
```

```
5       continue
        read(10,*) sze
        if(sze.gt.index) then
           bad=1
           goto 73
        endif
        do 20 j=0,sze-1
           read(10,*) ind
           c(j) = ind
20      continue
        do 25 j=0,Nparts-1
           read(10,*) x(j), y(j)
25      continue
        totcount=0
        wtotcount=0
        highcount=0
        lowcount=0
        midcount=0
        wlowcount=0
        whighcount=0
        blowcount=0
        bhighcount=0
        btotcount=0
        do 30 j=0,Nparts-1
           if(y(j).gt.4.0d0*slicewidth.and.
     +          y(j).lt.yside-4.0d0*slicewidth) then
              totcount=totcount+1
              shortcount=0
              indj=c(j)
              ind2j=c(j+1)-1
              if(x(j).lt.slicewidth.or.x(j).gt.xside-slicewidth) then
                 wtotcount=wtotcount+1
                 do 35 k=indj,ind2j
                    if(c(k).ne.j) then
                       if(x(c(k)).gt.slicewidth.and.
     +                     x(j).lt.slicewidth) then
                          shortcount=shortcount+1
                       elseif(x(c(k)).lt.xside-slicewidth
     +                        .and.x(j).gt.xside-slicewidth) then
                          shortcount=shortcount+1
                       endif
                    endif
35               continue
                 if (shortcount.le.1) lowcount=lowcount+1
                 if (shortcount.eq.2) midcount=midcount+1
                 if (shortcount.ge.3) highcount=highcount+1
                 if (shortcount.le.1) wlowcount=wlowcount+1
                 if (shortcount.ge.3) whighcount=whighcount+1
              else
                 btotcount=btotcount+1
                 do 45 k=indj,ind2j
                    if(c(k).ne.j) then
                       shortcount=shortcount+1
                    else
                       write(*,*) 'Bulk particle is on the boundary'
```

```
                  endif
 45               continue
                  if (shortcount.le.5) lowcount=lowcount+1
                  if (shortcount.eq.6) midcount=midcount+1
                  if (shortcount.ge.7) highcount=highcount+1
                  if (shortcount.le.5) blowcount=blowcount+1
                  if (shortcount.ge.7) bhighcount=bhighcount+1
               endif
            endif
 30       continue

          write(11,*) dble(frame)*dble(interval)*dble(interval2)*dt*
     +         dble(Nparts)/(xside-1.0d0)/yside*2.0d0/sqrt(3.0d0),
     +         dble(lowcount+highcount)/dble(totcount),totcount
          write(12,*) dble(frame)*dble(interval)*dble(interval2)*dt*
     +         dble(Nparts)/(xside-1.0d0)/yside*2.0d0/sqrt(3.0d0),
     +         dble(wlowcount+whighcount)/dble(wtotcount),wtotcount
          if (btotcount.ne.0) then
             write(13,*) dble(frame)*dble(interval)*dble(interval2)*dt*
     +            dble(Nparts)/(xside-1.0d0)/yside*2.0d0/sqrt(3.0d0),
     +            dble(blowcount+bhighcount)/dble(btotcount),btotcount
          endif
 15    continue
       close(unit=11)
       close(unit=12)
       close(unit=13)
       close(unit=10)

 73    if(bad.eq.1) write(*,*) 'Need to increase index'

       end
```

C.9 calcspace.f

```
       program calcspace

*/*********************************************
*/     Program for calculating the spacing between
*/     clusters in the thin-slit system
*/*********************************************

       implicit none
       integer index
       parameter (index=200000)
       integer Nparts, i, ind, n, sze, bad
       integer k, frame, j, indj, nbins
       integer ind2j,c(0:index), bin
       double precision x(0:index), y(0:index), tcount
       double precision slicewidth,xside,yside, interval2
       double precision space, sp(index), dt, interval
       double precision fcount, aspace, maxlen
       parameter (maxlen=30.0d0)


       bad=0
```

```
      slicewidth = 0.05d0
      nbins=INT(maxlen/slicewidth)
      if(nbins.gt.index) then
         bad=1
         goto 73
      endif
      do 99 i=1,nbins
         sp(i)=0.0d0
 99   continue

      open(unit=9,file='datafile',status='old')
      read(9,*)
      read(9,*)
      read(9,*)
      read(9,*)
      read(9,*) dt
      read(9,*) interval
      close(unit=9)

      open(unit=10,file='triangles',status='old')
      read(10,*) Nparts
      read(10,*)
      read(10,*) n
      read(10,*) xside
      read(10,*) yside
      read(10,*) interval2
      if(Nparts.gt.index) then
         bad=1
         goto 73
      endif
      open(unit=11,file='spacing',status='new')
      open(unit=12,file='space-vs-t',status='new')
      tcount=0.0d0
      do 15 frame=0,n-1
         fcount=0.0d0
         aspace=0.0d0
         do 5 i=0,index
            x(i) = 0.0d0
            y(i) = 0.0d0
            c(i) = 0
 5       continue
         read(10,*) sze
         if(sze.gt.index) then
            bad=1
            goto 73
         endif
         do 20 j=0,sze-1
            read(10,*) ind
            c(j) = ind
 20      continue
         do 25 j=0,Nparts-1
            read(10,*) x(j), y(j)
 25      continue
         do 30 j=0,Nparts-1
            if(x(j).ge.xside*0.5d0.and.x(j).le.xside*1.5d0.and.
```

```
     +          y(j).ge.yside*0.5d0.and.y(j).le.yside*1.5d0) then
                indj=c(j)
                ind2j=c(j+1)-1
                do 45 k=indj,ind2j
                   if(c(k).eq.j) write(*,*) 'Particle is on boundary'
                   tcount=tcount+1.0d0
                   fcount=fcount+1.0d0
                   space=sqrt((x(j)-x(c(k)))*(x(j)-x(c(k)))+
     +                  (y(j)-y(c(k)))*(y(j)-y(c(k))))
                   if(space.gt.maxlen) then
                      bad=2
                      goto 73
                   endif
                   bin=INT(space/slicewidth)
                   sp(bin)=sp(bin)+1.0d0
                   aspace=aspace+space
 45             continue
             endif
 30       continue
          write(12,*) dble(frame)*interval*interval2*dt,aspace/fcount
 15    continue
       do 999 i=1,nbins
          write(11,*) (dble(i)-0.5d0)*slicewidth,sp(i)/tcount/slicewidth
 999   continue

       close(unit=12)
       close(unit=11)
       close(unit=10)

 73    if(bad.eq.1) write(*,*) 'Need to increase index'
       if(bad.eq.2) write(*,*) 'Need to increase maxlen'
       end
```

C.10 plottri.pro

```
pro plottri,x,y

;*********************************
;    Program to plot the connectivity
;    (as defined by Delaunay
;    triangulation) of a set of
;    points in 2D
;*********************************

triangulate,x,y,tr,conn=c

for i=0,n_elements(tr)/3-1 do begin
    g=[tr[*,i],tr[0,i]]
    oplot,x[g],y[g]
endfor

end
```

C.11 colortri.pro

```
pro colortri,x,y,c,xside,yside,xper=xper

;*************************************
;    Program to plot the defect structure
;    of a set of points in 2D
;*************************************



circle=findgen(17)*2.*!Pi/16.
usersym,cos(circle),sin(circle),/fill

xsd=xside
if(not keyword_set(xper)) then xsd=xsd-1.

rho=1.*n_elements(x)/xsd/yside
lenscl=1./sqrt(2.*rho/sqrt(3.))

for i=0,n_elements(x)-1 do begin
    nlist=c[c[i]:c[i+1]-1]
    if(not keyword_set(xper)) then begin
        if (x(i) lt lenscl/2.+0.5 or x(i) gt xside-lenscl/2.-0.5) then begin
            count=0
            for j=0,n_elements(nlist)-1 do begin
                if (nlist(j) ne i) then begin
                    if (x(nlist(j)) gt lenscl/2.+0.5 and x(i) lt $
                    lenscl/2.+0.5) then begin
                        count = count + 1
                    endif else begin
                        if (x(nlist(j)) lt xside-lenscl/2.-0.5 and x(i) gt $
                        xside-lenscl/2.-0.5) then begin
                            count = count + 1
                        endif
                    endelse
                endif
            endfor
            if count le 1 then begin
                oplot,[x(i)],[y(i)],psym=8
            endif else begin
                if count ge 3 then begin
                    oplot,[x(i)],[y(i)],psym=5
                endif
            endelse
        endif else begin
            if n_elements(nlist) le 5 then begin
                oplot,[x(i)],[y(i)],psym=8
            endif else begin
                if n_elements(nlist) ge 7 then begin
                    oplot,[x(i)],[y(i)],psym=5
                endif
            endelse
        endelse
    endif else begin
        if n_elements(nlist) le 5 then begin
            oplot,[x(i)],[y(i)],psym=8
```

```
        endif else begin
            if n_elements(nlist) ge 7 then begin
                oplot,[x(i)],[y(i)],psym=5
            endif
        endelse
    endelse
endfor

return
end
```

Bibliography

[1] Rabinow, J. *AIEE Trans.*, **1948**, *67*, 1308–1315.

[2] Gravesen, P.; Branebjerg, J.; Jensen, O. S. *J. Micromech. Microeng.*, **1993**, *3*, 168–182.

[3] Doyle, P. S.; Bibette, J.; Bancaud, A.; Viovy, J.-L. *Science*, **2002**, *295*, 2237.

[4] Minc, N.; Fütterer, C.; Dorfman, K. D.; Bancaud, A.; Gosse, C.; Goubault, C.; Viovy, J.-L. *Anal. Chem.*, **2004**, *76*, 3770.

[5] Rosensweig, R. *Ferrohydrodynamics.* Cambridge University Press, 1985.

[6] Winslow, W. M. *J. Appl. Phys.*, **1949**, *20*, 1137.

[7] Nèel, L. *Ann. Geophys.*, **1949**, *5*, 99.

[8] Ivey, M.; Liu, J.; Zhu, Y.; Cutillas, S. *Phys. Rev. E*, **2000**, *63*, 011403–1.

[9] Mohebi, M.; Jamasbi, N.; Liu, J. *Phys. Rev. E*, **1996**, *54*(5), 5407–5413.

[10] Liu, J.; Lawrence, E. M.; Wu, A.; Ivey, M. L.; Flores, G. A.; Javier, K.; Bibette, J.; Richard, J. *Phys. Rev. Lett.*, **1995**, *74*(14), 2828–2831.

[11] Ukai, T.; Maekawa, T. *Phys. Rev. E*, **2004**, *69*, 032501.

[12] Squires, T. M.; Quake, S. R. *Rev. Mod. Phys.*, **2005**, *77*(3), 977–1026.

[13] Dendukuri, D.; Pregibon, D. C.; Collins, J.; Hatton, T. A.; Doyle, P. S. *Nat. Mater.*, **2006**, *5*, 365–369.

[14] Xia, Y.; Whitesides, G. *Annu. Rev. Mater. Sci.*, **1998**, *28*, 153–184.

[15] Carletto, P.; Bossis, G. *J. Phys.: Condens. Matter*, **2003**, *15*, S1437.

[16] Helseth, L. E.; Backus, T.; Johansen, T. H.; Fischer, T. M. *Langmuir*, **2005**, *21*, 7518.

[17] Hatch, A.; Kamholz, A. E.; Holman, G.; Yager, P.; Böhringer, K. F. *J. Microelectromech. Syst.*, June 2001, *10*(2), 215–221.

[18] Hayes, M. A.; Polson, N. A.; Garcia, A. A. *Langmuir*, **2001**, *17*, 2866.

[19] Rida, A.; Gijs, M. A. M. *Appl. Phys. Lett.*, **2004**, *85*(21), 4986.

[20] Rida, A.; Gijs, M. A. M. *Anal. Chem.*, **2004**, *76*, 6239.

[21] Inglis, D. W.; Riehn, R.; Austin, R. H.; Sturm, J. C. *Appl. Phys. Lett.*, **2004**, *85*(21), 5093.

[22] Randall, G. C.; Doyle, P. S. *Phys. Rev. Lett.*, **2004**, *93*(5), 058102.

[23] Haw, M. D. *J. Phys.: Condens. Matter*, **2002**, *14*, 7769–7779.

[24] Öttinger, H. C. *Stochastic Processes in Polymeric Fluids: Tools and Examples for Developing Simulation Algorithms.* Springer, Berlin, 1996.

[25] Frenkel, D.; Smit, B. *Understanding Molecular Simulation from Algorithms to Applications.* MPG Books Ltd, Bodmin, Great Britain, second edition, 2002.

[26] Russel, W. B.; Saville, D. A.; Schowalter, W. R. *Colloidal Dispersions.* Cambridge University Press, New York, NY, 1989.

[27] Heyes, D.; Melrose, J. *J. Non-Newtonian Fluid Mech.*, **1993**, *46*, 1–28.

[28] Strating, P. *Phys. Rev. E*, February 1999, *59*(2), 2175–2187.

[29] Barenbrug, T. M. A. O. M.; Peters, E. A. J. F.; Schieber, J. D. *J. Chem. Phys.*, **2002**, *117*, 9202.

[30] Carpen, I. C.; Brady, J. F. *J. Rheol.*, November/December 2005, *49*(6), 1483–1502.

[31] Peters, E. A. J. F.; Barenbrug, T. M. A. O. M. *Phys. Rev. E*, **2002**, *66*, 056701.

[32] Lawrence, E. M.; Ivey, M. L.; Flores, G. A.; Liu, J.; Bibette, J.; Richard, J. *Int. J. Mod. Phys. B*, **1994**, *8*, 2765–2777.

[33] Haghgooie, R.; Doyle, P. S. *Phys. Rev. E*, **2004**, *70*, 061408.

[34] Haghgooie, R.; Doyle, P. S. *Phys. Rev. E*, **2005**, *72*, 011405.

[35] Li, R. H. C.; Doyle, P. S. *Langmuir*, **2006**, *22*, 3601–3605.

[36] Kosterlitz, J.; Thouless, J. *J. Phys. C*, **1973**, *6*, 1181.

[37] Halperin, B. I.; Nelson, D. R. *Phys. Rev. Lett.*, **1978**, *41*, 121.

[38] Young, A. P. *Phys. Rev. B*, **1979**, *19*, 1855.

[39] Kusner, R. E.; Mann, J. A.; Kerins, J.; Dahm, A. J. *Phys. Rev. Lett.*, **1994**, *73*(23), 3113.

[40] Zahn, K.; Lenke, R.; Maret, G. *Phys. Rev. Lett.*, **1999**, *82*(13), 2721–2724.

[41] Zahn, K.; Maret, G. *Phys. Rev. Lett.*, **2000**, *85*(17), 3656.

[42] Branício, P. S.; Rino, J.-P.; Studart, N. *Phys. Rev. B*, **2001**, *64*, 193413.

[43] Binder, K.; Sengupta, S.; Nielaba, P. *J. Phys.: Condens. Matter*, **2002**, *14*, 2323.

[44] Jaster, A. *Phys. Rev. E*, **1999**, *59*(3), 2594.

[45] Bagchi, K.; Andersen, H. C.; Swope, W. *Phys. Rev. Lett.*, **1996**, *76*(2), 255.

[46] Watanabe, H.; Yukawa, S.; Ozeki, Y.; Ito, N. *Phys. Rev. E*, **2004**, *69*, 045103(R).

[47] Terao, T.; Nakayama, T. *Phys. Rev. E*, **1999**, *60*(6), 7157.

[48] Schweigert, I. V.; Schweigert, V. A.; Peeters, F. M. *Phys. Rev. Lett.*, **2000**, *84*(19), 4381.

[49] Bubeck, R.; Bechinger, C.; Neser, S.; Leiderer, P. *Phys. Rev. Lett.*, **1999**, *82*(16), 3364.

[50] Bubeck, R.; Leiderer, P.; Bechinger, C. *Progr. Colloid Polym. Sci.*, **2001**, *118*, 73.

[51] Lai, Y.-J.; I, L. *Phys. Rev. E*, **2001**, *64*, 015601(R).

[52] Kong, M.; Partoens, B.; Peeters, F. M. *Phys. Rev. E*, **2003**, *67*, 021608.

[53] Kong, M.; Partoens, B.; Matulis, A.; Peeters, F. M. *Phys. Rev. E*, **2004**, *69*, 036412.

[54] Chakrabarti, J.; Krishnamurthy, H. R.; Sood, A. K.; Sengupta, S. *Phys. Rev. Lett.*, **1995**, *75*(11), 2232.

[55] Wei, Q.-H.; Bechinger, C.; Rudhardt, D.; Leiderer, P. *Phys. Rev. Lett.*, **1998**, *81*(12), 2606.

[56] Frey, E.; Nelson, D. R.; Radzihovsky, L. *Phys. Rev. Lett.*, **1999**, *83*(15), 2977.

[57] Teng, L.-W.; Tu, P.-S.; I, L. *Phys. Rev. Lett.*, **2003**, *90*(24), 245004.

[58] Segalman, R. A.; Hexemer, A.; Kramer, E. J. *Macromol.*, **2003**, *36*, 6831.

[59] Segalman, R. A.; Hexemer, A.; Kramer, E. J. *Phys. Rev. Lett.*, **2003**, *91*(19), 196101.

[60] Piacente, G.; Schweigert, I. V.; Betouras, J. J.; Peeters, F. M. *Phys. Rev. B*, **2004**, *69*, 045324.

[61] Lin, K. H.; Crocker, J. C.; Prasad, V.; Schofield, A.; Weitz, D. A.; Lubensky, T. C.; Yodh, A. G. *Phys. Rev. Lett.*, **2000**, *85*, 1770.

[62] Dullens, R. P. A.; Kegel, W. K. *Phys. Rev. Lett.*, **2004**, *92*, 195702.

[63] de Villeneuve, V. W. A.; Dullens, R. P. A.; Aarts, D. G. A. L.; Groeneveld, E.; Scherff, J. H.; Kegel, W. K.; Lekkerkerker, H. N. W. *Science*, **2005**, *309*, 1231.

[64] Auer, S.; Frenkel, D. *Phys. Rev. Lett.*, **2003**, *91*(1), 015703.

[65] Blanco, A.; Chomski, E.; Grabtchak, S.; Ibisate, M.; John, S.; Leonard, S. W.; Lopez, C.; Meseguer, F.; Miguez, H.; Mondia, J. P.; Ozin, G. A.; Toader, O.; van Driel, H. M. *Nature*, **2000**, *405*, 437.

[66] Saado, Y.; Golosovsky, M.; Davidov, D.; Frenkel, A. *Phys. Rev. B*, **2002**, *66*, 195108.

[67] Stendahl, J. C.; Li, L.; Claussen, R. C.; Stupp, S. I. *Biomaterials*, **2004**, *25*, 5847.

[68] Zhao, B.; Hu, H.; Mandal, S. K.; Haddon, R. C. *Chem. Mater.*, **2005**, *17*, 3235.

[69] van Blaaderen, A.; Ruel, R.; Wiltzius, P. *Nature*, **1997**, *385*(6614), 321.

[70] Guo, Q.; Arnoux, C.; Palmer, R. E. *Langmuir*, **2001**, *17*, 7150.

[71] Su, G.; Guo, Q.; Palmer, R. E. *Langmuir*, **2003**, *19*, 9669.

[72] Pesché, R.; Kollmann, M.; Nägele, G. *Phys. Rev. E*, **2001**, *64*, 052401.

[73] Zahn, K.; Méndez-Alcaraz, J. M.; Maret, G. *Phys. Rev. Lett.*, **1997**, *79*(1), 175–178.

[74] Zhang, H.; Widom, M. *Phys. Rev. E*, **1995**, *51*, 2099.

[75] Reichhardt, C.; Reichhardt, C. O. *Phys. Rev. Lett.*, **2003**, *90*, 095504.

[76] Nelson, D. *Phase Transitions and Critical Phenomena.* Academic Press, London, 1983. edited by C. Domb and J.L. Lebowitz.

[77] Strandburg, K. J. *Rev. Mod. Phys.*, **1988**, *60*(1), 161.

[78] Löwen, H. *Phys. Rev. E*, **1996**, *53*(1), R29.

[79] Gao, J.; Luedtke, W. D.; Landman, U. *Phys. Rev. Lett.*, **1997**, *79*(4), 705–708.

[80] Broughton, J. Q.; Gilmer, G. H.; Weeks, J. D. *Phys. Rev. B*, **1982**, *25*(7), 4651.

[81] Allen, M. P.; Frenkel, D.; Gignac, W.; McTague, J. P. *J. Chem. Phys.*, **1983**, *78*(6), 4206.

[82] Xia, Y.; Whitesides, G. M. *Angew. Chem., Int. Ed. Engl.*, **1998**, *37*, 550.

[83] Dynal reports the magnetic susceptibility of a single M-270 bead to be 60×10^{-5} m^3/kg. When non-dimensionalized with the bead density for use in SI units the result $\chi = 0.96$ is obtained.

[84] Crocker, J. C.; Grier, D. G. *J. Colloid Interface Sci.*, **1996**, *179*, 298.

[85] Savin, T. *Multiple particle tracking to asses the microstructure of biological fluids.* PhD thesis, Massachusetts Institute of Technology, August 2006.

[86] Kalia, R.; Vashishta, P. *J. Phys. C*, **1981**, *14*, L643.

[87] Pieranski, P.; Strzelecki, L.; Pansu, B. *Phys. Rev. Lett.*, **1983**, *50*(12), 900.

[88] Neser, S.; Bechinger, C.; Leiderer, P. *Phys. Rev. Lett.*, **1997**, *79*(12), 2348.

[89] Bedanov, V. M.; Peeters, F. M. *Phys. Rev. B*, **1994**, *49*(4), 2667.

[90] Bubeck, R.; Leiderer, P.; Bechinger, C. *Europhys. Lett.*, **2002**, *60*(3), 474.

[91] Wang, H.; Zhu, Y.; Boyd, C.; Luo, W.; Cebers, A.; Rosensweig, R. E. *Phys. Rev. Lett.*, **1994**, *72*, 1929.

[92] Minc, N.; Bokov, P.; Zeldovich, K. B.; Fütterer, C.; Viovy, J.-L.; Dorfman, K. D. *Electrophoresis*, **2005**, *26*, 362.

[93] Liu, J.; Mou, T.; Zhu, Y.; Haddadian, E.; Pousset, J. *J. Intell. Mater. Syst. Struct.*, **1996**, *7*, 583.

[94] Grasselli, Y.; Bossis, G.; Lemaire, E. *J. Phys. II France*, **1994**, *4*, 253.

[95] Zhou, L.; Wen, W.; Sheng, P. *Phys. Rev. Lett.*, **1998**, *81*, 1509.

[96] Gross, M. *Phys. Rev. E*, **1998**, *58*, 6124.

[97] Halsey, T. C.; Toor, W. *Phys. Rev. Lett.*, **1990**, *65*, 2820.

[98] Martin, J. E.; Odinek, J.; Halsey, T. C. *Phys. Rev. Lett.*, **1992**, *69*, 1524.

[99] Fermigier, M.; Gast, A. P. *J. Colloid Interface Sci.*, **1992**, *154*(2), 522–539.

[100] Howard, J. *Mechanics of Motor Proteins and the Cytoskeleton.* Sinauer Associates, Inc., Sunderland, Massachusetts, 2001.

[101] Furst, E. M.; Gast, A. P. *Phys. Rev. E*, **2000**, *62*, 6916.

[102] Klingenberg, D. J. *AIChE J*, **2001**, *47*, 246.

[103] Uejima, H. *Jpn. J. Appl. Phys.*, **1972**, *11*, 319.

[104] Volkova, O.; Cutillas, S.; Bossis, G. *Phys. Rev. Lett.*, **1999**, *82*, 233.

[105] Parthasarathy, M.; Klingenberg, D. J. *J. Non-Newtonian Fluid Mech.*, **1999**, *81*, 83.

[106] Kuzhir, P.; Bossis, G.; Bashtovoi, V. *J. Rheol.*, **2003**, *47*, 1373.

[107] Kuzhir, P.; Bossis, G.; Bashtovoi, V.; Volkova, O. *J. Rheol.*, **2003**, *47*, 1385.

[108] Bonnecaze, R. T.; Brady, J. F. *J. Chem. Phys.*, **1992**, *96*, 2183.

[109] Tamura, H.; Doi, M. *J. Phys. Soc. Jpn.*, **1992**, *61*, 3984.

[110] Pappas, Y.; Klingenberg, D. J. *Rheol. Acta*, **2006**, *45*, 621.

[111] Klingenberg, D. J.; Zukoski, C. F. *Langmuir*, **1990**, *6*, 15.

[112] Melle, S.; Calderón, O. G.; Rubio, M. A.; Fuller, G. G. *J. Non-Newtonian Fluid Mech.*, **2002**, *102*, 135.

[113] Melle, S.; Calderón, O. G.; Rubio, M. A.; Fuller, G. G. *Phys. Rev. E*, **2003**, *68*, 041503.

[114] Martin, J. E. *Phys. Rev. E*, **2000**, *63*, 011406.

[115] Melle, S.; Martin, J. E. *J. Chem. Phys.*, **2003**, *118*, 9875.

[116] Gast, A. P.; Zukoski, C. F. *Adv. Colloid Interface Sci.*, **1989**, *30*, 153.

[117] Promislow, J. H. E.; Gast, A. P.; Fermigier, M. *J. Chem. Phys.*, **1995**, *102*(13), 5492.

[118] Deen, W. M. *Analysis of Transport Phenomena.* Oxford University Press, New York, 1998.

[119] Klingenberg, D. J.; van Swol, F.; Zukoski, C. F. *J. Chem. Phys.*, **1991**, *94*, 6160.

[120] Brunet, E.; Degré, G.; Okkels, F.; Tabeling, P. *J. Colloid Interface Sci.*, **2005**, *282*, 58.

[121] Leighton, D.; Acrivos, A. *J. Fluid Mech.*, **1987**, *181*, 415.

[122] Wu, D.; Luo, Y.; Zhou, X.; Dai, Z.; Lin, B. *Electrophoresis*, **2005**, *26*, 211–218.

[123] Hayes, M. A.; Polson, N. A.; Phayre, A. N.; Garcia, A. A. *Anal. Chem.*, **2001**, *73*, 5896.

[124] Helgesen, G.; Skjeltorp, A. T.; Mors, P. M.; Botet, R.; Jullien, R. *Phys. Rev. Lett.*, **1988**, *61*(15), 1736–1739.

[125] Hoerstrup, S. P.; Zund, G.; Schoeberlein, A.; Ye, Q.; Vogt, P. R.; Turina, M. I. *Ann. Thorac. Surg.*, **1998**, *66*, 1653.

[126] Klucher, K. M.; Gerlach, M. J.; Daley, G. Q. *Nucleic Acids Res.*, **1997**, *25*, 4858.

[127] Fu, A. Y.; Spence, C.; Scherer, A.; Arnold, F. H.; Quake, S. R. *Nat. Biotechnol.*, **1999**, *17*, 1109.

[128] Stange, G.; Casteele, M. V. D.; Heimberg, H. *Methods Mol. Med.*, **2003**, *83*, 15.

[129] Higuchi, A.; Yamamiya, S.; Yoon, B. O.; Sakurai, M.; Hara, M. *J. Biomed. Mater. Res.*, **2004**, *68A*, 34.

[130] Polouckova, A.; Vodvarkova, A.; Kobylka, P.; Hruba, A.; Gasova, Z.; Marinov, I.; Fales, I.; Sedlacek, P.; Kozak, T.; Stary, J. *Neoplasma*, **2001**, *48*, 374.

[131] Cummings, E. B. *IEEE Eng. Med. Biol. Mag.*, **2003**, *22*, 75.

[132] Voldman, J.; Braff, R. A.; Toner, M.; Gray, M. L.; Schmidt, M. A. *Biophys. J.*, **2001**, *80*, 531.

[133] MacDonald, M. P.; Spalding, G. C.; Dholakia, K. *Nature*, **2003**, *426*, 421.

[134] Schumm, M.; Lang, P.; Taylor, G.; Kuci, S.; Klingebiel, T.; Buhring, H. J.; Geiselhart, A.; Niethammer, D.; Handgretinger, R. *J. Hematother.*, **1999**, *8*, 209.

[135] Partington, K. M.; Jenkinson, E. J.; Anderson, G. *J. Immunol. Methods*, **1999**, *223*, 195.

[136] Moore, L. R.; Zborowski, M.; Sun, L.; Chalmers, J. J. *J. Biochem. Biophys. Methods*, **1998**, *37*, 12359.

[137] Perotti, C.; Fante, C. D.; Viarengo, G. L.; Bergamaschi, P.; Tinelli, C.; Bellotti, L.; Marchesi, A.; Parisi, C.; Salvaneschi, L. *Stem Cells Dev.*, **2004**, *13*, 350.

[138] Nakamura, M.; Decker, K.; Chosy, J.; Comella, K.; Melnik, K.; Moore, L.; Lasky, L. C.; Zborowski, M.; Chalmers, J. J. *Biotechnol. Prog.*, **2001**, *17*, 1145.

[139] Pregibon, D. C.; Toner, M.; Doyle, P. S. *Langmuir*, **2006**, *22*, 5122.

[140] Randall, G. C.; Doyle, P. S. *Proc. Natl. Acad. Sci. USA*, **2005**, *102*(31), 10813.